Universidade de Aveiro Departamento de Engenharia de Materiais e Cerâmica
2013

Muhammad Asif Rafiq

Propriedades electromecânicas de materiais à base de niobato de potássio e sódio

Electromechanical properties of engineered lead free potassium sodium niobate based materials

Universidade de Aveiro
2013
Departamento de Engenharia de Materiais e Cerâmica

Muhammad Asif Rafiq

Propriedades electromecânicas de materiais à base de niobato de potássio e sódio

Electromechanical properties of engineered lead free potassium sodium niobate based materials

Tese apresentada à Universidade de Aveiro para cumprimento dos requisitos necessários à obtenção do grau de Doutor em Ciencia e Engenharia de Materiais, realizada sob a orientação científica da Doutora M. Elisabete Costa, Professora Auxiliar, e da Doutora Paula M. Vilarinho, Professora Associada, ambas do Departamento de Engenharia de Materiais e Cerâmica da Universidade de Aveiro.

Dissertation presented to the University of Aveiro to obtain the Doctor degree in Materials Science and Engineering, under scientific supervision of Dr. M. Elizabete Costa, Assistant Professor, and Dr. Paula M. Vilarinho, Associated Professor, both at the Department of Materials and Ceramics Engineering of the University of Aveiro.

Apoio financeiro da FCT.

To my Parents, Wife, Kids
and Teachers

o júri

presidente

Prof. Doutor Nelson Fernando Pacheco da Rocha
Professor Catedrático da Universidade de Aveiro

Prof. Doutor Joaquim Manuel Vieira
Professor Catedrático da Universidade de Aveiro

Prof. Doutor Ricardo Jiménez Riobóo
Tenured Scientist CSIC do Instituto de Ciencia de Materiales de Madrid

Prof. Doutor Abílio de Jesus Monteiro Almeida
Professor Associado da Faculdade de Ciências da Universidade do Porto

Prof. Doutor Mário António Caixeiro Castro Pereira
Professor Auxiliar da Escola de Ciências da Universidade do Minho

Prof. Doutora Maria Elizabete Jorge Vieira da Costa
Professora Auxiliar da Universidade de Aveiro

Acknowledgements

The work for this thesis was done during the last four years 2010 – 2013 in the Department of Materials and Ceramics Engineering. First year was focused mainly on the completion of the course work and planning for the experimental work, which I did in the coming years.
I am most grateful to my supervisors Prof. M. Elisabete V. Costa, and Prof. Paula M. Vilarinho for their support, advice and guidance for the completion of this work.

Without external collaborations, it would have been difficult to work on all of our ideas and explore new corridors, as we did. I am thankful to Prof. Ian M. Reaney (Uni. of Sheffield, UK), for the support and discussions related to the transmission electron microscopy analysis. I am also thankful to Dr. Marco Deluca and Prof. Peter Supancic (Institut für Struktur- und Funktionskeramik, Montanuniversitaet Leoben, Austria) for the Raman spectroscopy studies and discussions and for welcoming and hosting me in Leoben, Austria, as well.

The effort of the staff members of the department; Maria Joao, Ana Ribeiro, Celia Miranda, Marta Ferro, Bruno Almeida, Jacinto Alves, Octávio Contente and Luisa Costa were invaluable. I would like to thank all of them.
Gratitude to all my colleagues of the Electroceramics group: Amit Mahajan, Monika Tomczyk, Sebastian Zlotnik, Rui Pinho, Xiaoli Nathalie Barroca. Xinming Su, Dr. Nivas Babu, Dr. Venkata Saravanan and Dr. Javier Pérez for the positive attitude, friendly working environment and to the skills and knowledge, which really helped me a lot!

I am also highly thankful to family and friends for their support during difficult times.

Above all, I would like to thank my wife (Amara), son (Ahad) and daughter (Aroush) for not complaining and always backing me. I know, I have given a lot of their time to this work!

Finally, I would like to thank FCT, COST, and University of Engineering and Technology, Lahore, Pakistan for the necessary funding and support.

Muhammad Asif Rafiq
Aveiro, Portugal

palavras-chave

Niobato de sódio e potássio, $K_{0.5}Na_{0.5}NbO_3$, KNN, materiais isentos de chumbo, materiais policristalinos, cristais simples, cerâmicos texturizados, propriedades dielélectricas, piezoeléctricas, ferroeléctricas, electromecânicas, domínios ferroeléctricos.

resumo

O niobato de sódio e de potássio, $K_{0.5}Na_{0.5}NbO_3$ (KNN), é o material isento de chumbo mais promissor para substituir o titanato zirconato de chumbo (PZT), que ainda é o líder de mercado utilizado para sensores e actuadores. Para tornar o KNN verdadeiramente competitivo, é necessário compreender e melhorar as suas propriedades. Esse objectivo é perseguido no presente trabalho através de diferentes abordagens, visando o estudo das propriedades intrínsecas do KNN e a subsequente identificação de estratégias apropriadas, como por exemplo a dopagem e a texturização, para desenhar melhores materiais à base de KNN para as aplicações pretendidas. Assim, no presente trabalho, fabricaram-se e caracterizaram-se cerâmicos de KNN dopado e não dopado, de KNN não estequiométrico e de KNN texturizado. Adicionalmente cresceram-se e caracterizaram-se cristais simples de KNN de elevada qualidade.

Os cerâmicos de KNN (não dopado, dopado com Mn e não-estequiométrico (NST)) foram preparados pelo método convencional de mistura de óxidos, tendo-se subsequentemente medido as suas propriedades eléctricas e analisadas as respectivas estruturas e microestruturas. No caso dos cerâmicos dopados com Mn bem como no dos cerâmicos NST verificou-se existir uma estreita janela de composição monofásica associada à dopagem e não estequiometria na posição-A. Nos cerâmicos NST a variação da razão (A/B) influencia o ciclo de histerese da polarização ferroeléctrica (*P-E*), verificando-se a obtenção de respostas dieléctricas e piezoeléctricas melhoradas para pequenos desvios da estequiometria (A/B = 0.97). No que se refere ao KNN dopado com Mn, quando comparado com o KNN não dopado cujos ciclos de histerese são não saturados, verificou-se que a dopagem no lugar B conduz a uma curva (*P-E*) mais saturada e a uma melhoria significativa de propriedades. Usou-se a espectroscopia de impedância para esclarecer o papel do Mn, tendo-se estabelecido uma correlação entre defeitos/transporte de carga e a resposta ferroeléctrica do $K_{0.5}Na_{0.5}NbO_3$ (KNN) e do KNN dopado com Mn. À temperatura ambiente a condução eléctrica no KNN, associada ao transporte por buracos, é minimizada pela dopagem com Mn. A adição de Mn incrementa assim a resistividade do cerâmico, o que permite melhorar a saturação do ciclo (*P-E*). A temperaturas elevadas a condução passa a ser dominada pela movimento de lacunas de oxigénio ionizadas cuja concentração aumenta com a dopagem com Mn.

Preparam-se também cristais simples de KNN recorrendo-se a um método de fluxo de alta temperatura. Usou-se um fluxo modificado com adição de B_2O_3 para crescer cristais a uma temperatura relativamente baixa. Caracterizou-se a qualidade química e cristalográfica dos cristais por análise de DRX, EDS e ICP. Os cristais obtidos exibiram propriedades com valores elevados, designadamente uma permitividade dieléctrica de 29,100 à temperatura de transição da fase tetragonal para fase cúbica, uma polarização remanescente 19,4 $\mu C/cm^2$ e um coeficiente piezoeléctrico de 160 pC/N, valores estes superiores aos dos cerâmicos convencionais de KNN. Usou-se pela primeira vez a microscopia de força piezoeléctrica para caracterizar a estrutura de domínios dos monocristais de KNN. Foi possível observar que os cristais simples de KNN orientados segundo <001>, evidenciaram um padrão de estrutura de domínios, com domínios de 180º dispostos paralelamente e domínios de 90º dispostos em zig-zag. Com base na comparação entre cristais e cerâmicos de KNN é possível sustentar-se que a presença nos cristais simples de um tal padrão de domínios ordenados com longo alcance, ausente nos cerâmicos, é responsável pelas propriedades melhoradas dos cristais simples de KNN. Espera-se que os presentes resultados, ao estabelecerem uma relação entre o padrão de estrutura de domínios, uma espécie de impressão digital, e a resposta dielétrica e ferroelétrica dos cristais simples e ao indicarem vias para se atingirem propriedades maximizadas em materiais de KNN, venham a ter fortes implicações na expansão do uso dos materiais de KNN.

Caracterizaram-se também os monocristais ferroeléctricos de KNN por espectroscopia de Raman, obtendo-se pela primeira vez evidências que permitem a atribuir a estrutura cristalina de simetria monoclínica ao KNN. As intensidades dos fonões A′ , A" e A' + A" foram calculadas teoricamente e comparadas com os dados experimentais em função da rotação de cristal, o que permitiu a determinação precisa dos coeficientes do tensor Raman para modos (non-leaking) em KNN monoclínico. No contexto da literatura este estudo confirma que a atribuição da simetria monoclínica é mais adequada do que a ortorrômbica. Este estudo constitui ainda uma base para a avaliação não-destrutiva da distribuição de domínios por espectroscopia Raman em materiais ferroelétricos isentos de chumbo, à base de KNN e com estruturas complexas.

Procurando aprofundar a compreensão do comportamento eléctrico dos cristais simples e dos cerâmicos de KNN, com o objectivo de desenhar materiais com propriedades optimizadas, realizou-se um estudo comparativo ao nível de defeitos e transporte de carga, usando-se para tal a espectroscopia de impedância. Os monocristais apresentam menor condutividade do que os materiais policristalinos homólogos para temperaturas até 200 ºC ao passo que, acima desta temperatura, são os materiais policristalinos quem apresenta menor condutividade. O comportamento de baixa temperatura (T < 200 ºC) reflecte as diferentes condições de processamento dos cerâmicos e dos cristais, que são responsáveis pelo menor teor de defeitos transportadores de carga no caso dos cristais simples. À medida que a temperatura aumenta, (T > 200 ºC) os monocristais tornam-se agora mais condutores do que as amostras policristalinas nas quais as fronteiras de grão actuam como barreiras ao transporte de carga eléctrica. Para temperaturas ainda mais elevadas a diferença de condutividade entre cristais e cerâmicos é incrementada devido à contribuição da condução iónica nos cristais. Efectivamente, para a gama de temperatura elevada (T > 300 ºC),calcularam-se valores da energia de activação de 1,60 e 0,97 eV que confirmam um transporte de carga associado a condução iónica e a lacunas de oxigénio ionizadas, em cristais simples e em cerâmicos, respectivamente. Sugere-se assim que, dependendo da aplicação em em vista, os cristais, com baixo teor de defeitos e propriedades electromecânicas melhoradas serão uma escolha indicada para aplicações a temperaturas próximas da temperatura ambiente ao passo que, para altas temperaturas, os cerâmicos, menos condutores, serão a opção mais indicada.

Com o objectivo de desenhar as propriedades dos materiais policristalinos de KNN na mira de um desempenho semelhante ao dos cristais simples, prepararam-se e estudaram-se as propriedades de cerâmicos de $(K_{0.5}Na_{0.5})_{0.98}Li_{0.02}NbO_3$ (KNNL) com orientação (00l), usando cristais simples de KNN como partículas modelo para produzir cerâmicos texturizados por crescimento de grão modelado (do inglês “template grain growth”). A escolha dos cristais simples como partículas modelo baseou-se no facto destas possuírem boas propriedades, aqui usadas como ferramenta indutora de melhores propriedades nos cerâmicos de KNN. A análise DRX revelou que os cerâmicos preparados com partículas modelo evidenciavam uma estrutura monoclínica à temperatura ambiente e um fator de Lotgering (*f*) de 40 %, o que confirma o desenvolvimento de textura cristalográfica. Estes cerâmicos texturizados apresentam um padrão de domínios ordenado com longo alcance que consiste em domínios de 90º e de 180º, semelhante ao observado nos cristais simples. Observaram-se valores elevados de constante dieléctrica (13017 na transição de fase C/T), de polarização ferroelétrica ($2P_r$ = 42,8 μC/cm^2) e de coeficiente piezoelétrico (d_{33} = 280 pC/N) nos cerâmicos KNNL texturizados, quando comparados com os cerâmicos não orientados. Sugere-se que esta resposta eléctrica se deve ao padrão de domínioordenados, observado nas amostras texturizadas. Os resultados obtidos, quando comparados com dados anteriormente reportados para cerâmicos de KNN texturizados confirmam a superioridade das propriedades obtidas, que se atribui à estrutura de domíneos observada. Este estudo fornece uma abordagem que pode ser de grande utilidade para a melhoria das propriedades dos cerâmicos piezoelétricos à base de KNN.

Globalmente considerados, os presentes resultados configuram um importante contributo para o conjunto dos conhecimentos sobre as propriedades do niobato de sódio e de potássio: demonstrou-se que existe uma relação entre o padrão de estrutura de domínios e a resposta dieléctrica, ferroeléctrica e piezoeléctrica de cristais simples e de cerâmicos de KNN e apontou-se uma via para a melhoria das propriedades dos cerâmicos através da texturização. Prevê-se assim que este contributo tenha um impacto significativo na viabilização do uso generalizado do KNN em detrimento dos materiais à base de chumbo.

Key words

Potassium sodium niobate, $K_{0.5}Na_{0.5}NbO_3$; KNN, lead free, polycrystalline ceramics, single crystals, textured ceramics, dielectric, piezoelectric, ferroelectric, domains, electromechanical.

Abstract

$K_{0.5}Na_{0.5}NbO_3$ (KNN), is the most promising lead free material for substituting lead zirconate titanate (PZT) which is still the market leader used for sensors and actuators. To make KNN a real competitor, it is necessary to understand and to improve its properties. This goal is pursued in the present work via different approaches aiming to study KNN intrinsic properties and then to identify appropriate strategies like doping and texturing for designing better KNN materials for an intended application. Hence, polycrystalline KNN ceramics (undoped, non-stoichiometric; NST and doped), high-quality KNN single crystals and textured KNN based ceramics were successfully synthesized and characterized in this work.

Polycrystalline undoped, non-stoichiometric (NST) and Mn doped KNN ceramics were prepared by conventional ceramic processing. Structure, microstructure and electrical properties were measured. It was observed that the window for mono-phasic compositions was very narrow for both NST ceramics and Mn doped ceramics. For NST ceramics the variation of A/B ratio influenced the polarization (*P-E*) hysteresis loop and better piezoelectric and dielectric responses could be found for small stoichiometry deviations (A/B = 0.97). Regarding Mn doping, as compared to undoped KNN which showed leaky polarization (*P-E*) hysteresis loops, B-site Mn doped ceramics showed a well saturated, less-leaky hysteresis loop and a significant properties improvement. Impedance spectroscopy was used to assess the role of Mn and a relation between charge transport – defects and ferroelectric response in $K_{0.5}Na_{0.5}NbO_3$ (KNN) and Mn doped KNN ceramics could be established. At room temperature the conduction in KNN which is associated with holes transport is suppressed by Mn doping. Hence Mn addition increases the resistivity of the ceramic, which proved to be very helpful for improving the saturation of the *P-E* loop. At high temperatures the conduction is dominated by the motion of ionized oxygen vacancies whose concentration increases with Mn doping.

Single crystals of potassium sodium niobate (KNN) were grown by a modified high temperature flux method. A boron-modified flux was used to obtain the crystals at a relatively low temperature. XRD, EDS and ICP analysis proved the chemical and crystallographic quality of the crystals. The grown KNN crystals exhibit higher dielectric permittivity (29,100) at the tetragonal-to-cubic phase transition temperature, higher remnant polarization (19.4 $\mu C/cm^2$) and piezoelectric coefficient (160 pC/N) when compared with the standard KNN ceramics.

KNN single crystals domain structure was characterized for the first time by piezoforce response microscopy. It could be observed that <001> - oriented potassium sodium niobate (KNN) single crystals reveal a long range ordered domain pattern of parallel 180° domains with zig-zag 90° domains. From the comparison of KNN Single crystals to ceramics, It is argued that the presence in KNN single crystal (and absence in KNN ceramics) of such a long range order specific domain pattern that is its fingerprint accounts for the improved properties of single crystals. These results have broad implications for the expanded use of KNN materials, by establishing a relation between the domain patterns and the dielectric and ferroelectric response of single crystals and ceramics and by indicating ways of achieving maximised properties in KNN materials.

Polarized Raman analysis of ferroelectric potassium sodium niobate $(K_{0.5}Na_{0.5})NbO_3$ (KNN) single crystals was performed. For the first time, an evidence is provided that supports the assignment of KNN single crystals structure to the monoclinic symmetry at room temperature. Intensities of A′, A″ and mixed A′+A″ phonons have been theoretically calculated and compared with the experimental data in dependence of crystal rotation, which allowed the precise determination of the Raman tensor coefficients for (non-leaking) modes in monoclinic KNN. In relation to the previous literature, this study clarifies that assigning monoclinic phase is more suitable than the orthorhombic one. In addition, this study is the basis for non-destructive assessments of domain distribution by Raman spectroscopy in KNN-based lead-free ferroelectrics with complex structures.

Searching a deeper understanding of the electrical behaviour of both KNN single crystal and polycrystalline materials for the sake of designing optimized KNN materials, a comparative study at the level of charge transport and point defects was carried out by impedance spectroscopy. KNN single crystals showed lower conductivity than polycrystals from room temperature up to 200 ºC, but above this temperature polycrystalline KNN displays lower conductivity. The low temperature ($T < 200$ ºC) behaviour reflects the different processing conditions of both ceramics and single crystals, which account for less defects prone to charge transport in the case of single crystals. As temperature increases ($T > 200$ ºC) single crystals become more conductive than polycrystalline samples, in which grain boundaries act as barriers to charge transport. For even higher temperatures the conductivity difference between both is increased due to the contribution of ionic conduction in single crystals. Indeed the values of activation energy calculated to the high temperature range ($T > 300$ ºC) were 1.60 and 0.97 eV, confirming the charge transport due to ionic conduction and ionized oxygen vacancies in single crystals and polycrystalline KNN, respectively. It is suggested that single crystals with low defects content and improved electromechanical properties could be a better choice for room temperature applications, though at high temperatures less conductive ceramics may be the choice, depending on the targeted use.

Aiming at engineering the properties of KNN polycrystals towards the performance of single crystals, the preparation and properties study of (001) – oriented $(K_{0.5}Na_{0.5})0.98Li_{0.02}NbO_3$ (KNNL) ceramics obtained by templated grain growth (TGG) using KNN single crystals as templates was undertaken. The choice of KNN single crystals templates is related with their better properties and to their unique domain structure which were envisaged as a tool for *templating* better properties in KNN ceramics too. X-ray diffraction analysis revealed for the templated ceramics a monoclinic structure at room temperature and a Lotgering factor (*f*) of 40% which confirmed texture development. These textured ceramics exhibit a long range ordered domain pattern consisting of 90º and 180º domains, similar to the one observed in the single crystals. Enhanced dielectric (13017 at T_C), ferroelectric ($2P_r$ = 42.8 μC/cm^2) and piezoelectric (d_{33} = 280 pC/N) properties are observed for textured KNNL ceramics as compared to the randomly oriented ones. This behaviour is suggested to be due to the long range ordered domain patterns observed in the textured ceramics. The obtained results as compared with the data previously reported on texture KNN based ceramics confirm that superior properties were found due to ordered repeated domain pattern. This study provides an useful approach towards properties improvement of KNN-based piezoelectric ceramics.

Overall, the present results bring a significant contribution to the pool of knowledge on the properties of sodium potassium niobate materials: a relation between the domain patterns and di-, ferro-, and piezo-electric response of single crystals and ceramics was demonstrated and ways of engineering maximised properties in KNN materials, for example by texturing were established. This contribution is envisaged to have broad implications for the expanded use of KNN over the alternative lead-based materials.

Contents

List of Tables

List of Figures

List of Symbols

A	Area of the Electrodes
a, b, c	Unit Cell Parameters
C_o	Linear Capacitor ($\sim$ 1 µF)
C_p	Capacitance of a Parallel Plane Capacitor
d_{33}	Piezoelectric Coefficients
d_{hkl}	Spacing between Atomic Planes
E	Electric Field
E_{ac}	ac Electric Field
E_P	Poling Electric Field
f	Lotgering Factor
hkl	Miller Indexes
$I_{(hkl)}$	XRD Peak Intensities of all the (hkl) Plane Reflections
k_{ij}	Electromechanical Coupling Coefficient
$P_{(00l)}$	Percentage of (00l) Orientation in the XRD Pattern
P_i	Polarization Vector
P_o	P(00l) for the Randomly Oriented Powder
P_r	Remanent Polarization
P_S	Spontaneous Polarization
Q_i	Ionic Charge
Q_m	Mechanical Quality Factor
R	Resistance
S_{ij}	Strain
t	Tolerance Factor
tan δ	Dielectric Loss
T_C	Curie Temperature
T_{jk}	Applied Stress
V	Volume of the Unit Cell
V_{ac}	ac Voltage
ε'	Real Part of the Permittivity

ε''	Imaginary Part of the Permittivity
ε_o	Dielectric Permittivity of the Vacuum (8.85×10^{-12} F/m)
ε_r	Relative Dielectric Permittivity
θ_{hkl}	Bragg Angle
λ	Wavelength
ρ	Density
ρ_r	Relative Density
ω	Frequency

Abbrevations

ac	Alternating Current
AR	Aspect Ratio
BLSF	Bi-Layer Structured Ferroelectrics
BLT	$(Bi,La)_4Ti_3O_{12}$
dc	Direct Current
DW	Domain Wall
FWHM	Full Width at the Half-Maximum
HTS	High-Temperature Solution
KDP	Potassium Dihydrogen Phosphate
KNN	Potassium Sodium niobate
LFP	Lead free piezoelectrics
MPB	Morphotropic Phase Boundary
NBT-BT	$Na_{1/2}Bi_{1/2}TiO_3$-$BaTiO_3$
ODF	Orientation Distribution Function
P-E	Polarization-Electric Field
PFM	Piezoresponse Force Microscopy
PZN-PT	$Pb(Zn_{1/3}Nb_{2/3})O_3$ - $PbTiO_3$
PZT	Lead Zirconate Titanate
RoHS	Restriction of Hazardous Substances
RT	Room Temperature
RTGG	Reactive Templated Grain Growth
S-E	Strain-Electric Field
SEM	Scanning Electron Microscopy
TD	Theoretical Density
TGG	Templated Grain Growth
TP	Thermal Profile
WEEE	Waste from Electrical and Electronic Equipment
XRD	X-Ray Diffraction

CHAPTER 1

Introduction

1. Introduction

1.1 Problem statement

Smart and functional materials have become quite common in our daily life. As producers, consumers and applications constantly require improved performance at low costs, smart and functional materials are a focus of great interest within the materials science and engineering community. The incorporation of smart materials is increasing in a growing range of products at a rapid rate of almost 12 % per year. Indeed the market of smart materials that in 2005 was $ 8.1 billion increased to around $ 22 billion in 2011 and is expected to pass $ 40 billion in 2016 [1, 2]. By definition, smart materials are those which undergo transformations (e.g., changes in the shape, size, etc.) throughout physical interactions, sensing a change in its environment and adapting to correct such a change through the use of a feedback system [1], whereas functional materials cover a broader range of materials whose physical and chemical properties are sensitive to changes in the environment, such as temperature, pressure, electric field, magnetic field, etc., having the ability of performing a certain “function” under a determined stimulus

[3]. Figure 1-1 shows the category-wise market share of smart materials and it is worth mentioning that piezoelectric-materials accounts for 50 % of the total market [1]. Examples of smart materials are

- Piezoelectric materials
- Electrostrictive materials
- Magnetostrictive materials
- Shape memory materials
- Electrochromic materials
- Phase change materials

Piezoelectric materials, the largest group among smart materials, whose sensing and actuating capabilities account for a large number of applications, span most industrial sectors [1, 4]. The major applications in a broader category are:

1. Actuators and Motors,
2. Sensors,
3. Transducers, and
4. Structural materials

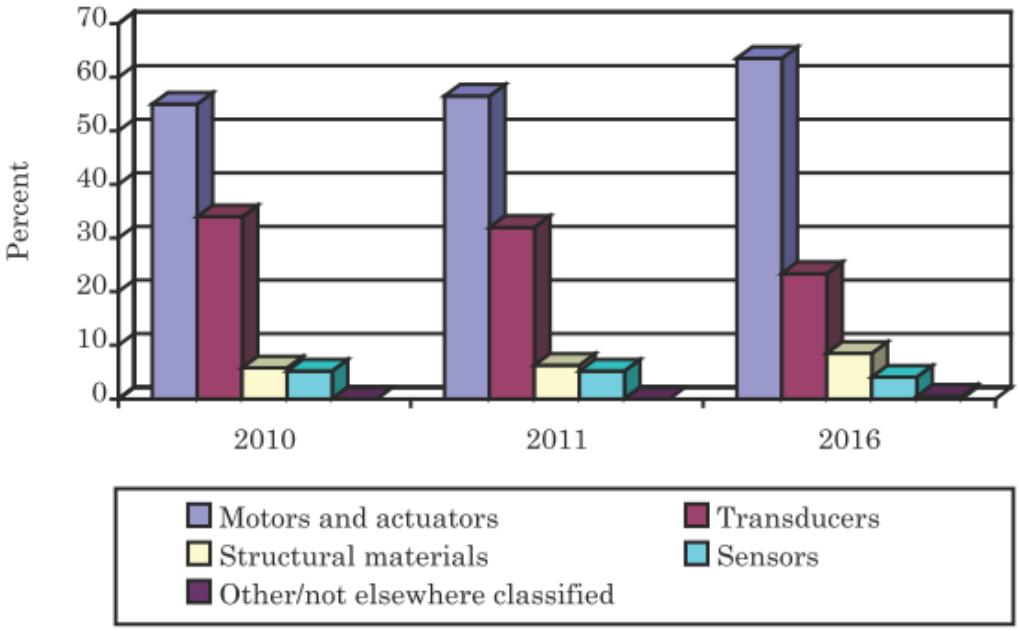

Figure 1-1. Forecast of the global market for smart materials between 2010-2016 [1].

By far, the most successful piezoelectric ceramics (piezoceramics) on the market belong to the solid solution $PbZrO_3$-$PbTiO_3$ (commonly designated as PZT). There are however others lead based materials such as $Pb(Zn_{1/3}Nb_{2/3})O_3$-$PbTiO_3$ (PZN-PT) and $Pb(Mg_{1/3}Nb_{2/3})O_3$-$PbTiO_3$ (PMN-PT) with giant electromechanical response that are commercially important as well [5]. Due to their superior dielectric, piezoelectric and electromechanical coupling coefficients, PZT based compositions are the leader materials for the modern sensors, actuators and transducers applications.

On the downside PZT contain more than 60 wt % of lead. Lead as a metal has been commonly used for thousands of years because of easy availability and extraction. In addition it is highly forgeable and ductile as well as easy to melt. But the toxicity of lead is also known for long ago. Lead is more dangerous to the children and some of the consequences of lead poisoning in children include; behavioural disorders, learning difficulties, and low IQ, while acute lead poisoning can lead to hypertension and renal failure. The best way of prevention is to avoid the contact with leaded materials [6-8]. As a consequence, EU environmental regulations were issued to stop the use of lead in all fields [9]. The awareness of PZT toxicity concerns has driven from the late 90's, the search for novel lead free piezoelectrics (LFP) able to respond to an endless list of demanding applications as mentioned in Figure 1-1.

Currently lead free piezoelectrics to substitute PZT under consideration belongs to perovskites, aurivillus oxide type layered structure and tungsten bronze families. The aurivillus oxide and tungsten bronze ones show in general inferior electromechanical properties when compared with PZT compounds. Among the perovskite family, the most promising lead free compounds, under consideration are: $K_{0.5}Na_{0.5}NbO_3$ (KNN), $Na_{0.5}Bi_{0.5}TiO_3$ (NBT) and $BaTiO_3$ (BT) [10-12]. Amid these materials, BT has lower T_C and the high T_C of KNN and NBT (higher than PZT) points them as promising candidates for high temperatures applications (T > 350 ºC). This becomes particularly relevant as the useful temperature range ensuring full piezoelectric activity roughly extends to 1/2 T_C. Regarding NBT, MPB compositions belonging to NBT-$BaTiO_3$ and ternary system with $(K,Bi)TiO_3$ with maximized properties have been reported [13]. However contrarily to PZT, the MPB is strongly curved and an anti-ferroelectric phase with a depolarization

temperature (T_d), occurs below T_C thereby penalizing their usefulness as its depolarization occurs well below T_C.

Consequently amongst the lead free perovskites family and bases on the premise that the still modest properties can be enhanced, $K_{1-x}Na_xNbO_3$ (x = 0.5) based compositions offer a high potential to be exploited, as possible substitutes to PZT based ones. Indeed, the improved performance of single crystals compared with the polycrystals counterpart is well known [14, 15] and encouragingly KNN single crystals, as other lead based ferroelectric single crystals of $PbZn_{1/3}Nb_{2/3}O_3$–$PbTiO_3$ (PZN-PT), $PbMg_{1/3}Nb_{2/3}O_3$–$PbTiO_3$ (PMN-PT) [5, 15], have shown better dielectric and electromechanical properties (d_{33} = 160 pC/N) [16, 17], nearly twice as compared to their ceramic counterparts. In addition, the development of texture in ferroelectric ceramics is an alternative strategy for increasing the piezoelectric response of these materials due to the inherent anisotropy in the material properties [18]. In this way, we may achieve properties lying between those of single crystals and randomly oriented ceramics. The intensity of the enhanced response depends on the material crystallographic orientation which cannot be exploited in randomly oriented polycrystalline materials. Furthermore, it is well know that currently there is a need of replacing some raw materials that under extinction and soon will be inexistent and also they are located in some geopolitical places that limit the access to them, which indirectly controls their price like rare earth elements. Hence, the use of rare earth elements need to be avoided and substitutes are indeed required. This might be very soon a problem to some functional materials and, namely, electroceramics, that rely on heavy rare earth dopant contents.

To make KNN based materials commercially interesting and competitive with PZT it is necessary to accumulate scientific and technological knowledge on KNN system and to enhance their electromechanical performance. This requires developing adequate KNN based compositions, optimised processing conditions and engineer the microstructure in the case of ceramics, aiming at for obtaining dense and compositionally homogeneous KNN-based materials with reliable, sufficiently high and thermally stable electromechanical properties for specific applications.

1.2 Objectives

Within this context the main objective of this work is to contribute to the pool of knowledge on $(K_{0.5}Na_{0.5})NbO_3$ materials towards its application as possible substitutes of PZT and without the use of rare earth elements by:

1. contributing to understand the processing limitations inherent to KNN - based materials which leads to the formation of second phases / defects and degradation of the physical properties;
2. contributing to understand the differences between the behaviour of KNN single crystals and polycrystals, via the use of nanoscale characterization tools;
3. fabricating textured KNN ceramics templated by KNN single crystals and establishing the relations between the degree of texture and the anisotropy of the dielectric and ferroelectric properties;
4. contributing to understand the role of some dopants on the electromechanical performance of KNN ceramics.

1.3 Organization of the thesis

The present thesis is organized in five (5) chapters. In chapter 1, description of the problem and objectives of this work are presented.

Chapter 2 is dedicated to the literature review, aiming to update the reader with the state of the art regarding the fundamentals of ferroelectric and piezoelectric phenomena and description of the properties and production of KNN single crystals, polycrystalline and textured ceramics.

In chapter 3, experimental procedures and characterization techniques used in this work are explained.

The obtained results are presented, analyzed and discussed in the next chapter (4) in the following order. Firstly, the results for the polycrystalline KNN ceramics (4.1) followed by the single crystals (4.2) and finally the textured ceramics (4.3).

The last chapter (5) of this thesis presents the general conclusions of the work and outlines some future work for its completion.

CHAPTER 2

Fundamentals and background on lead free materials / state of the art

2. Fundamentals and background on lead free materials / state of the art

2.1 Abstract

Piezoelectric and ferroelectric phenomena in related materials are very important from the applications point of view. So, in this chapter, the fundamentals associated with the piezoelectric and ferroelectric phenomena are explained. Lead based and lead free materials along with properties are discussed. $K_{0.5}Na_{0.5}NbO_3$ (KNN) properties - currently one of the promising lead free materials and the object of this thesis are benchmarked to other materials families. A critical analysis concerning the properties of doped and undoped ceramics and KNN single crystals was made. Single crystals of ferroelectric materials are receiving a great attention, because of maximised ferroelectric and piezoelectric properties. Thus, methods for growing ferroelectric single crystals, in particular the high-temperature self-flux solution method are introduced. Other than the properties, single crystals can be used to study the intrinsic properties of the material and the origin of the better performance can be understood, in case of ferroelectrics, from the orientation and domains point of view. Polycrystalline ceramics normally show moder-

ate properties associated with their anisotropic intrinsic character and presence of grain boundaries; therefore different methods to minimize anisotropic and to obtain textured piezoelectric ceramics, in particular, by templated grain growth method, will also be described. Finally, the studies of the ferroelectric domains in KNN ceramics and crystals are presented and discussed.

2.2 Fundamentals

2.2.1 Dielectrics

Dielectrics and insulators can be defined as materials with high electrical resistivities [4, 19, 20]. Dielectrics do not conduct electricity due to the very low density of free charge carriers and, because of this, they can perform insulating functions. However, dielectrics exhibit a unique behaviour when placed under the effect of an electrical field. The ability of the dielectric to store charge in a capacitor is the simplest practical application of a dielectric, which is related to the polarization of the dielectric under the electric field. When an electric field *E* is applied to an ideal insulator, there is no long-range charge transport, as in a conductor, solely a short-range dislocation of the positive and negative charge centre which causes the appearance of electric dipole moments in the material. The material is called a dielectric. The dielectric is said to be polarized. When an electric field is applied to a dielectric material, partial charge compensation is achieved by polarization. Polarization ($\vec{P}$) is defined as the sum of all dipole moments ($\vec{p}$) per unit volume (V) and is represented as,

$$\vec{P} = \frac{\sum_i \vec{p}_i}{V} \qquad \textit{Equation 2-1}$$

Several polarization mechanisms can occur within a dielectric material include atomic, ionic, dipolar and space charge polarization; each is related to the nature of the charged entities which suffer charge displacement or to the nature of the displacement [4, 20]. Electronic polarization is based on the displacement of the negatively charged electron shell against the positively charged core; ionic polarization describes the displacement of the positive and negative sublattices with an applied field; orientational

polarization which deals with alignment of permanent dipoles; space charge polarization is caused by accumulation of mobile charges at the interfaces and surfaces of materials.

2.2.2 Dielectric constant and loss

When a dielectric material is placed between the plates of a capacitor, the capacitance of the capacitor is increased by a factor (ε_r), called the relative permittivity, which can be obtained taking into account the sample thickness (t) and the area of the electrodes (A), using the following expression,

$$\varepsilon_r = \frac{C_p\, t}{\epsilon_0 A} \qquad \textit{Equation 2-2}$$

Where C_p is the capacitance of the parallel plane capacitor and ε_o is the dielectric permittivity of the vacuum (8.85×10^{-12} F/m). Ferroelectric materials are not ideal capacitors and a dielectric loss ($tan\ \delta$) expressed by the ratio of the imaginary part (ε'') and real part ($\varepsilon' = \varepsilon_r$) of the permittivity as

$$tan\delta = \frac{\varepsilon''}{\varepsilon'} \qquad \textit{Equation 2-3}$$

2.2.3 Crystals systems

Crystals are classified into 32 point groups based on their symmetry [19-21] as shown in Figure 2-1. These point groups are divided into two classes which include those with a center of symmetry and those without. There are 21 non-centrosymmetric point groups, 20 (except point group 432) of which exhibit piezoelectricity (explained in the next section). Of the 20 point groups, 10 of the crystal classes contain a unique axis where the dipole moment is oriented in the unstrained condition i.e. they exhibit spontaneous polarization (ferroelectricity). Ferroelectric materials are essentially non-centrosymmetric and most important ferroelectric materials have perovskite structure including $K_{0.5}Na_{0.5}NbO_3$ (KNN), the material of interest in this work.

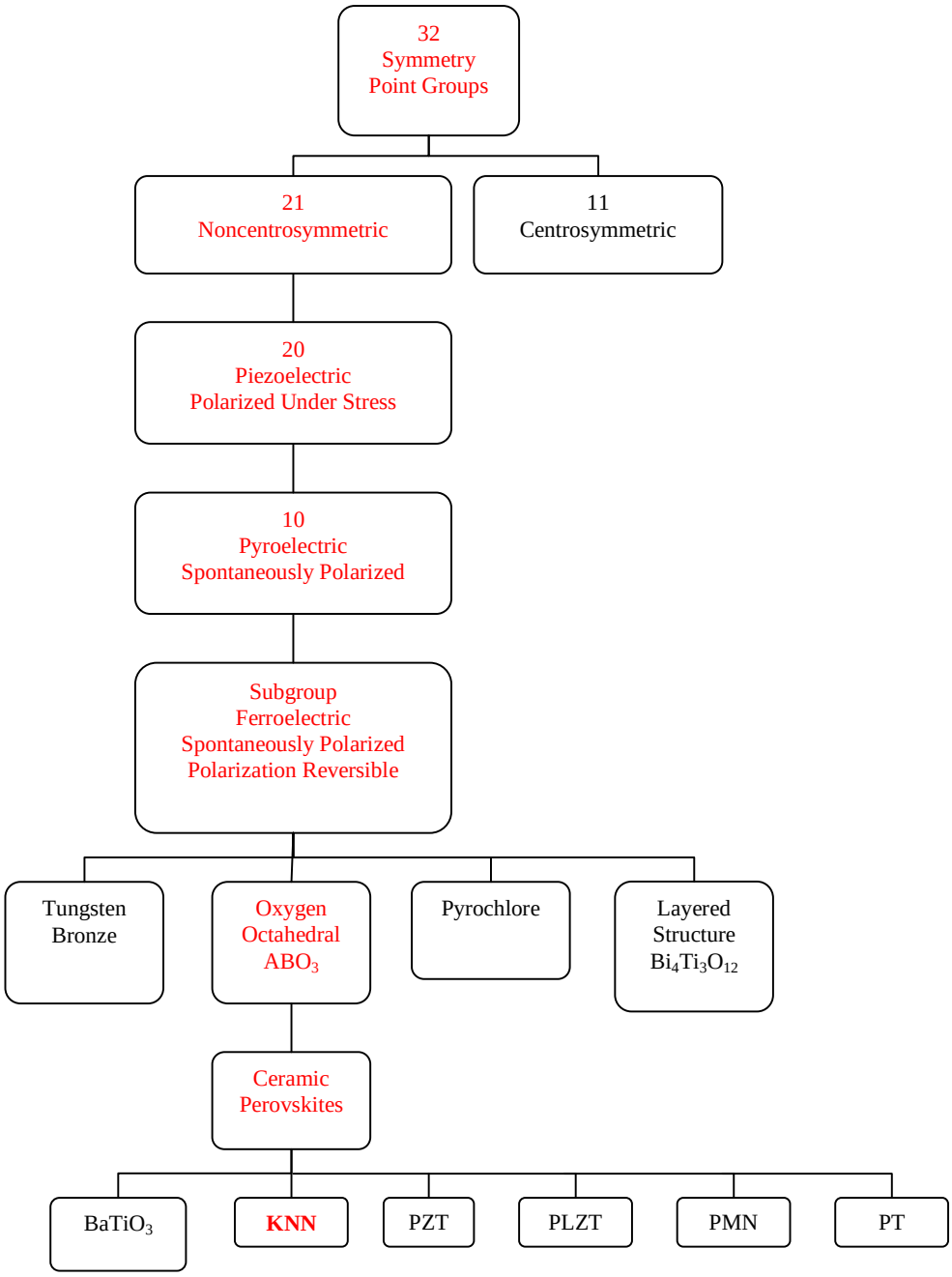

Figure 2-1. Materials classification based on the symmetry point group, adapted from [21].

2.2.4 Piezoelectricity

Jacques and Pierre Curie discovered in 1880, an unusual characteristic of certain crystalline minerals: when subjected to a mechanical force, the crystals became electrically polarized. Tension and compression generated voltages of opposite polarity and in proportion to the applied force – this effect is called piezoelectric effect. Subsequently, the converse of this relationship was confirmed and called inverse piezoelectric effect in which, if one of these voltage-generating crystals was exposed to an electric field it lengthened or shortened according to the polarity of the field, and in proportion to the strength of the field [21] and is shown in Figure 2-2.

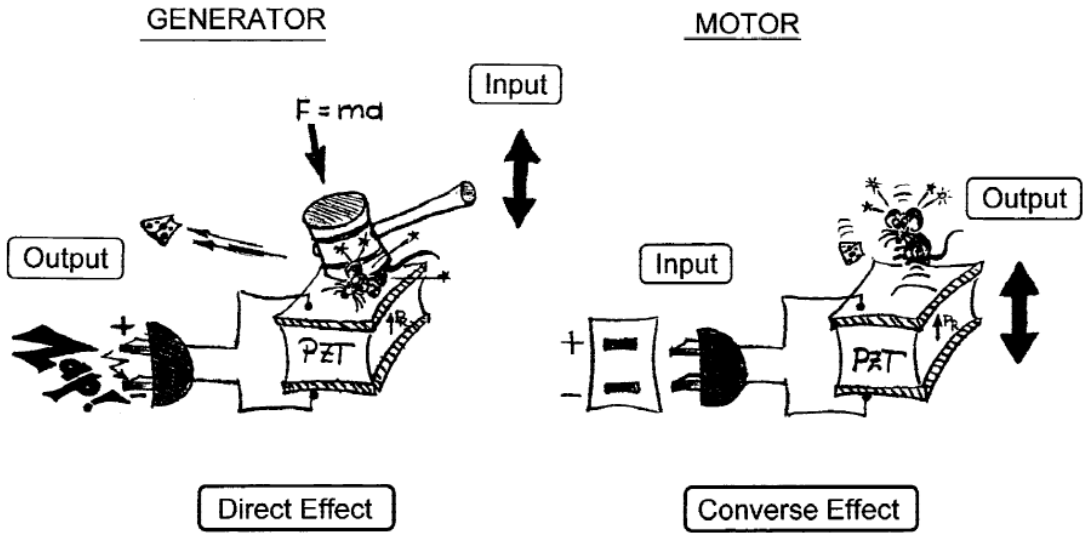

Figure 2-2. Piezoelectric effect in ferroelectric ceramics (left) direct and (right) inverse piezoelectric effect [21].

Mathematically, direct and inverse piezoelectric effect can be described as, respectively,

$$P_j = d_{ij} \times T_i \qquad \textit{Equation 2-4}$$

$$S_j = d_{ij} \times E_i \qquad \textit{Equation 2-5}$$

where, d_{ij} is the piezoelectric coefficient, E_i the applied field, S_j the strain, P_j the polarization and T_i is the applied stress. The d_{33} coefficient is normally the most reported coefficient for both direct and converse piezoelectric measurements.

2.2.5 Pyroelectricity

Pyroelectric materials exhibit a spontaneous polarization that has a strong dependence on temperature because the dipole moments vary as the crystal expands or contracts. The electric field developed across a pyroelectric crystal can be extremely large when it is subjected to a small change in temperature [19]. The pyroelectric effect can be described in terms of the pyroelectric coefficient (P) that is related to the change in spontaneous polarization (dP_s) as a function of temperature (dT) as:

$$P = \frac{dP_s}{dT} \qquad \textit{Equation 2-6}$$

Since polarization is a vector as in piezoelectricity, the value of piezoelectric coefficient is dependent on the direction of measurement.

$$P = \frac{dP_{si}}{\Delta T} \qquad \textit{Equation 2-7}$$

where i = 1, 2, 3.

2.2.6 Ferroelectricity

Ferroelectricity was discovered in 1921 by J. Valasek during an investigation of the anomalous dielectric properties of Rochelle salt, $NaKC_4H_4O_6 \cdot 4H_2O$ [22]. The ferroelectricity in a second material, the potassium di hydrogen phosphate (KH_2PO_4, KDP) was discovered almost 14 years after. A. von Hippel in the 1940's reported ferroelectricity in barium titanate ($BaTiO_3$). Now this group of ferroelectric materials has been extended up to 250 pure materials and many more mixed crystal systems. Currently, and with this advent of a "sensor based society" in which smart sensing

applications, including consumer electronics, robotics, prosthetics, health care, safety equipment, environmental monitoring, homeland security and space flight, will be strategic enabling technologies, functional smart materials like ferroelectrics have a key role [3, 4]. Besides being application driven, the current interest in ferroelectrics lies also in the lack of basic understanding of ferroelectricity although research has been going on for almost fifty years. Only a certain number of pyroelectric crystals have the additional property that the direction of the spontaneous polarization can be modified by applying an external electric field or mechanical stress. Ferroelectricity is the reversibility in a polar crystal of the direction of the electric dipole by means of an applied electric field. These materials are called ferroelectrics. Another characteristic feature of ferroelectrics is the presence of domains that is due to the orientation of dipole moments within the grain of the material.

2.2.6.1 Domains in ferroelectric

A region with the spontaneous polarization (P_s) pointing in one direction that can be reoriented by electric field is called a ferroelectric domain [21, 23]. The origin of domains is related to the minimization of elastic and electrostatic energy. The configuration of ferroelectric domains in a material is largely dependent on the crystal structure. Crystal structures are significant as it determine the set of available polarization directions. The spontaneous polarization in an ideal ferroelectric crystal can be distributed with equal probability among several crystallographic directions of the centro-symmetric prototype structure in the paraelectric phase. For example, barium titanate ($BaTiO_3$) is in a paraelectric phase with zero net polarization above the Curie temperature (T_C = 120 °C), but transforms to a polar tetragonal phase in the temperature range 5 °C to 120 °C. The polar tetragonal phase has six stable polarization directions in all <100> axis [24, 25]. The orthorhombic system provides twelve possible polarization directions in all <110> directions whereas, rhombohedral has eight in <111> directions. Figure 2-3 shows the various phases adopted by barium titanate over a range of temperatures along with the polarization directions [24].

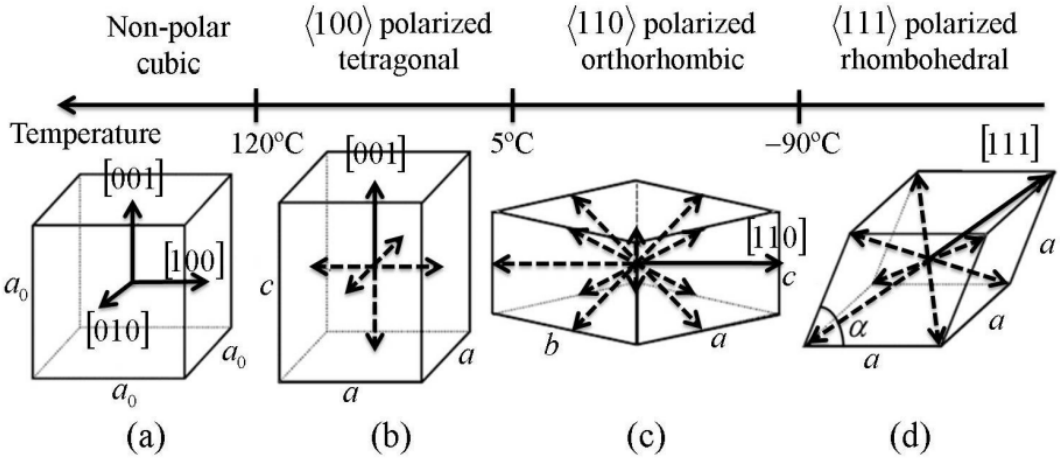

Figure 2-3. Phase transformations in barium titanate along with the polarization directions. (a) cubic crystal system; (b) tetragonal system with 6 polarization directions; (c) orthorhombic system with 12 polarization directions; and (d) rhombohedral system with 8 polarization directions [24, 26].

Thin interfaces, where domains meet are known as domain walls. Domain walls are normally restricted to certain crystallographic orientations depending on the crystal structure of the compound [27, 28]. For example, in case of tetragonal phase, the spontaneous polarization orients only along three mutually perpendicular crystallographic directions, giving rise to two types of domain walls: the walls that separate domains with oppositely oriented polarization (called 180°- walls), and those which separate domains with mutually perpendicular polarization (called 90° walls). The 90° walls are both ferroelectric and ferroelastic domain walls, because they separate regions with different orientation of the polarization and strain. Since the formation of the domain walls requires some energy, there is a certain amount of energy (domain wall energy, W_{dw}) associated with them, in addition to the elastic energy (W_e) due to 90º domains [29]. Figure 2-4a and b shows the schematic representation of 180º and 90º domain walls. The switching of polarization by 180º does not involve elastic deformation, while the switching of 90º does involve elastic deformation, and the energy of both should be different [24].

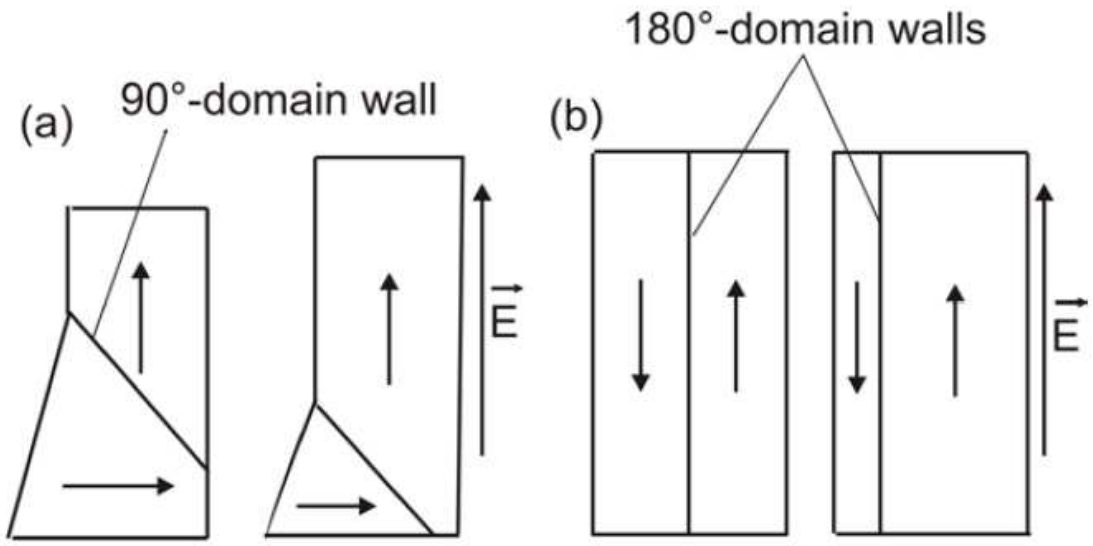

Figure 2-4. Schematic representation of (a) 90º and (b) 180º domains and domain walls [20] . Arrows indicate polarization direction within one domain.

Domain patterns in real crystal from the energy considerations point of view, depend on many factors, including the defect type and concentration, stress and electric history, temperature range relative to T_C, the history of the crystal growth and boundary conditions, such as the overall average strain and polarization states caused by imposed displacements and charges at the crystal surfaces [26]. In reality, multiple nucleation sites and external forces such as electrical and / or elastic ones are always present during crystal growth, due to which, in real systems, a unique global minimum cannot be achieved and the stable state is only a local energy minimum, which prevents the ferroelectric system from reaching a single domain state. Hence, real crystals consist of multiple domains, separated by domain walls. The domain walls have well-defined orientations that minimize energy by maintaining compatibility of strains and polarizations across the wall. That is the reason of particular patterns or domain structures in crystals. In general, the presence of a large mechanical stress in a crystal results in the development of non-180º domains wall configured to minimize the strain [29, 30]. Thus, the natural state of a ferroelectric crystal is generally multidomain configuration and properties are largely dependent on the domain configurations.

2.2.6.2 Poling of ferroelectrics

Polycrystalline ceramics have crystallites which are randomly oriented giving rise to zero net polarization. Piezoelectricity appears in the ferroelectric ceramics only, when randomly oriented domains are aligned through the poling process [31]. Poling of ferroelectrics involves the application of a direct current electric field which is normally higher than the coercive field of the material to obtain a net remanent polarization. It is mainly applied at elevated temperatures to enhance the alignment of the domains in the field direction. A complete orientation in the direction of the field is shown in Figure 2-5 (center), when the applied field is removed, most of the crystallites remain in their aligned direction while others try to return to more energetically favourable positions Figure 2-5 (right) and the image on left presents the randomly oriented domains. Electrodes are applied on the surfaces of the samples for the poling process to be successful [20].

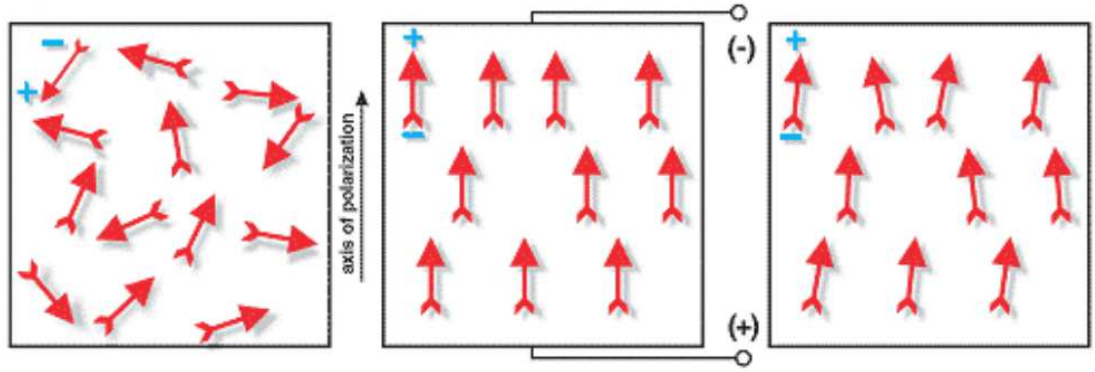

Figure 2-5. Crystallite orientation at the: (left) initial state, (centre) polarization in DC electric field, (right) on removing the electric field, some crystallites revert to more energetically favourable positions [32].

So, the study for ferroelectric domains in the piezoelectric materials is very important for a better understanding of their properties. A number of techniques can be used to study the structure and distribution of domains. Some of the most widely used techniques include scanning probe, optical, polarization light, transmission electron, and scanning electron microscopy.

2.2.6.3 Polarization switching and hysteresis loops

Ferroelectric materials are characterized by a spontaneous polarization (P_s). Ferroelectric properties of some pyroelectric crystals cannot be derived or predicted from the crystal structure but can only be verified experimentally and depends on the polarization response to the applied electric field. Ferroelectrics are characterised by the unique hysteretic response of the polarization as a function of the electric field. From the energy consideration point of view, the hysteresis loop can be explained by the potential energy of the central cation of the perovskite unit cell that has the form of a double well as shown in Figure 2-6a. An external field in the opposite direction to the polarization direction moves the central cation from the potential minimum towards the octahedra-centre and thus reduces the polarization. The polarization is reversed after the field reaches its threshold value. When the field is removed, the cation stays in this well [19, 20, 33]. This spontaneous polarization (dipole moment per unit volume) normally arises due to the small displacements of some of the ions from their centro-symmetric position in the unit cell of their crystallographic structure. Some other ordering processes (e.g. order-disorder) can also result in a reversible dipole moment. Figure 2-6b illustrates the unit cell of the ABO_3 perovskite-type structure for the $BaTiO_3$ showing the corresponding ionic displacements (Ti^{4+} ion). Electrical properties are strongly dependent on crystal structure and the orientation of spontaneous polarization usually coincides with crystallographic axes. Ferroelectric properties are generally limited to particular temperature range and posses a transition temperature (Curie point, T_C), below which the crystals are polar (non-centro-symmetric) and above which they present a centro-symmetric structure and, then, lose the spontaneous polarization. In this state, the material is termed as paraelectric.

The most commonly accepted feature of ferroelectricity is the polarization hysteresis which shows the nonlinearity in the relation between the polarization (P) and the applied electric field (E). Dielectric displacement (D) is approximately equal to polarization and is the physical quantity that corresponds to the stored electric charge per unit area. When an electric field is applied to a ferroelectric material, the dipoles begin to align with the field. Saturation polarization (P_s) is reached when there is no further increase in polarization with increasing field. If the field is reduced to zero, the polariza-

tion will decrease, but will not fall back to zero rather to a value lower than P_s known as the remanent polarization P_r. To reduce the value of polarization to zero, it is necessary to apply a field in the opposite direction. The field at which polarization is zero called the coercive field (E_c). If the field is further increased in the opposite direction, it will reach saturation polarization P_s. When the electric field is reduced again to zero, there is remanent polarization P_s but in the negative direction [4, 20, 33]. Further increase of the field will bring the polarization back to P_s. A typical polarization-field hysteresis along with the schematic of the domains is shown in Figure 2-6c.

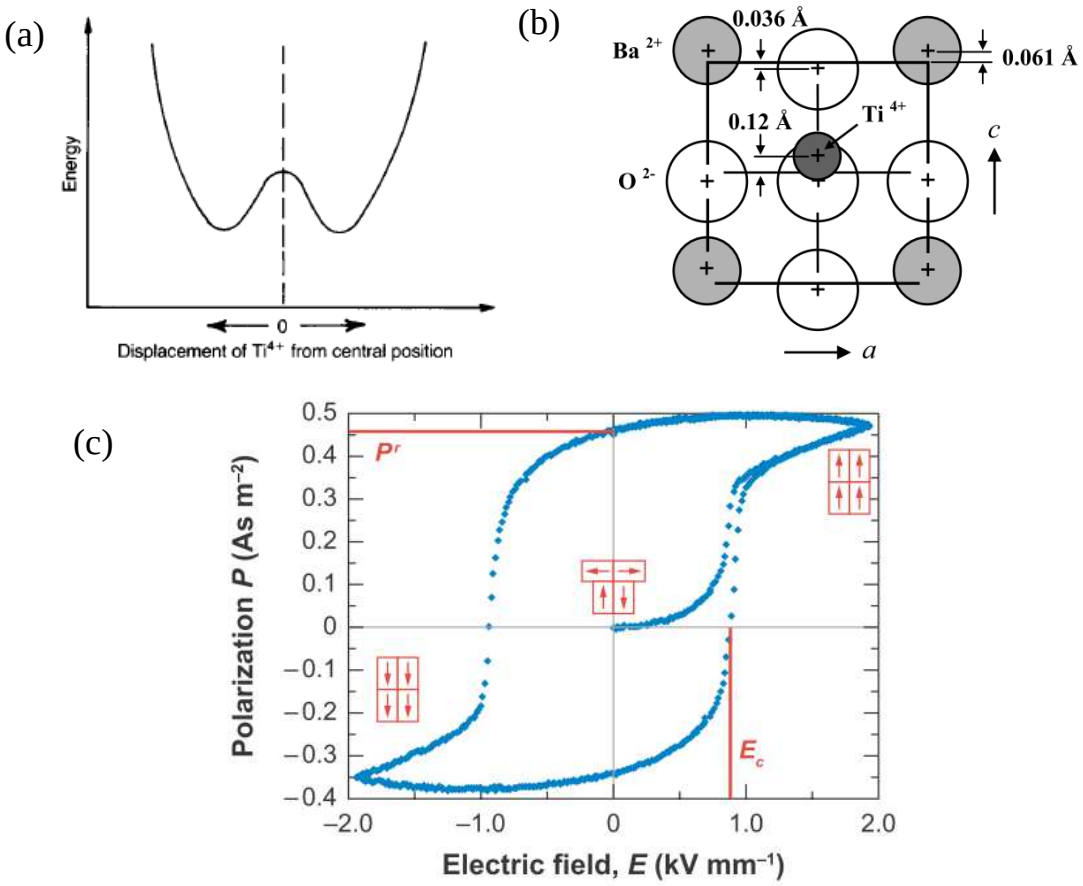

Figure 2-6. Variation of the (a) potential energy of central cation (Ti^{4+} in case of $BaTiO_3$) in perovskite unit cell along c axis [20]and (b) view of the unit cell of the ABO_3 - type perovskite structure for $BaTiO_3$ Showing the relative displacement of the central Ti^{4+} ions to the O^{2-} ions and (c) polarization hysteresis loops of PZT [34].

2.3 Role of defects in ferroelectrics

Perfect crystals, in which all sites are occupied by identical atoms or ions do not exist at temperatures above 0 *K* [35]. Real materials always contain defects and the defects concentration increases with temperature. Structural imperfections such as vacancies (point defects), dislocations (line defects), grain boundaries (planar defects), and inclusions (volume defects) can occur in ceramic materials. Point defects are equilibrium defects present at all temperatures above 0 *K*. Intrinsic point defects are electrons and holes, interstitials (Frenkel disorder), vacancies (Schottky disorder) and antistructure (substitutional A-atom on the B-site) [36, 37]. These defects occur due to thermodynamics reasons or due to impurity accommodation. Extrinsic point defects are doping elements. Interfaces, like grain boundaries and surfaces can also be considered as defects and has a significant impact on the properties of the materials. In perovskites, the possible charge carriers are electrons, holes and oxygen vacancies [38] and oxygen vacancies are the most mobile ionic species in perovskite oxides [38]. Also, there is no evidence of interstitial defects in perovskites and only vacancies may be needed to be considered [39].

Perovskite oxides that have found application in industry often have transition metal cations such as Co, Mn, etc., which have partially filled d or f orbital. Because of that, these cations can change their valence state to a higher or lower oxidation state, depending on the temperature and oxygen ambient. Depending on the ratio of these cations, the perovskite oxide can be metal deficient or have excess metal. A metal deficiency (higher oxidation state of metal) results in cation vacancies, whereas excess metal is accommodated as interstitial cations. In addition, defects can be present on the oxygen sublattice. The nature of disorder within the lattice governs the electronic and ionic properties of these oxides and thus, their defect chemistry is of great technological and academic interest.

These vacancies could be the result of substitutional impurities or intrinsic disorder. Thermodynamics requires that the lattice remains neutral, and therefore if a host ion is replaced by an impurity cation of lesser charge (acceptor impurity) or higher charge (donor impurity) the lattice must compensate to neutralize the charge difference. An acceptor cation possesses less positive charge than the host cation, which can be visual-

ized as a deficiency of positive charge, i.e. a negative charge. Therefore, compensating positively charged defects such as holes or oxygen vacancies are formed. Similarly, to offset the positive charge due to a donor cation, negatively charged defects such as electrons or cation vacancies must be present. In addition, the impurity cations have a site preference determined by their charge and ionic radii; large cations replace larger ions and vice versa. Finally, if the host cations, i.e. transition metal cations, are present in lower / higher oxidation states, they can be treated as acceptor/donor impurities.

Unfortunately, K and Na are volatile in KNN like PZT and defect chemistry is difficult to understand and explain for these materials. But, it's very important to understand the type of defects and how these defects interact with domain and domains walls. In these materials, the oxygen vacancies can be created due to the volatility of the constituent elements.

$$2Na_{Na} + 2K_K + 2O_O \leftrightarrow K_2O + Na_2O + 2V'_{Na} + 2V'_K + 2V_{\ddot{O}}$$
$$V_K \rightarrow V'_K + h^{\cdot}$$
$$V_{Na} \rightarrow V'_{Na} + h^{\cdot}$$

Equation 2-8

These positively charged holes can be free or localized depending on the concentration of oppositely charged defects. In addition, oxygen vacancies $V_{\ddot{O}}$ may be formed during the sintering process at high temperatures and subsequently oxidized during the cooling process as expressed by Equation 2-9:

$$V_O^{\cdot\cdot} + \frac{1}{2}O_2 \rightarrow O_O^{\times} + 2h^{\cdot} \qquad \textit{Equation 2-9}$$

where $V_O^{\cdot\cdot}$ and $O_O^{\times}$ denote the vacancy and $O_O^{\times}$ at the oxide ion site respectively. $h^{\cdot}$ indicates free carrier holes.

2.4 Perovskite structure

Perovskite-type ferroelectric crystal (e.g. $PbTiO_3$ and $K_{0.5}Na_{0.5}NbO_3$; KNN) consists from the crystallographic point of view of two sub-lattices, one made of cations (A^+) and the other one of oxygen octahedra surrounding the second cation (BO_6^-) shown

in Figure 2-7. Cations are located at the four-fold symmetry axis. They are displaced from the centre of the anion-lattice. Therefore, such a crystal possesses an inner electric field, a permanent electric moment and a spontaneous polarization [20].

Perovskite-related compounds can be synthesized with an extremely wide variety of combinations of chemical elements due to several reasons [19, 40]

(1) the perovskite structure accommodates both large A-site and small B-site cations;

(2) distortions of the ideal cubic structure provide further flexibility for incorporating cations of different sizes;

(3) the structure is remarkably tolerant of vacancy formation and atomic-scale inter-growths with other structural motifs.

In the perovskite structure (ABO_3), the A-site can be either M^{1+} (Na, K, etc.), M^{2+} (Ca, Sr, Ba, etc.), or M^{3+} (La, Fe, etc.) and the B-site can be occupied by M^{5+} (Nb, Sb etc.), M^{4+} (Ce, Ti, etc.), or M^{3+} (Mn, Fe, etc.) respectively. The ideal close-packed perovskite (ABO_3) structure consists of infinite three-dimensional, corner-sharing BO_6 octahedra with a dodecahedrally coordinated A-site in the centre of a cavity generated by eight surrounding octahedra. However, the ideal perovskite structure is rarely obtained at ambient temperature/pressure due to the strict constraints placed on the ionic sizes of A, B and O. The Goldschmidt tolerance factor (t) [41] based on the geometrical packing of charge spheres, can be used to describe the distortion of the perovskite structure from the ideal configuration.

The Goldschmidt tolerance factor, *t*, is determined from ionic radii, as follows;

$$t = \frac{(r_A + r_o)}{\sqrt{2}(r_B + r_o)} \qquad \textit{Equation 2-10}$$

The ideally packed perovskite structure is simple cubic, $t = 1$. However, a large number of perovskite structures are distorted to orthorhombic, rhombohedral or tetragonal which can be approximated as cubic with deviation from 1.

2.5 Common inorganic ferroelectric oxides

Based on the unit-cell structure, the general group of inorganic ferroelectric oxides can be divided in the following sub-groups:

(1) Tungsten-bronze

(2) Pyrochlore

(3) Bismuth layer-structure and

(4) Perovskites, ABO_3

Among these four groups, perovskite family is by far the most important one from the properties / economical point of view. Some of the most important compositions of this family are $BaTiO_3$, $PbTiO_3$, $Pb(Zr_xTi_{1-x})O_3$, $(Pb_{1-x}La_x)TiO_3$, $Pb(Zn_{1/3}Nb_{2/3})O_3$-$PbTiO_3$ (PZN-PT), $Pb(Mg_{1/3}Nb_{2/3})O_3$-$PbTiO_3$ (PMN-PT) and $K_xNa_{1-x}NbO_3$ (KNN), which represent the bulk of the ferroelectric ceramics manufactured in the world today.

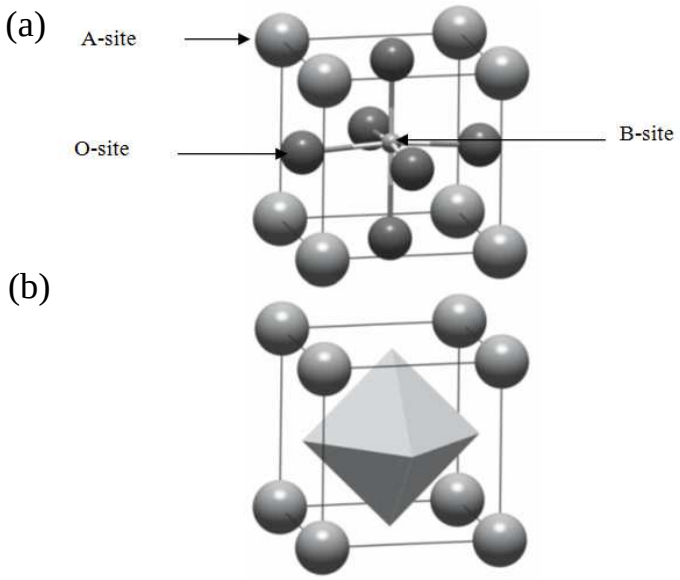

Figure 2-7. Perovskite crystal structure (a) atomic model (b) the polyhedron [19].

2.5.1 Ferroelectric perovskite family

As stated before, the perovskite family is the most important ferroelectric family and KNN is the prominent lead free composition. The research in KNN as a ferroelectric material has been ongoing since 1950´s but the discovery of excellent ferroelectric and

electromechanical performance of lead zirconate titanate ($PbZrO_3$-$PbTiO_3$; PZT) based ceramics catapulted PZT to levels of research, development and commercialization so far not achieved in KNN, and slowed down the research on KNN in the early period upto 1990's.

Though compositions within the lead zirconate titanate solid solution, PZT are some of the most widely used as smart materials, systems as $Pb(Zn_{1/3}Nb_{2/3})O_3$-$PbTiO_3$ (PZN-PT) and $Pb(Mg_{1/3}Nb_{2/3})O_3$-$PbTiO_3$ (PMN-PT) with giant electromechanical response have also been used for electromechanical based applications [5]. The high electromechanical properties of $Pb(Zr_xTi_{1-x})O_3$ (PZT) found close to the morphotropic phase boundary (MPB) with a composition of about x = 0.5 [33], which separates the tetragonal P4mm (Ti-rich) and the rhombohedral R3m (Zr-rich) phases, are the main reason to be used in sensors, actuators and transducers. Optimized piezoelectric properties close to the MPB [33] were believed to be due to a polarization rotation mechanism [42] owing to the presence of finely twinned phases. Table 2-1 shows the properties of non-MPB lead based compositions, whose properties are comparable to KNN ceramics. But, within the MPB PZT compositions, the facility of tailoring 'hard' and 'soft' PZT material by doping, made it an unique materials from applications point of view [33, 43]. Hard and soft PZT ceramics are classified on the basis of electrical properties. Hard materials generally shows low dielectric permittivity, losses while high coercive field and mechanical quality factor as compared to soft materials (for specific values, see *Table 2-2*). Additionally, the high Curie temperature *(T_C)* results in the excellent thermal stability of PZT and allows its use at operational temperatures of about 175 ºC. *Table 2-2* compares the properties of various morphotropic phase boundary (MPB), lead based commercial bulk ceramics and single crystals showing a range of properties useful for various applications. Generally, the hard materials are commercially used for applications like ultrasonic cleaning, transducers, sonars, medical therapy, and ultrasonic welding whereas, the soft materials are used for sensors, actuators, low power generator receivers, hydrophones, gyroscopes, accelerometers, inkjet printers and bimorphs. For the detailed information on properties and applications of commercially available piezoelectric materials, the web-pages of commercial manufacturers like Morgan electroceramics and PI ceramics are referred [44, 45].

Table 2-1. Room temperature electrical properties of non-morphotropic phase boundary lead based piezoelectric materials along with KNN ceramic for comparison purpose.

Material	**Structure**	**Curie point (T_C)**	**Dielectric constant**	**Piezoelectric strain constant**		**Electromechanical coupling coefficient**		**Mechanical quality factor**	**Refs.**
		°C	1 KHz	pC/N					
				d_{33}	d_{15}	K_{33}	K_{15}	Q_m	
$PbTiO_3$ (modified)	Perovskite	470	190	56	68	0.30	-	100	[46, 47]
$(Pb,Ba)Nb_2O_6$ (PBN)	Tungsten Bronze	400	300	85	100	0.30	-	15	[48]
$BaTiO_3$	Perovskite	120	1500	190	270	0.49	0.48	100	[33]
$(Na_{1/2}Bi_{1/2})TiO_3$ (NBT)	Perovskite	335 T_d	500	74	19	0.42	0.11	225	[49]
$Sr_2(Nb_{0.5}Ta_{0.5})_2O_7$	Perovskite layer structure (PLS)	820	75 (1MHz)	2.6	-	-	-	-	[50]
$K_{0.5}Na_{0.5}NbO_3$	Perovskite	420	~400	80-160		0.40			[51-54]

Table 2-2. Room temperature electrical properties of selected MPB, lead based perovskite piezoelectric materials.

Material	**Composition**	**Curie point (T_C)**	**Dielectric constant**	**Piezoelectric strain constant**		**Electromechanical Coupling coefficient**		**Mechanical quality factor**	**Refs.**
	x = mole % PT	°C	1 KHz	pC/N					
				d_{33}	d_{15}	K_{33}	K_{15}	Q_m	
$Pb(Mg_{1/3}Nb_{2/3})O_3$-PT (PMN-PT)	33	160	5000	690	~210	0.73	0.40	75	[55]
PZT 5H (Navy VI – Soft PZT)	~48	193	3500	590	~270	0.75	0.39	65	[56, 57]
PZT-8 (Navy III - Hard PZT)	~48	300	1000	220	~37	0.70	0.30	1000	[57]
$(Na,Bi)TiO_3$-PT (NBT-PT)	12	307	410	110	~35	0.56	0.20	220	[49]
$Pb(Zr_{0.52}Ti_{0.48})O_3$ (undoped PZT)	48	360	800	220	~93	0.67	0.31		[33, 58]
$Pb(Zn_{1/3}Nb_{1/3})O_3$ (PZN-PT single crystal)	8	165	4200	2070		0.94			[5, 59]
$Pb(Mg_{1/3}Nb_{2/3})O_3$-PT (PMN-PT single crystal)	30	150	2890	730		0.81			[5, 59]
$Pb(Mg_{1/3}Nb_{2/3})O_3$-PT (PMN-PT single crystal)	35	160	3100	1240		0.92			[5, 59]
$Pb(Mg_{1/3}Nb_{2/3})O_3$ –PT (PMN-PT single crystal)	35	167	1950	2000					[60]

As mentioned before, more recently environmental and health concerns towards lead specific legislation in Europe (DIRECTIVE 2002/95/EC) and the same followed by other world regions like the state of California (California health and safety code 25214.9–25214.10.2) towards the use of environment friendly materials [61, 62] have once again re-ignited the interest in KNN and thus since 1990's [9] an exponential increase in the research activities on the topic has been observed and is obvious from the enormous increase in the number of publications on the topic of lead free piezo – ferro-electrics, since 2000 (Figure 2-8).

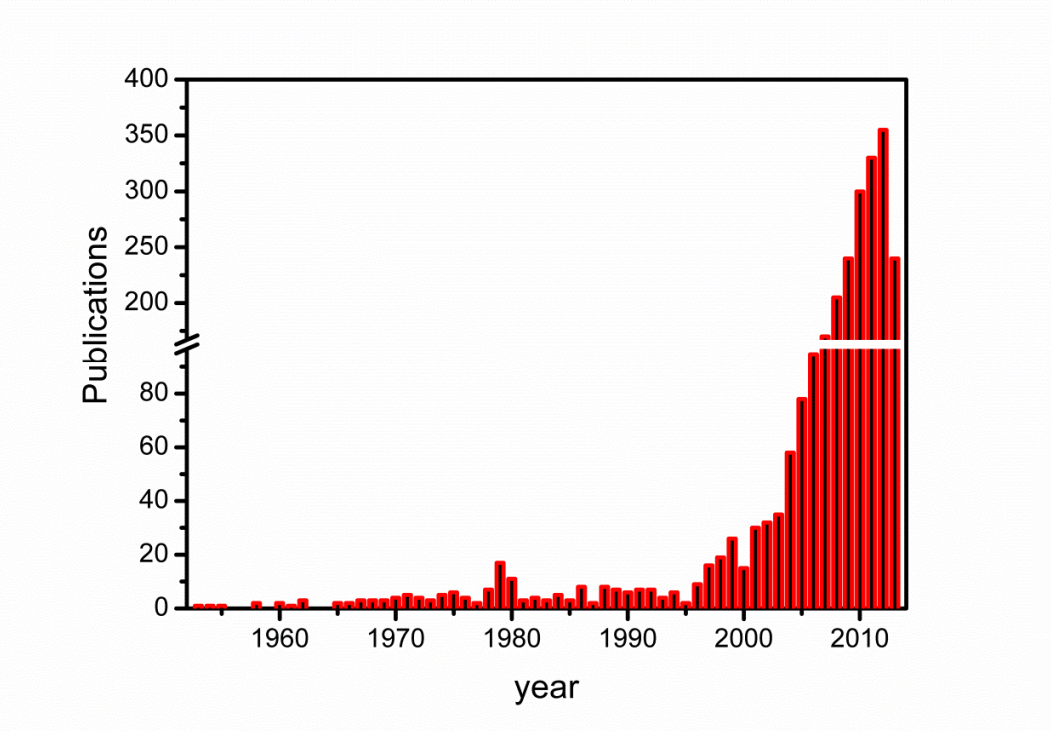

Figure 2-8. Publications on lead-free piezoceramics in refereed journals for the time range from 1951 to September 2013. This statistic results from the counting of relevant papers citing lead free compositions. The search was conducted in ''ISI Web of Science'' and ''Sciencedirect'' with key words such as ''lead-free'', ''piezoelectric'', ''ferroelectric'', ''KNN'' and similar.

Within the perovskite, most promising lead free ferroelectrics under consideration are: $K_{0.5}Na_{0.5}NbO_3$ (KNN), $Na_{0.5}Bi_{0.5}TiO_3$ (NBT) and $BaTiO_3$ (BT) [10-12]. Figure 2-9a and b presents the electromechanical properties and planar coupling coefficient of lead based and lead free materials. BT has a low T_C (120 °C) and BNT shows a depolariza-

tion temperature (T_d) below T_C. From the applications point of view, the maximum temperature of operation for piezoelectrics is normally half of the Curie temperature (T_C), which narrows down the application range of these materials. Hence, KNN is one of the leading lead-free ferro- and piezoelectric materials, owing to the relatively high $T_C \approx 420$ °C, good piezoelectric properties (piezoelectric constant. d_{33} = 80 pC/N) and electromechanical coupling coefficient (48 %) [54].

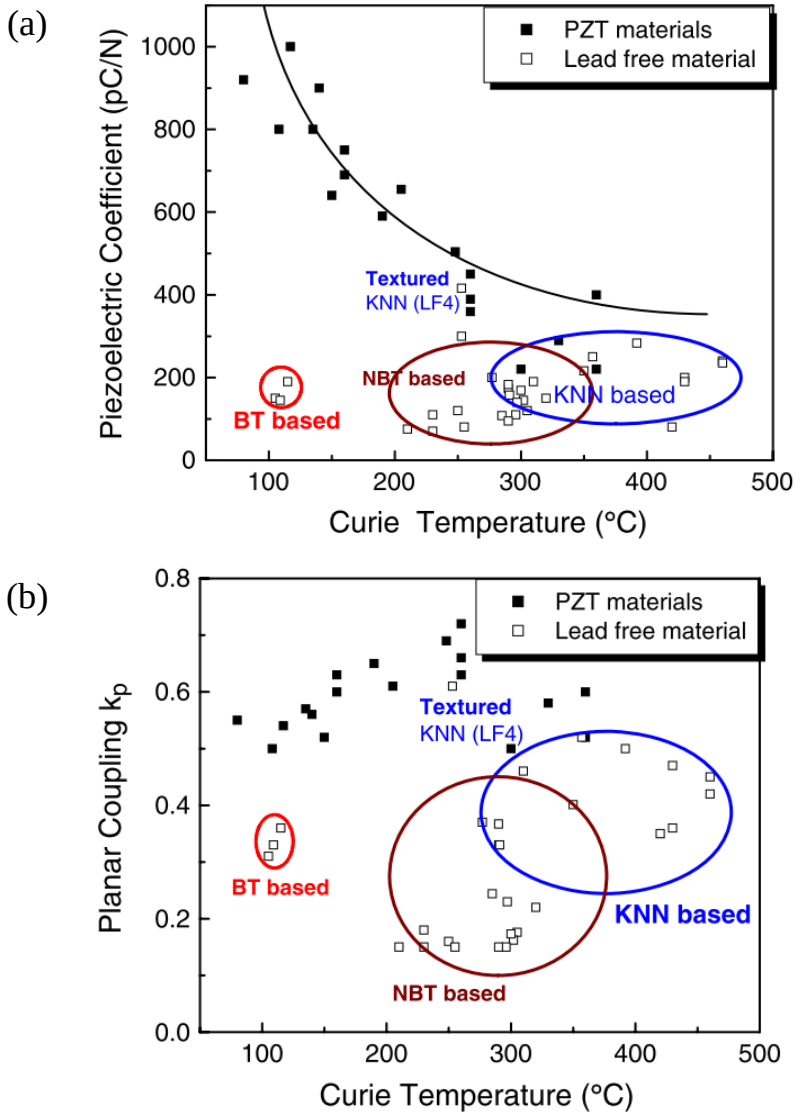

Figure 2-9. Room temperature values for various polycrystalline materials of: (a) piezoelectric coefficient (d_{33}) vs. curie temperature (T_C) and (b) planar coupling coefficient (K_p) vs. T_C [10]

Figure 2-10 shows the timeline for the important landmarks in the KNN based ceramics research from the early work on KNN [63] to the ground breaking work of Saito *et al.* in KNN based ceramics [64]. The earliest work was done by Shirane *et al.* on the dielectrical properties and phase transition of $NaNbO_3$ and KNN single crystals and bulk ceramics [63]. The early work used conventional mixed oxide method for the synthesis of KNN [51, 65] but to improve the properties, hot pressing (HP) [54, 66] and hot isostatic pressing ((HIP) [65] were also used. It is obvious from the Figure 2-10, that not much research was carried out in KNN from 1960 to 1990, which was due to the better properties of other materials like PZT and $BaTiO_3$, as mentioned before. It became popular again among researchers after 1990. After the report of improved properties of KNN doped with Li, Ta and Sb, this composition got a lot of attention and many reports with these dopant were published in the recent past [67-71]. This heavily doped system has a marked disadvantage that the high piezoelectric performances are due to an orthorhombic to tetragonal polymorphic phase transition (T_{O-T}) occurring near room temperature [72] restraining the thermal stability of piezoelectric properties and becoming a "bottleneck" for practical applications. Furthermore, the scarcity of materials (Ta is very expensive) and toxicity of Sb is also known. So, it is very important to look for other dopants and strategies to enhance the electromechanical response of KNN over a wide temperature range and for wide range of applications. Also, recently, non-traditional methods like spark plasma sintering (SPS) were used to prepare ceramics with density more than 99% which showed d_{33} of 160 pC/N, twice as compared with atmospheric sintered ceramics [73].

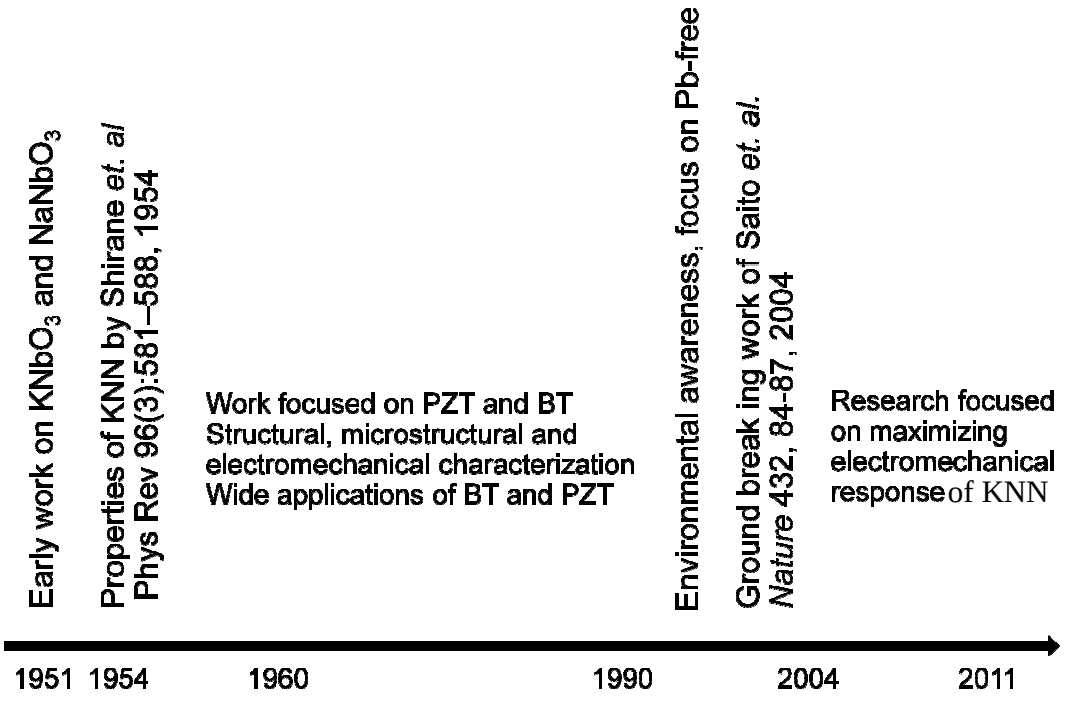

Figure 2-10. Timeline of the advancement of KNN based ceramics.

2.6 Phase diagram of $KNbO_3$–$NaNbO_3$

Similar to PZT, KNN is a solid solution between ferroelectric $KNbO_3$ and antiferroelectric $NaNbO_3$. Binary phase diagram of the corresponding system (1-x)$KNbO_3$–x($NaNbO_3$) is shown in Figure 2-11 [33]. The so-called "morphotropic phase boundary (MPB)" separating two orthorhombic ferroelectric phases was identified at x ~ 0.5 [33], which is actually a polymorphic phase transition (PPT). $K_{0.5}Na_{0.5}NbO_3$ is the most studied composition and is widely called as KNN because compositions lying close to the morphotropic phase boundary (MPB), showed superior properties of piezoelectric constant (d_{33} = 80 pC/N), electromechanical coupling coefficient (K_p = 36-40%), mechanical quality factor (Q_m = 130), and relative dielectric constant (ε_r = 290), when it was prepared by ordinary sintering process [33, 54] and without dopant.

According to phase diagram (Figure 2-11) phase boundaries were revealed at 52.5%, 67.5%, 82.5% and 98% $NaNbO_3$ [33]. It can be observed from the phase diagram

of KNN that only a small amount of potassium (2 %) in $NaNbO_3$ changes the structure. In an early work on KNN, Shirane *et al.* calculated the cell parameter as monoclinic, and treated it as orthorhombic for easier comparison with tetragonal and cubic phases [63]. After that, many researchers used orthorhombic phase to define the KNN structure. Ahtee *et al.* [74] refined the neutron diffraction data of $K_xNa_{1-x}NbO_3$ (x = 0.02 and 0.1) compositions by using orthorhombic and monoclinic symmetry, and proposed that the monoclinic symmetry seems to be more correct, also mentioning that the difference between the two structures is very small. Monoclinic phase was reported also in nanosized pulverized KNN ceramics [75, 76]. Recently, many researchers used an orthorhombic phase for the refinement of the cell parameters of $K_{0.5}Na_{0.5}NbO_3$ at room temperature from X-ray diffraction (XRD) [77] and neutron data [78], although report of monoclinic phase from the refinement of cell parameters a = 4.0001 Å, b = 3.9473 Å , c = 3.9997 Å with angle β = 90°30' was also published in the KNN system [79]. Therefore, there is a need of clarity concerning the structure of KNN.

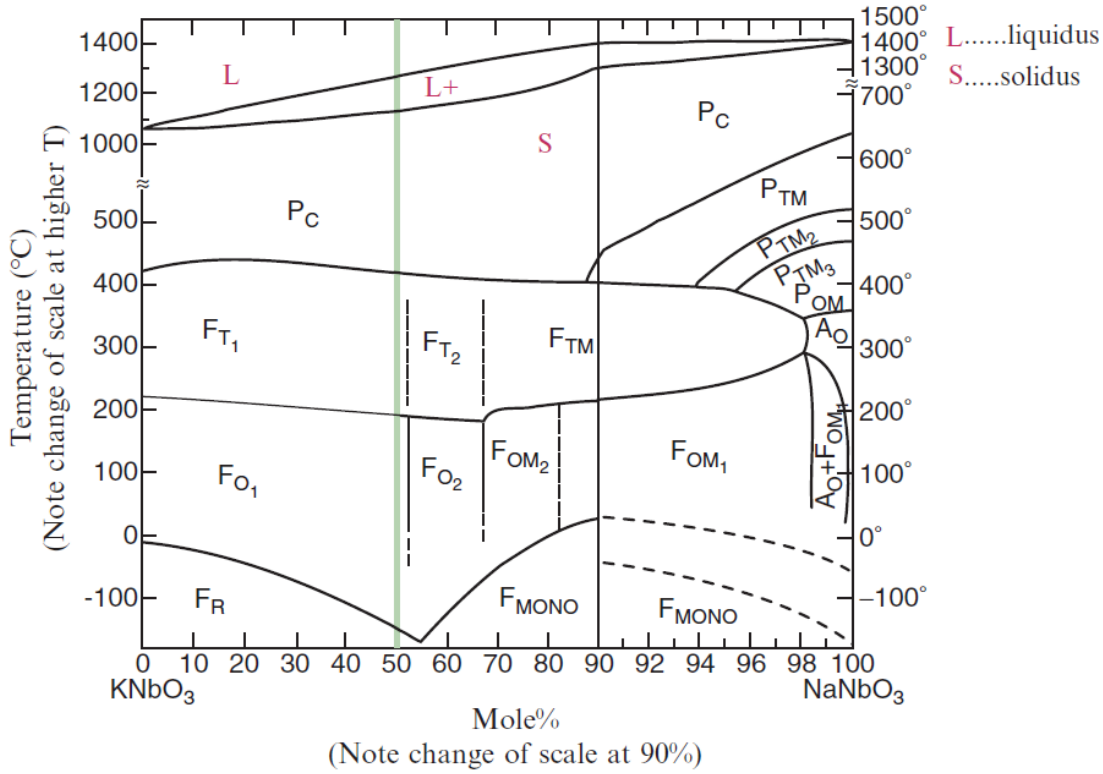

Figure 2-11. Binary phase diagram of $KNbO_3$-$NaNbO_3$ [33]

2.7 Synthesis and properties of $K_{0.5}Na_{0.5}NbO_3$ (KNN) based ceramics

The most widely used synthesis route for KNN powders has been the solid-state reaction starting from oxides and carbonates precursors like K_2CO_3, Na_2CO_3, and Nb_2O_5 with typical calcination temperatures between 850 °C and 950 °C [51, 65, 66] by considering the following global chemical reaction.

$$1/4\ Na_2CO_3 + 1/4\ K_2CO_3 + 1/2\ Nb_2O_5 \longrightarrow (Na_{0.5}K_{0.5})NbO_3 + 1/2\ CO_2$$

Equation 2-11

One of the most important obstacles hindering the further development of KNN as commercial piezoceramics is the difficulty in processing monophasic and dense ceramics by conventional methods. The problem arises due to the hygroscopic and volatile nature of (K_2CO_3) [80]. Similar limitations were earlier found in PZT and other lead based system, but this problem was solved by adequate processing. Currently monophasic, stoichiometric PZT compositions with controlled lead losses and even compatible with low cost low melting point non noble metals, such as Cu and polymeric polyamides have been developed [81, 82].

Pure KNN is difficult to sinter by atmospheric sintering (AS) and without the use of isostatic pressing [65]. Dense ceramics can be produced by alternative processes like hot pressing (HP) [51, 54, 66], hot isostatic pressing (HIP) [66], and spark plasma sintering (SPS) [53] methods. The piezoelectric properties were also improved in the HP and HIP processed KNN samples due to improved densification [66]. Although, by SPS, higher density and better d_{33} values were achieved, but the lower ferroelectric properties (remanent polarization of 6.5 $\mu C/cm^2$) were obtained due to very fine grain size [83].

Table 2-3. Density (ρ) and piezoelectric coefficient (d_{33}) of KNN ceramics sintered by various sintering methods

Sintering method	Density	Relative density*	d_{33}	References
	g cm^{-3}	%	pC/N	
KNN (AS)	4.25	94.24	80	[54]
	4.20	93.13		[51]
	4.30	94.46	110	[51]
	–	94-95	70-90	[52]
KNN (HP)	4.46	98.89	160	[54]
	4.50	99.78		[66]
KNN (HIP)	4.50	99.78		[65]
KNN (SPS)	4.48	99.33	145	[53]

* Theoretical density= 4.51g/cm^3

Figure 2-12a shows the example of temperature dependence of the dielectric constant (frequency of measurement not mentioned) for $(K_{0.5}Na_{0.5})_{1-x}Li_x(Nb_{1-y}Ta_y)O_3$ with x = 0, 0.03, 0.1 and y = 0, 0.20, 0.40. All the samples dielectric curves exhibit two maxima corresponding to two phase transitions. Curie temperature increased to 499 ºC for KNN doped with 10 mole % Li (designated as KNN-L10T0) as compared to 415 ºC for $K_{0.5}Na_{0.5}NbO_3$ (designated as KNN-std). For Ta = 0.40 (designated as KNN-L0T40) and Li = 0.03; Ta = 0.20 (designated as KNN-L3T20), the Curie temperature reduced to 168 ºC and 323 ºC respectively. The additions of Li and Ta both lower the tetragonal to orthorhombic phase transition temperature [84].

Figure 2-12b shows the example of polarization – electric field hysteresis of undoped and doped KNN ceramics. KNN ceramics showed higher P_r, which might be due to the leaky P-E loop and contribution due to leakage current [78]. Similar kind of leaky loops have also been reported either for undoped KNN or doped KNN (doped with Li and Ta, Li and Sb [69, 78, 85, 86] [87] and attributed to conduction and space charge effects [88, 89]. Still, there is lack of knowledge about this issue and this need to be resolved.

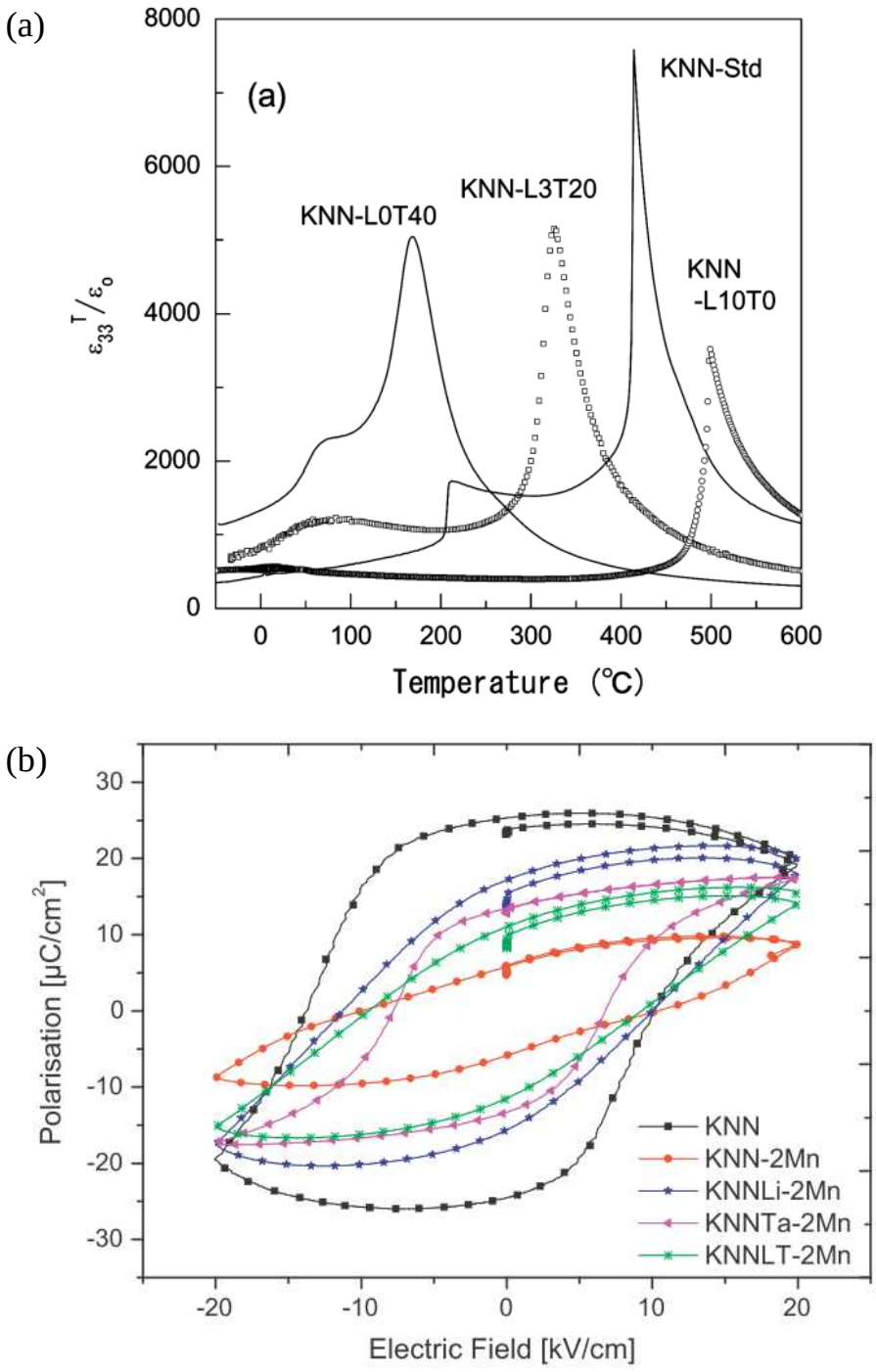

Figure 2-12. (a)Temperature dependence of dielectric constant for KNN-Std, KNN-L10T0, KNN-L0T40 and KNN-L3T20 [84] and (b) polarization – electric field hysteresis curve of KNN based ceramics [78].

2.8 Properties of doped KNN ceramics

In the perovskite structure, various elements can occupy A or B-sites. Some examples for the A-site dopants in KNN are Li, Mg, Ca, Sr, Ba, La, Eu [90-95] and B-site dopants are W, Ce, Ti, Mn, Fe, Ta [89] respectively. The goal of intentional doping is to improve the densification and tailor the properties of the material for specific application.

The best properties reported so far at room temperature were obtained in KNN ceramics when doping with Li, Ta and Sb [64]. An overview of the properties obtained by doping as reported by many researchers is shown in Table 2-4. It is obvious that the density and electromechanical properties of doped ceramics are improved as compared to undoped KNN to a certain extent, without lowering the T_C to great extent, but the properties did not reach the level, where it can be compared with the PZT and replace it for the industrial application.

Table 2-4. Properties of KNN based ceramics, abbreviations used are, KNNL – Li doped, KNNT – Ta doped, KNNLT – Li and Ta co-doped, KNNLTS – Li, Ta and Sb doped, KNNAg –Ag doped, KNNLS- Li and Sb doped. The properties observed by these dopants are representative of values obtained even for other dopants.

Composition	**MPB**	**Sinter Aid**	ρ	ε_r	$\tan\delta$	d_{33}	K_p	T_C	P_r	E_c	**Refs.**
			g/cm^3	1 kHz		pC/N		°C	µC / cm^2	kV / cm	
$K_{0.5}Na_{0.5}NbO_3$				290	0.04	80	0.35	420			[65]
$K_{0.5}Na_{0.5}NbO_3$ (HP)			4.46	420		160					[54]
KNN		CuO		1200							[67]
		KCN				180					[96]
		KCT				190			20	9.8	[97]
(1-x)KNN-xLiNbO$_3$	5-7 %		4.24-4.42	300-760	0.037-0.04	210-235	0.29-0.52		10-25	10-34	[98-101]
(1-x)KNN-xLiTaO$_3$	5-6%			570 (10 kHz)	0.05 (10 kHz)	200	0.36	430			[71]
(1-x)KNN-xLiSbO$_3$	4.8-5.6%			1372	0.019	286	0.51	385			[102]

2.9 Single crystals growth

2.9.1 Methods of growing single crystals

A single crystal is characterized by a long-range atomic order, extending over many atomic diameters and having a repetitive structure. Crystals normally shows fixed shape rigidity, and good mechanical strength. In crystals, often a strong relation between crystal orientation and optical, electrical and mechanical response was observed. Crystal growth is time intensive, expensive and more difficult as compared to polycrystals. However, single crystals exhibit better properties than their polycrystalline counterparts and in fact crystals provide an opportunity to measure a material's intrinsic behavior in the absence of grain boundaries, which are inevitably present in the polycrystalline ceramics. Grain boundaries in polycrystalline materials have usually a deleterious effect on the physical properties and in particular on those that exhibit a dependence on the crystallographic orientation. Hence the comparison of single crystals and polycrystalline properties can be helpful in the process of establishing the relations between processing and properties, and ultimately in the process of designing polycrystals with optimised performance.

The most often employed methods for single crystal growth can be divided into two principal groups. 1) growth from a melt and 2) growth from solution.

2.9.1.1 Growth from the melt

Most important methods of single crystal growth from the melt are Czochralski, Bridgman-Stockbarger and Verneuli and are named after those who invented them. These methods can be used for compositions, which melt congruently, i.e., the same crystalline phase (composition) exists before and after melting. The melt is cooled down carefully to form a single crystal and normally a seed crystal is used to prepare the single crystal. Growth from the melt requires some conditions including:

1. the material must melt congruently;
2. the material must not decompose before melting;
3. the material must not undergo a solid state phase transformation between melting point and room temperature.

A lot of hard work and information is necessary to start the growth run for a specific composition.

Though restricted to the systems that fulfill the above conditions, growth from the melt has some advantage like,

1. a fast growth rate (cm/h), which depends on the heat transfer.
2. a large variety of techniques were developed (e.g. crystal pulling and zone solidification).

Some examples of the crystals produced by this method include silicon, germanium, and gallium arsenide. Silicon crystals, which is most widely used in the electronic devices is grown in sizes of 30 cm in diameter. Crystal growth is an important subject within the materials science. For a deep understanding of the crystal growth, some references [103-106] are suggested.

Most of the ceramics have high melting temperature, so melt growth cannot always be used. Also, in some cases, glass is formed instead of single crystal due to the higher viscosity of the melt [105].

2.9.1.2 Growth from solution (flux)

In the growth from solution, the chemical components of the crystal are dissolved in a liquid medium or flux and are allowed to crystallize slowly as the temperature goes down. Different solution growth techniques have been employed based on the medium used, like water solution growth at room temperature, hydrothermal and flux growth techniques.

The most commonly used term for crystal growth from high temperature solution is flux growth. This method allows the growth of single crystals of a wide range of materials. The components of desired materials are dissolved in a solvent i.e. the flux. The main advantage of the method is growth below the melting point. Flux growth method can be used for high melting materials and thermal strain is lower in crystals due to relatively low growth temperature. The main disadvantage is lower growth rates as compared to the crystal growth from the melt. Crystals grown by flux method are generally smaller in size and difficult to separate the crystals from the flux. There is a

risk of incorporation of some impurities in the crystals (due to the presence of the flux) [107].

High temperature solution growth is one of the oldest processes for crystal growth and is largely used for preparing crystals for research purposes [103, 105]. The basic process is simple i.e. a suitable solution is cooled slowly. The desired composition plus the selected flux are put inside a platinum crucible (inert material) covered with platinum lid and the crystallization takes place when the high temperature solution is allowed to become critically supersaturated by cooling. Figure 2-13 presents schematically a pseudo-binary system of the flux and the solute, where the three different possible ways to achieve the required supersaturation for crystal growth are represented [106]:

(1) Crystal growth by slow cooling when the temperature is decreased from A to B and growth occurs along the arrow to C at varying growth temperature.

(2) Crystal growth by flux evaporation when the solvent, or a part of it, is evaporating and the solute concentration increases from D to E at constant growth temperature. This method is frequently used for aqueous and organic solutions.

(3) Crystal growth by vertical temperature gradient transport when the crystal grows in a colder region G of the furnace, while the crystallized material is continuously replaced at the furnace hotter region F, generally by dissolution of the polycrystalline nutrient. Since the growth temperature in each region of the furnace is constant, this steady state method is particularly suitable for the growth of solid solutions.

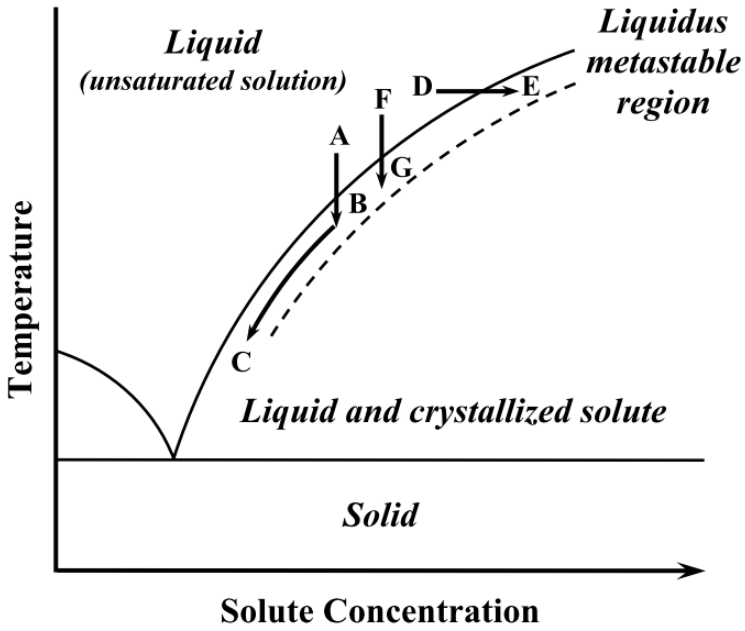

Figure 2-13. Schematic of a pseudo-binary system of flux and solute [106].

One of the main constraints is to find the suitable solvent. Additional constraints include definition of optimized heating / cooling cycles and suitable sized crucibles. The most common fluxes are oxides or fluorides like PbO, PbF_2, Bi_2O_3, B_2O_3, Na_2O or KF [105]. The choice of the flux depends on the composition of the crystal to be grown. The key points to which might be helpful for the crystal growth include: flux should have a low melting point, low solubility in the growth crystal, the viscosity of the solution should be low, should not attack the growth container, and the residual melt should be easily separated from the crystals [105, 106].

Figure 2-14 shows the flux systems mostly used by the researchers along with the useful temperature range for each flux system [105]. It is obvious, that specific flux can be used for a wide temperature range, whereas, flux is more effective in a certain temperature range (highlighted).

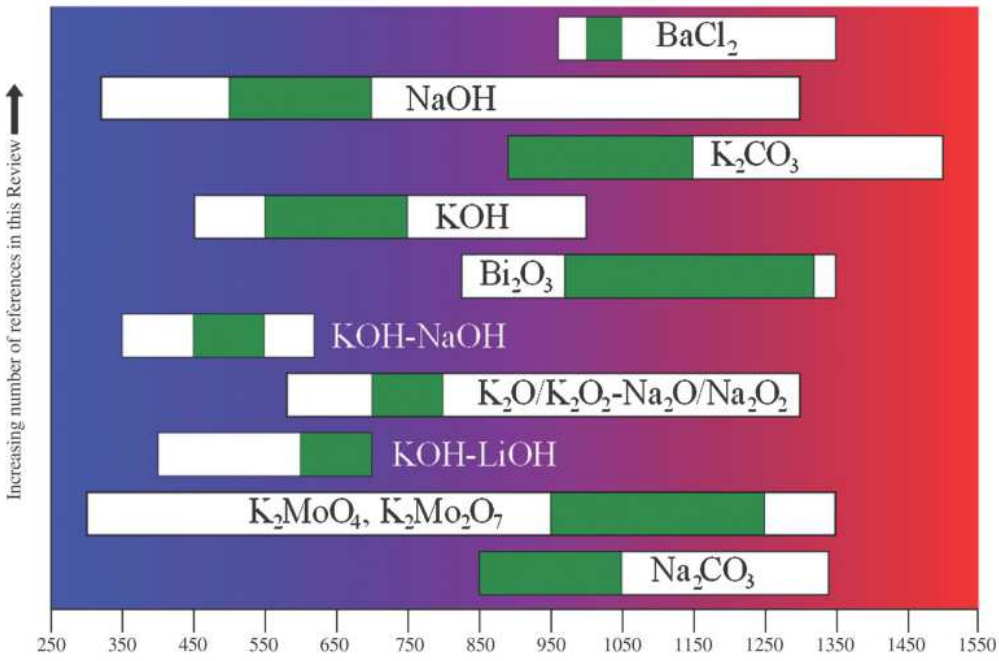

Figure 2-14. Various flux systems, most commonly reported as well as the range of working temperatures. The optimal temperature ranges are indicated in green [105].

2.9.2 KNN single crystals

In the recent past, a few reports on the growth and properties of KNN single crystals have been published, which are quite less when compared to polycrystalline KNN [30, 108-111]. The better electromechanical properties (d_{33} = 2500 pV/N) of lead based ferroelectric single crystals like $Pb(Zn_{1/3}Nb_{2/3})O_3$-$PbTiO_3$ and $Pb(Mg_{1/3}Nb_{2/3})O_3$-$PbTiO_3$ which is almost five times more than the bulk PZT [5] were the origin of the research on KNN single crystals and encouragingly, KNN single crystals have shown better electromechanical properties as compared to their ceramic counterparts [16, 112]. Various methods were used to produce KNN single crystals. Kizaki *et al.*, used a molten salt method (in molten salt method, the solvent is a molten salt or oxide and in this case, NaF and KF were used as flux), to produce KNN single crystals but were unable to measure crystal properties due to higher crystal conductivity. When Mn was added, resistivity was quite significantly improved [113]. KNN grown by solid state crystal growth (SSCG) was reported by some researchers. The basic principle for the SSCG is the abnormal grain growth. In this method, a single crystal is buried in a powder matrix

as a seed and long dwell time at high temperature are used. In case of $(K_{0.5}Na_{0.5})NbO_3$, $KTaO_3$ used as the seed crystal [17, 114], but grown crystals contains a lot of porosity as it can be observed in Figure 2-15a. Hot pressing (HP) was used to reduce the porosity in the grown crystals and it also proved helpful to some extent as obvious in Figure 2-15b [17, 114].

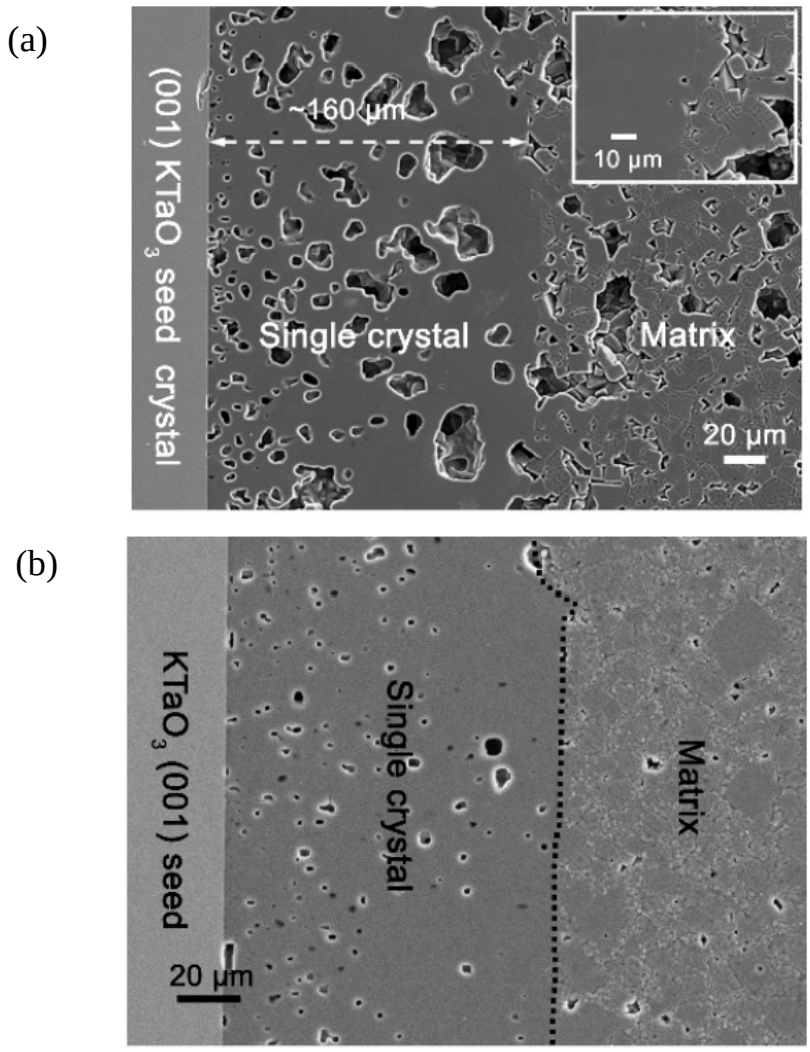

Figure 2-15. SEM micrographs of (a) KNN (the inset shows the boundary between the matrix and the single crystal) [108] and (b) $[Na_{0.5}K_{0.5})_{0.97}Li_{0.03}](Nb_{0.8}Ta_{0.2})O_3$ single crystal layer grown on a (001) $KTaO_3$ seed crystal [115].

Most of the articles published on the growth of single crystals reported, emphasizing the growth conditions and only some of them reported the properties. As a summary

of the current literature on KNN single crystals, Table 2-5 summarizes the various methods to grow single crystals, crystal orientation and properties of undoped and doped KNN single crystals. For the crystals grown by solid state crystal growth, only domains observed by polarization light microscopy and transmission electron microscopy were reported [115, 116]. This might be due to fact that crystal is embedded in the powder matrix. Undoped KNN single crystals showed the higher d_{33} values of ~ 160 pC/N as compared to 90 pC/N for polycrystalline ceramics [16, 112]. The relation between the domains and electromechanical properties is still missing in the literature.

Table 2-5. Production method and properties of KNN single crystals. Abbreviations used are Solid state crystal growth (SSCG), high temperature self flux method (HTSF).

Composition	**Method**	**Seed crystal / Flux**	ε_r	d_{33}	T_C	P_r	E_c	**Refs.**
			1 kHz	pC/N	°C	µC / cm^2	kV / cm)	
$K_{0.5}Na_{0.5}NbO_3$	SSCG	$KTaO_3$						[116]
$K_{0.5}Na_{0.5}NbO_3$	HTSF	K_2CO_3	240	160	393			[117]
$K_{0.56}Na_{0.44}NbO_3$	HTSF	K_2CO_3		130	433			[111]
$[(Na_{0.5}K_{0.5})_{0.97}Li_{0.03}](Nb_{0.8}Ta_{0.2})O_3$	SSCG	$KTaO_3$		180				[115]
$K_{0.5}Na_{0.5}NbO_3$	SSCG, $K_4CuNb_8O_{23}$	$KTaO_3$						[108]
$K_{0.5}Na_{0.5}NbO_3$	SSCG, $K_4CuNb_8O_{23}$	$KTaO_3$						[118]
$K_{0.5}Na_{0.5}NbO_3$	Flux method	KF–NaF	226	148	407	18	20	[112]
$K_{0.5}Na_{0.5}NbO_3$	Floating zone (FZ)					27	22.2	[30]
$(Na_{0.5}K_{0.5})(Nb_{0.995}Mn_{0.005})O_3$						106	14.8	
$(Na_{0.5}K_{0.5})(Nb_{0.995}Mn_{0.005})O_3$	Flux method	KF–NaF	424 (10 kHz)	161	407	52	13	[109]

2.10 Texturization

The development of texture in ferroelectric ceramics is an alternative strategy that has been used for increasing the piezoelectric response of these materials due to the inherent anisotropy in their properties. In this way, one may achieve properties lying between those of single crystals and those of the randomly oriented ceramics. It is difficult to achieve high piezoelectric response in randomly oriented KNN polycrystalline materials as is obvious in Table 2-4, in which that d_{33} is limited between 200-300 pC/N for many dopants. The fabrication of most bulk ferroelectric ceramics starts with powder preparation (mixing and firing process). The powder is then pressed to the required size, shape and then the green sample is thermally processed (sintering) for its densification and mechanical integrity. Some processing methods that have been traditionally used to fabricate electroceramics are extrusion, die pressing, slip casting, injection molding, tape casting etc. The powder processing steps have a very strong influence on the characteristics and final properties. In general, ceramics are formed by randomly oriented micrometric grains, which may vary in crystalline structure, composition, size, shape, and in term of internal stress to which they are subjected. For further studies on the preparation and properties of ferro- and piezoelectric ceramics, exists several references [20, 33, 40, 119]. Indeed the intensity of the enhanced response in the textured ceramics depends on the material crystallographic orientation. In uniaxial ferroelectrics, or in materials where the spontaneous polarization is confined to a plane, texturing enables a more efficient alignment of the polar vector, increasing in this way the poling efficiency and consequently leadingto an improvement in the electrical properties [120]. Thus, this effect cannot be fully exploited in randomly oriented polycrystalline materials. Consequently, textured ceramics of piezoelectric materials are being considered of a special scientific and commercial interest [121]. Some examples of highly textured ceramics with optimised properties are $Bi_4Ti_3O_{12}$, $Sr_2Nb_2O_7$, $CaBi_4Ti_4O_{15}$, $Pb(Mg_{1/3}Nb_{2/3})O_3$-$PbTiO_3$ (PMN-PT), $Sr_{0.53}Ba_{0.47}Nb_2O_6$ and $(Na_{1/2}Bi_{1/2})TiO_3$ - $BaTiO_3$ [18]. Therefore, the study of texturing in KNN ceramics is of fundamental importance for tailoring their piezoelectric, ferroelectric and dielectric properties, and thus improves the sensing and actuating capabilities for various devices.

One of the most promising routes for controlled crystallographic and morphologic texture developments in polycrystalline ceramic bodies is the templated grain growth (TGG) [18]. In TGG, texture is developed by sintering and annealing the compacted ceramics, which contains large template particles mostly of template size between 5–50 µm and fine matrix powder. Texturing, which in simple words is Ostwald ripening-type process (i.e. the large grains grow at the expense of the finer matrix grains), and the lattice match ensures that the nucleation of the growing phase occurs on the templates surface and then, a further heating drives to densification and subsequently to grain growth. Difference in the surface free energy between the matrix grains and the larger template particles plays a very important role in the texturization process. If the matrix is a precursor of the final ceramic phase, the template particles can act as nucleation sites and control the phase transformation of the matrix. This process is referred in the literature as reactive TGG (RTGG) because the dual role of the templates [18, 122]. In this case, the templates must react with the matrix to obtain the desired final phase, which takes the morphological form of the templates. The degree of texture depends on the template size, shape and composition and the obtained properties are largely dependent on the degree of texture. The degree of texture is normally expressed in terms of Lotgering factor (*f*), which is calculated from the X-ray diffraction pattern, and defined as the fraction of the area textured with the crystallographic plane of interest using

$$f = \frac{P_{00l} - P_0}{1 - P_0} \qquad \textit{Equation 2-12}$$

where, $P_{00l} = \sum I_{00l} / \sum I_{hkl}$ and $P_0 = \sum I^0_{00l} / \sum I^0_{hkl}$, with I_{hkl} and I^0_{hkl} being the intensities of (hkl) planes for the textured and randomly oriented samples, respectively.

Being based on a standard powder processing and sintering, TGG achieves texture at a significantly lower cost as compared to other techniques used for texturing like hot forging or hot pressing.

2.10.1 Textured KNN ceramics

In KNN based ceramics, the texturing has been mainly done by using tape casting technique and by using various shapes of $NaNbO_3$ as template material, although

some other templated materials e.g. plate like $BaTiO_3$ has also been used. In general, the properties have been improved and piezoelectric constant has been increased to more than 300 pC/N. Table 2-6 shows the properties of textured KNN (undoped and doped) ceramics reported in the literature.

Table 2-6. Production methods and properties of KNN textured ceramics along with properties.

Composition	**Method**	**Lotgering factor**	ε_r	*tan δ*	d_{33}	T_C	P_r	E_c	**Refs.**
			1 kHz		pC/N	°C	(μC / cm^2)	(kV / cm)	
$K_{0.5}Na_{0.5}NbO_3$									
$(K_{0.5}Na_{0.5})_{0.98}Li_{0.02}NbO_3$	Tape Cast Plate-like $NaNbO_3$,	98%	263		192, 208	439	22.1	12.7	[123]
$(K_{0.5}Na_{0.5})(Nb_{0.85}Ta_{0.15})O_3$		99%	413		184	322			[123]
$K_{0.45}Na_{0.55}NbO_3$	Screen printing, plate-like NaNbO3.		432 (‖) 331(⊥)	0.06 (‖) 0.04(⊥)		401	18.4 (‖) 18.6(⊥)	10.1 (‖) 10.4(⊥)	[124]
$(Na_{0.50}K_{0.47}Li_{0.03})(Nb_{0.8}Ta_{0.2})O_3$	tape casting, plate-like NaNbO3				310	320	11	14	[125]
$K_{0.5}Na_{0.5}NbO_3$	tape cast Plate like $BaTiO_3$ (BT) templates		810 (‖) 331(⊥)		163		29.5 (‖) 14.4(⊥)		[126]
$(K_xNa_{1-x})_{0.946}Li_{0.054}NbO_3$	Tape cast plate-like $NaNbO_3$ particles	80 %	646	0.05	231–254	450	24.9		[127]

So far, the best properties achieved in KNN based ceramics doped with Li, Ta and Sb was obtained only after texturing [64]. Saito *et al.*, also used the RTGG method with whisker shaped, $NaNbO_3$ as template to produce <001> oriented textured KNN based ceramics($(K_{0.44}Na_{0.52}Li_{0.04})(Nb_{0.86}Ta_{0.10}Sb_{0.04})O_3$ designated as LF4T [64, 128] and having comparable properties to PZT (PZT4; commercial composition) as can be seen in

Table 2-7 with a Lotgering factor of almost 90 %. Some other reports on oriented KNN based ceramics e.g. doped with Sb, by using $NaNbO_3$ template are also reported with improved properties as compared to the randomly oriented counterparts but lower than the Saito report [123, 129]. Uptill now, there is very limited data available for the textured KNN ceramics by the conventional ceramic method by using TGG process. Still, there exists a lack of understanding for the relationship between orientation, domains and electrical properties in KNN based ceramics.

Table 2-7. Comparison of properties of KNN (LF4T) with PZT4.

Compositon	**Curie temperature (°C)**	**Piezoelectric Coupling coefficient**	**Piezoelectric charge constant (pC/N)**		**Dielectric constant**
	T_C	K_p	d_{33}	d_{31}	
LF4T (Saito KNN composition) [64]	253	0.61	416	152	1570
PZT4 [45]	250	0.60	410	170	2300

2.11 Domains in KNN based ceramics

As already explained in the previous sections, domains are very important to understand and improve the properties. Here we will discuss the domain studies reported for KNN based ceramics and single crystals in the literature. Figure 2-16a and b shows domains in the undoped KNN ceramics and single crystal reported by transmission electron microscope (TEM) respectively. Bulk ceramics showed the fringe type domains [130], whereas, 180º domains of nearly 50 nm size and 90º domains of 100-300 nm were reported for the same crystals grown by solid state crystal growth method [116].

(a)

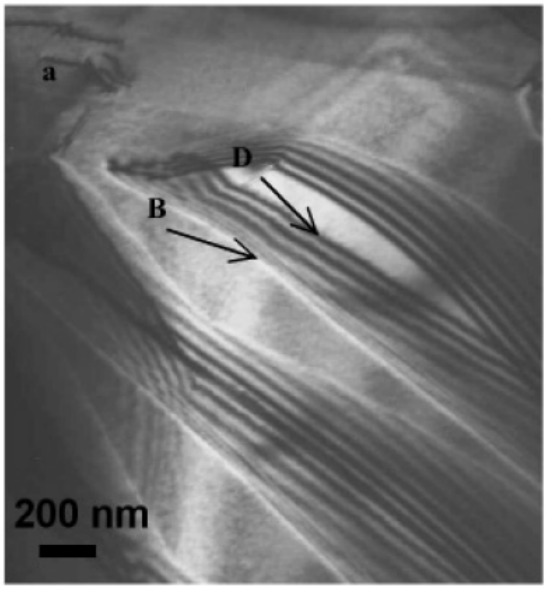

(b)

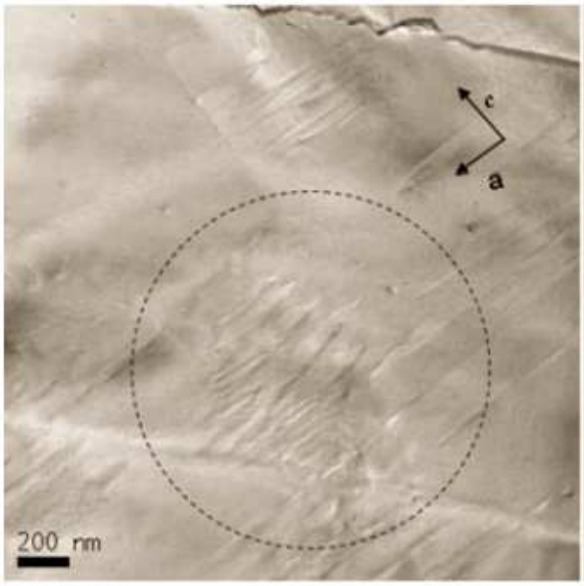

Figure 2-16. TEM microstructures of ferroelectric domains of (a) KNN polycrystalline sintered at 1100 ºC for 2 h [130] and (b) KNN single crystal showing 180º domain and wedge shape domains [116].

Figure 2-17 shows the piezo-response force microscopy (PFM) images of doped KNN composition $(K_{0.44}Na_{0.52}Li_{0.04})(Nb_{0.86}Ta_{0.1}Sb_{0.04})O_3$, close to the so called morphotropic phase boundary (MPB), where tetragonal / orthorhombic phases coexist. The studies were made on the ceramics synthesized by abnormal grain growth. The crystallographic planes presented in the images were calculated by assuming the coexistence of

orthorhombic and tetragonal phases. Furthermore, it was claimed that the domain wall formed by (010) plane, and domains are separated by $(1\bar{1}0)$ and (110) with an angle of nearly 90º is due to orthorhombic phase and broad stripes next to these domains were assigned as $[\bar{1}0\bar{1}]$ and [101] (also shown as schematic in the inset), which is possible only by considering the orthorhombic phase [25].

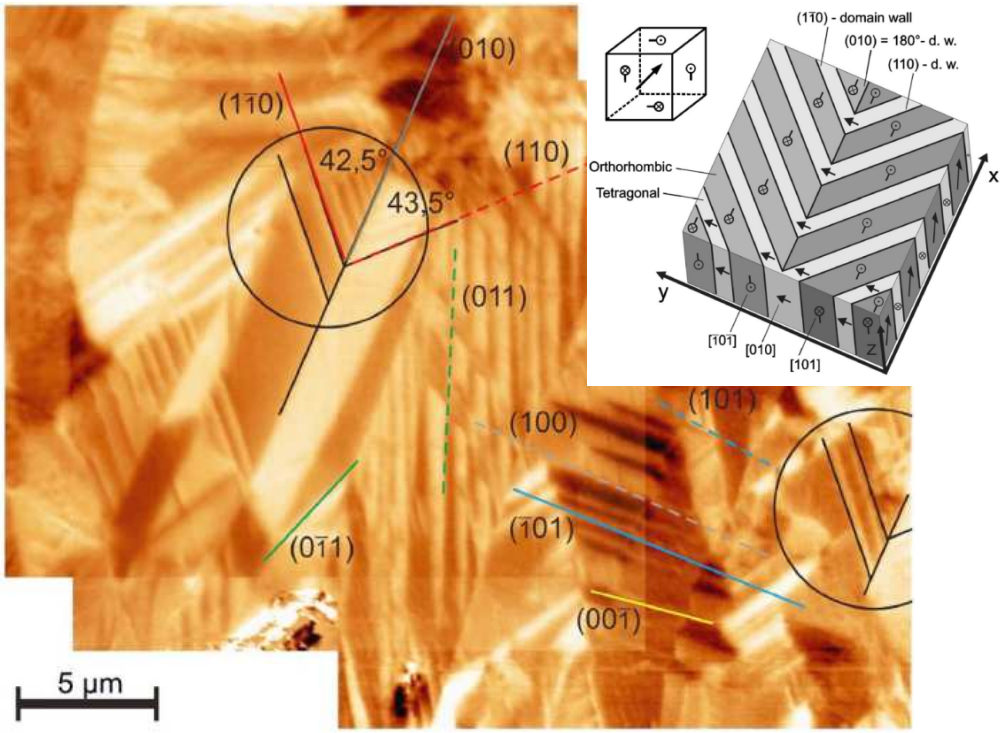

Figure 2-17. In plane PFM images of $K_{0.44}Na_{0.52}Li_{0.04}Nb_{0.86}Ta_{0.1}Sb_{0.04}O_3$. Crystallographic planes were calculated assuming MPB of orthorhombic and tetragonal structure. Inset shows the schematic of the domain pattern [25].

Figure 2-18a and b shows the domain studies of KNN ceramics by confocal Raman spectroscopy coupled to atomic force microscopy (AFM). The ceramics were prepared by microwave hydrothermal synthesis. The Raman domain studies were analyzed based on the fact that different kind of domains presents different Raman spectra. The AFM domain studies were done on a chemically etched sample having a grain size of ~ 60 µm. It was claimed that domains in topographic image was observed because the sample was etched chemically and etchants reacted at a different chemical rate to different crystallographic orientations. The topography analyses confirm the 90º

and 180º domains. The domain studies were analyzed based on the fact that adjacent stripes present different Raman spectra. This measurement shows that there are relevant differences related to the polarization direction in the striped regions corresponding to alternate in-plane and out-of-plane orientation.

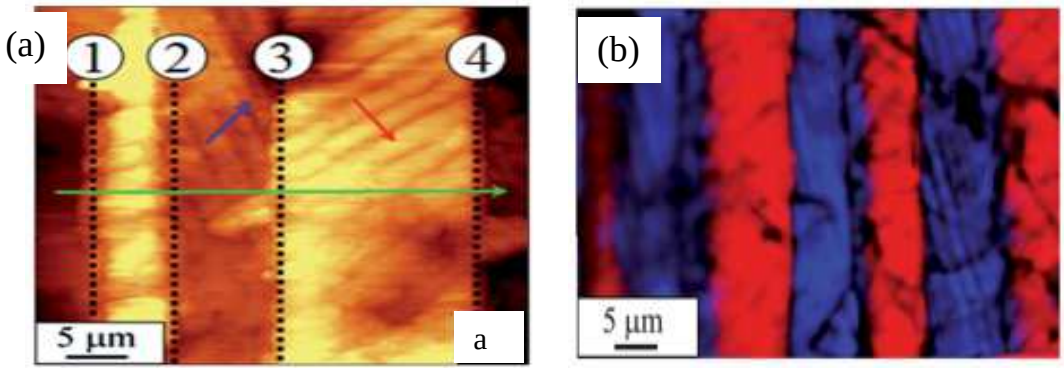

Figure 2-18. Characterization of KNN ceramics through AFM: (a) AFM image of the showing the domain structure and (b) Raman map of domain structure exhibiting differences between average spectra of adjacent striped domains separated by a 90º domain wall [131].

2.12 Summary

There exists a billion of dollars market for the piezoelectric applications and currently PZT is the most widely used material. The major problem with PZT is the toxicity of lead. Since 1990's, lead free materials have great attention due to environmental and health concerns to replace lead based ones. This chapter reviewed the properties of various lead based and lead free families. Among these, KNN is a promising material with a high potential to become commercially viable, based on the high Curie temperature and possibility to engineer the electromechanical properties. An overview of the state-of-the-art of the knowledge on KNN was presented. It is obvious that mechanisms responsible for the inferior properties in KNN polycrystals need to be understood by doing a comparison study between polycrystalline and single crystal. Then, concepts need to be applied to make robust KNN materials. Figure 2-19 shows the current situation of KNN based ceramics and the arrow in the image shows the main objective of this work. In literature, KNN based materials with high d_{33} are due to the so called MPB, and

properties are not stable with temperature. So, our objective is to design the KNN based ceramics with high Curie temperature as well as high intermediate phase transitions temperature from monoclinic to tetragonal phase.

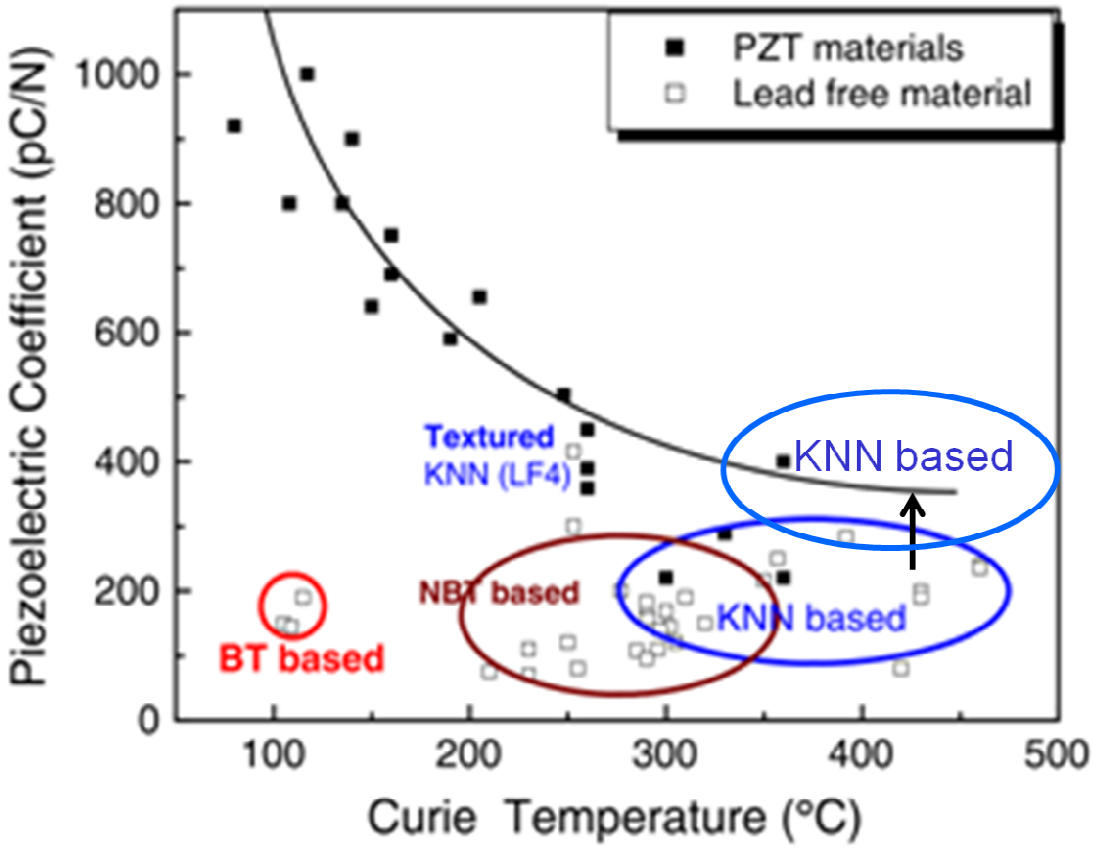

Figure 2-19. Piezoelectric coefficient versus Curie temperature for the lead based and lead free families. The black arrow in the image shows the main objective of this work.

CHAPTER 3
Experimental

3. Experimental

3.1 Abstract

This chapter is dedicated to the description of the strategy used to approach the stated problem of this thesis that allowed to fulfill the defined objectives. Hence, this chapter describes the processing of bulk ceramics (doped, undoped and textured) and the growth of high quality KNN single crystals. This is followed by a brief presentation of the experimental techniques used to characterize the structure, microstructure, dielectric, ferroelectric, piezoelectric properties and to study ferroelectric domain studies of both single crystals and polycrystals. This part gives details on preparation of the samples for characterization.

3.2 Introduction

The experimental work carried out in this work is schematically presented in Figure 3-1.

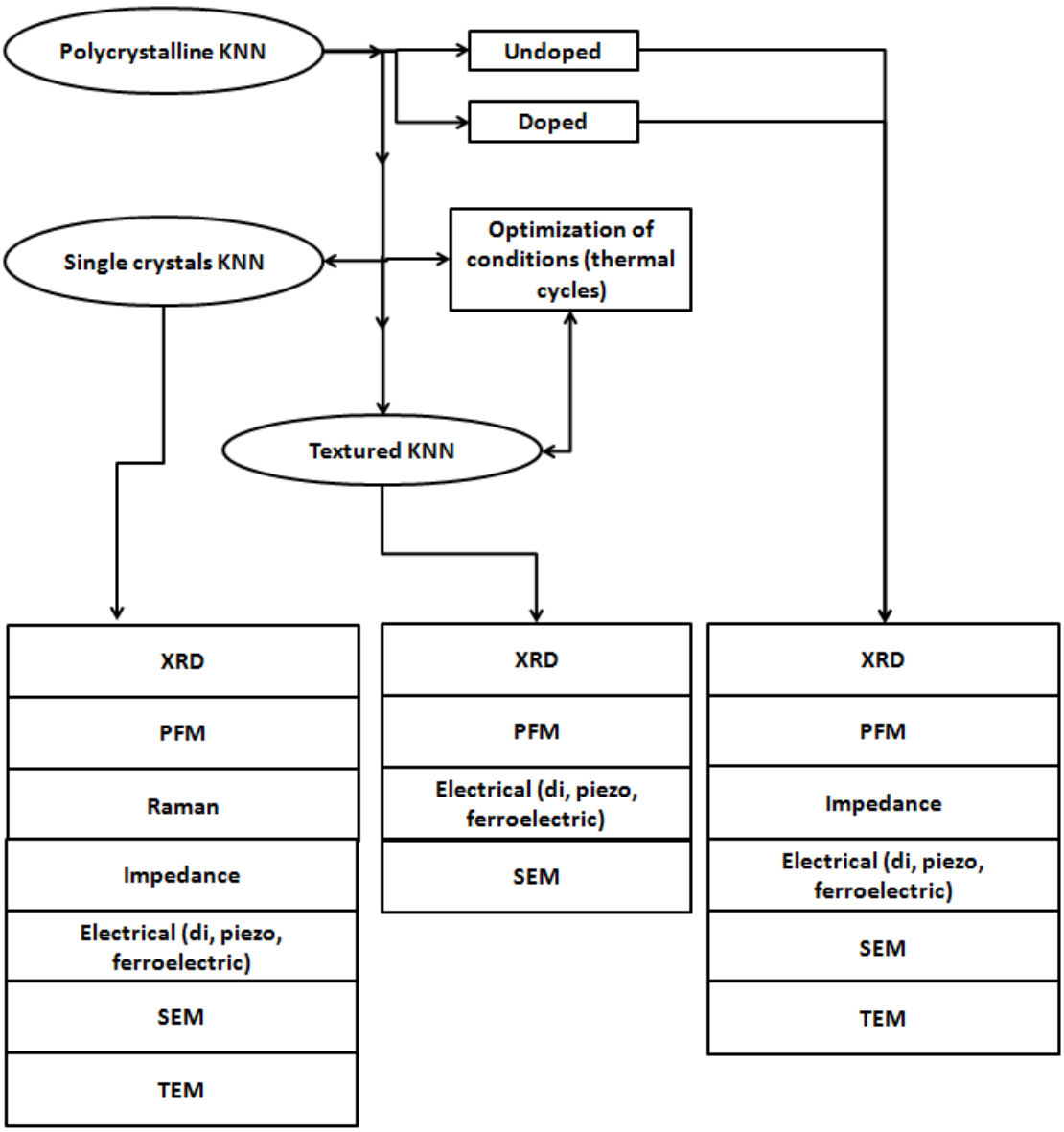

Figure 3-1. Flow chart of the work plan performed in this work.

Undoped, doped and non stoichiometric KNN ceramics were prepared by sintering KNN powders synthesised by conventional ceramic processing. For comparison purposes and to be used as seeds in textured KNN ceramics, KNN single crystals were grown by flux method. The raw materials used for this research are mainly commercial powders whose level of purity and source are shown in Table 3-1.

Table 3-1 Raw powders used in the synthesis of KNN based piezoelectric ceramics and single crystals.

Chemical name	**Chemical formula**	**Purity**	**Source**
Potassium carbonate	K_2CO_3	≥99%	Merck
Sodium carbonate	Na_2CO_3	≥ 99.5%	Chempur
Niobium oxide	Nb_2O_5	99.9%	Chempur
Manganese oxide	MnO	99%	Aldrich
Lithium carbonate	Li_2CO_3	99%	Merck
Boron oxide	B_2O_3	95%	Merck

The experimental details of each of these processes are presented below and in some cases, specific details presented in each sub chapter of chapter 4.

3.3 Doped and undoped polycrystalline ceramics

3.3.1 Undoped KNN ceramics

Undoped ceramics having composition $K_{0.5}Na_{0.5}NbO_3$ (KNN) ceramics were prepared by conventional mixed oxide route.

3.3.2 Non-stoichiometric (NST) KNN

Non-stoichiometric $(K_{0.5}Na_{0.5})NbO_3$ with A/B of 0.90, 0.95, 0.97, 0.98, 0.99, 1.0, 1.01, 1.02, 1.03, 1.05, and 1.10 were produced. A stands for A-site K and Na and B stands for B-site Nb.

3.3.3 Mn doped KNN ceramics

The Mn doped KNN ceramics with global formula $(K_{0.5}Na_{0.5})_{1-2x}Mn_xNbO_{3-\delta}$ and $(K_{0.5}Na_{0.5})Nb_{1-2/5y}Mn_yO_{3-\delta}$, where [x=0, 0.0005, 0.0009, 0.00125, 0.0025 and 0.005, whereas, y=0, 0.005, 0.01, 0.015 and 0.02)] were prepared.

The polycrystalline KNN powders were synthesized via solid-state reaction. The sequence of the steps for the preparation of the KNN bulk ceramics corresponding to the compositions mentioned above are shown in Figure 3-2. The steps described in the bracketed portion of the diagram upto ball milling after calcination are common both to

the ceramics and single crystal. From this stage, the route changed for the bulk ceramics and single crystals powder. Then, for the KNN bulk ceramics, powder were pressed to form pellets in a die having diameter of 10 mm, first by applying uniaxial pressure of 170 MPa and then by cold isostatic pressing at a pressure of about 200 MPa for two minutes. These pellets were sintered at 1100 °C, for 2 h in air at a heating and cooling rate of 2 °C / min in a tube furnace. The details for the single crystals are explained below.

3.4 KNN single crystal

The polycrystalline KNN powders were first synthesized via solid-state reaction as explained in the previous section. After the bracketed region (after calcination), for preparing KNN single crystals, a mixture of K_2CO_3 and B_2O_3 (9:1) was selected as the flux and mixed by ball milling for 5 h. Various thermal profiles as presented in Figure 3-4 with different combinations of flux were used. The pre-calcined KNN powders were mixed with the flux mixture in a proportion of (4:1) by ball-milling for 5 h. Then 60 g of the KNN flux mixture was loaded into a Pt crucible (inner dia. - 55 mm, height – 60 mm) and tightly sealed with a Pt lid. Pt crucible was filled almost 75 % of the total volume to avoid the over pressure inside the crucible. The Pt crucible was then inserted into a larger alumina crucible (inner dia. - 60 mm, height – 80 mm), and sealed with alumina powder, to minimize the evaporation of the flux at high temperature as schematics shown in Figure 3-3.

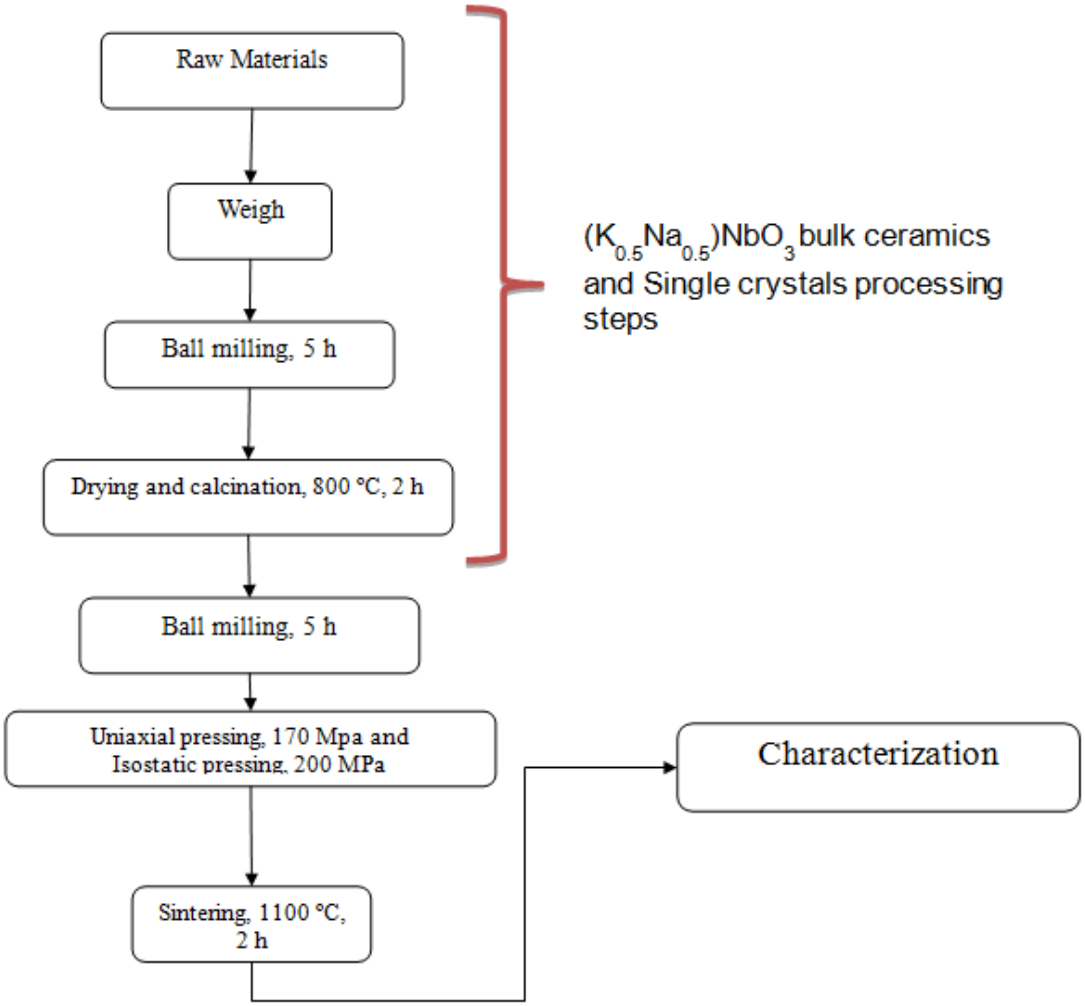

Figure 3-2. Steps followed for the preparation of KNN bulk ceramics and single crystals.

The alumina crucible was placed into a vertical furnace equipped with an automatic temperature controller. The mixture was then heated following the thermal profiles (Figure 3-4) i.e. (1) heating from room temperature to 1000 °C at a rate of 150 °C/h and dwelling at this temperature for 2 h (premelting step); (2) heating to a maximum temperature (between 1200-1250 °C) at 50 °C/h and dwelling there for 10 h; (3) slow cooling from the maximum temperature to 1150 °C at 5 °C/h, from 1150 °C to 1000 °C at 10 °C/h, from 1000 °C to 600 °C at 20 °C/h, and then down to room temperature at 150 °C/h. After the growth procedure, the crystals were separated from the solidified flux. This was a slow process that took a few days.

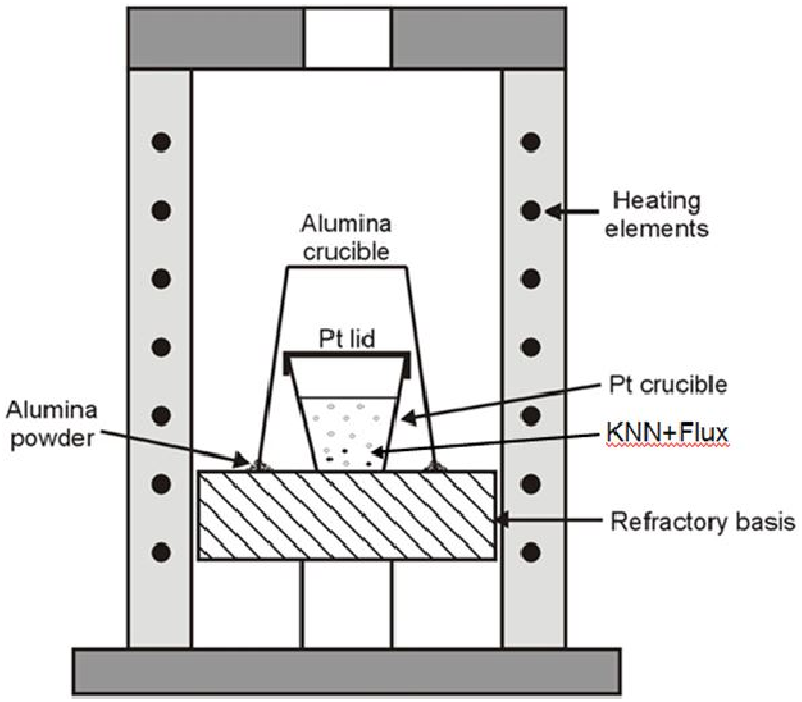

Figure 3-3. Schematic representation of the used setup for the high temperature self-flux growth of KNN single crystals.

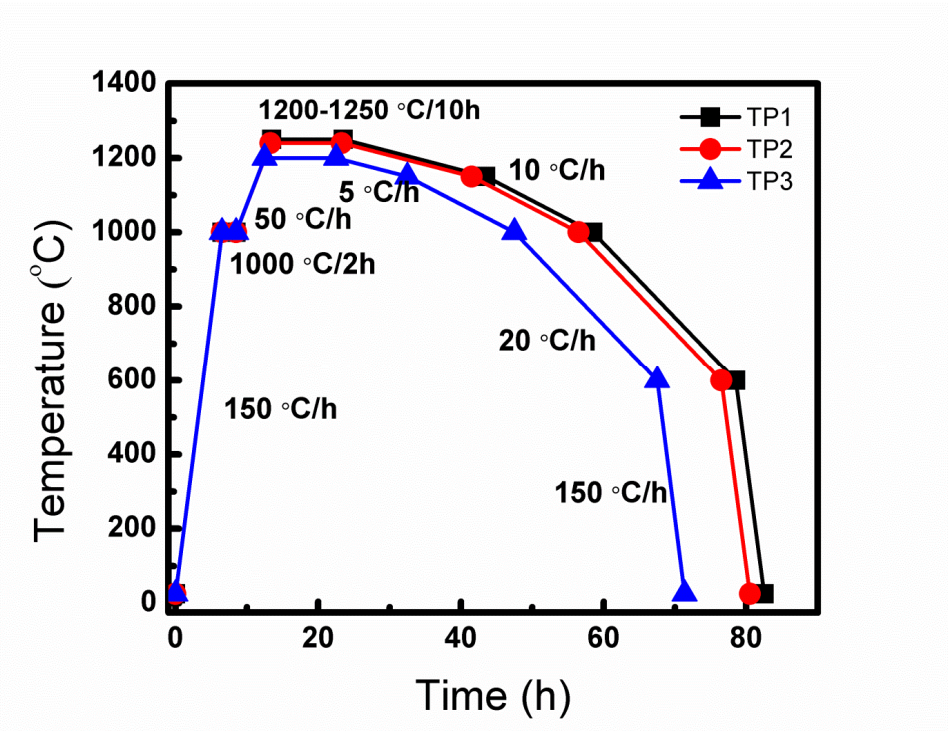

Figure 3-4. Furnace thermal profiles (TP1, TP2 and TP3) used for the growth of KNN single crystals.

The crucible was placed in a beaker with water for several hours / days to dissolve the solidified flux. Then, the crystals were washed in water several times and with a sonication step to dissolve any remaining flux. This step was repeated until the crystals were cleaned. After that the single crystals were characterized as presented in Figure 3-1.

3.5 KNN textured ceramics processing

3.5.1 Processing and conditions

To produce textured KNN ceramics by templated grain growth (TGG), calcined KNN powders previously prepared, as described above Figure 3-2 were used. After calcination, these powders were milled again (average particle size of ~ 1 µm) and dried in an oven at ~ 120 ºC for several hours, being thus considered ready to be used as a matrix powder for TGG.

The preparation of textured KNN ceramics by TGG implies the use of templates, as well. In the present case, for the homoepitaxial TGG of KNN ceramics and as indicated above, the templates used are KNN single crystals previously grown. Cleaned crushed crystals (10 wt %) with rectangular shape and the [001] orientation perpendicular to the major face were crushed in a mortar to pass through a 325-mesh sieve (45 µm of nominal aperture size). Figure 3-5 shows the anisometric template particles thus obtained with a plate-like morphology and average size of ~ 40 × 20 × 8 µm. Matrix and templates were mixed and stirred in ethanol for 2 h until the mixture was homogeneous, and subsequently dried in air at 120 ºC. The processing steps to produce textured KNN ceramics are also shown in Figure 3-6.

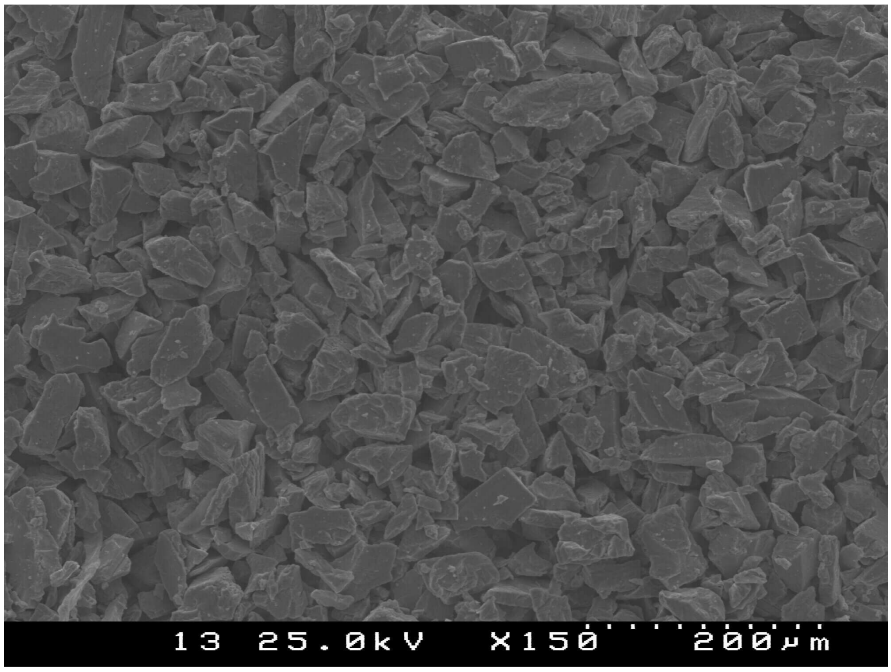

Figure 3-5. SEM micrographs of KNN template particles used as seeds for TGG process.

3.6 Experimental techniques

3.6.1 X-ray diffraction (XRD)

X-ray Powder diffraction is an essential technique for crystalline phase identification and crystal structure refinement. Because the wavelength of X-rays (from few angstroms to 0.1 angstrom) is comparable to the size of atoms, they are ideally suited for probing the structural arrangement of atoms and molecules in a wide range of materials. A monochromatic X-ray beam with a wavelength (λ) incident onto a crystalline material at an angle (θ) leads to diffraction, when the distance travelled by the rays reflected from successive planes differs by a complete number n of wavelengths [132]. Bragg's law is the basic governing principle in this technique, expressed through the equation [133]

$$n\lambda = 2dsin\theta \qquad \textit{Equation 3-1}$$

where *d* is a spacing distance between the lattice planes and λ is the wavelength and θ is the angle of incidence.

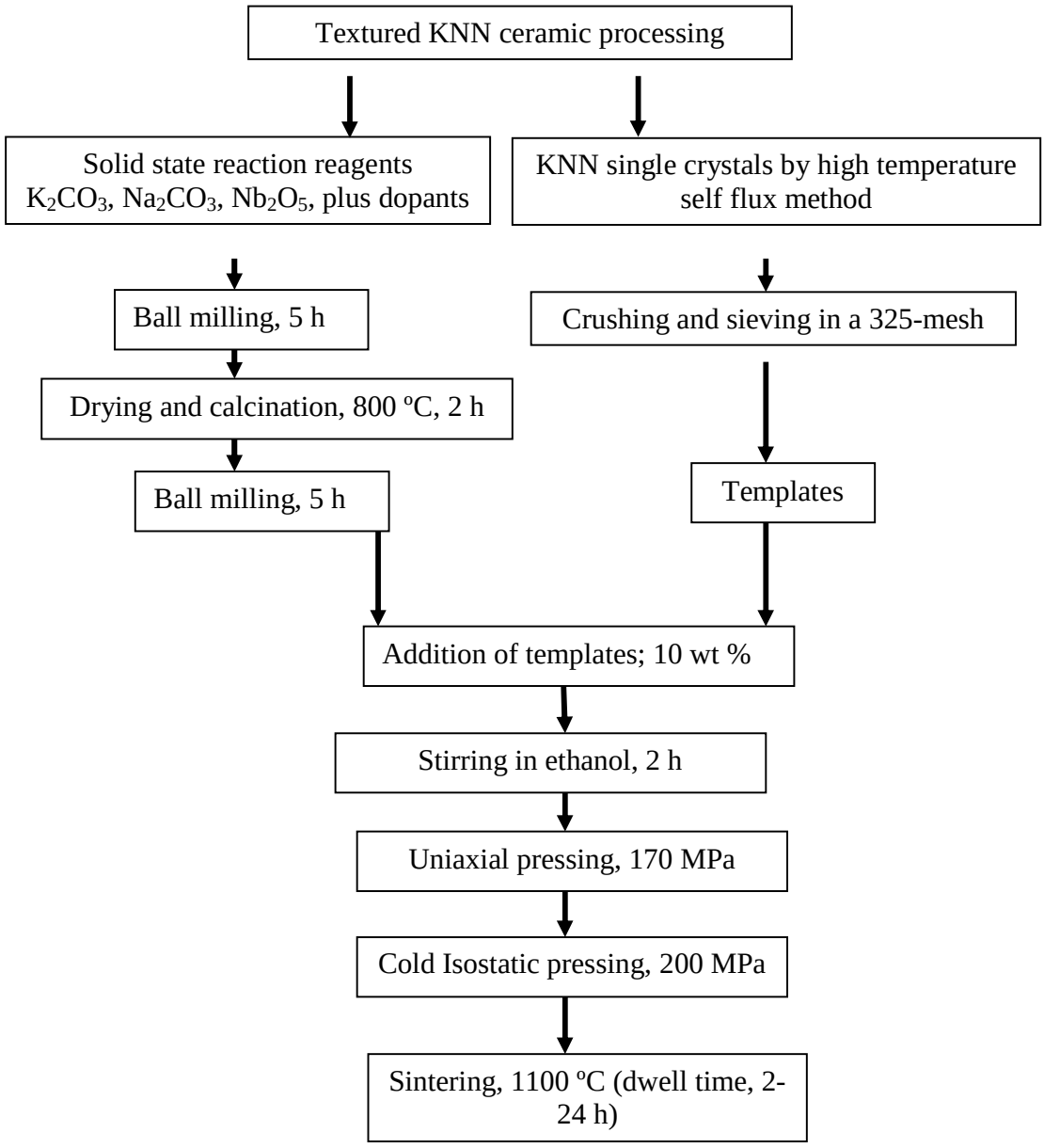

Figure 3-6. Processing steps for the fabrication of textured KNN ceramics by TGG.

The condition for maximum intensity contained in Bragg's law allows calculating details about the crystal structure. The crystal phase assemblage in this work was mainly evaluated by X-ray powder diffraction (XRD, Rigaku, D/Max-B, Cu-Kα radiation; λ = 0.15064 nm) at room temperature. The XRD was typically operated at 50 kV and 30 mA. θ-2θ scans at rate of 1º/min with step 0.02º between 20-60º were mostly adopted in the current experiments.

The degree of texture is normally expressed in terms of Lotgering factor (*f*), which is calculated from the X-ray diffraction pattern, as explained in Chapter 2 and Equation 2-12.

Texture quality can be evaluated by pole figure measurement, which measures the intensity of a given XRD peak as the sample rotates about two orthogonal axes, thus collecting the sum of the lattice plane reflection signals from a large number of crystallites in a polycrystalline material. The principle, in order to determine the orientation of a given lattice plane, (hkl), is as follows: the detector is first set to the proper Bragg angle, 2θ, of the diffraction peak of interest and then the sample is rotated in a goniometer until the lattice plane hkl is in the reflection condition i.e. the normal to the lattice plane is the bisectrix between incident and diffracted beam.

Rocking curve is often used to reveal the orientation of planes with an orientation close to parallel to the sample surface. For a fixed θ-2θ position, plane positioned at different tilt position with θ are brought to diffraction by varying tilt.

For further reading and understanding the basics, reference is recommended [134].

3.6.2 Scanning and transmission electron microscope

Scanning electron microscopy (SEM) is a micro-analytical technique, which offers a much higher resolution as compared to optical microscopy, hence capable to image or analyze materials that cannot generally be observed with the resolution offered by optical techniques, thus allowing a detailed analysis of the grain growth and morphology of the studied material.

In SEM, an electron beam source emits electrons, which are then collected and focused by lenses to form few nanometers sized probes. Deflection coils are used to operate the electron beam and to scan the sample surface. Simultaneously, another electron beam runs over a TV monitor screen in a synchronized mode. The image magnification is the ratio of the scanned monitor range to the scanned sample range and it is easily controllable by beam deviation elements. Primary electron beam interacts with the specimen surface resulting in different emitted signals (secondary and back scattered electrons, X-ray radiation, etc.), which can be registered with the appropriate

detector [135]. The microstructures of the samples surface were characterized by using secondary electron in scanning electron microscope; SEM, S4100, Hitachi, Tokyo, Japan, coupled with EDS (QUANTAX 400, Bruker, Berlin, Germany).

Samples preparation for SEM analysis was carried out according to different procedures depending on the type of sample, i.e. sintered ceramic or powder sample. Concerning sintered bodies, they were ground and polished slowly by gradually reducing the micron size of the polishing papers, to remove all the scratches and get a mirror like surface. Several thermal treatments on the polished samples were tested in order to reveal the grain boundary and grain morphology for SEM observation. The thermal treatments were done at high temperatures between 1000 ºC and 1050 ºC for different times from 1 to 30 min, including quenching from 1050 ºC to room temperature. For SEM measurements the polished and etched samples were pasted in a special sample holder using a conductive carbon paste and dried for 12 h in an oven at 120 ºC. Then, the samples were covered with a thin layer of carbon in order to improve the quality of the image. The carbon deposition process was performed using an Emitech K950 carbon deposition chamber equipped with a turbo pump. Regarding the powder samples, very small quantity of powders were dispersed in liquid (water or ethanol), and then with the help of dropper a drop is placed on the glass slide and dried. After that, the procedure of placing the glass slide on the sample holder and carbon deposition was the same as explained above.

Image analysis for some of the images in the present work of the SEM micrographs, to measure grain size and distribution was performed by Image J. Some modifications in the SEM micrographs were necessary to perform the image analysis and were done in the following way: contrast enhancement, median filtering and threshold to obtain suitable binary images. The grain sections were manually drawn and then grain size was calculated for each grain.

To complement and gain insight by increasing the resolution, transmission electron microscope (TEM) was used to further characterize KNN. Hitachi 9000, Tokyo, Japan TEM was used in this work. In a TEM setup, a thin specimen is illuminated with electrons (the primary electrons). Whatever part is transmitted is projected onto a screen for the user to see. The relatively darker and lighter areas of the image represent those

areas of the samples where pronounced diffraction and little or no diffraction of the incident electron occur, irrespective of the direction of the diffraction, respectivley. An image in TEM can be formed by using the central spot of unscattered electrons, or by some or all of the scattered electrons. The type of the electrons is chosen by an insertion of aperture into the back focal plane of the objective lens, thus blocking out most of the diffraction pattern except that which is visible through the aperture. If the direct beam is selected, the resultant image is called a bright-field image, and if scattered electrons of any form are selected, a dark-field image is formed. Electron diffraction appears, when projector lens is focused in the back focal plane of the objective lens [137].

To meet the requirements of transparency, for TEM observations, sample thickness was reduced by using Gatan disc grinder to ~20 µm. the sample was then glued to a copper ring and ion beam polished using a precision ion polishing system (PIPS; model 691, Gatan, Pleasanton, CA, USA) until a small hole appeared. For further reading, reference of a book [137] is recommended.

3.6.3 Raman spectroscopy

Raman effect was first predicted by Smekal in 1923 and was first observed by Raman in 1928. In the initial experiments, sunlight was focused by telescope and filters and visual observation of colour change in the scattered light was observed, which was related to the materials structure. The main spectroscopies employed to detect vibrations in molecules are based on the processes of infrared absorption and Raman scattering. Spectra could be evaluated from small sample volumes, coloured samples, solids, liquids and gases and samples at high temperature, in dilute solutions, under vacuum and in a variety of other non-standard conditions. Samples can be employed in all kind of physical state. In practice, modern Raman spectroscopy is simple. Variable instrument parameters are few, spectral manipulation is minimal and a simple interpretation of the data may be sufficient. Not only had an aid to routine analysis - but opens up the possibility of time resolved spectroscopy and kinetic studies. Raman spectroscopy and its related techniques are now finding application across a wide range of research activity and increasingly becoming standard techniques in academic and industrial analytical laboratories.

Simply stated, the Raman effect can be described as “the inelastic scattering of light by matter”. When a photon of visible light, too low in energy to excite an electronic transition, interacts with a molecule it can be scattered in one of three ways: elastic, inelastic and Rayleigh. Figure 3-7 shows the basic processes which occur for one vibration. At room temperature, most molecules, but not all, are present in the lowest energy vibrational level. Since the virtual states are not real states of the molecule but are created when the laser interacts with the electrons and causes polarization, the energy of these states is determined by the frequency of the light source used. The Rayleigh process will be the most intense process since most photons scatter this way. It does not involve any energy change and consequently the light returns to the same energy state. The scattering process from the ground vibrational state (*m*) leads to absorption of energy by the molecule and its promotion to a higher energy excited vibrational state (*n*). This is called Stokes scattering. However, due to thermal energy, some molecules may be present in an excited state such as shown in Figure 3-7. Scattering from these states to the ground state m is called anti-Stokes scattering and involves transfer of energy to the scattered photon. The relative intensities of the two processes depend on the population of the various states of the molecule. The populations can be worked out from the Boltzmann equation but at room temperature, the number of molecules expected to be in an excited vibrational state other than any really low-energy ones will be small.

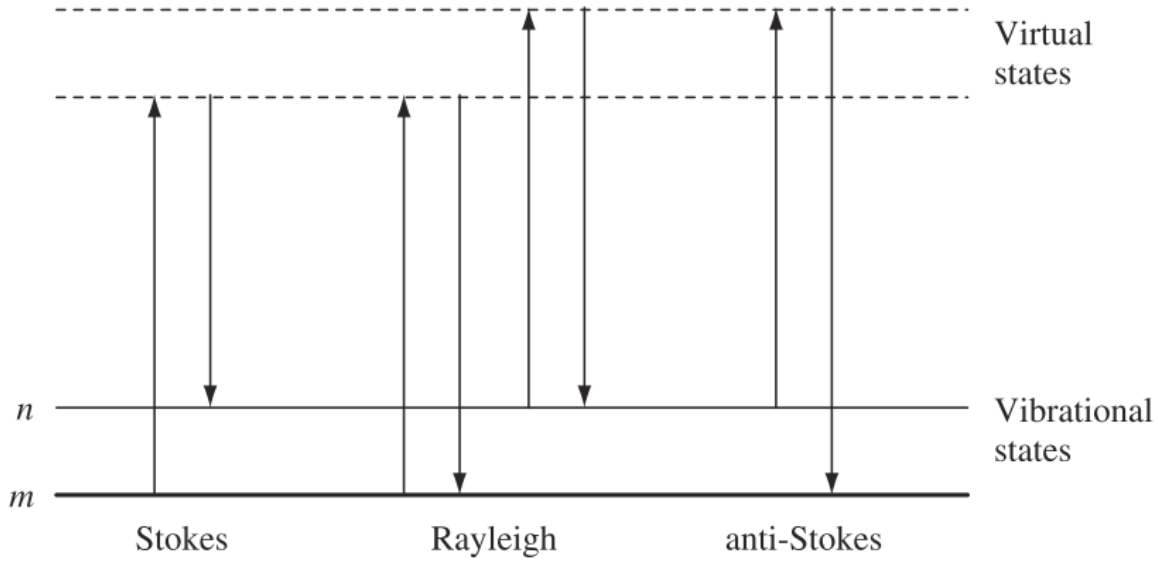

Figure 3-7. Diagram of the Rayleigh and Raman scattering processes. The lowest energy vibrational state m is shown at the foot with states of increasing energy above it. Both the low energy (upward arrows) and the scattered energy (downward arrows) have much larger energies than the energy of a vibration.

In the present study, Raman spectroscopy experiments were performed with a Raman microprobe (LabRAM HR 800, Horiba Jobin Yvon, Villeneuve d'Ascq, France) with single monochromator and edge filter (filter cut-off at 100 cm^{-1}). The 514.55 nm laser excitation was employed in the backscattered configuration with a lateral spatial resolution of 1 μm (Long-working distance 100x objective lens, NA = 0.8, Olympus, Tokyo, Japan). The measurements were done in the group of Dr. Marco Deluca (Institute für Struktur- und Funktionskeramik, Montanuniversitaet Leoben, Austria). For further reading on the topic, reference [138] can be consulted.

3.6.4 Ferroelectric hysteresis loop measurements

The single crystal and ceramic samples were painted with silver electrodes on both faces to make them electrically conductive. The polarization of the samples was conducted with the sample immersed in silicone oil, to avoid the electric breakdown in air. For the determination of the polarization versus electric field (*P-E*), the hysteresis loops, a ferroelectric tester, Aixact, TF analyzer 1000 was used, equipped with ferroelectric module. The equipment detects the current response of the device under test through

the feedback method. This setup uses a current to voltage converter. This setup has an advantage over Sawyer-Tower circuit that it greatly reduces the influence of the parasitic capacitance and back voltage [139].

The input parameters can be selected in order to control the hysteresis measurement including frequency (1 Hz to 1 kHz), variable amplitude of the driving voltage (maximum 10 kV), waveform (triangular or sinusoidal) and number of points recorded to plot the loop (400 used in this work). The current applied to the samples was auto-controlled by the acquisition software.

The measurement system has an option of applying a pre-polarization pulse to establish the negative state of relaxed remanent polarization. This was then followed by three consecutive excitation signals, each separated by 1 second of relaxation time as presented in Figure 3-8. Loops are measured in pulse 1 and 3. Pulse 1 starts from the negative relaxed remanent polarization and increase / decrease to obtain the ferroelectric polarization cycle. Cycle 2 is used to drive the sample into the positive remanent polarization without measuring the data. Finally cycle 3 starts from the positive relaxed remnant polarization and decrease / increase until complete the cycle. The data files reports these two cycles plus a third cycle obtained from the combination of the second half of the two real measurements.

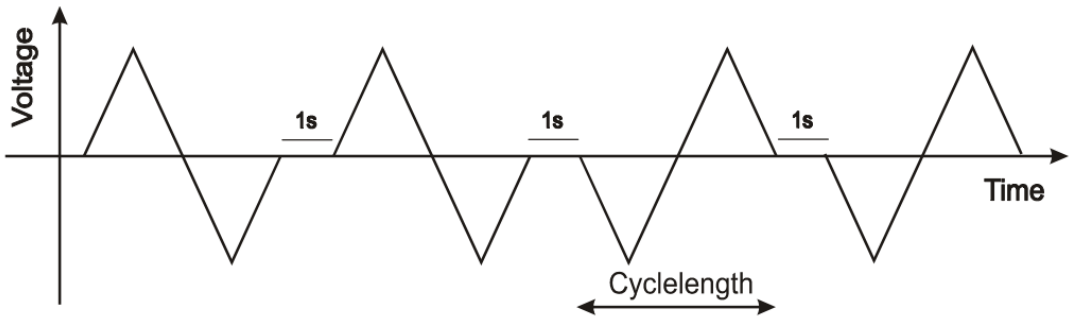

Figure 3-8. Schematic of the excitation signal for hysteresis measurement.

3.6.5 Dielectric measurements

Dielectric properties are important parameters which are helpful for understanding polarization mechanism in ferroelectric materials. In the practice, the dielectric permittivity is obtained from the capacitance measurements under an ac electric field and is a function of frequency.

Dielectric properties were measured from room temperature up to maximum 550 ºC using a Hewlett-Packard precision LCR Meter (Model HP 4284A) connected to a PC via a GPIB card and working in the frequency range from 100 Hz to 1 MHz. During the measurements, the sample was kept inside a vertical furnace where temperature was controlled using an Eurotherm 2404 controller and a thermocouple positioned very close to the sample without touching it, reaching a temperature control with a precision of ± 1 ºC.

3.6.6 Impedance spectroscopy

Complex impedance spectroscopy (IS) is a powerful non-destructive method, widely used to characterize electrical materials [140, 141]. Complex IS measurements provides a complete electrical characterization of materials as compared to the dielectric constant or loss measurements, especially if these measurements are restricted to single frequency measurements. A great strength of IS relies on the possibility of characterizing the different electrically-active regions in a material, both qualitatively and quantitatively by identifying their individual contribution for the overall material electrical properties, as is the case of grain bulk and grain boundaries or any other interface in the microstructure of polycrystals or single crystals such as their interfaces with the conducting electrodes [142, 143].

Different formalisms may be used to exploit the electrical response of the material to an applied alternate electric field such as the complex impedance (Z^*), the complex Modulus (M^*), the complex Admittance (A^* or Y^*) and the complex permittivity (ε^*). They are interrelated and can be expressed as,

$$M* = j\omega C_0 Z*$$
$$\epsilon* = (M*)^{-1}$$
$$Z* = (A*)^{-1}$$
$$A* = j\omega_0 C_0 \varepsilon*$$

Equation 3-2

where ω is the angular frequency ($\omega = 2\pi f$, where f is the frequency expressed in Hz), C_o is the vacuum capacitance of the measuring cell; $C_o = \varepsilon_o A/t$, where ε_o is the permittivity of free space (8.854x 10^{-14} F/cm), t is the cell thickness and A the electrodes area. A suitable combination of these different formalisms may be very helpful for the sake of identifying and quantifying the individual contributions of the various regions (bulk of the grain, grain boundary, etc.) to the overall electrical response of the material under analysis.

Complex impedance Z* is composed of a real part (Z') and of an imaginary part (Z''), i.e. $Z^* = Z' - Z''j$, with $j=\sqrt{-1}$, when depicted in a complex plane, the variation of Z'' with Z' as the frequency of the electric field increases, one semicircle or succession of two or more semicircles in the frequency domain is frequently obtained as illustrated in Figure 3-9. The interpretation of such impedance response is of utmost importance in view of elucidating the material regions that account for the overall impedance spectrum and very importantely for each of the individual semicircles. The assessment of each semicircle origin is facilitated if an appropriate electric circuit model can be used to describe the frequency response of the material. For an electric circuit model composed of a resistance R in a parallel to a capacitance C, ($R/\!/C$), it may be demonstrated that its impedance Z^* will vary with the field frequency in such a way that a perfect semicircle is traced when plotting Z'' against Z'. Hence, when the impedance response of a material is expressed by a series of semicircles, an electric circuit model encompassing a series of ($R/\!/C$) elements will be an appropriated choice.

Taking the example shown in Figure 3-9, where three semicircles are present, the first semicircle (from the right to the left) describes the impedance variation for the range of the lower frequencies while the last semicircle depicts the impedance variation corresponding to the range of the higher frequencies. To each semicircle, one can associate a time constant which is defined by the product ($R.C$). Based on considerations

of resistance and capacitance magnitudes, the arc lying in the high frequency range normally manifests the contribution of the grain interior having a resistance R_b and a capacitance C_b, while the precedent arc usually reflects the grain boundary effects modelled by a resistance R_{gb} parallel to a capacitance C_{gb}. In some cases, a third semicircle appears at very low frequencies due to the electrode-sample interface effects. For the case presented in Figure 3-9, an electrical circuit model consisting of a series of the three (R//C)s, will adequately describe the impedance data. For further details and understanding see the reference [144].

In conclusion, when supported by an appropriate equivalent circuit model, IS is a non-destructive technique that allows to deconvolute an overall electrical response in terms of its individual electrical components while determining their origin and quantifying their magnitude.

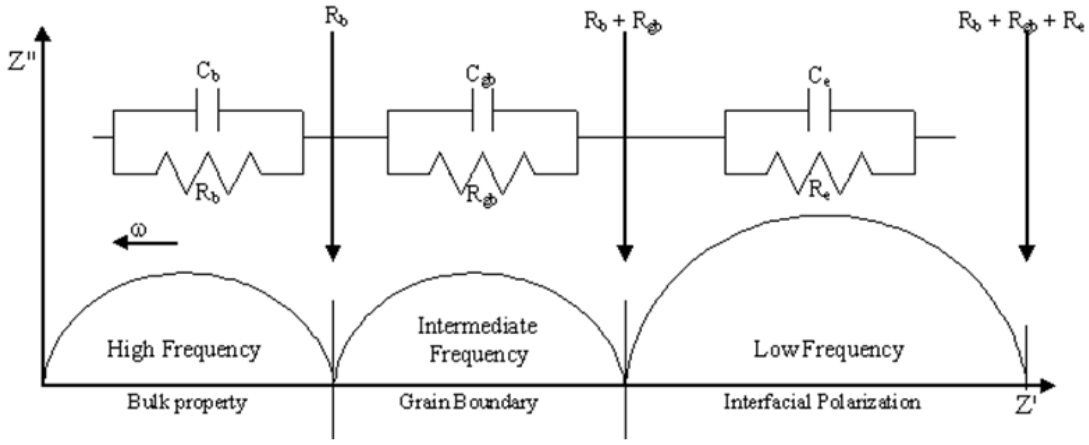

Figure 3-9. Various components in a complex impedance plane. Each of these semicircles can be represented by an equivalent RC combination as indicated [144].

3.6.7 Piezoelectric coefficient

Piezoelectric coefficient (d_{33}) is an important parameter for the application point of view. Direct piezoelectric coefficient has been measured by applying fixed force of 250 x 10^{-3} N by using Berlincourt method in this work. Schematic of the equipment is shown in Figure 3-10. The use of the equipment is pretty simple. The sample to be tested

is placed between the two probes (top and bottom probe). Then move the adjust knob and lightly clamp the specimen and equipment will display the d_{33} value on the screen. The equipment can be used to measure d_{33} of piezoelectric ceramics, polymers, and single crystals of various shapes. The equipment used in this work is Berlincourt meter, Sinocera, YE 2730A.

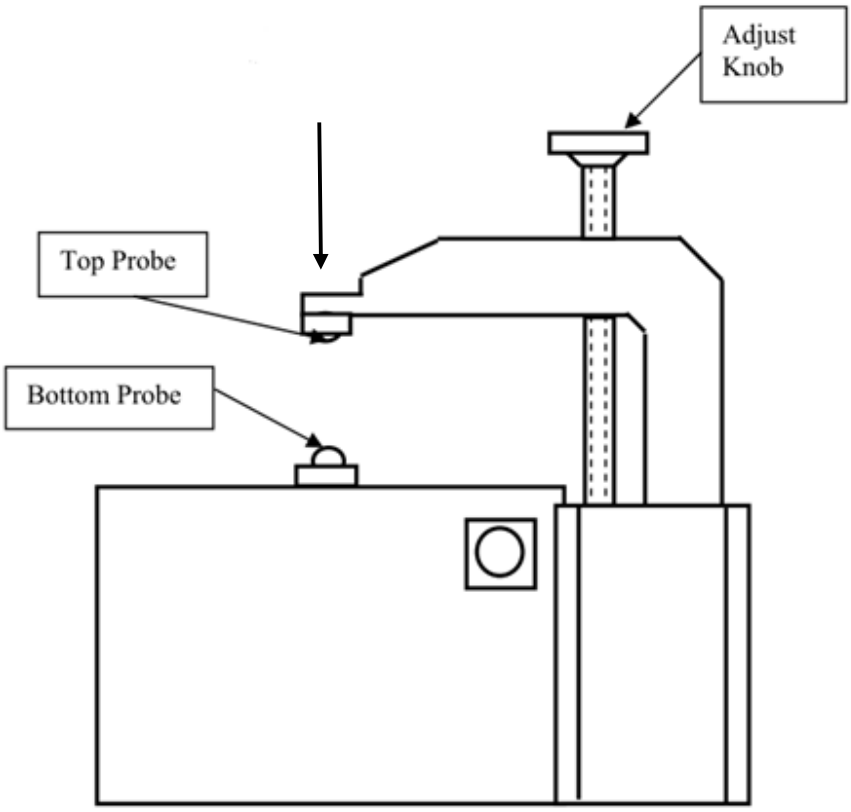

Figure 3-10. Schematic of the Berlincourt equipment.

3.6.8 Piezo-response force microscope

Piezo-response force microscopy (PFM), is a modification of scanning probe microscope (SPM) specially adapted for local piezoelectric measurements [145, 146]. PFM mode is based on the detection of local electro-mechanical vibrations of a cantilever induced by a probing ac electric signal applied between the conductive tip of the PFM and the bottom electrode of a insulator specimen as shown schematically in Figure 3-11 [147]. The examination of the domain structure in this thesis was also carried out by

PFM (Multimode, NanoScope IIIA, Veeco Instruments). A brief description of PFM is presented here and for more information, some excellent reviews can be found in the literature [145, 146, 148, 149]. Figure 3-11 shows an experimental setup used for piezoresponse force microscopy measurements. The tip is brought into contact with the crystal surface and the cantilever deformation is measured by the laser deflection onto a four quadrant detector. The up / down deflection of the cantilever is fed into a feedback adjusting the static force.

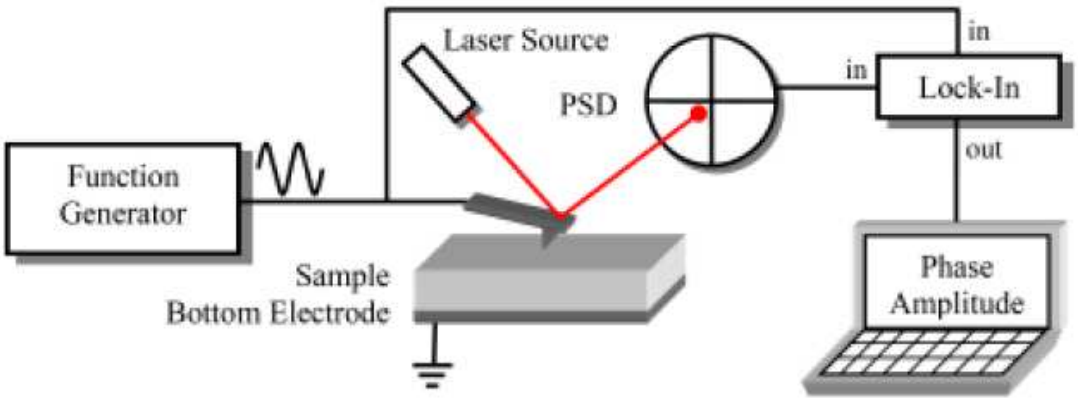

Figure 3-11. Piezoresponse force microscopy experimental setup. An ac voltage is applied between the tip and the bottom electrode. Cantilever deflection is measured as an electrical signal to record the topography and piezo response image [147].

PFM is capable of detecting not only out-of-plane domains, where the spontaneous polarization direction is normal to the crystal plane and which induce vertical vibrations of the cantilever, but also in-plane domains, where the spontaneous polarization lies within the plane of the crystal, and where the shear strain induces lateral oscillations detected via friction by the torsion of the cantilever as presented in the Figure 3-12.

For the stress-free homogeneously polarized ferroelectric material polarized in z-direction, the vertical displacement after applying the voltage can be expressed as follows:

$$\Delta Z = d_{33}V + \frac{Q_{333}}{t}V^2 \qquad \textit{Equation 3-3}$$

where V is the applied voltage, t is the sample thickness, d_{33} and Q_{333} are piezoelectric and electrostrictive coefficients, respectively. Under the external voltage $V_{tip} = V_{dc} + V_{ac}cos\omega t$, the surface displacement consists of a dc component, and the contributions at first and second harmonics. The first harmonics is measured by PFM as follows:

$$\Delta Z_\omega = d_{33}V_{ac} + \frac{Q_{333}}{t}V_{dc}V_{ac} \qquad \textit{Equation 3-4}$$

The sign of the piezoelectric effect depends on the orientation of the polarization and applied field as shown schematically in Figure 3-12.

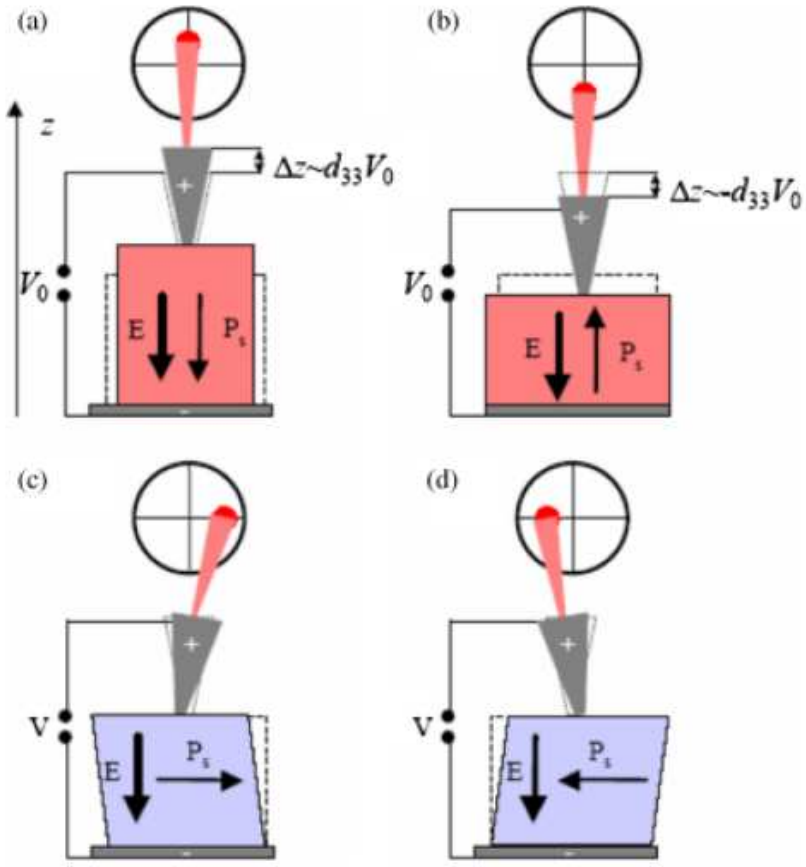

Figure 3-12. Piezoelectric effect in a ferroelectric investigated by piezo-force response microscopy. (a), (b) shows the vertical movement (d_{33} effect) of the cantilever (OPP signal). (c), (d) shows shear deformation (d_{15}) effect causing lateral deflection of laser beam (IPP signal) [147].

CHAPTER 4
Results and discussion

4. Results and discussion

4.1 Bulk ceramics: Non-stoichiometric and Mn doped KNN ceramics

4.1.1 Effect of non-stoichiometry on the structure and electrical properties of $K_{0.5}Na_{0.5}NbO_3$ ceramics

4.1.1.1 Abstract

Non stoichiometric potassium sodium niobate ($K_{0.5}N_{0.5}NbO_3$; KNN) piezoelectric ceramics having perovskite structure (ABO_3) with precisely controlled A/B ratio ($K_{0.5}N_{0.5}$/Nb) of 0.9 - 1.1 was synthesized by solid state method. X-Ray Diffraction showed a narrow window for monophasic ceramics between A/B ratio of 1.0 - 1.02, whereas, secondary phase was identified as $K_3Nb_{5.4}O_{15}$. Higher density values were shown by the ceramics with A/B ratio in the close vicinity of 1.0. The dielectric properties were evaluated as a function of temperature and frequency in the frequency range of

100 Hz to 1 MHz. The Curie temperature (T_C) exhibits a tendency to increase for A/B ratio > 1.0. Optimum properties with high remanent polarization of 19 μC/cm^2, d_{33} of 105 pC/N was observed for A/B of 0.97.

4.1.1.2 Introduction

KNN is considered a viable replacement of PZT owing to the relatively high Curie temperature ($T_C \approx 420$ °C), good ferroelectric properties, high electromechanical coupling coefficient, especially when produced by hot pressing [54]. The properties were further modified by doping to maximize specific properties [64, 67, 84, 150], and KNN modified by Li, Sb and Ta and texturing showed high piezoelectric properties [64, 151].

Besides the inferior properties of KNN compared to the PZT, there are still some issues related with processing that are limiting the full exploitation of KNN based materials. The difficulties in getting stoichiometric and monophasic KNN compositions have been attributed to the hygroscopic nature of alkali metal carbonates such as K_2CO_3 and Na_2CO_3 and difficulties in controlling the volatilization of K and Na during the processing at high temperatures, as is the case of ceramics processing. To overcome this limitation, excess of potassium and sodium have been regularly used in the fabrication of KNN ceramics. Even in one of the pioneer works on KNN, 0.1 mole % excess of alkaline carbonate was used to compensate for the alkali losses [65]. Since then, it has been considered that excess of alkaline precursors is essential for improving densification and electromechanical properties of KNN. However, it is well known that these high quantities of alkaline oxides will markedly affect the sintering trajectory of the ceramics, resulting in heterogeneous microstructures and the final dielectric response [152-154]. It is important from the application point of view to optimise the processing conditions.

Some work on the sintering behavior, structure and properties has already been reported mainly on the A-site non-stoichiometric KNN ceramics [155-157]. Effect of non-stoichiometry only on sintering behaviour on undoped KNN [157, 158] has been reported. Effect of A-site non-stoichiometry on the structure and properties of Li doped KNN ceramics, where non-stoichiometry showed significant changes in the XRD pattern and decrease in Curie temperature (T_C) with deficiency and vice versa of A-site and reduction in piezoelectric properties as A-site content increased [155, 156]. It is already

known that small deviation from stoichiometry can affect the properties of electroceramics [159, 160]. No systematic work has been reported on the non-stoichiometry and properties relationship at A and B-site of KNN perovskites. Therefore, the aim of this work is to clarify the effect of non-stoichiometry of A or B-site of KNN system in order to evaluate the properties with reference to stoichiometry point of view. Here we prove that small deviations of the stoichiometry of $K_{0.5}N_{0.5}NbO_3$ (KNN) are beneficial for the piezoelectric and dielectric response of KNN ceramics.

4.1.1.3 Experimental procedure

Ceramic samples were prepared according to compositions $(K_{0.5}Na_{0.5})_{0.90}NbO_{2.95}$, $(K_{0.5}Na_{0.5})_{0.95}NbO_{2.975}$, $(K_{0.5}Na_{0.5})_{0.97}NbO_{2.985}$, $(K_{0.5}Na_{0.5})_{0.98}NbO_{2.99}$, $(K_{0.5}Na_{0.5})_{0.99}NbO_{2.995}$, $(K_{0.5}Na_{0.5})_{1.0}NbO_3$, $(K_{0.5}Na_{0.5})_{1.01}NbO_{3.005}$, $(K_{0.5}Na_{0.5})_{1.02}NbO_{3.01}$, $(K_{0.5}Na_{0.5})_{1.03}NbO_{3.015}$, $(K_{0.5}Na_{0.5})_{1.05}NbO_{3.025}$ and $(K_{0.5}Na_{0.5})_{1.10}NbO_{3.05}$ were prepared as described in Chapter 3. Sintering was carried out at 1100 ºC for 2 h. The density of the ceramics was measured by Archimedes method. The crystal phase assemblage was evaluated by X-ray powder diffraction (XRD, Rigaku, D/Max-B, Cu-Kα radiation) in the 2θ range from 20° to 60° with a step size of 0.02°. The microstructure was observed by scanning electron microscopy (SEM, Hitachi S-4100). For electrical characterization, the opposite faces of the pellets were polished to ensure parallel surfaces, and silver electrodes were painted onto them. The dielectric constant (ε_r), was measured by a precision LCR Meter (HP 4284A) under an applied electric field of 1 *V* in the frequency range of 100 Hz to 1 MHz. The ferroelectric properties were measured by a ferroelectric tester, Aixact, TF analyzer 1000. The piezoelectric constant d_{33} was evaluated by a Berlincourt piezoelectric meter, Sinocera, YE 2730A.

4.1.1.4 Results and Discussion

XRD patterns of sintered samples are shown in Figure 4-1. All the XRD peaks of the sintered KNN can be attributed orthorhombic phase with slight monoclinic distortion. For A/B of 1.0, lattice parameters and volume of the unit cell were calculated from XRD pattern after refinement by the FullProf software and was found to be a = 3.9997 Å, b = 3.9478 Å, and c = 3.9981 Å, angle β of 90°21' and volume 63.129 $Å^3$.

These values matched closely to the previously reported by Tellier *et al* [79]. The window for the monophasic samples within the detection limit is quite narrow and lies between the A/B ratios of 1.0 - 1.02. The results are in agreement with earlier report, where slight deficiency in A-site resulted in secondary phases in Li doped KNN ceramics [155]. Additional peaks of secondary phases appear for all other samples and extra peaks were matched and identified as $K_3Nb_{5.4}O_{15}$ (Pdf No. 04-010-8979).

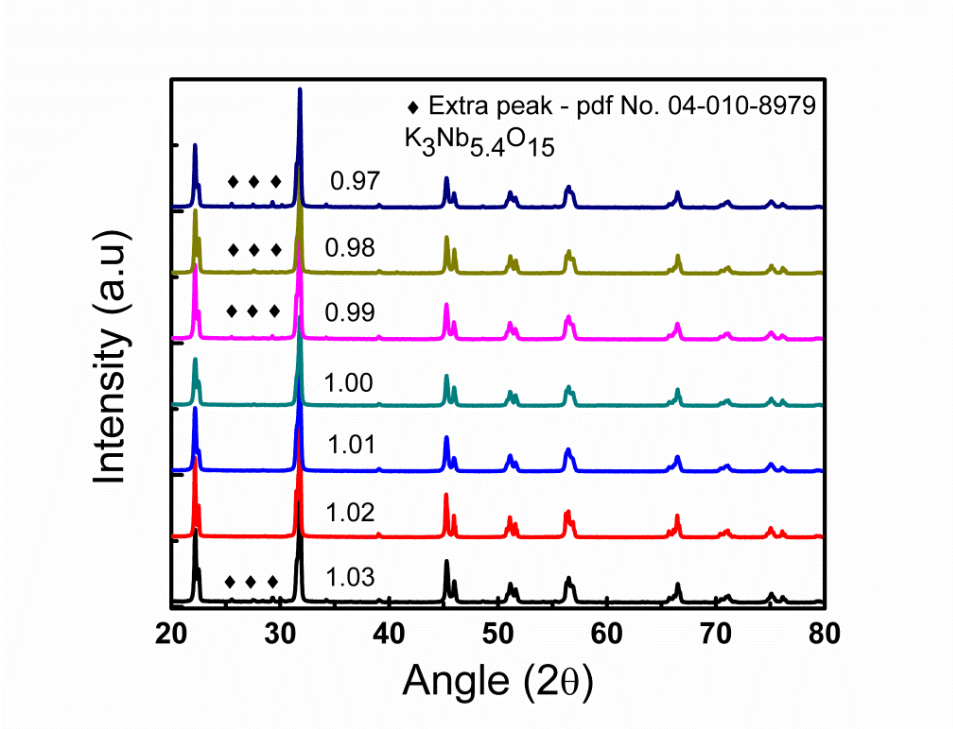

Figure 4-1. XRD patterns of KNN ceramicswith different A/B ratios (denotes $K_3Nb_{5.4}O_{15}$ - Pdf No. 04-010-8979 phase peaks).*

Density values of KNN ceramics sintered at 1100 ºC for 2 h, shown in Figure 4-2. The higher density values were obtained for the ceramics close to A/B of 1.0, which is consistent with literature value [158]. In case of A/B more or less than 1.0, density values started decreasing and the decrease is more for the composition far away from 1.0. The decrease is more evident when A/B > 1.0 (richer in A-site; K+Na). Higher density values obtained for A/B between 0.97 - 1.01.

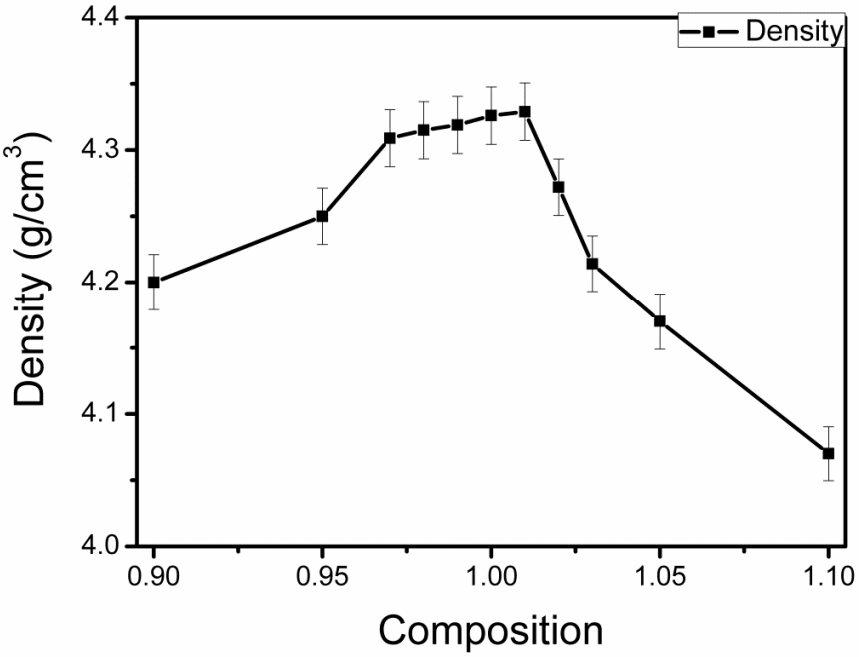

Figure 4-2. Density of KNN ceramics sintered at 1100 °C for 2 h. Dense samples were obtained close to A/B 1.0.

The SEM micrographs of KNN ceramics sintered at 1100 ºC for 2 h, shown in Figure 4-3. Average grain size of ~1.8 µm was observed for A/B 1.0. It was also observed that grain size is bigger for the A/B > 1.0 (richer in K+Na) and for of 1.10, grain size increased to 6 µm (more than three times) as compared to 1.8 µm for A/B of 1.0. This observation is similar to the A-site deficient (K+Na), Li doped KNN ceramics [155], but opposite to the one reported for the same composition by Liu *et al*. [156].

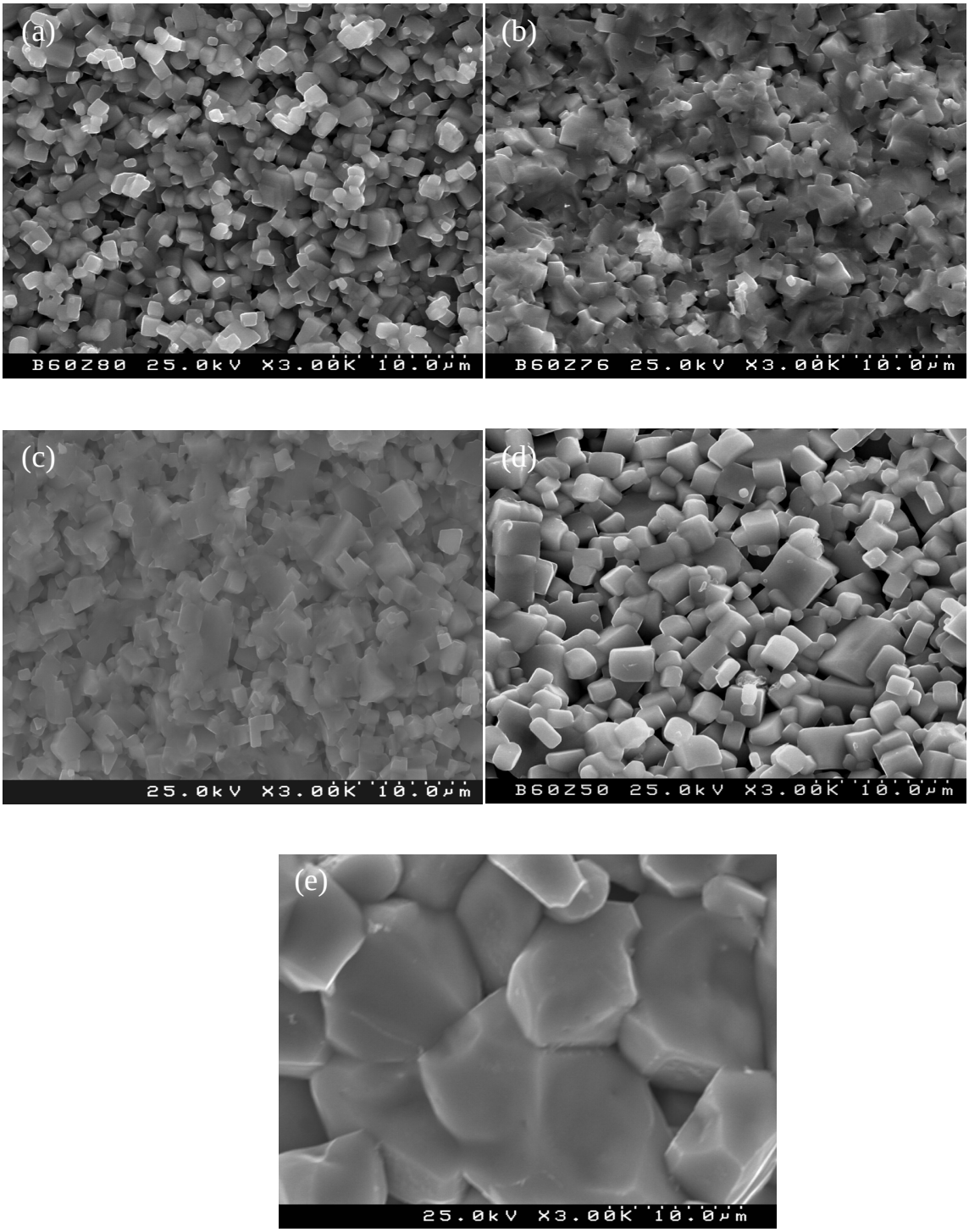

Figure 4-3. Microstructures of KNN ceramics with A/B of (a) 0.97 (b) 0.99 (c) 1.0 (d) 1.02 and (e) 1.05. Grain size increase was observed when A-site (K and Na) ratio increased i.e. A/B > 1.

Temperature dependence of the dielectric constant is shown in Figure 4-4 measured at a frequency of 1 kHz. For all KNN ceramics showed two phase transition temperature corresponds to monoclinic / orthorhombic to tetragonal (T_{O-T}) and tetragonal to cubic (T_{T-C}). The T_{O-T} transition temperature for KNN was found to be 217 °C, while T_C was 417 °C, which are close to the reported values in the literature [97, 161]. The dielectric constant values of the ceramics decreased as the A/B increased from 0.97 to 1.03. T_C increased, when ratio is above 1.0 and reached to maximum reached to 429 ºC for 1.03 and vice versa for the of K/Na deficient (less than 1.0) which is similar behaviour as reported in the nonstoichiometric Li doped KNN ceramics [155, 156] and lowering of T_C was explained on the basis of shrinkage of crystal parameters caused by oxygen vacancies to maintain the charge balance [85]. For the clarity purpose, the data from 350 ºC to 470 ºC is shown as inset in Figure 4-4. The dielectric constant values and T_C values are shown in Table 4-1.

Table 4-1. Electrical properties, remanent polarization (P_r) and coercive field (E_c) of KNN ceramics.

A/B ratio	**Dielectric constant at R T**	T_C	**Dielectric constat at** T_C	P_r	E_c
		ºC		µC/cm^2	kV/cm
0.97	550	415	5303	17.4	13.6
0.99	480	417	5147	5.5	8.8
1.0	450	417	4087	13.1	9.1
1.01	436	420	5151	-	-
1.02	300	424	4004	-	-
1.03	170	429	2007	-	-

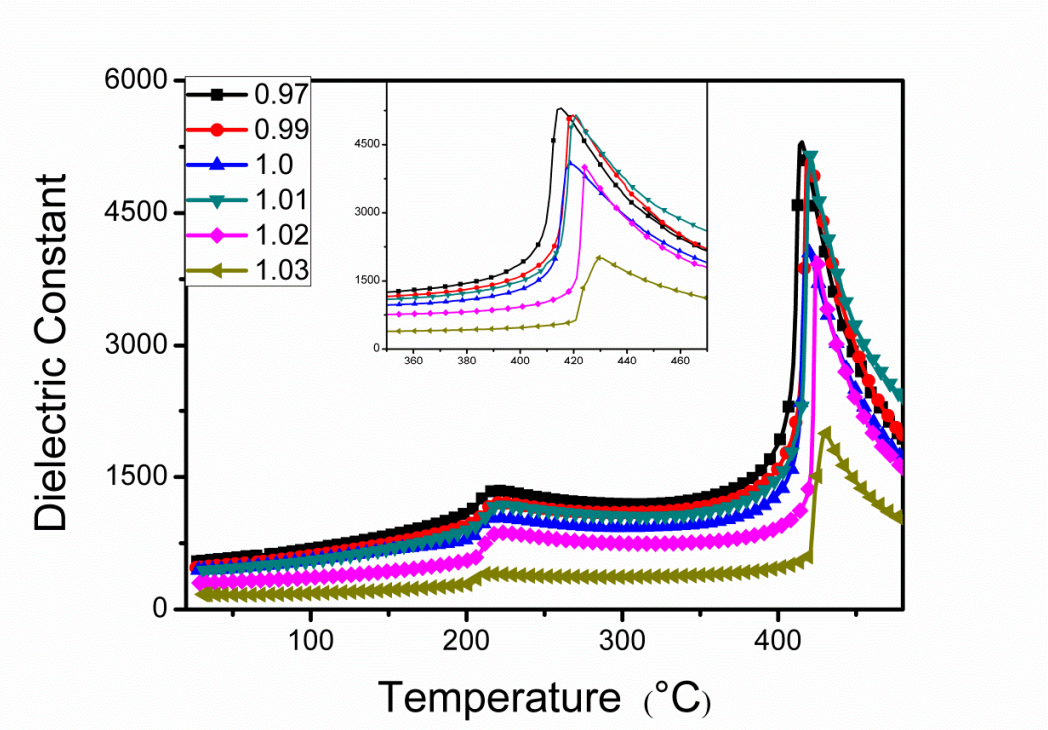

Figure 4-4. Temperature dependence of dielectric constant of KNN ceramics at 1 kHz. T_C increased for A/B >1.

Polarization versus electric field hysteresis loops at 40 Hz for KNN ceramics at room temperature are shown in Figure 4-5. Stoichiometric KNN presents a remnant polarization (P_r) of 13.1 µC/cm^2 and a coercive field (E_c) of 9.1 kV/cm, which are slightly lower than the reported values, but the shape of P-E loop also indicated the existence of leakage current [88, 89]. KNN ceramics with A/B of 0.97 possess high remanent polarization and coercive field of 17.4 µC/cm^2 and 13.6 kV/cm, respectively and P-E loop showed very low / minor hint of leakage. This result is similar to the A-site deficient Li doped KNN ceramics [155]. The composition A/B of 0.99 presented low leakage, but the polarization values are also low, whereas, A/B ratio of 1.01 (K+Na rich) and higher showed higher leakage currents.

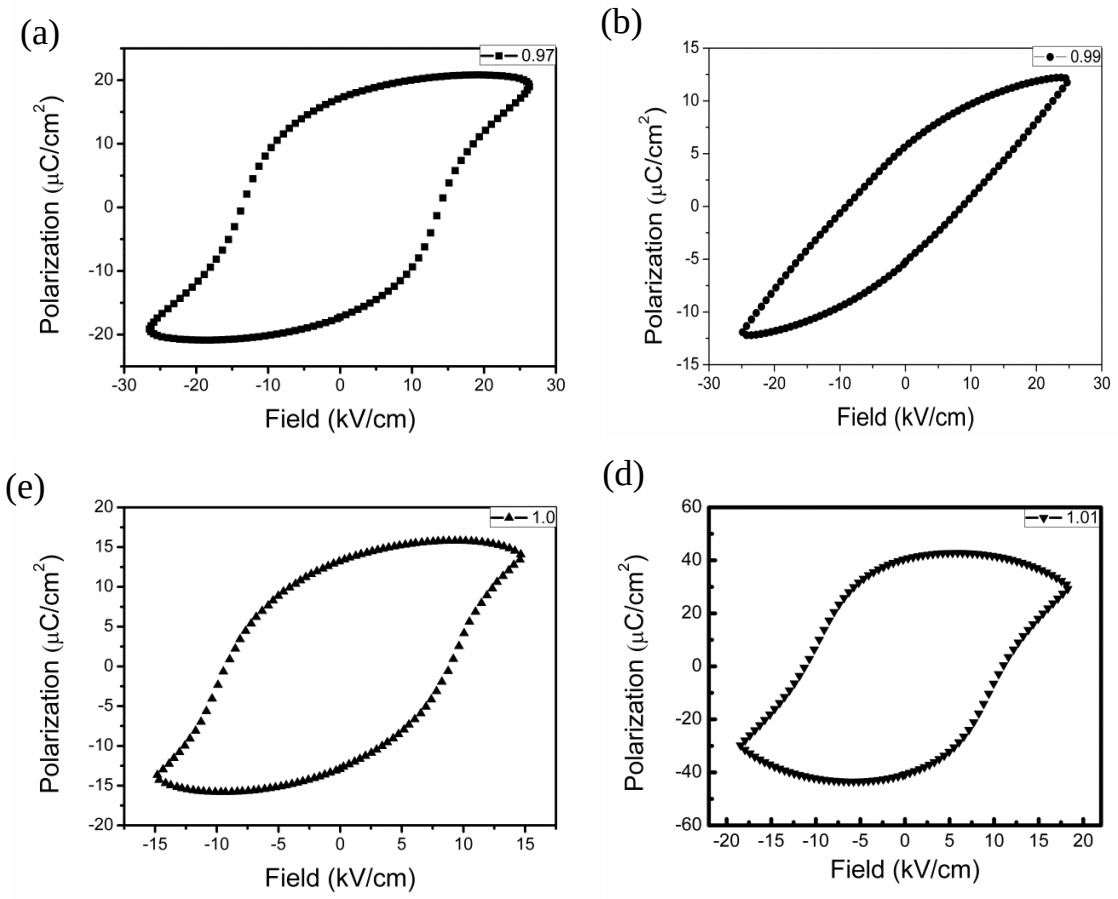

Figure 4-5. Variation of P-E hysteresis loops of KNN ceramics. Leakage current increased as the A/B > 1.

The variation of the room temperature piezoelectric constant d_{33} of KNN ceramics is illustrated in Figure 4-6. The highest d_{33} values were obtained close to A/B = 1.0 and the maximum values of 103 pC/N was obtained for A/B of 0.97, which is higher than the stoichiometric KNN and opposite to the A-site deficient Li doped KNN ceramics [155, 156]. The dielectric constant values are also higher for the same composition and the density is also among the higher values in spite of the fact that second phase detected in this composition. This result is very interesting, as most of the literature stresses for better properties to have A/B of 1.0 or higher, but in this case the dielectric and piezoelectric properties are better for A/B < 1. Although, more work is required to understand this behaviour and role of second phase. The samples were poled prior to d_{33} measurement by applying a field of 2 kV/cm for half an hour at 100 °C. It was not

possible to pole samples of 0.9 and 1.1 due to lower density and higher leakage current, so, we were not able to measure the d_{33} for those samples.

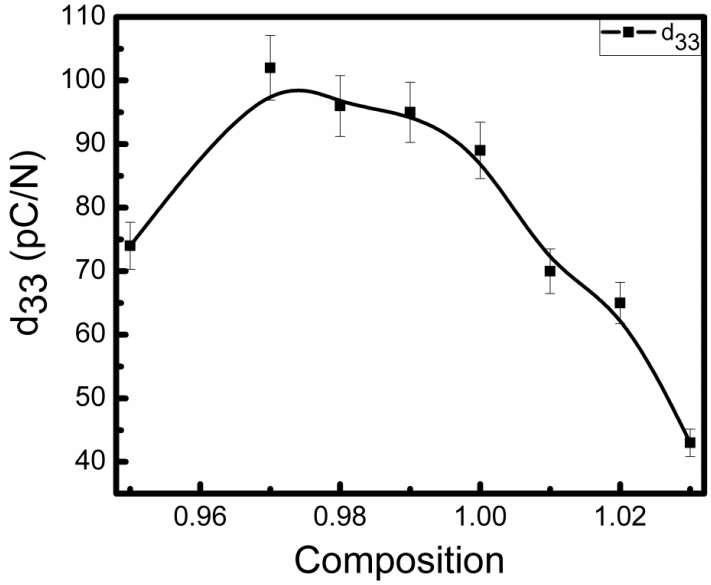

Figure 4-6. Variation of piezoelectric constant (d_{33}) with variation of A/B in KNN ceramics. Highest d_{33} values were obtained close to A/B 1.0 and maximum value obtained for 0.97. Solid line is guide to the eye.

4.1.1.5 Conclusions

The effect of A/B ratio on the structure, density, dielectric and piezoelectric response was analysed in KNN ceramics prepared by conventional solid oxide method. The monophasic window was found to be small i.e. A/B of 1.0 - 1.02. Excess of A-site (K+Na) resulted in increase of grain size and lowering of dielectric properties with increase in T_C. The variation of A/B influenced the polarization hysteresis loop and better results were obtained for the 0.97 and showed higher P_r and E_c as compared to the other KNN samples. In conclusion, small deviations of the stoichiometry of $K_{0.5}N_{0.5}NbO_3$ (KNN) are beneficial for the piezoelectric and dielectric response of KNN ceramics. Figure 4-7 shows some of the conclusions of this section.

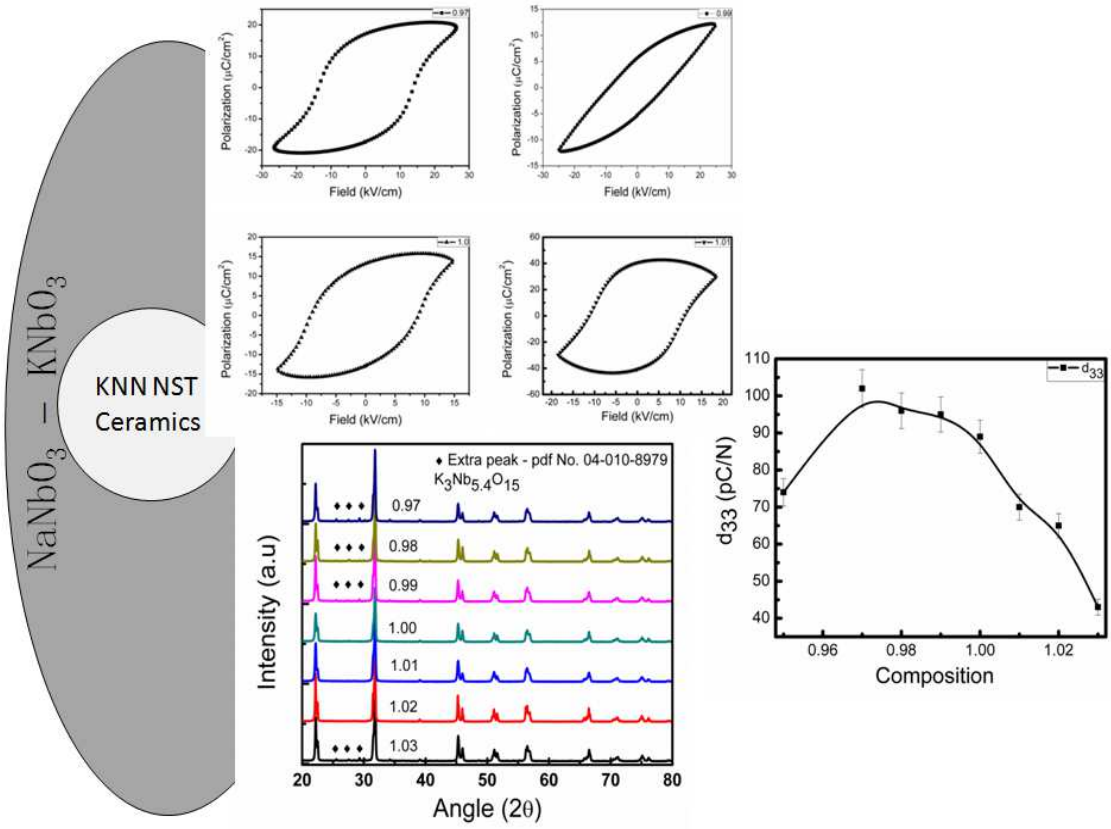

Figure 4-7. Image explaining the conclusions of this section. It can be observed that only small compositional window is available for monophasic and better properties KNN material.

4.1.2 Effect of Mn-doping on the structure and properties of KNN ceramics

4.1.2.1 Abstract

A and B-site doped Mn doped KNN ceramics were prepared by conventional sintering of powders prepared by mixed oxide method. A-site Mn doped ceramics has a very narrow window of solubility for single phase ceramics, but the density decreased dramatically. B-site doped Mn ceramics has a solubility limit of 0.5 mole % and improvement in relative density from 94.9 % to 95.3%. B-site doped Mn ceramics showed significant improvement in the polarization-electric field hysteresis loop and a well saturated, less-leaky hysteresis loop was observed. So, the relation between charge transport – defects and ferroelectric response is explained for $K_{0.5}Na_{0.5}NbO_3$ (KNN) and Mn doped KNN ceramics. At room temperature, the conduction in KNN is associated with hole transport and can be suppressed by Mn doping. Because of that a less leaky ferroelectric hysteresis loop is obtained for Mn doped KNN. At high temperatures, the conduction is dominated by the motion of ionized oxygen vacancies which concentration

increases with Mn doping. This work is adding relevant information on KNN and leverages its potential application.

4.1.2.2 Introduction

Though the piezoelectric constant (d_{33}) for KNN doped with Li, Ta and Sb was reported to exceed 300 pC/N and reached 416 pC/N when further improved by domain engineering, but the Curie temperature reduced to 253 ºC [64]. Improvement of properties in KNN based ceramics has been attempted by chemical substitutions [64, 67, 84, 150], sintering aids such as $K_{5.4}CuTa_{10}O_{29}$ (KCT) and CuO [67, 96, 162], texturing, [64, 151] hot pressing, [54] domain engineering and controlling the poling process [163]. However there are still many practical problems, like temperature stability of the properties, which hinders a full industrial application of KNN. The volatility of KNN constituents has been considered responsible for the low density and high defects concentration in KNN ceramics, which enhance electrical conduction with detrimental effects on its ferroelectric behaviour.

Indeed, values for remanent polarization (P_r), extracted from the polarization-electric field (*P-E*) hysteresis loops, have been reported to be higher than the saturation polarization ones, which was thought to be due to the leakage current and space charge contributions [89, 164] in undoped [78, 85] and doped KNN (doped with Li and Ta [69, 86], Li and Sb [78, 87] ceramics. Leakage current has a strong detrimental influence on the polarization switching and poling process, being difficult to attain optimized piezoelectric properties in a material with high leakage currents, turning it unsuitable for industrial applications. Mn is frequently used as a “loss suppresser” dopant in lead-based ceramics [165-167] to enhance mechanical quality factor (Q_m) and to reduce dielectric losses ($tan\ \delta$). In addition, Mn has been an effective and indispensable dopant in lead free compositions, such as $BaTiO_3$ [168], $SrTiO_3$ [169], $KNbO_3$ [170-172] and $KTaO_3$ among others, for improving ceramics density, dielectric losses and electromechanical properties. Concerning KNN, Mn has been reported to reduce the leakage current of KNN single crystals [110], to slightly affect the phase transition temperature from orthorhombic to tetragonal ($T_{O\text{-}T}$) and the Curie temperature in doped KNN ceramics [77]. Due to its several oxidation states, manganese can occupy A- or B-sites of the

perovskite lattice depending on its amount, valence state and synthesis conditions. So, in KNN ceramics, based on the properties, the occupancy site of Mn was suggested either to be on A- or B-site [77]. However, although a large amount of research has been carried out in KNN based systems, the Mn effect on the electrical properties of KNN ceramics has not yet been systematically addressed and so the effect still remains unclear.

The purpose of this study is to clarify the role on the electrical properties of Mn doping at the A and B-site of KNN ceramics. For that electrical properties and microstructure was characterized and conduction and charge transport in undoped and B-site Mn doped KNN is assessed by impedance spectroscopy (IS) and the contributions to impedance arising from the bulk, grain-boundary and electrode / ceramic interface are distinguished and discussed. The relation between charge transport, defects and ferroelectric response is established. Identifying and understanding the conduction behaviour in this system will be critically helpful to understand the beneficial role of Mn in the polarization hysteretic response of KNN ceramics and hence to contribute to the pool of knowledge on KNN, aiming to make it a viable alternative to PZT.

4.1.2.3 Experimental procedure

$(K_{0.5}Na_{0.5})_{1-2x}Mn_xNbO_{3-\delta}$ where, x= 0, 0.0005, 0.0009, 0.00125, 0.0025, 0.005 and $(K_{0.5}Na_{0.5})(Nb_{1-0.4x}Mn_x)O_{3-\delta}$ where x= 0, 0.005, 0.01, 0.015 and 0.02, hereafter called as KMn_xNN; KNN, $KMn_{0.05}NN$, $KMn_{0.09}NN$, $KMn_{0.125}NN$, $KMn_{0.250}NN$ and $KMn_{0.50}NN$ for A-site doped Mn ceramics and $KNNMn_x$; $KNNMn_{0.5}$, $KNNMn_1$, $KNNMn_{1.5}$, and $KNNMn_2$ for B-site Mn doped ceramics respectively, were prepared were prepared as described in Chapter 3. Sintering was carried out at 1100 ºC for 2 h in air for all the compositions.

Ceramics density was measured by Archimedes method. The crystal phase assemblage was evaluated by X-ray powder diffraction (XRD, Rigaku, D/Max-B, Cu-K_α radiation) in the 2θ range from 20° to 60° with a step size of 0.02°. Scanning electron microscopy / energy dispersive spectroscopy (SEM / EDS, Hitachi S-4100) and transmission electron microscopy (TEM, Hitachi H-9000) was used to assess the effect of Mn substitution on the microstructure of KNN ceramics. Using the SEM micrographs of

polished and thermally etched sections, the grain size was calculated based on the cords methods and the average grain size, *G*, was determined from the average equivalent diameter, by using a multiplying factor of 1.22.

For electrical characterization, opposite faces of the ceramic disks were polished to ensure parallel surfaces and then silver electrodes were placed onto them. High temperature dielectric properties from 30 °C to 480 °C were measured with a precision LCR Meter (HP 4284A) under an ac electric field of 1 *V* in the frequency range from 100 Hz to 1 MHz. The bulk ac conductivity, resistance and capacitance of the material have been evaluated from the complex impedance spectrum measured at different temperatures. Ferroelectric hysteresis loops were measured using a ferroelectric tester, Aixact, TF analyzer 1000, at a frequency of 50 Hz.

4.1.2.4 Results and discussion

Figure 4-8 presents the XRD patterns of A and B-site doped KNN ceramics sintered at 1100 °C for 2 h. Both systems reveal a single phase perovskite of orthorhombic symmetry with slight monoclinic distortion upto 0.009 and 0.05 mole % for A and B-site doped KNN, respectively. Above that limit, secondary phase starts to appear and can be clearly observed for high Mn contents in both cases. This extra phase which matches closely to $K_{5.75}Nb_{10.85}O_{30}$ (Pdf No. 00-038-0297) was identified as tetragonal tungsten bronze having lattice parameters of 12.579 Å x 12.579 Å x 3.983 Å and is known to be present in $KNbO_3 – Nb_2O_5$ system [173].. The solid solubility limit of Mn in the A and B-site of KNN is rather small, being even smaller for the A-site doped Mn-ceramics based on the XRD results, which is indeed expected based on the ionic radii considerations. Mn have smaller ionic radius of (Mn^{2+} = 67 pm, Mn^{3+} = 58 pm; Mn^{4+} = 53 pm) than the value of 164 and 139 pm, which are the values of ionic radii of K^+ and Na^+ respectively [174].

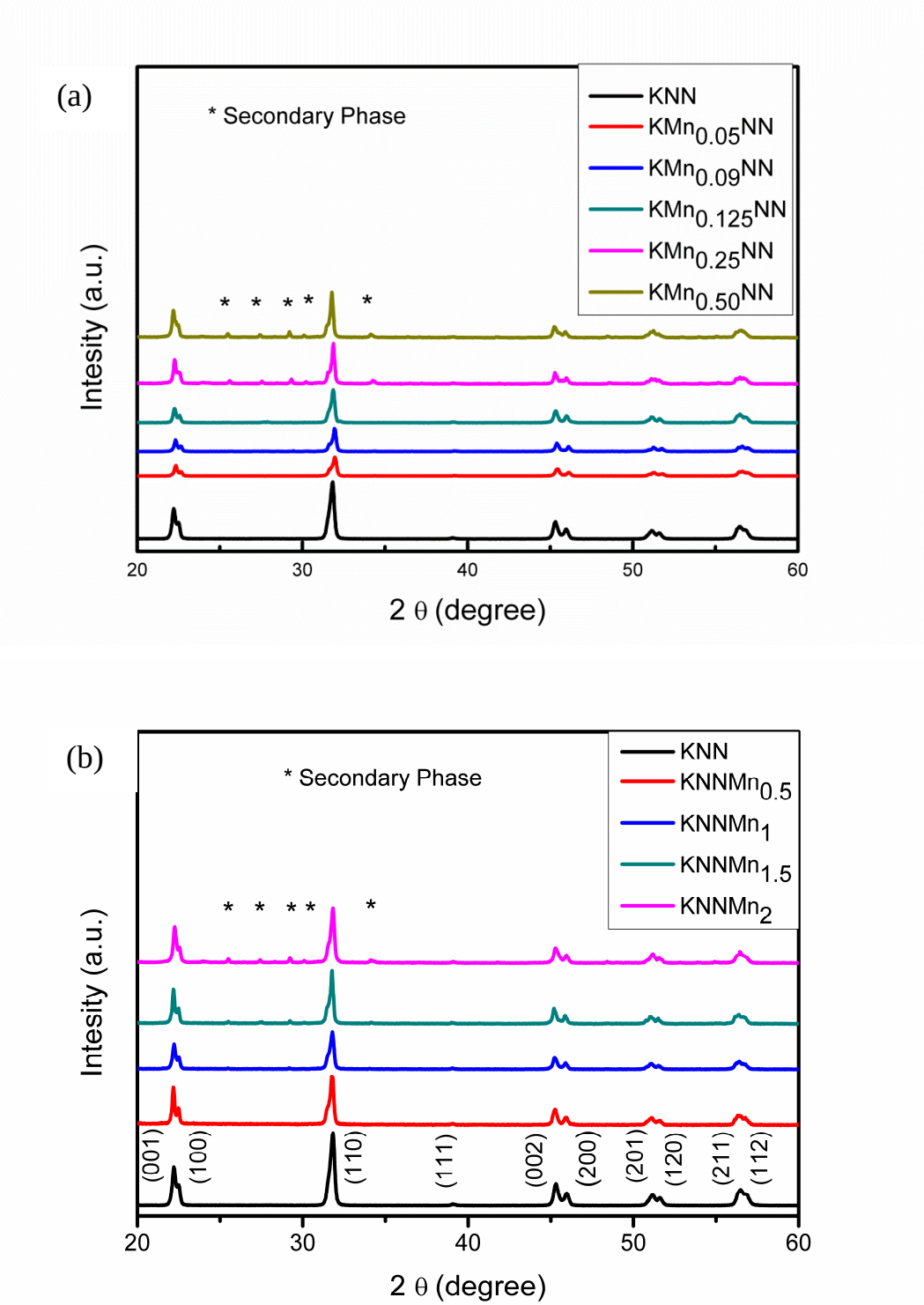

Figure 4-8. XRD profiles of sintered (a) KMn_xNN and(b) $KNNMn_x$ ceramics sintered at 1100 ºC for 2 h in air (denotes $K_{5.75}Nb_{10.85}O_{30}$; Pdf No. 00-038-0297 phase peaks). Extra peaks observed after compositons $KMn_{0.09}NN$ for A-site and $KNNMn_{0.5}$ for B-site Mn doped KNN ceramics respectively.*

For the monophasic-phasic compositions ($KMn_{0.05}NN$, $KMn_{0.09}NN$ for A-site Mn doped and $KNNMn_{0.5}$ for B-site Mn doped KNN ceramics), the lattice parameters and volume of the unit cell were calculated from the XRD patterns after refinement by FullProf software and are presented in Table 4-2. The lattice parameters of undoped KNN ceramics match closely to the values already reported in the literature [79]. For A-site Mn doped ceramics, lattice parameters (a, b, c) increased while a decrease in the angle β was noted, but volume increased, as the Mn content is increased. This behaviour is similar to A-site Li doped KNN ceramics [175]. This increase in the volume may be the result of strains in the unit cell, which should increase T_C. The increase in the T_C was indeed observed in the dielectric response versus temperature, which verified the XRD data and will be later explained. However in the case of Mn doped at B-site with Mn addition lattice parameters and unit cell volume decrease which might be an indication of the substitution of Nb^{5+} by Mn^{3+} or Mn^{4+} with smaller ionic radii (0.58 Å, and 0.53 Å, respectively), as compared to Nb^{5+} (0.64 Å). A similar trend in lattice parameters variation was also observed in B-site Mn doped $SrTiO_3$ ceramics [169, 176, 177].

Table 4-2. Lattice parameter of A and B-site Mn doped ceramics. Lattice parameters decrease in the case of B-site doping and increase in the case of A-site doping.

	Composition	**a (Å)**	**b (Å)**	**c (Å)**	***β***	**Vol.((Å^3)**
	KNN	3.9997	3.9478	3.9981	90°21'	63.129
A-site	$KMn_{0.05}NN$	4.0184	3.9489	4.0021	90°16'	63.509
	$KMn_{0.09}NN$	4.0198	3.9501	4.0022	90°10'	63.570
B-site	$KNNMn_{0.5}$	3.9950	3.9448	3.9946	90°24'	62.952

Figure 4-9 compares the density of KMn_xNN and $KNNMn_x$ ceramics sintered at 1100 ºC for 2 h. In the case of KMn_xNN, the density values decrease abruptly relatively to undoped KNN after small amounts of Mn addition and keep on decreasing as more and more Mn is added at A-site. The density values decay from 4.28 to 3.95 g/cm^3 of the density as moving from the undoped KNN till the 0.50 mole % Mn at A-site respectively. In the case of $KNNMn_x$, the density increased up to a maximum relative density

of 95.3 % for the 0.5 mole % Mn (KNN theoretical density = 4.51 g/cm^3), being maintained above the density values of the undoped KNN until 1.0 mole % of Mn doping and then started decreasing as further Mn was added. The data is presented for all ceramics. Dotted line in Figure 4-9 separates the monophasic region (left side of the dotted line) from two phase region (right side of dotted line).

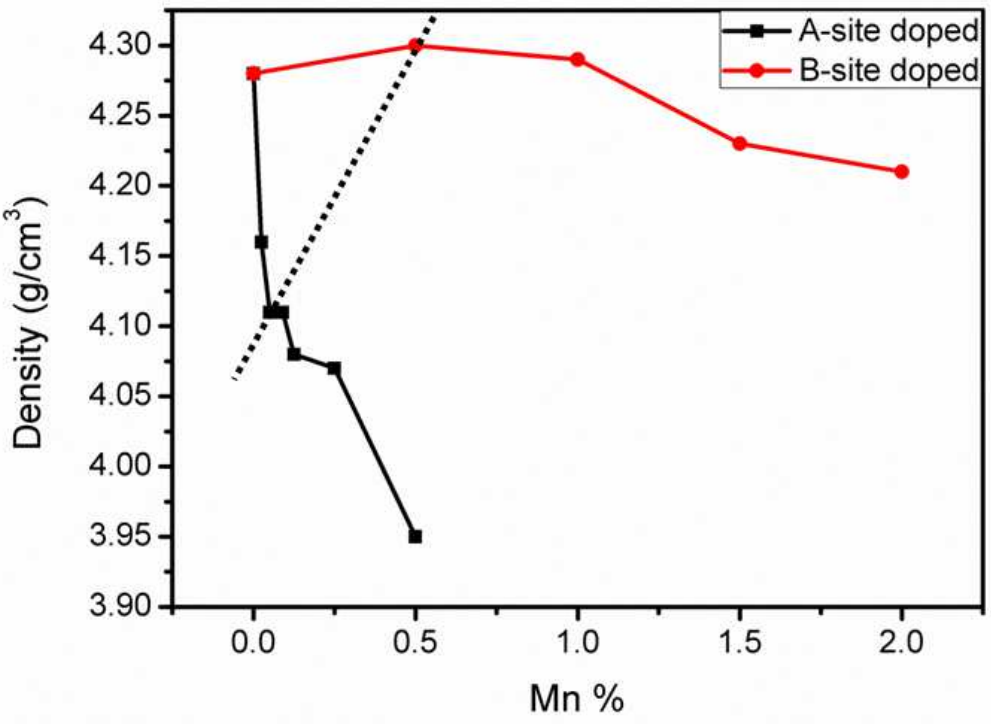

Figure 4-9. Density of KMn_xNN and $KNNMn_x$ ceramics sintered at 1100 °C for 2 h as a function of Mn content. Maximum density was achieved for 0.5 mole % Mn doped at B-site.

Figure 4-10 presents the microstructure for A and B-site Mn-doped KNN ceramics. Dense microstructure with average grain size (~ 1.8 µm) was observed for polished and thermally etched surface for undoped and B-site doped ceramics. For 2 mole % Mn-content bimodal grain distribution was observed. For KMn_xNN (A-site) ceramics, the samples were very soft, which might be due to the low density values and it was very difficult to prevent the pulling off the material during the polishing stage. The microstructure of $KMn_{0.05}NN$ is shown in Figure 4-10d. A lot more pulling of the material was observed as compared to the B-site doped $KNNMn_x$.

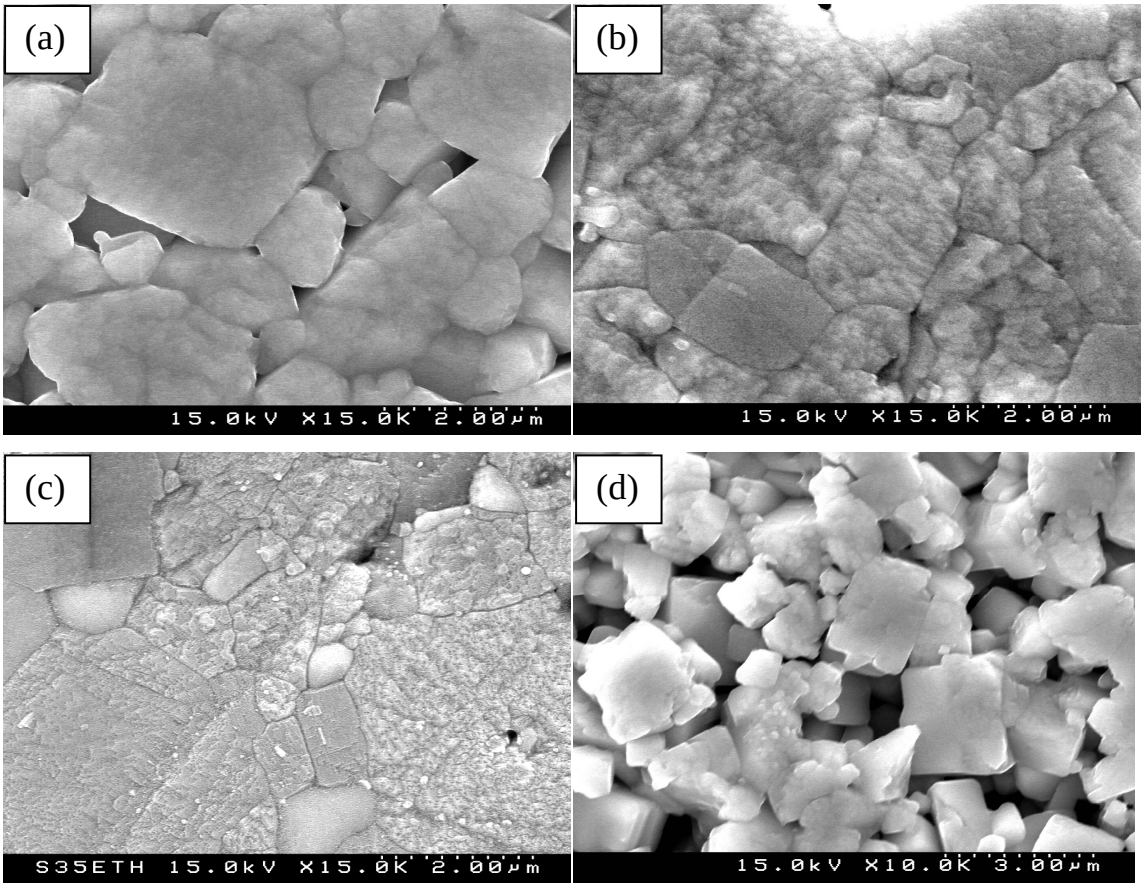

Figure 4-10. SEM micrograph of KMn_xNN and $KNNMn_x$ (a) KNN (b) $KNNMn_{0.5}$ (c) $KNNMn_2$ and (d) $K Mn_{0.05}NN$. B-site Mn doped ceramics showed dense microstructure as compared to the A-site Mn doped ceramics.

Figure 4-11 shows the TEM microstructure of undoped and $KNNMn_{0.5,}$ $KNNMn_2$ (B-site doped) KNN ceramics. Undoped KNN ceramics contained large (>1 µm wide) wedge shaped ferroelectric domains as can be observed in Figure 4-11a. $KNNMn_{0.5}$ exhibited a well defined domain structure as was observed with widths approximately an order of magnitude smaller than those in undoped KNN as can be seen in Figure 4-11b. These wedge shaped domains are also reported in the $PbZr_{1-x}Ti_xO_3$ (PZT) high performance ceramics close to the morphotropic phase boundary (MPB) ranging from x= 45- 60 and lead free $Ba(Zr_{0.2}Ti_{0.8})O_3$-$x(Ba_{0.7}Ca_{0.3})TiO_3$ studied by transmission electron (TEM) [178-182]. In $KNNMn_2$ (B-site doped), the presence of a second phase was observed by XRD as explained in the previous sections. Electron diffraction patterns from the second

phase were consistent with tetragonal tungsten bronze (TTB) structured compound (Figure 4-11d), confirming the XRD analysis. The domain structure became increasing complex as Mn concentration increased, suggesting that the presence of Mn on the B-site disrupts polar order. These microstructure details elucidate reasons that may account for the inferior electrical properties of KNN at higher Mn concentration.

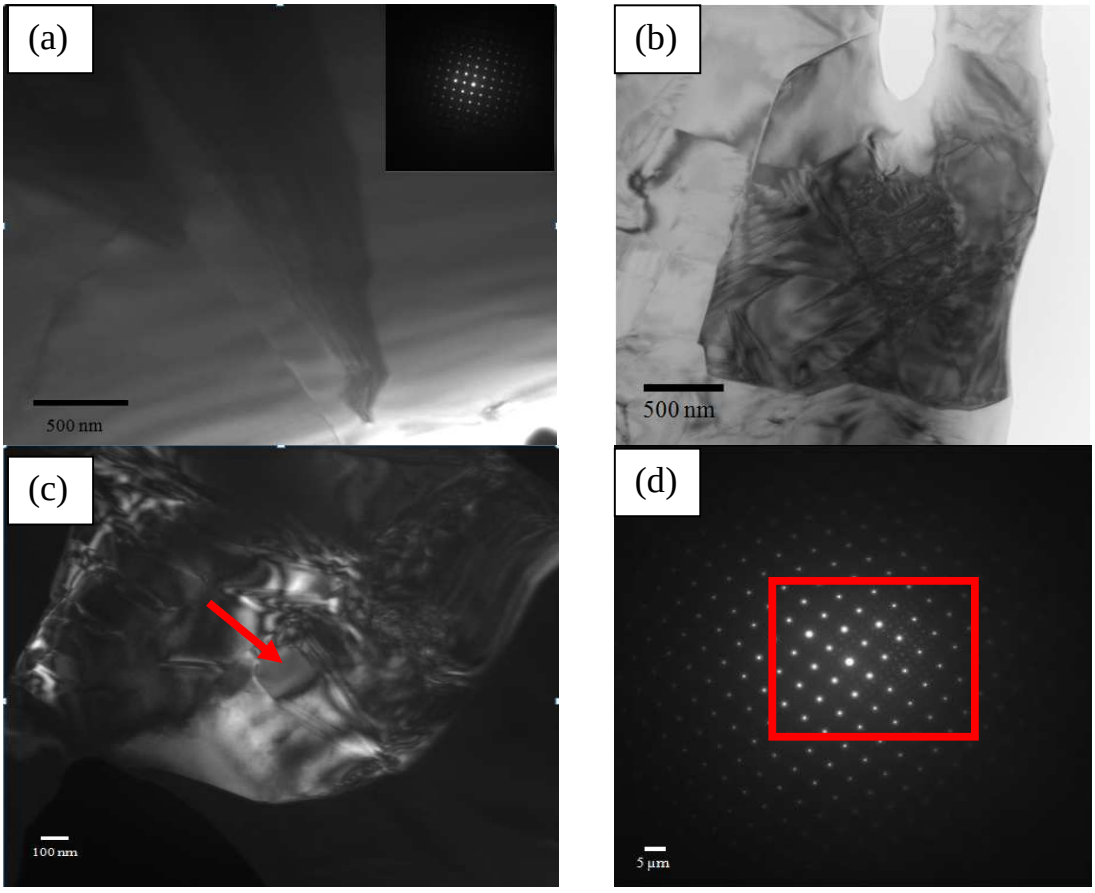

Figure 4-11. Ferroelectric domains in undoped KNN ceramics (a) and B-site Mn doped KNN ceramics $KNNMn_{0.5}$ (b) $KNNMn_{0.5}$; (c) $KNNMn_2$; (d) electron diffraction pattern with second phase. Domains become tangled due to higher Mn content.

Temperature dependence of the dielectric constant and losses for monophasic A and B-site doped KNN ceramics is shown in Figure 4-12. All the dielectric curves exhibit two maxima corresponding to the two phase transitions that characterises KNN in this temperature range. [65, 80, 161]. The $T_{O\text{-}T}$ phase transition temperature was found to be 217 °C, while T_C was measured as 417 °C, which are very close to the reported

values [97, 161]. T_C increased from 417 °C to 425 ºC and 423 ºC for A-site ($KMn_{0.05}NN$ and $KMn_{0.09}NN$) and decreased to 415 ºC for B-site ($KNNMn_{0.5}$), respectively. $T_{O\text{-}T}$ also varied slightly from 217 °C for the undoped KNN to 215 ºC and 210 ºC for A-site ($KMn_{0.05}NN$ and $KMn_{0.09}NN$) and to 193 ºC for B-site ($KNNMn_{0.5}$), respectively. Dielectric loss values for all the samples were below 1 up to 400 °C as observed in Figure 4-12b.

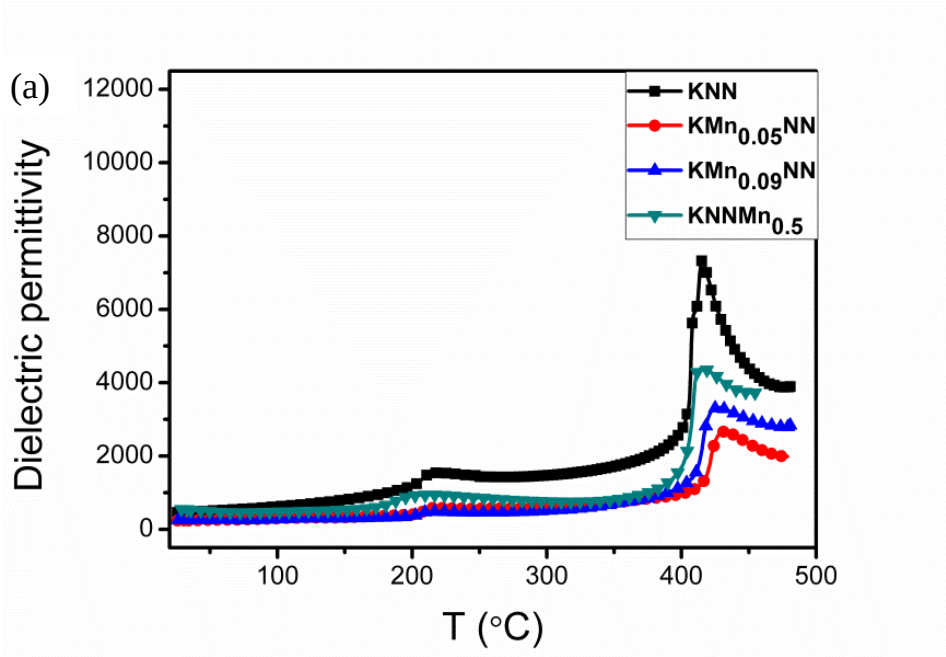

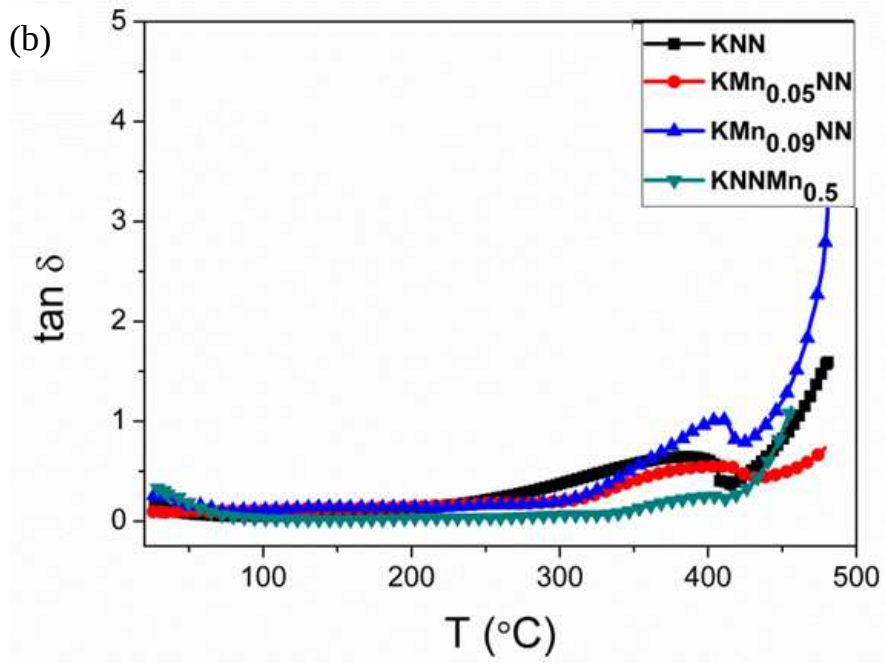

Figure 4-12. Variation of dielectric permittivity (a) and dielectric loss (b) with temperature at 1 kHz for monophasic-phasic A and B-site Mn doped KNN ceramics.

For the A-site doped ceramics (KMn_xNN), hysteresis loops could not be obtained because of the very high leakage current and porosity of these ceramics as compared to $KNNM_x$ ceramics. Polarization hysteresis (*P-E*) loops measured at room temperature and at a frequency of 50 Hz are presented in Figure 4-13, for undoped (KNN) and B-site doped $KNNMn_x$ ($KNNMn_{0.5}$, $KNNMn_{1.5,}$ and $KNNMn_2$) ceramics. Undoped KNN exhibits a leaky P-E loop with a remanent polarization (P_r) of 13.1 μC/cm^2 and a coercive field (E_c) of 9.1 kV/cm. Similar kind of leaky loops have also been reported either for undoped KNN [78, 85] or doped KNN (doped with Li and Ta [69, 86], Li and Sb [78, 87] and attributed to conduction and space charge effects [88, 89]. However, for $KNNMn_{0.5}$ a well saturated leakage-free hysteresis loop was obtained with P_r and E_c of 13.8 μC/cm^2 and 11.7 kV/cm, respectively (Figure 4-13). Further additions of Mn at the B-site were detrimental to the P-E loops and a decrease of remanent polarization was observed, which may be related with the appearance of the second phase as was observed by X-ray diffraction. Because of the improved leaky behaviour, one may assume that small amounts of Mn (0.5 mole %; $KNNMn_{0.5}$) was effective in reducing the

conductivity or increasing the resistivity of doped ceramics as compared to undoped KNN; but a further understanding on the conduction mechanisms and charge transport is required. So, the conductivity of both undoped and B-site Mn doped KNN ($KNNMn_{0.5}$) ceramics was systematically examined.

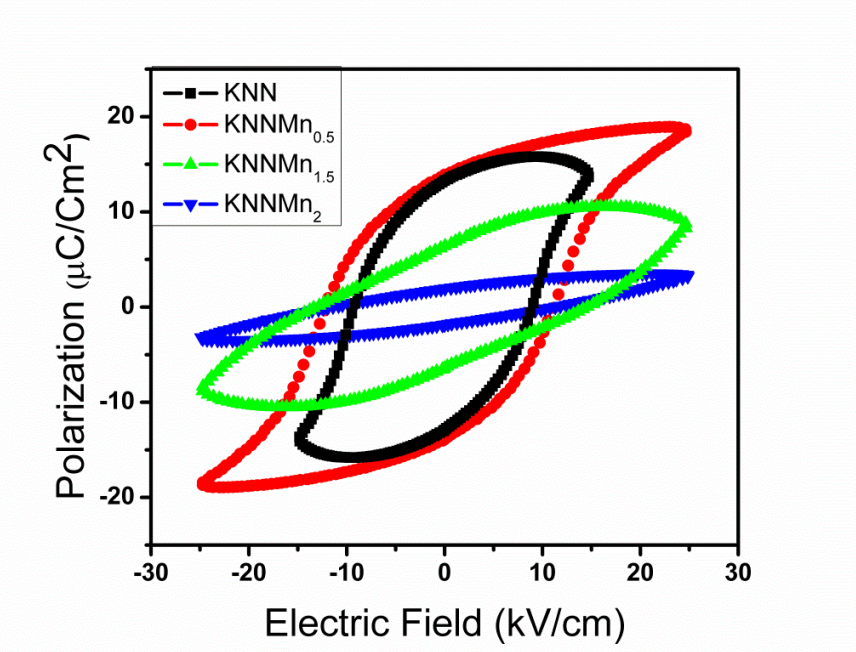

Figure 4-13. Polarization hysteresis (P-E) loops of $(K_{0.5}Na_{0.5})(Nb_{1-0.4x}Mn_x)O_{3-\delta}$ ceramics at a frequency of 50 Hz. For 0.5% Mn doped ($KNNMn_{0.5}$), a well saturated leakage free hysteresis loop was obtained with P_r and E_c of 13.8 μC/cm^2 and 11.7 kV/cm, respectively

The temperature and frequency dependence of ac conductivity of KNN doped ceramics at frequencies (1 kHz, 10 kHz, 100 kHz and 1 MHz) is depicted in Figure 4-14. The intrinsic conductivity (σ_ω) response is given by:

$$\sigma_\omega = \sigma_{dc} + A\omega^n \qquad \textit{Equation 4-1}$$

where σ_{dc} stands for the dc conductivity, ω for the angular frequency and the exponent n lies in the range ($0 < n < 1$) [183]. For $KNNMn_{0.5}$, ac conductivity follows a distinct pattern depending on the temperature range and, if below or above the transition temperature (~250 ºC): at low temperature (25 ºC < T < 250 ºC) a trend for a slight decrease

of the conductivity with temperature increase is observed, particularly evident at low frequencies, while for T > 250 ºC the conductivity increases as the temperature increases. The ac conductivity increases as well with the increase of the measuring frequencies especially at low temperatures as shown Figure 4-14. The dispersive behaviour at room temperature narrowed at high temperatures [184]. A similar behaviour has been observed in other systems, as $YMnO_3$ [185] and $Pb(Fe_{1/2}Nb_{1/2})O_3$ ceramics [184]. Being consistent with universal dielectric response (UDR) law [186], the ac conductivity increases with measuring frequencies especially at low temperatures.

Figure 4-14b illustrates the ac conductivity as a function of the temperature for undoped and $KNNMn_{0.5}$ ceramics at 1 MHz. Clearly, three different regimes can be distinguished: region I from (30 ºC – 180 ºC; 220 ºC – 350 ºC), region II from 180 ºC - 220 ºC, region III from 350 ºC - 400 ºC for KNN; and for $KNNMn_{0.5}$, : region I from (30 ºC - 180 ºC; 220 ºC – 250 ºC), region II from 180 ºC to 220 ºC and region III from 250 ºC to 400 ºC, corresponding to different types of conduction mechanisms.

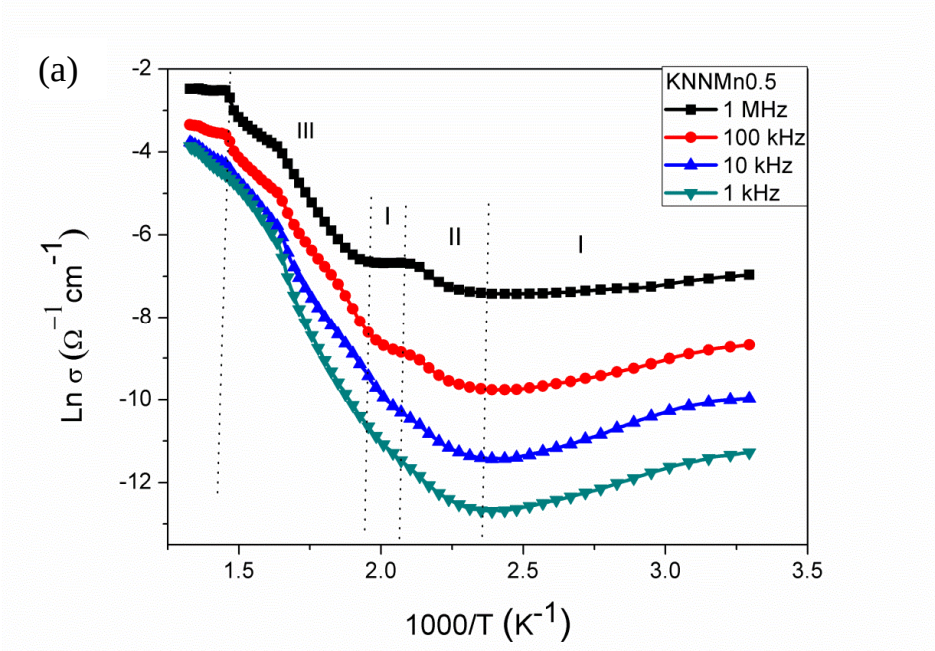

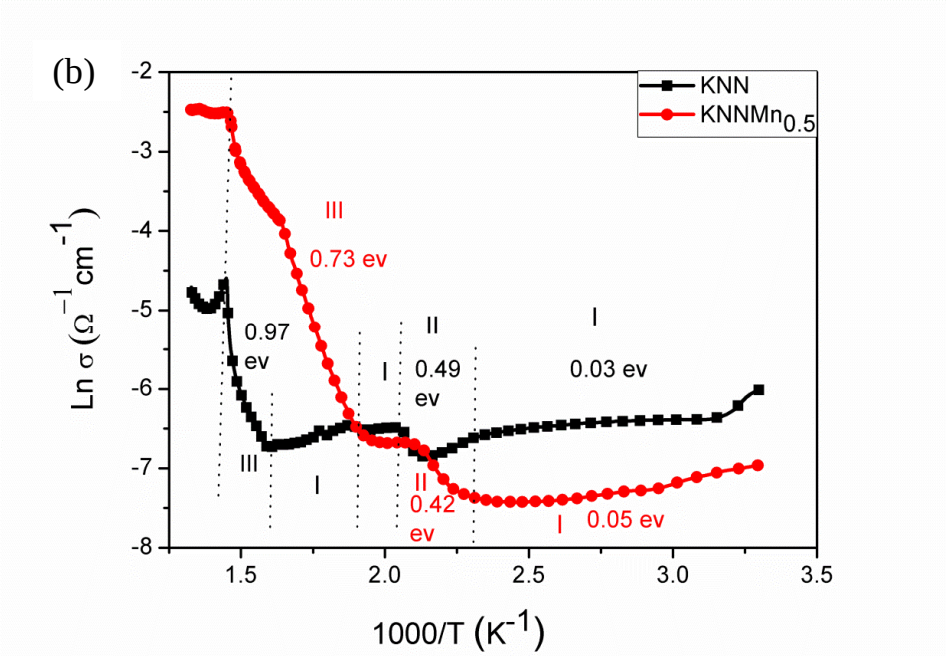

Figure 4-14. Temperature dependence of ac conductivity of (a) $KNNMn_{0.5}$ doped ceramics at 1 kHz, 10 kHz, 100 kHz and 1 MHz (b) KNN and $KNNMn_{0.5}$ doped ceramics at 1MHz. Three different regions with different conduction mechanisms were identified and the activation energy for each region is indicated.

In order to clarify the conduction mechanisms responsible for the observed behaviour, the values of the activation energy for conduction (σ_{ac}) was calculated assuming Arrhenius behaviour:

$$\sigma_{ac} = \sigma_0 \exp^{\left(-\frac{E_a}{K_b T}\right)} \qquad \textit{Equation 4-2}$$

where σ_0 stands for the pre-exponential term, K_b for Bolzmann constant, T for absolute temperature and E_a for the activation energy of conduction.

The activation energies of conduction obtained for KNN and $KNNMn_{0.5}$ in region I (30 ºC - 180 ºC; 220 ºC – 250 ºC) for KNN; (30 ºC - 180 ºC; 220 – 350 ºC) for $KNNMn_{0.5}$, were calculated to be 0.03 eV and 0.05 eV respectively, which correspond to hole hopping conductivity in p-type ferroelectric ceramics [184, 187]. In the temperature range 180 °C – 220 °C (region II) a ferroelectric phase transition occurs, responding for the observed discontinuities in the curves. The calculated activation energy values of

0.49 eV and 0.42 eV for KNN and $KNNMn_{0.5}$ respectively match well with values reported for phase transition as for example for $Pb(Fe_{1/2}Nb_{1/2})O_3$ ceramics [184]. In the temperature region from 250 °C to 400 °C for KNN and 350 ºC to 400 °C for $KNNMn_{0.5}$ (region III), the calculated activation energies were 0.97 and 0.73 eV for KNN and $KNNMn_{0.5}$ respectively. For ferroelectric perovskites, values of activation energy for conduction in the range of 0.6 - 1.2 eV indicate that the electrical conduction is due to the motion of doubly ionized oxygen vacancies [184, 188], which are considered some of the most mobile ionic species in perovskites [188, 189]. The calculated activation energies for KNN and $KNNMn_{0.5}$ and the proposed conduction mechanism are presented in Table 4-3.

Table 4-3. Activation energy of ac conduction (E_a) and pre-exponential (σ_0) factor for KNN and $KNNMn_{0.5}$ ceramics at 1 MHz, 100 kHz and 10 kHz along with the proposed conduction mechanism for three regions.

Region	**Composition**	**Frequency (1 MHz)**		**Frequency (100 kHz)**		**Frequency (10 kHz)**		**Proposed Mecha-nism of Cond.**	**Refs.**
		E_a	$Ln\ \sigma_0$	E_a	$Ln\ \sigma_0$	E_a	$Ln\ \sigma_0$		
		eV	$\Omega^{-1}cm^{-1}$	eV	$\Omega^{-1}cm^{-1}$	eV	$\Omega^{-1}cm^{-1}$		
I	KNN	0.03	-7.36	0.06	-11.06	0.03	-10.61	Hole hopping	This work and [184, 187]
	$KNNMn_{0.5}$	0.05	-8.88	0.09	-13.51	0.16	-16.27		
II	KNN	0.49	3.97	0.48	2.78	0.26	-4.30	Phase change	This work and [184]
	$KNNMn_{0.5}$	0.42	4.17	0.40	1.55	0.34	-2.28		
III	KNN	0.97	11.00	0.99	10.01	0.81	5.54	Doubly ionized oxygen vacancies	This work and [184, 188]
	$KNNMn_{0.5}$	0.73	9.93	0.80	9.91	0.93	11.76		

In perovskites, the possible charge carriers are electrons, holes and oxygen vacancies [38]. It has been assumed that KNN exhibits a p-type conductivity [190] due to the volatile nature of K and Na, which results in the formation of cationic vacancies, V'_K, V'_{Na} during the processing as described by Equation 2-8 in Chapter 2. p-type conduction

at room temperature has been observed for ferroelectrics like $PbTiO_3$ [38], $Bi_4Ti_3O_{12}$ [191] and KNN single crystals [110, 192] . In fact, the increase in the electrical conductivity was observed for the KNN ceramic annealed in the O_2 atmosphere, suggested hole conduction (p-type conduction in KNN ceramic). Furthermore, our results for the activation energy for region I, corresponding to temperatures close to room temperature, confirm a p-type conduction for KNN and Mn doped KNN [184, 187]. As suggested the formation of cation vacancies due to the volatilization is compensated by the creation of hole carriers. In addition, oxygen vacancies $V_{\ddot{O}}$ may be formed during the sintering process at high temperatures and subsequently oxidized during the cooling process as expressed by Equation 2-9 in Chapter 2. The charge transport by hole carriers is even confirmed by the slight decrease of conductivity with increasing temperature, in the low temperatures range, for KNN (Figure 4-14b).

Considering that Mn doping at Nb sites $[(K_{0.5}Na_{0.5})(Nb_{1-0.4x}Mn_x)O_{3-\delta}]$ and according to Equation 4-3, the substitution of Nb^{5+} ions with Mn^{2+} induces the formation of oxygen vacancies ($V_{\ddot{O}}$):

$$2MnO \rightarrow 2Mn'''_{Nb} + 2O_O^{\times} + 3V_{\ddot{O}} \qquad \textit{Equation 4-3}$$

where Mn'''_{Nb} stands for Mn ions at Nb sites. In the presence of holes Mn^{2+} may oxidise according to the equation:

$$2Mn'''_{Nb} + 2h^{\cdot} \rightarrow 2Mn''_{Nb} \qquad \textit{Equation 4-4}$$

As a consequence, the concentration of hole carriers will decrease, being responsible for the observed decrease of the conductivity at room temperature when doping KNN with Mn. A similar defect chemistry is known to occur for lead based titanates [38]. Furthermore, the oxidation of Mn as proposed in Equation 4-4 supports the XRD observation in which the decrease of the lattice parameters and unit cell volume was attributed to the substitution of Nb^{5+} mainly by Mn^{3+} or Mn^{+4} with smaller ionic radii (Figure 4-8 and Table 4-2).

At higher temperatures (T > 250 °C), the activation energy calculated for region III (Table 4-3) indicates that the conduction process is dominated by the motion of oxygen vacancies [184, 188]. Indeed it is well known that the mobility of oxygen vacancies increases with increasing temperature [38, 184, 188, 193]. At lower temperatures (lower than 250 °C), the oxygen vacancies exhibit low mobility and thus have minor contribution to conduction; however, with the increase in temperature, as they are thermally activated they contribute to the observed electrical behaviour.

The information disclosed by the ac conductivity behaviour allowed us to identify the possible conducting species / mechanisms, as hole hopping and oxygen vacancies, and their dependence on the temperature, but did not give any information on the location of these species in terms of the ceramic microstructure, i.e. grain and grain boundaries. Besides affecting the electrical response, it is also well known that defects location affects grain boundary mobility and grain growth and, as a consequence the ceramic microstructure and the ferroelectric domain patterns, which are responsible for the ferroelectric and piezoelectric response of these materials, as KNN. Therefore we used impedance spectroscopy (IS) to further exploit the responsible phenomena for the resistivity increase in $KNNMn_{0.5}$ ceramics.

Figure 4-15a and b depicts the frequency dependence of the imaginary part of both the complex impedance Z^* and the complex modulus M^*, i.e. Z'' and M'', for undoped KNN and $KNNMn_{0.5}$ at 35 °C, respectively. As observed, Z'' and M'' maxima occur at different frequencies, thus indicating that two *RC* (resistance in parallel to a capacitance) contributions might be considered to describe the impedance curves. Accordingly an equivalent electric circuit comprising two *RC* circuits (*R* parallel to *C*) connected in series (shown in Figure 4-15a) was used to model the impedance experimental data assisted by Zview software (Ver. 3.2c, Scribner Associates, Inc). A non ideal capacitance was required for an optimum fit of the circuit model to the experimental data. Each *RC* module presents one resistance and one capacitance that were assigned to the resistance and capacitance of the grain interior (bulk) and of the grain boundary. As the variations of electrode metal were not followed by any significant change of impedance data in the studied frequency range (100 Hz – 1 MHz), contributions from electrode interface to Z^* were discarded. Furthermore, it is evident that the *RC* module

corresponding to the grain bulk accounts for the impedance measured at the highest frequency (1 MHz). The resistance values of the bulk (R_b) and of the grain boundary (R_{gb}) allowing a good fit to experimental data of undoped KNN were found to be 5.83 x 10^5 and 3.90 x 10^6 Ω, respectively. Doping KNN with 0.5 mole % Mn increased these values to 6.41 x 10^5 and 1.16 x 10^7 Ω, respectively. It was thus observed that although the addition of 0.5 mole % of Mn to KNN ($KNNMn_{0.5}$) increased the resistance of both bulk and grain boundary, the major impact was felt on grain boundary resistance which increased from 3.90 x 10^6 to 1.16 x 10^7 Ω at 35 °C. The resistance increase of both bulk and grain boundary upon Mn addition accounts for the observed leakage free P-E loop of $KNNMn_{0.5}$ ceramics by increasing the overall resistivity of the ceramics at room temperature.

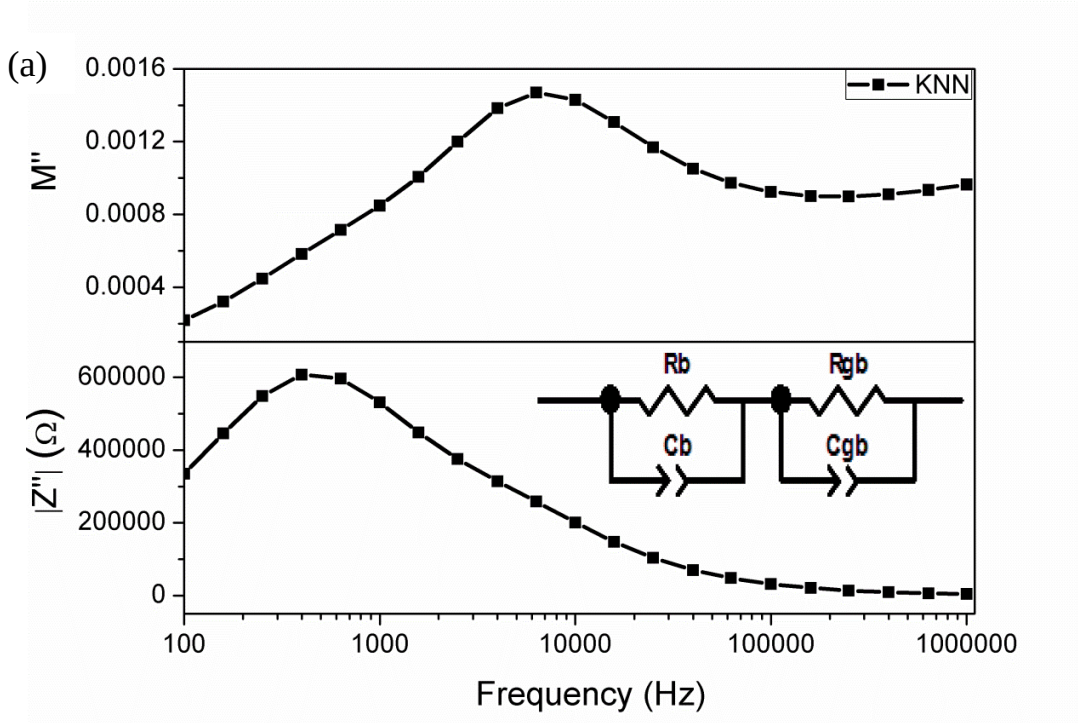

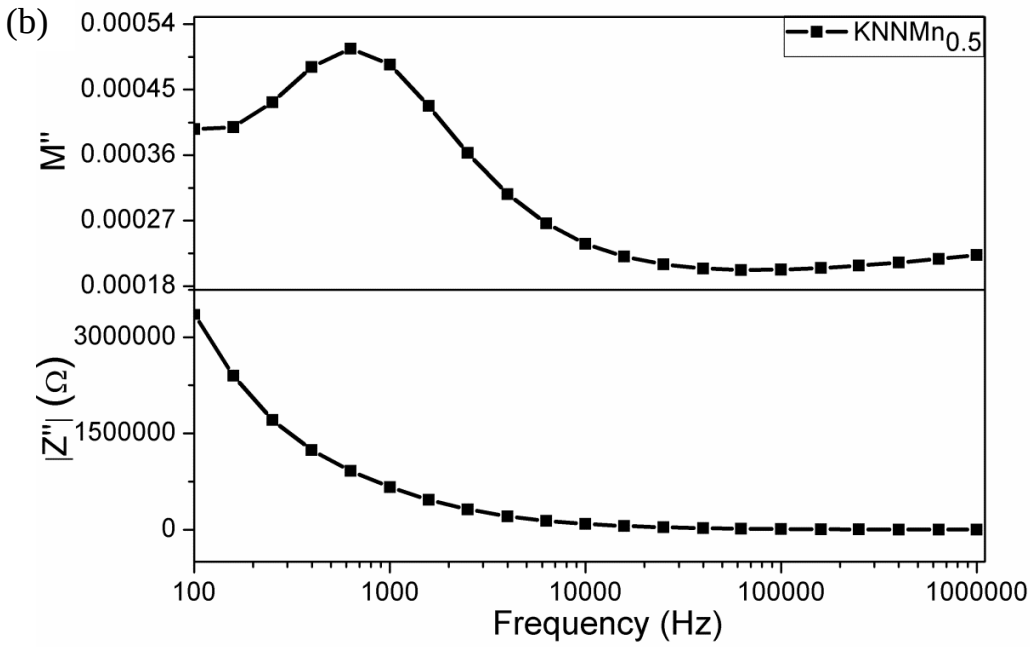

Figure 4-15. Variations of the imaginary parts of the impedance (Z´´) and of the modulus (M´´) with the frequency for (a) undoped KNN and (b) $KNNMn_{0.5}$ ceramics, at 35 °C. Squares (■) represent the experimental data and the solid lines shows fitting results according to the model.

Attempting to follow the temperature dependence of Mn effect, IS data obtained at different temperatures (30 ºC < T < 480 ºC) were also analysed. Figure 4-16 shows the Z'' and M'' curves versus frequency for a temperature range between 325 °C to 480 °C for KNN and $KNNMn_{0.5}$, respectively. As can be seen, Z'' and M'' exhibit a very well defined peak, whose maxima for both Z'' and M'' occur at different frequencies. So, the same electric model consisting of two R and C was used to extract the resistance and capacitance values for bulk and grain boundary. Table 4-4, presents the values of R_b, C_b and R_{gb}, C_{gb} that represent the resistance, capacitance of bulk (grain interior), and grain boundary respectively, obtained from the equivalent circuit. The peak maxima for Z'' and M'' lowered as the temperature increased, thus indicating the decrease in the resistance and the increase in the capacitance, being the maximum of the capacitance (M'') observed close to the Curie temperature, which was an expected result.

Table 4-4. Resistance and capacitance of bulk and grain boundaries of KNN and $KNNMn_{0.5}$ ceramics after fitting with electric circuit.

T	**KNN**		**$KNNMn_{0.5}$**		**KNN**		**$KNNMn_{0.5}$**	
(°C)	R_b	C_b	R_b	C_b	R_{gb}	C_{gb}	R_{gb}	C_{gb}
	Ω	F	Ω	F	Ω	F	Ω	F
35	5.83×10^{5}	2.40×10^{-10}	6.41×10^{5}	7.46×10^{-10}	3.90×10^{6}	4.90×10^{-10}	1.16×10^{7}	5.58×10^{-10}
100	1.40×10^{6}	2.04×10^{-10}	3.26×10^{6}	1.99×10^{-10}	2.49×10^{7}	1.35×10^{-10}	1.13×10^{8}	7.91×10^{-11}
200	8.28×10^{5}	5.17×10^{-10}	1.33×10^{6}	4.77×10^{-10}	1.94×10^{7}	2.48×10^{-10}	5.93×10^{7}	1.36×10^{-10}
325	1.64×10^{5}	4.47×10^{-10}	2.71×10^{4}	2.04×10^{-9}	1.02×10^{6}	1.04×10^{-9}	1.18×10^{5}	7.77×10^{-9}
350	1.14×10^{5}	5.22×10^{-10}	5.63×10^{3}	2.85×10^{-9}	6.45×10^{5}	1.42×10^{-9}	3.21×10^{4}	9.34×10^{-9}
375	1.02×10^{5}	5.53×10^{-10}	2.98×10^{3}	3.40×10^{-9}	5.78×10^{5}	1.54×10^{-9}	1.66×10^{4}	1.03×10^{-8}
400	5.31×10^{4}	1.06×10^{-9}	2.02×10^{3}	4.88×10^{-9}	3.08×10^{5}	3.02×10^{-9}	1.01×10^{4}	1.35×10^{-8}
425	4.67×10^{4}	1.95×10^{-9}	1.42×10^{3}	6.97×10^{-9}	2.40×10^{5}	4.66×10^{-9}	7.54×10^{3}	2.17×10^{-8}
450	4.04×10^{4}	1.48×10^{-9}	8.56×10^{2}	6.41×10^{-9}	2.48×10^{5}	3.82×10^{-9}	5.82×10^{3}	2.35×10^{-8}
480	2.87×10^{4}	1.23×10^{-9}	3.39×10^{2}	3.63×10^{-9}	3.82×10^{5}	1.99×10^{-9}	4.44×10^{3}	2.29×10^{-8}

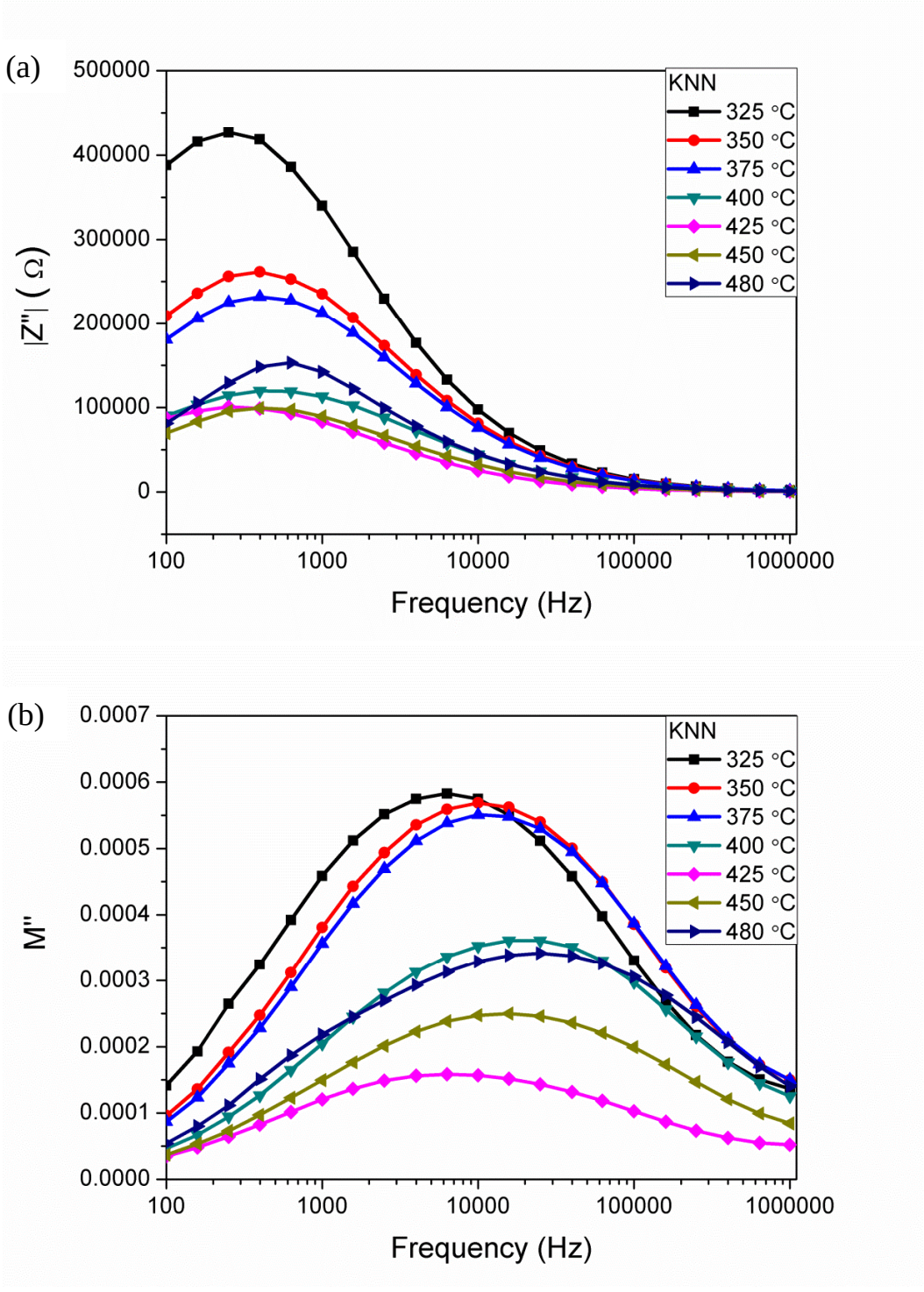
(a)
500000
400000
300000
200000
100000
0
|Z"| (Ω)
100
1000
10000
100000
1000000
Frequency (Hz)
KNN
325 °C
350 °C
375 °C
400 °C
425 °C
450 °C
480 °C
(b)
0.0007
0.0006
0.0005
0.0004
0.0003
0.0002
0.0001
0.0000
M"
100
1000
10000
100000
1000000
Frequency (Hz)
KNN
325 °C
350 °C
375 °C
400 °C
425 °C
450 °C
480 °C

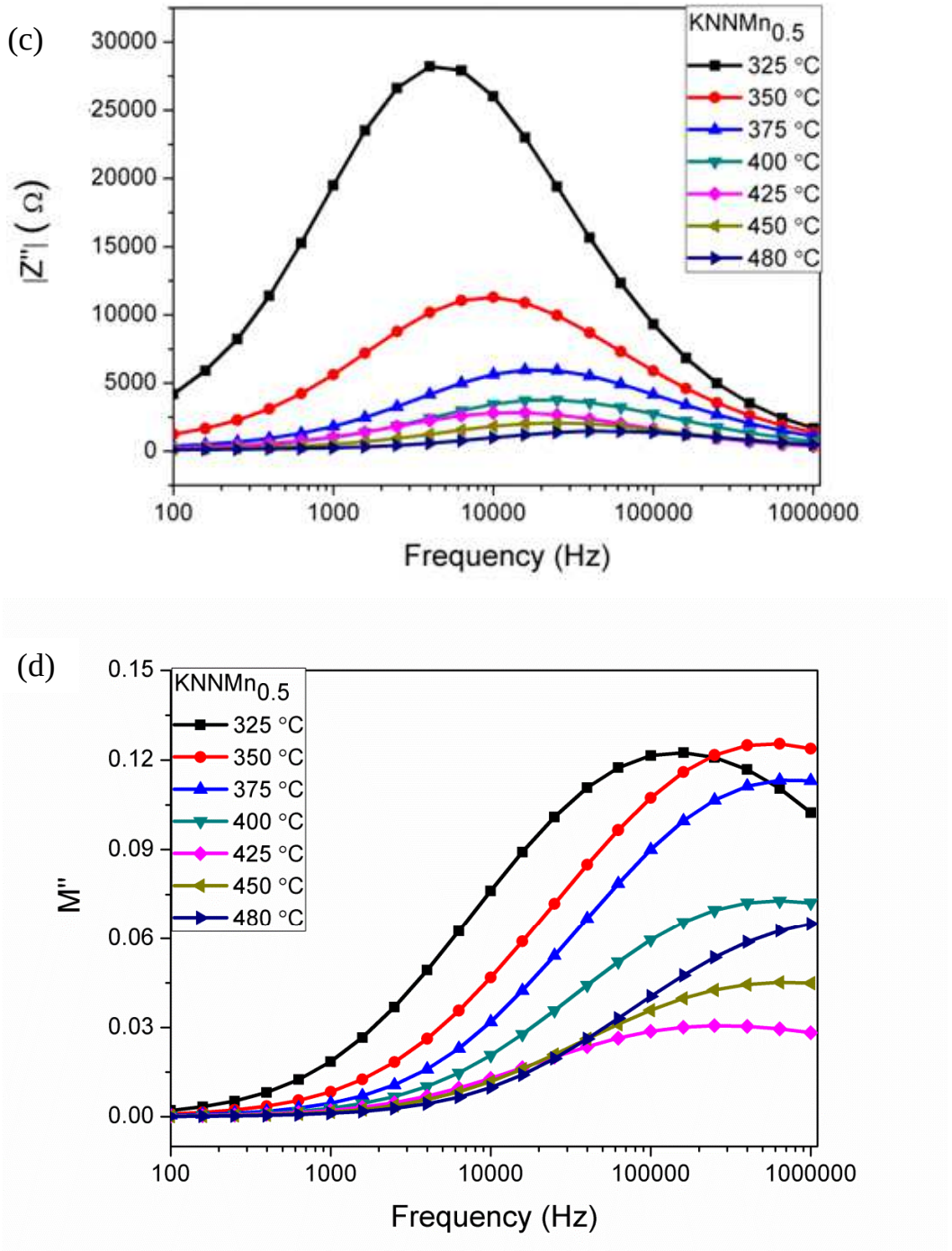

Figure 4-16. Variations of the imaginary parts of the impedance (Z´´) and of the modulus (M´´) with the frequency for (a), (b) for KNN and (c),(d) for $KNNMn_{0.5}$ at temperature between 325 °C and 480 °C. Symbols represent the experimental data and solid lines represent the fitting as per the model presented in Figure 4-15a.

Figure 4-17 shows the temperature dependence of R_b and R_{gb} for both KNN and $KNNMn_{0.5}$. Concerning resistance dependence on temperature, as discussed before, at room temperature, the resistance of bulk and grain boundary of $KNNMn_{0.5}$ are higher as compared to KNN ceramics, which was proposed to be due to hole consumed by the Mn addition at B-site, being the major increase observed at the grain boundary. This resistance correlation is maintained as the temperature increases but for a limited temperature interval (T < 250 ºC), since at higher temperature the resistances, R_b and R_{gb}, associated to undoped ceramics exceed the corresponding counterparts of doped samples. This decrease in the resistance may be due, as proposed above, to the presence of oxygen vacancies, which become mobile at higher temperatures. Now, from a careful analysis of the data (Figure 4-17) it can be observed, that at high temperature, the major impact was the decrease of R_{gb} of $KNNMn_{0.5}$, although a decrease in the R_b was also observed. This helped us to suggest that the defects, in this case (oxygen vacancies), which became mobile at high temperature.

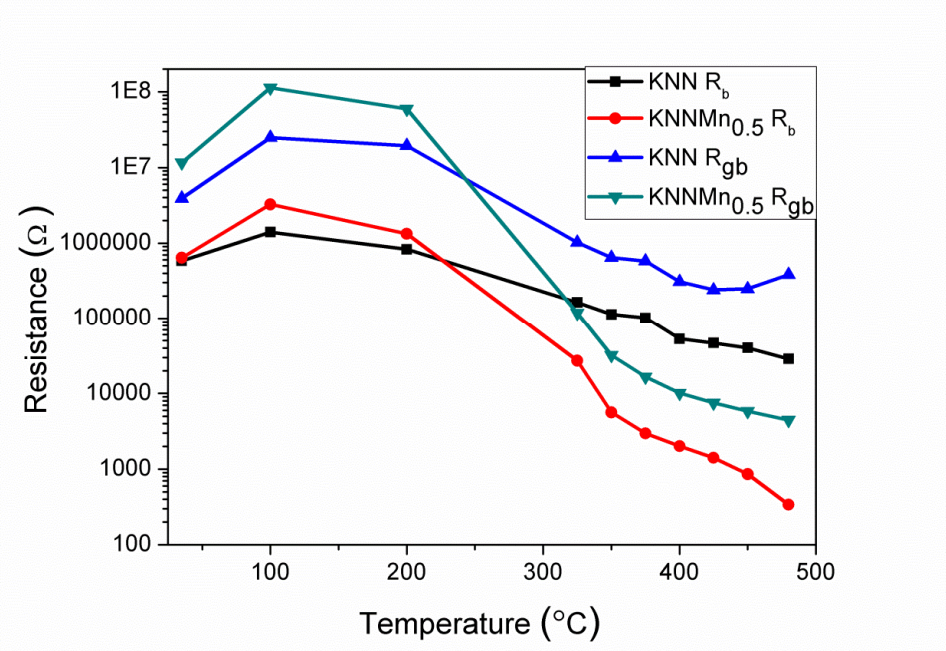

Figure 4-17. Variation of the bulk and grain boundary resistance of KNN and $KNNMn_{0.5}$ ceramics. It was observed that at room temperature, the major increase is in the grain boundary resistance and at high temperature; main decrease is in the grain boundary resistance, suggesting that playing defects are mainly located on the grain boundaries.

4.1.2.5 Conclusions

A and B- site doped KNN Ceramics (KNMN and KNNM) samples were successfully synthesized by conventional mixed oxide method, in which the intentional stoichiometric variation was made to incorporate the Mn at the desired A or B-site. The solid solubility limit for Mn in A and B-site was determined to be $KMn_{0.09}NN$ and $KNNMn_{0.5}$ respectively. The solubility limit in A-site was found to be much less (~5 times) than the B-site. A-site Mn doped samples were much soft and less dense than the B-site doped samples. Dielectric constant values were lower for A-site doped samples, whereas T_C increased for the A-site doped ceramics. It was observed that although Mn solid

solubility at the B site of KNN ceramics is small, Mn doped KNN ceramics present at room temperature an improved hysteretic response when compared with undoped KNN. The role of Mn doping at B-site on electrical behaviour of $K_{0.5}Na_{0.5}NbO_3$ (KNN) ceramics was assessed by impedance spectroscopy. The improved behaviour was related with defects and charge transport in the ceramics and their temperature dependence was discussed. KNN presents three different conductivity regimes as a function of the temperature, and the activation energies of ac conduction $E_{a,}$ were calculated to be 0.03 eV and 0.05 eV for KNN and Mn doped KNN ($KNNMn_{0.5}$), respectively for region I (30 °C - 180 °C; 220 °C – 350 °C for KNN ; 30 °C – 180 °C; 220 °C - 250 °C for $KNNMn_{0.5}$), 0.49 eV and 0.42 eV for region II (180 °C – 220 °C) and 0.97 and 0.73 eV for region III (350 °C to 400 °C for KNN; 250 °C to 400 °C for $KNNMn_{0.5}$) at 1 MHz. Accordingly it is suggested that the conduction at room temperature in KNN is associated with hole hopping and can be suppressed by Mn doping. As a consequence, a less leaky hysteresis loop is obtained. On the other hand, at high temperatures the conduction mechanism is dominated by the motion of doubly ionized oxygen vacancies, which concentration increases with Mn doping. Based on the variation of the resistance of grains and grain boundaries it is suggested that oxygen vacancies in KNN and Mn doped KNN ceramics are mainly located at the grain boundaries. Figure 4-18 shows some of the conclusions of this section.

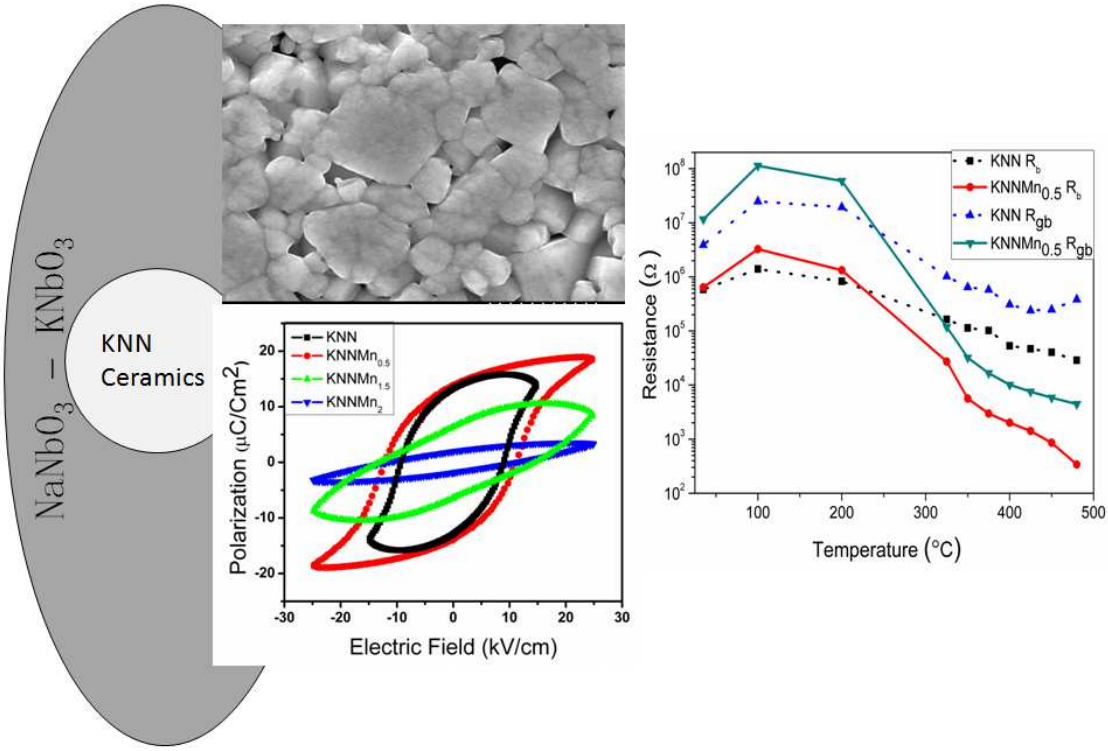

Figure 4-18. Image explaining some conclusions of this section. Small amount of Mn ($KNNMn_{0.5}$) improved the polarization hysteresis curve and was explained on the basis of mainly increase in the grain boundary resistance.

4.2 KNN single crystal: growth and characterization

4.2.1 Establishing the domain structure of $(K_{0.5}Na_{0.5})NbO_3$ (KNN) single crystals by piezoforce-response microscopy

4.2.1.1 Abstract

Single crystals of potassium sodium niobate (KNN) were grown by a modified self-flux method. The crystals were prepared with a boron-modified flux, used to obtain the crystals at a relatively low temperature. XRD, EDS and ICP analysis prove the chemical and crystallographic quality of the crystals. The grown KNN crystals have a high dielectric permittivity (29,100) at the tetragonal-to-cubic phase transition temperature, remnant polarization (19.4 $\mu C/cm^2$) and piezoelectric coefficient (d_{33} = 160 pC/N) when compared with the standard KNN ceramics. Piezoforce response microscopy, used for the first time to characterize the domain structure of <001> - oriented potassium sodium niobate (KNN) single crystals, revealed a long range ordered domain pattern of parallel 180° domains with zig-zag 90° domains. It is argued that the presence in KNN

single crystal (and absence in KNN ceramics) of such a long range order specific domain pattern that is its fingerprint accounts for the improved properties of single crystals. These results have broad implications for the expanded use of KNN materials, by demonstrating the relation between the domain patterns, dielectric and ferroelectric response of single crystals and ceramics, indicating ways of achieving maximised properties in KNN materials.

4.2.1.2 Introduction

The electromechanical response of any given system is very dependent on the crystalline phase content, crystallographic orientation, microstructure, interfaces and domain configurations. As already explained in the Chapter 2 (2.9), that is due to the improved performance of single crystals compared with polycrystals counterparts (properties are summarized in Table 2-1, Table 2-2 and Table 2-5. Crystals have been preferred for applications as actuators, surface acoustic wave (SAW) devices, electro-optic modulators, sonar, non-destructive testing and high performance medical transducers. It was also mentioned, that several methods have been developed for single crystal growth, but a very little data is available about the electrical properties. The reported values are also summarized in Table 2-5.

Ferroelectric domains in KNN ceramics have been reported using transmission electron microscopy (TEM) [116], scanning probe microscopy [25], polarization light microscopy [117], and by confocal Raman microscopy [131]. PFM is currently the most powerful technique to image and study domains and ferroelectric properties in lead based [194, 195], as well as lead free, ferroelectric materials [196] at the nanoscale. PFM enables the visualization of domain morphology which is largely dependent on the single crystal thermal history hence reflecting details of the production technique such as heating and cooling profiles based on the type of domains observed [197]. PFM can thus be used for tracking the footprints of the used crystal growth method. Additionally PFM allows domain switching as well, which probes the crystal in a condition close to that of the final performance. However the domain configuration of KNN single crystals has not yet been studied at the local scale by piezoforce response microscopy (PFM) and its relation to the macroscopic electrical properties is not well established.

The aim of the present work is twofold: i) to grow KNN single crystals at low temperatures ≤ 1250 °C, for a better control of the volatilization of K and Na, using an alternative B_2O_3-modified K_2CO_3 flux; and ii) to establish the relation between the macroscopic electrical properties and the domain configuration at the nanoscale of KNN single crystals and polycrystals. The dielectric, ferroelectric and piezoelectric properties of the grown crystals were assessed along the <001> orientation. The ferroelectric domains of these crystals were mapped by piezoforce response microscopy. The relation between the electric response at the local scale and macroscopic response of KNN single crystals and ceramics is established. This work intends to contribute to the pool of knowledge on KNN materials, to make them a viable alternative to PZT.

4.2.1.3 Experimental procedure

KNN single crystals and their bulk undoped ceramic counterparts were prepared as explained in Chapter 3. The crystal phase composition and crystallographic orientation of KNN crystals were evaluated by X-ray powder diffraction (XRD, Rigaku, D/Max-B, Cu-K_α radiation) and by single crystal X-ray diffraction (XRD, Bruker APEX II) at room temperature in the 20° to 70° 2θ range with a step length of 0.02°. The surface of the single crystals was observed by scanning electron microscopy (SEM, Hitachi S-4100). The elemental composition of the crystals was characterized by energy dispersive X-ray spectroscopy (EDS) attached to SEM (SEM/EDS, Hitachi SU-70), and inductive coupled plasma atomic emission spectrometry (ICP - AES, Jobin Yvon Activa-M).

For the electrical characterization, parallel faces of naturally shaped crystals (thickness, 100-200 µm) were polished, and silver paint was used as an electrode. Then, the dielectric constant (ε_r) was measured by a Precision LCR Meter (HP 4284A) in the frequency range from 100 Hz to 1 MHz. For the determination of the polarization versus electric field hysteresis loops (P-E), a ferroelectric tester (Aixact TF analyzer 1000) was used. The piezoelectric constant d_{33} was evaluated by a Berlincourt piezoelectric meter, Sinocera YE 2730A. The ferroelectric domain structure of KNN single crystals and ceramics was mapped by piezoresponse force microscopy (PFM) using a Multimode, NanoScope IIIA (Veeco Instruments). The PFM was equipped with an external lock-in amplifier (SR-830, Stanford Research), function generator (FG120, Yokogawa) and

voltage amplifier (7602, Krohn-Hite). A conductive SPM probe tip by PPP-NCHR Nanosensors, Switzerland (length: 125 µm, thickness: 4.0 µm, width: 30 µm, resonance frequency: 355 kHz, spring constant: 50 N/m) was used. To induce piezoelectric deformation, an external ac voltage signal with amplitude of 10 – 30 V and frequency of 50 kHz and 5 kHz was applied to the crystals, for out-of phase and in-phase imaging, respectively. The amplitude and phase of the cantilever deflection were detected using a lock-in amplifier. The upper crystal face was polished before the measurements and the silver paint was used as bottom electrode.

4.2.1.4 Results and discussion

The crystal growth conditions and typical KNN crystal dimensions are summarized in Table 4-5 and illustrated in Figure 4-19a. Thermal profiles and their explanation has already been presented in the experimental section (Chapter 3). KNN single crystals grew mostly in the form of platelet-like shape with a size distribution between of 2 x 2 x 0.5 and 8 x 3 x 3 mm. Different dwelling temperatures and flux compositions and concentrations were tried. For the flux containing only K_2CO_3 and the dwelling temperature of 1250 °C, the obtained crystals are relatively large, 4.5 x 4.0 x 2 mm. When a small content of B_2O_3 was added to the flux (10 wt % in the flux), crystals of almost similar size and with more regular shape (platelet like) were obtained at a low temperature of 1200 °C.

Table 4-5. Preparation conditions and maximum crystal size of as-produced KNN crystals

Thermal Profile	**Maximum Temp. for Crystal Growth (°C)**	**Complex flux composition (wt %)**		**Average crystal size (L x W) (mm)**
		K_2CO_3	B_2O_3	
1	1250	100	0	4.5 x 4
2	1240	90	10	4 x 3.2
3	1200	90	10	4 x 3

The top and lateral views of the microstructure of KNN crystals prepared under TP3 profile (Table 4-5) are shown in Figure 4-19b and c, which represents the general microstructure of the obtained KNN crystals. As observed the larger faces of the plate shaped crystal are quite smooth and the lateral sides present a layered structure where growth steps are clearly visible. The large faces, which are perpendicular to the c axis, were the ones with a slow growth rate and thus dominate the crystal morphology. It is known that for a given flux, the final morphology of a crystal produced under a certain temperature profile reflects the solution supersaturation variation during the growth run. As previously reported, a high degree of supersaturation causes dendritic growth, hopper growth or flux inclusions whereas faceted crystals, such as those obtained in the present work, require lower supersaturation [30, 105]. KNN single crystals with layered surfaces were also previously reported by floating zone method [30]. The KNN layered surfaces of the crystals grown in our work suggest that the TP3 temperature profile used allowed adequate supersaturation conditions that favoured a two dimensional nucleation layer growth. Additionally, the smooth surfaces corresponding to [00l] facets are probably the crystal surfaces of lowest specific energy, since its area is maximized by crystal growth. EDS and ICP - AES analysis of the crystals prepared under the same run conditions

TP3) revealed only the presence of K, Na and Nb elements (Table 4-6). Also according to these results, the stoichiometry of the crystals is quite close to the nominal one. Under the detection limits of the equipment, boron from the flux could not be identified in the analysed crystals.

(a)

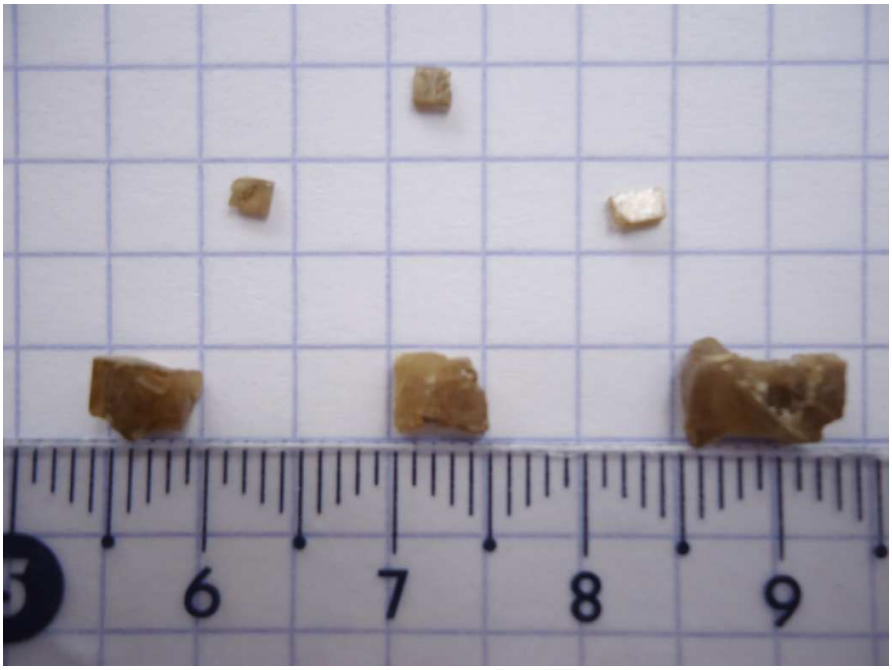

(b)

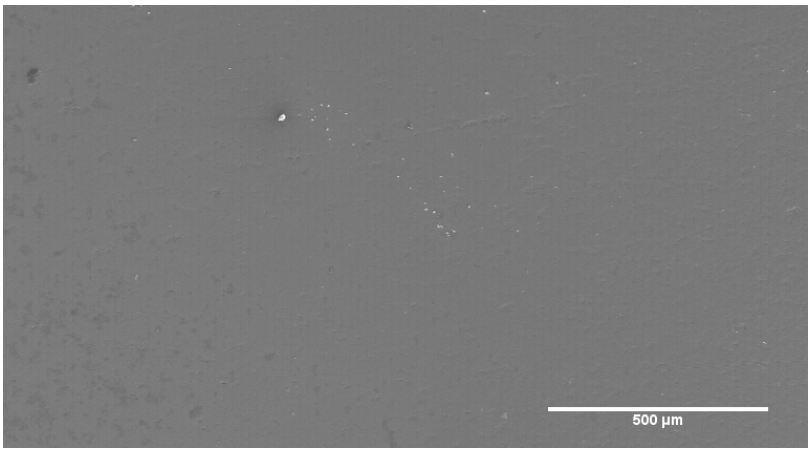

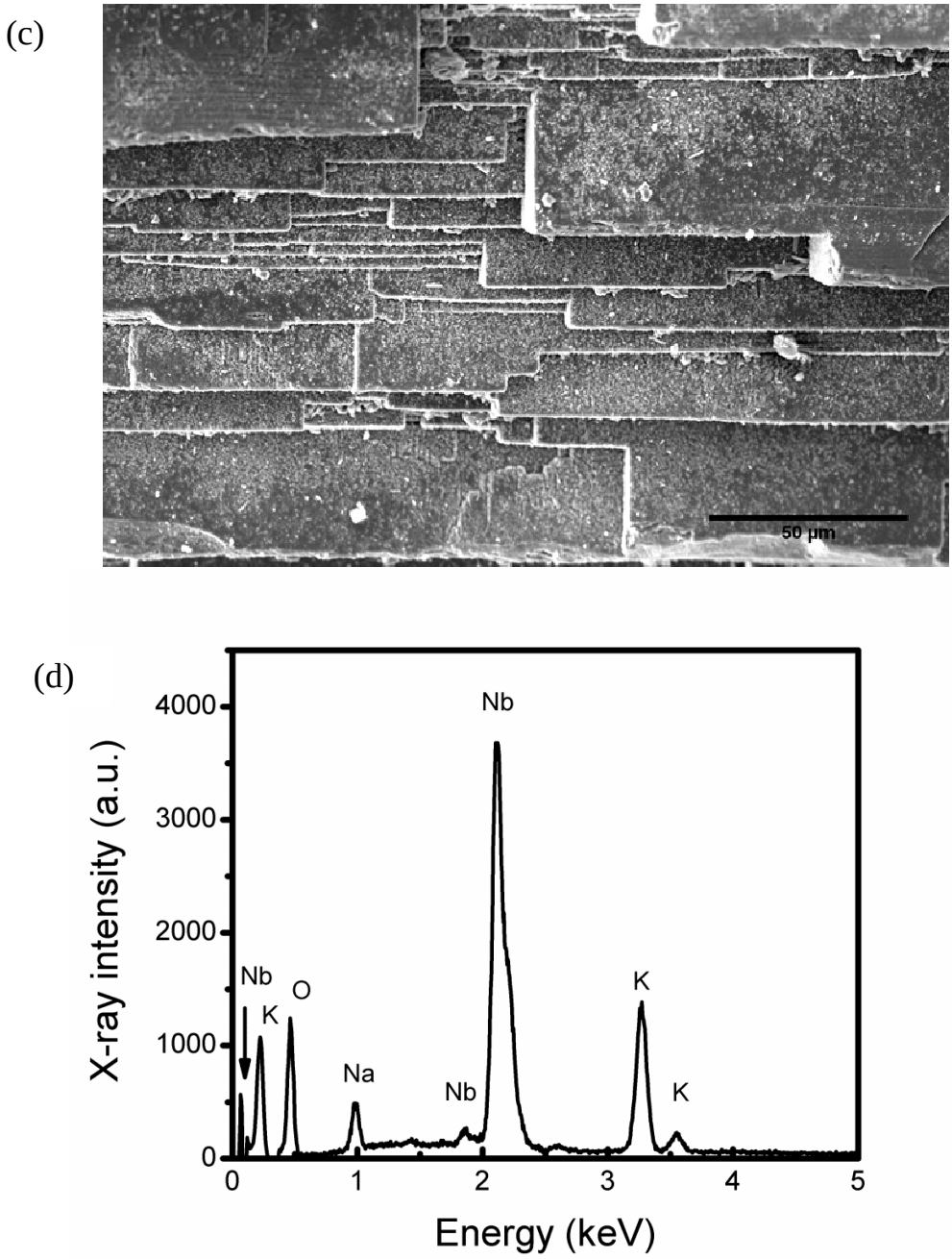

Figure 4-19. A photograph of the modified self-flux grown KNN crystals: larger crystals were collected from the top of Pt crucible and the small ones from the bottom (a); top view SEM micrograph of KNN crystals face showing a smooth surface (b); lateral side view SEM micrograph of KNN crystals revealing a layered structure where growth steps are clearly visible (c) and EDS spectra of KNN single crystals where only K, Na, and Nb were detected (d).

Table 4-6. Data of the chemical analysis performed by EDS and ICP on the prepared KNN crystals.

Elements	**Nominal Composition**	**EDS**	**ICP-AES**
	(at. %)	(at. %)	(at. %)
K	10	10.45	10.75
Na	10	9.77	9.62
Nb	20	20.47	20.50
B	0	< 0.01	< 0.01
O	60	59.31*	59.13*

Oxygen is calculated from the stoichiometry

Figure 4-20 depicts the XRD patterns of KNN crystals prepared under TP3, milled KNN crystal powders and KNN bulk ceramics for comparison purposes (Table 4-5). The XRD profiles of the milled single crystal powders and KNN bulk ceramics are similar. All the analyzed crystals, even those obtained under distinct growth conditions, exhibit similar XRD patterns that correspond to the orthorhombic structure with slight monoclinic distortion. No impurity phases were found in any of the prepared crystals, under the resolution limits of the X-ray diffractometer used. (001) and (002) are the preferred reflections in the case of single crystals (Figure 4-20). The calculated unit cell parameters of KNN crystals are a = 3.9997 Å, b = 3.9478 Å, c = 3.9981 Å with $\beta = 90°22'$, being close to the values previously reported in the literature [79].

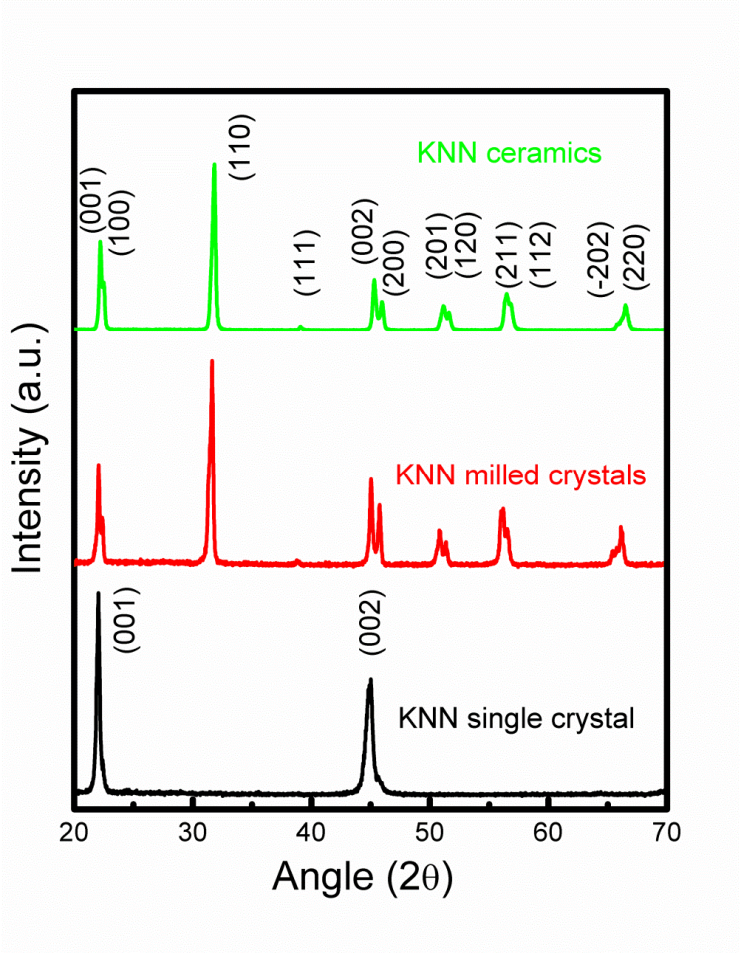

Figure 4-20. X-ray powder diffraction patterns of polycrystalline KNN powders, milled KNN crystals, and single crystal. Peak positions are the same for the bulk ceramics and milled single crystals, whereas (001) and (002) are the preferred reflections for the KNN single crystals.

It is known that the ferroelectric and electromechanical response of a material is directly related to its polar domain structure. In ferroelectric crystals/ceramics, energy minimization results in multiple domains, separated by domain walls. The domain walls have well-defined orientations that minimize energy by maintaining compatibility of strains and polarization across the wall. Thus, particular patterns, or domain structures, occur, and these dictate the effective properties of the crystals. PFM is a powerful tool to image ferroelectric domains at the nanoscale and to study their switching behavior [194, 195]. However, the domain configuration of KNN single crystals has not yet been reported by PFM. In orthorhombic ferroelectrics with monoclinic distortion, such as

KNN, 60°, 90°, 120° and 180° domain walls can be formed [25]. In addition, the best piezoelectric properties (d_{33} = 416 pC/N) have been reported in Li, Ta and Sb doped KNN ceramics, in which grains were aligned along the <001> direction [64].

Figure 4-21 shows the topography and PFM images of (001) KNN single crystals (Figure 4-21a-d) and bulk ceramics (Figure 4-21e-f) respectively. The bright and the dark contrast in the PFM images represent the direction of orientation of the polarization vectors in their respective planes; dark regions represent the orientation into the bulk of the crystal and the bright regions pointing towards the surface of the crystal. It was observed and evident from the shown images that the PFM contrast is independent of topography effects, indicating that the acquired PFM signal has not been influenced by the cross talk with topography signal in both cases i.e. single crystals and bulk ceramics. A complex domain pattern was observed in the single crystals which consists of zig-zag 90° domains (circled in Figure 4-21b) and parallel 180° domains (arrows in Figure 4-21b) which were assembled in a regular fashion as shown in the schematic of Figure 4-21b. For clarity purposes a zoomed image of the zig-zag area is shown in Figure 4-21c and d (topography and piezo-response image, respectively). In this case, as in the previous one the piezo-response image is free of topography effects. The domain length varies between 6.5 - 12 µm and average domain width was about 2.6 µm for 180º domains, whereas, these values were 3 - 5 µm and 1.5 µm for 90º domains.

A domain pattern, consisting of a 90º and 180º domain arrangement, was previously observed by transmission electron microscopy (TEM) [116] for KNN crystals grown by the solid state method [116]. However, in a recent article, Inagaki *et al.* reported by polarization microscopy for flux grown KNN crystals that only zig-zag 90° domains could be observed in undoped KNN, whereas only 180º domains were present in Mn-doped KNN crystals [30]. The zig-zag type domain pattern in KNN was attributed to existing internal stresses which were reduced by Mn addition, thus giving rise to 180º domains as a dominant pattern in Mn doped KNN single crystals [30]. However, for the undoped KNN single crystals grown in the present work, both zig-zag and 180º domains structures coexist, which, based on Inagaki *et al.* observations, might indicate the presence of lower internal stresses compared to the single crystals reported by themselves [30]. The effects of cooling rates during crystal growth on the domain structure

are still poorly understood, and a preliminary work by Inagaki *et al.* clearly indicate a dependence of the domain patterns on the cooling rate [31]. Very interestingly, these authors show that for high cooling rates only 90° domains were present, whereas for low cooling rates 60° and 90° domains coexist [31]. Accordingly the mixed patterns of 90° and 180° domains as depicted in Figure 4-21b might be related with the several cooling profiles used in the present work. No evidence of 60° and 120° domains could be observed in our single crystals, as in the PFM study of doped KNN ceramics by Herber *et al* [25] .

For the bulk ceramics with an average grain size of 1.5 µm, randomly oriented domains were observed in the PFM image. 90° domains patterns (circled in Figure 4-21f) were present as well but only at a localized scale, not forming a long ordered arrangement. Similar types of patterns have also been reported for Li, Ta and Sb doped KNN ceramics, having much bigger grain size of 50 µm, by Herber *et al* [25]. The absence of specific domain patterns repeating regularly on a long scale reflects the grain size and grain boundary effects, as it is already known that complex self organized domains, like those one observed in the present large sized KNN crystals, can only be formed in bulk ceramics with large grains of several square micrometers [29].

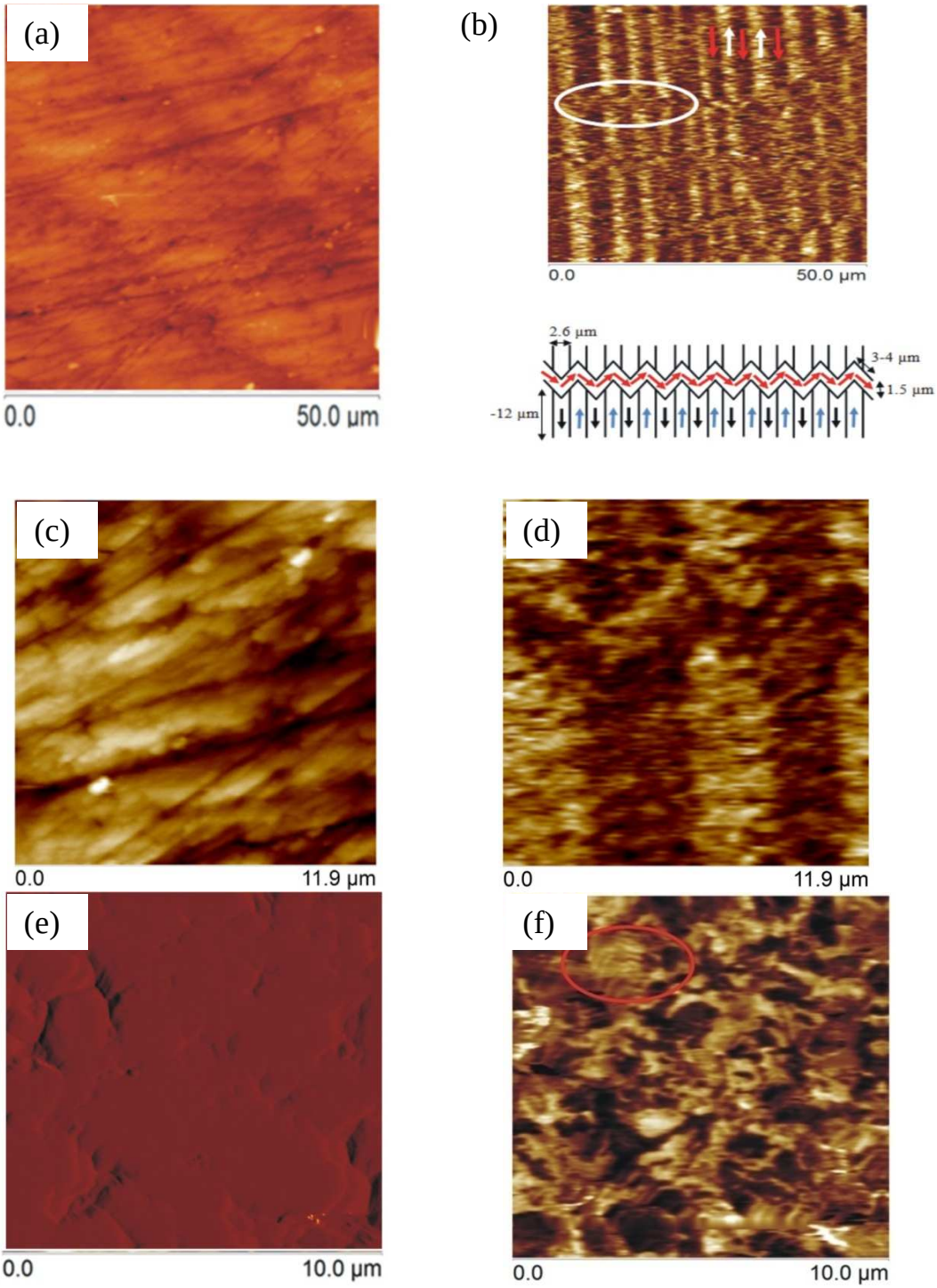

Figure 4-21. Out-of-plane images of KNN single crystal and bulk ceramics. Topography (a) and(c) piezo-force microscopy response image b) and d) for KNN single crystals and topography(e) and(f) piezo-force microscopy response image of bulk ceramics. KNN single crystals show a clear distinct domain pattern with a long range ordered array of 90º and 180º domains whereas domains are randomly oriented in the bulk ceramics.

The switching of domains was confirmed by applying ± 30 *V* (poling the crystals), and later crystal was scanned with 5 *V* peak-to-peak ac voltage. The results are presented in Figure 4-22a, where bright and dark regions correspond to the regions poled with +30 and -30 *V*, respectively. The poling field causes changes in the domains of KNN single crystal (i.e. the contrast in Figure 4-22a is bright for the outer square, while dark contrast domains are visible in central part of Figure 4-22a) indicating full polarization switching. Figure 4-22b represents the PFM signal taken along the line in the piezoresponse image of the poled sample. Overall, it was possible to switch the polarization direction by applying electric field of suitable polarity thus confirming the switching of the domains, which was not reported by any other method used to study domains in the KNN crystals.

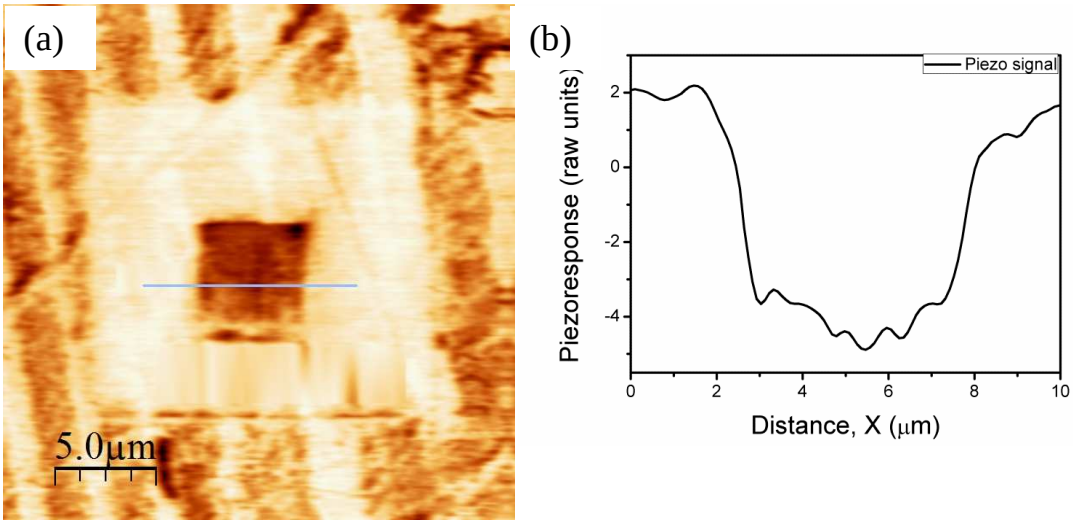

Figure 4-22. Piezoresponse images showing (a poling) for the KNN crystals and(b) signal along the line shown in (a). The images showed a distinct domain pattern. Domain switching was observed by the application of voltage of suitable polarity.

For deep analysis of the herringbone type domain structure, we took a closer look on the domain pattern and corresponding signal. The out-of-plane (OPP) and in-plane (IPP) both images showed a well-defined domain pattern. To identify the domain configuration, we analyzed the piezo-signal along the lines shown in Figure 4-23a and b (marked 1 in both images). Figure 4-23c represents one such profile which showed that

both the OPP and IPP components have opposite magnitude and phase spatially. Furthermore, it was also observed that maxima and minima for the OPP and IPP signals are coincident along the spatial direction, which is an indication, that for these domains both in-plane and out-of-plane signals co-exists, and that polarization is not normal to the crystal surface but forms an angle with the crystal normal, which might reflect the monoclinic distortion [198-200]. In the piezo-image (Figure 4-23a, marked 2), 90° and 180° domains can be observed and the angle between two planes is close to 90°, which formed between (001) and (010) and it is obvious that these domains are separated by [011] direction.

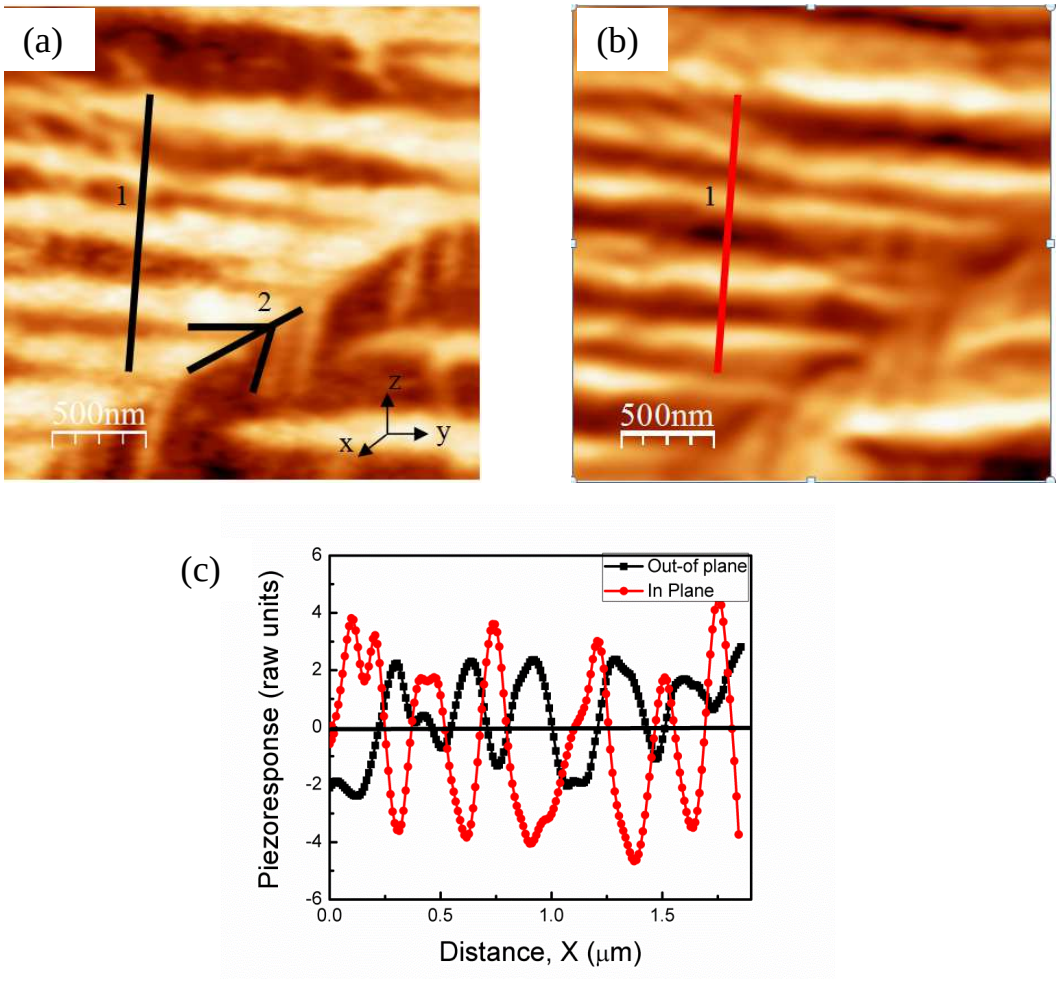

Figure 4-23. Domain structure for KNN single crystal: (a) OPP PFM image, (b) IPP PFM image and (c) cross-sectional profile for the line shown in the OPP and IPP PFM images.

Concerning the macroscopic dielectric response, Figure 4-24 represents the temperature dependence of the dielectric constant on the (001) face of KNN crystals at a frequency of 1 kHz. For comparative purposes, the dielectric response of KNN ceramics having a relative density of 95 % is also presented. Two peaks in the dielectric permittivity were observed in these curves, which can be correlated to the phase transition from orthorhombic / monoclinic to tetragonal at around 215 °C, and from tetragonal to cubic at 429 °C (T_C) and are close to the values reported in the literature [33, 63, 201]. The dielectric constant at room temperature is about 300, and at the high temperature plateau (extending from 215 °C to 350 ºC) it reaches the value of 2550, which is higher than that of the bulk ceramics (1540). The dielectric constant value at the second transition temperature, (from tetragonal to cubic) is 29100, which is higher than that of the bulk ceramics (7322) and to previously reported values of ~7000 and between 10000 [117] and 14000 for single crystals [111, 112].

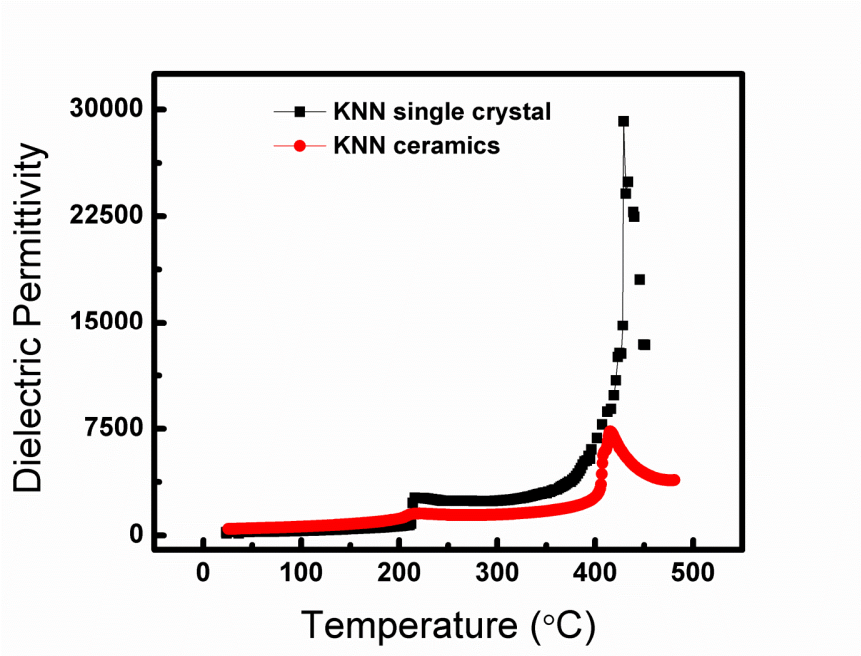

Figure 4-24. Temperature dependence of the dielectric constant (ε_r) of KNN crystals (thickness ≈ 200 µm) and KNN bulk ceramics along (001) orientation. Single crystals show higher values of permittivity especially at higher temperatures than the bulk counterpart.

In terms of polarization behaviour, the hysteresis loop at room temperature on the (001) face crystals is presented in Figure 4-25, together with the hysteretic response of KNN bulk ceramics for comparison. The remnant polarization (P_r) and coercive field (E_c) at room temperature are 19.4 μC/cm^2 and 10.6 kV/cm for KNN single crystals, and 13 μC/cm^2 and 9.1 kV/cm for KNN polycrystals, respectively. Although only few data are available for the ferroelectric properties of KNN crystals, the values obtained are similar to the 18 μC/cm^2 and 17 μC/cm^2 reported in the literature for KNN crystals prepared by solid state crystal growth and flux method, respectively [17, 112]. As expected the remnant polarization (P_r) of the single crystals is higher than that of the bulk ceramics. In addition, the hysteresis loop of the single crystals is more square-shaped, and free from the space charge effect in comparison to the ceramic counterpart.

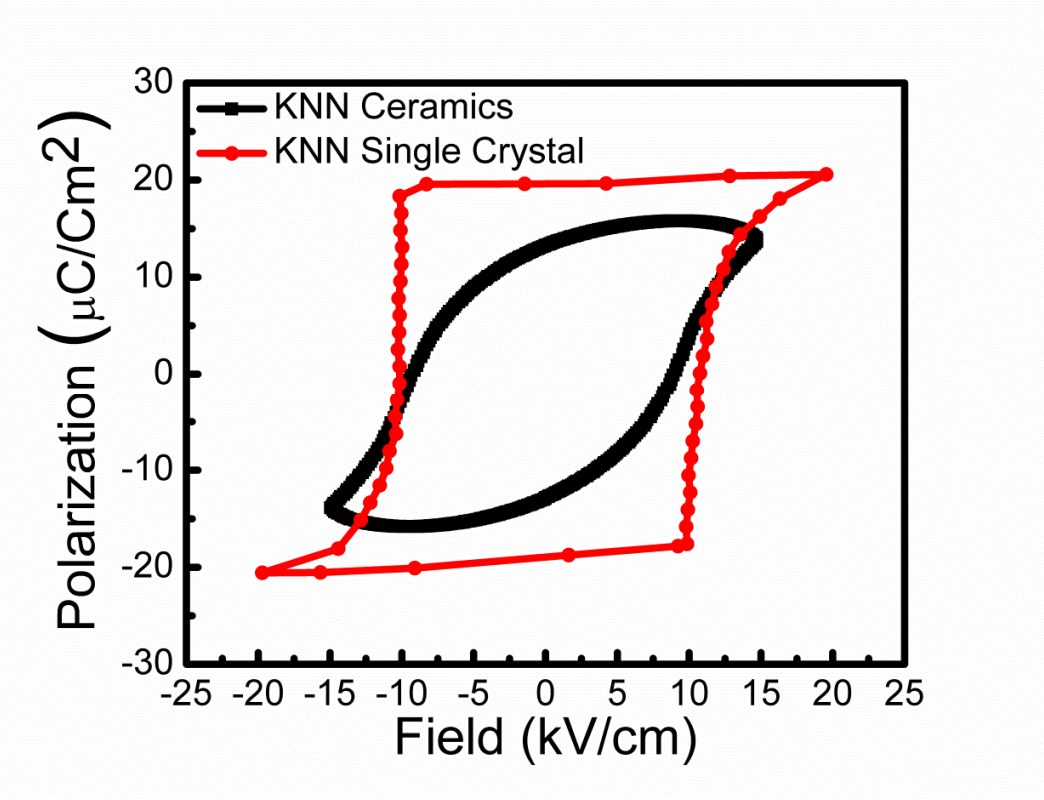

Figure 4-25. P-E hysteresis loop of KNN crystals (thickness ≈ 200 μm) and KNN bulk ceramic at a frequency of 40 Hz. Single crystals show higher remnant polarization and coercive field than the bulk counterpart

In accordance to the dielectric response, the piezoelectric coefficient (d_{33}) was evaluated at room temperature and values were found to be ~ 160 pC/N, which is similar to the previously reported values for KNN single crystals, which varies between 80 to 160 pC/N [111, 112] and twice the value of KNN polycrystals (89 pC/N).

Based on this evidence, the absence of the long range ordered specific domain pattern observed in polycrystalline KNN seems to contribute to the differences observed in the electrical responses of KNN single crystals and ceramics. The existence of this specific domain pattern is considered to account for the improved properties of KNN single crystals, including their higher dielectric and electromechanical response in comparison to the bulk ceramics.

4.2.1.5 Conclusions

Single crystals of $K_{0.5}Na_{0.5}NbO_{3;}$ (KNN) have been successfully grown by a modified self-flux method. The crystals were prepared with a boron-modified flux, used to obtain the crystals at a relatively low temperature. Additions of small amounts of boron oxide, used because of its low melting temperature (450 °C), increased the metastable region, thus enabling low temperatures for the growth of relatively large KNN crystals. XRD, EDS and ICP analysis prove the chemical and crystallographic quality of the crystals. Domain patterns of <001> oriented KNN crystals were assessed for the first time in this work by piezoforce response microscopy. These KNN single crystals have a high dielectric permittivity, especially at high temperatures, remnant polarization (19.4 $\mu C/cm^2$) and piezoelectric coefficient (160 pC/N). By comparison with the domain patterns of KNN ceramics, it is proposed that the enhanced properties of KNN single crystals might be due to the particular long range ordered domain pattern of parallel 180° domains with zig-zag 90° domains, existing in the single crystals, and absent in the ceramics. The local switching of the domains was confirmed by applying electric field of suitable polarity to the crystals in PFM poling experiment. This insight should provide a basis i) for the understanding the impact of local domain patterns on the improvement of the macroscopic properties, ii) to contribute to the pool of knowledge and therefore aid the development of KNN as a viable lead free alternative to PZT for practical applications. Figure 4-26 shows some of the conclusions of this section.

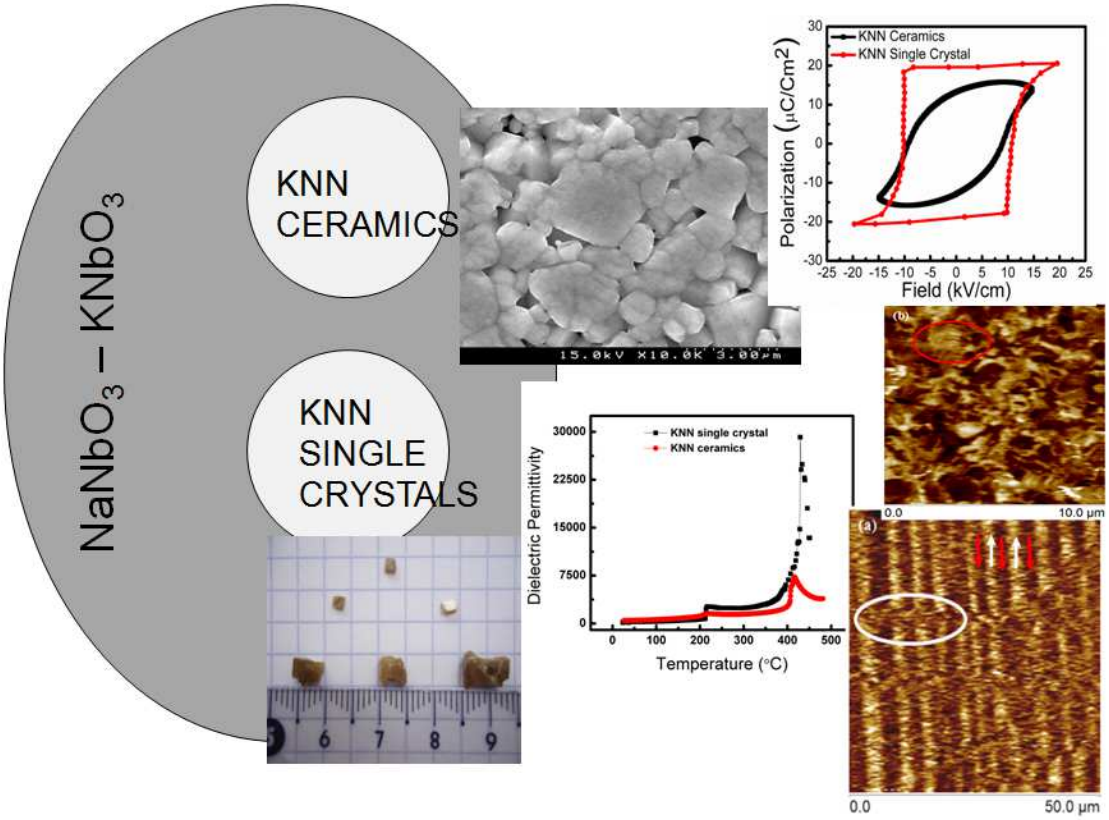

Figure 4-26. Image showing some conclusions of this section. Single crystals showed a repetitive domain pattern, higher dielectric and polarization values as compared to the bulk counterparts.

4.2.2 Precise determination of phonon constants in lead-free monoclinic $(K_{0.5}Na_{0.5})NbO_3$ (KNN) single crystals

4.2.2.1 Abstract

In this study, a polarized Raman analysis of ferroelectric potassium sodium niobate $(K_{0.5}Na_{0.5})NbO_3$ (KNN) single crystals prepared by high temperature self-flux method is presented. For the first time, the structure of KNN single crystals is assigned to the monoclinic symmetry in KNN single crystals. Intensities of A′, A″ and mixed A′+A″ phonons have been theoretically calculated and compared with the experimental data in dependence of crystal rotation, which allowed the precise determination of the Raman tensor coefficients for (non-leaking) modes in monoclinic KNN. In relation to the previous literature, this study clarifies that assigning monoclinic phase is more suitable than the orthorhombic one. In addition, this study is the basis for non-destructive assessments of domain distribution by Raman spectroscopy in KNN-based lead-free ferroelectrics with complex structures.

4.2.2.2 Introduction

KNN is a solid solution between $KNbO_3$ and $NaNbO_3$ and optimal piezoelectric properties appear when the K^+ / Na^+ ratio is 1:1 on the A-site of the ABO_3 perovskite [33, 54]. It can be observed from the phase diagram of KNN that only a small amount of potassium (2 %) in $NaNbO_3$ changes the structure. In an early work on KNN, Shirane *et al.* calculated the cell parameter as monoclinic, and treated it as orthorhombic for easier comparison with tetragonal and cubic phases [63]. Ahtee *et al.* [74] refined the neutron diffraction data of x = 0.02 and 0.1 compositions by using orthorhombic and monoclinic symmetry, and proposed that the monoclinic symmetry to be the correct one, also mentioning that the difference between the two structures is very small. Monoclinic phase was reported also in nanosized pulverized KNN powders [75, 76]. Recently, many researchers used an orthorhombic phase for the refinement of the cell parameters of $K_{0.5}Na_{0.5}NbO_3$ at room temperature from X-ray diffraction (XRD) [77] and neutron data [78], although report of monoclinic phase from the refinement of cell parameters was also published in the KNN system [79]. Knowledge about the structure is indispensable for understanding the origin of piezoelectric property. The structure ambiguity at the MPB in $Pb(Zr_xTi_{1-x})O_3$ (PZT) remained for long and Noheda *et al.* [202, 203] clarified it as monoclinic structure on the basis of powder synchrotron X-ray diffraction and claimed it to be the reason of enhanced electromechanical properties [204]. Therefore, there is a need of clarity concerning the structure of KNN as the crystal symmetry influences domain configuration, and electro-mechanical properties.

In the recent years, Raman spectroscopy has gained much attention (along with Piezoresponse Force Microscopy, PFM) as a technique for the visualization of domains in piezoceramics [205-210]. Although Raman cannot distinguish between 180° oriented domains and thus cannot detect their polarization, it can obtain a domain orientation distribution function (ODF) from in-plane rotation measurements under fixed light polarization [211-213]. In addition, the use of confocal techniques allows obtaining signal from the depth of the material, which PFM cannot reach. Building up an ODF by Raman measurements in polycrystalline KNN requires obtaining reliable single crystalline data, since the scattering efficiency depends on the Raman tensor parameters, which govern the selection rules at the unit cell scale [214]. Not much Raman spectroscopy

data is available for the KNN system and more specifically for KNN single crystals. Published data on undoped KNN polycrystalline materials assigned the Raman modes in a general way [75] or taking it as tetragonal [131]. For doped KNN ceramics, the assignment was done with tetragonal [215] or orthorhombic / tetragonal [210] phases, but never taking into account the possibility of a monoclinic symmetry.

In this study, we aim to shed some light on KNN structure by combining XRD and Raman measurements. In particular, we performed a precise Raman mode assignment according to the group theory and to the angular dependence of Raman mode intensity, confirming that the structure is monoclinic. The dependency of Raman modes (A′, A″ and mixed A′+A″) on crystal rotation was measured and theoretical predictions were compared with the experimentally observed phonon intensity changes, thus allowing the precise retrieval of Raman tensor coefficients for all investigated modes, which is mandatory for future ODF determination.

4.2.2.3 Experimental procedure

In this study, the KNN single crystals previously prepared by the self-flux method were used as explained in the previous sections and Chapter 3. Raman spectroscopy experiments were performed with a Raman microprobe (LabRAM HR 800, Horiba Jobin Yvon, Villeneuve d'Ascq, France) with single monochromator and edge filter (filter cut-off at 100 cm^{-1}). The 514.55 nm laser excitation was employed in the back-scattered configuration with a lateral spatial resolution of 1 µm (Long-working distance 100x objective lens, NA = 0.8, Olympus, Tokyo, Japan). This spot size enabled us focusing within a single domain of the KNN crystal, as confirmed by PFM analyses explained in the previous sections. The domain size varies in fact between 6.5 µm and 12 µm, and the average domain width is 2.6 µm. Spectra were collected in the following polarized configurations (in Porto notation [216]: $x(yy)\bar{x}$, $x(yz)\bar{x}$, $z(xx)\bar{z}$ and $z(xy)\bar{z}$, where x = [100], y = [010] and z = [001] with respect to the principal axes of the perovskite unit cell. Rotation experiments were performed either on (001) or (100) planes of the KNN crystals with the aid of a rotating microscope table eucentric with the optical axis of the microscope (rotation angles defined in terms of the Euler angles,

Figure 4-28a and b. Spectral fitting was performed with commercially available software (LABSPEC 4.02, Horiba Jobin Yvon) using Gaussian / Lorentzian functions.

4.2.2.4 Results and discussion

The intensity of a Raman spectrum measured in a micro-probe configuration when the incident laser is focused on a point depends from various factors involving both the material and the optical system. Each point in the illuminated volume contributes to the overall scattering with a spatial distribution of Lorentzian form [217, 218] that mainly depends on the efficiency of the optical system. Additionally, in absorbing materials such as KNN the effect of the absorption and refraction characteristics have to be taken into account [219]. The intensity of a Raman spectrum in dependence of depth (*i.e.* ignoring variations on the xy plane) when focusing on a point z_0 can be expressed as:

$$I(\Delta z) = \int_0^{\infty} e^{-2n\alpha z} \frac{p^2}{p^2 + \left[\frac{z}{n} - \Delta z\right]^2} dz \qquad \textit{Equation 4-5}$$

where $\Delta z = (z - z_0)$ is the focus depth, n is the refractive index of KNN, α the (effective) absorption coefficient, and p the probe response parameter. The absorption coefficient could be influenced by refraction effects, domains walls and defects within the material and is thus taken as an effective value; p is a parameter that generally depends only on the experimental setting of the Raman microscope and is defined according to laser wavelength, objective magnification and numerical aperture, and dimensions of the confocal hole.

In KNN, in order to determine the depth from which the intensity signal comes from when the laser is focused on the surface, the values of α and p have to be determined. This is done by translating (defocusing) the focal plane of the laser through the specimen surface (*i.e.* changing z_0 from negative to positive), and fitting the obtained intensity profile with Equation 4-5, taking α and p as variables. The result of this procedure for the present KNN single crystal is shown in Figure 4-27a for non-confocal

conditions; here the refractive index was taken as n = 2.21 (the value for $KNbO_3$ at 514.5 nm wavelength [220], and values of α = 0.004 µm^{-1} and p = 2.16 µm were obtained by fitting. The value of p is consistent with that obtained on opaque Si single crystals with the same optical configuration.

The depth of signal intensity, z_{p,z_0}, can be calculated from the percentage of the total intensity that is observed at a given focal point:

$$I_{obs} / I_{tot}(\%) = \frac{\int_0^{z_{p,z_0}} e^{-2n\alpha z} \frac{p^2}{p^2 + \left[\frac{z}{n} - \Delta z\right]^2} dz}{\int_0^{\infty} e^{-2n\alpha z} \frac{p^2}{p^2 + \left[\frac{z}{n} - \Delta z\right]^2} dz}$$

Equation 4-6

The calculation of the intensity profiles for three focal positions (z_0 = -10 µm, 0 µm, 10 µm; negative values indicate focusing above the material's surface) is shown in Figure 4-27b. As could clearly be seen, when the laser is focused on the material surface (z_0 = 0 µm), most of the intensity signal comes from within 10 µm depth, thus confirming that the volume probed is comprised in a single domain of the KNN crystal. In particular, $z_{50\%,0}$ = 1.96 µm; $z_{75\%,0}$ = 4.35 µm; $z_{90\%,0}$ = 9.39 µm; $z_{95\%,0}$ = 15.31 µm.

If lattice disorder is not taken into account, group theory predicts 33 Raman-active modes for the monoclinic *Pm* phase ($\Gamma_{Raman,Pm} = 22A' + 11A''$), whereas for the orthorhombic *Amm2* phase, 24 Raman-active modes are predicted ($\Gamma_{Raman,Amm2} = 8A_1 + A_2 + 7B_1 + 8B_2$) [221]. All of these modes except the A_2 in the *Amm2* symmetry are also IR active and thus are split into their longitudinal (LO) and transverse (TO) optical components. Many of the modes could not be visible due to the relaxation of selection rules caused by the disorder on the A-site; hence, the assignment of Raman spectra to either the monoclinic or the orthorhombic symmetry has to be done considering the angular dependence of the intensity of the observed modes.

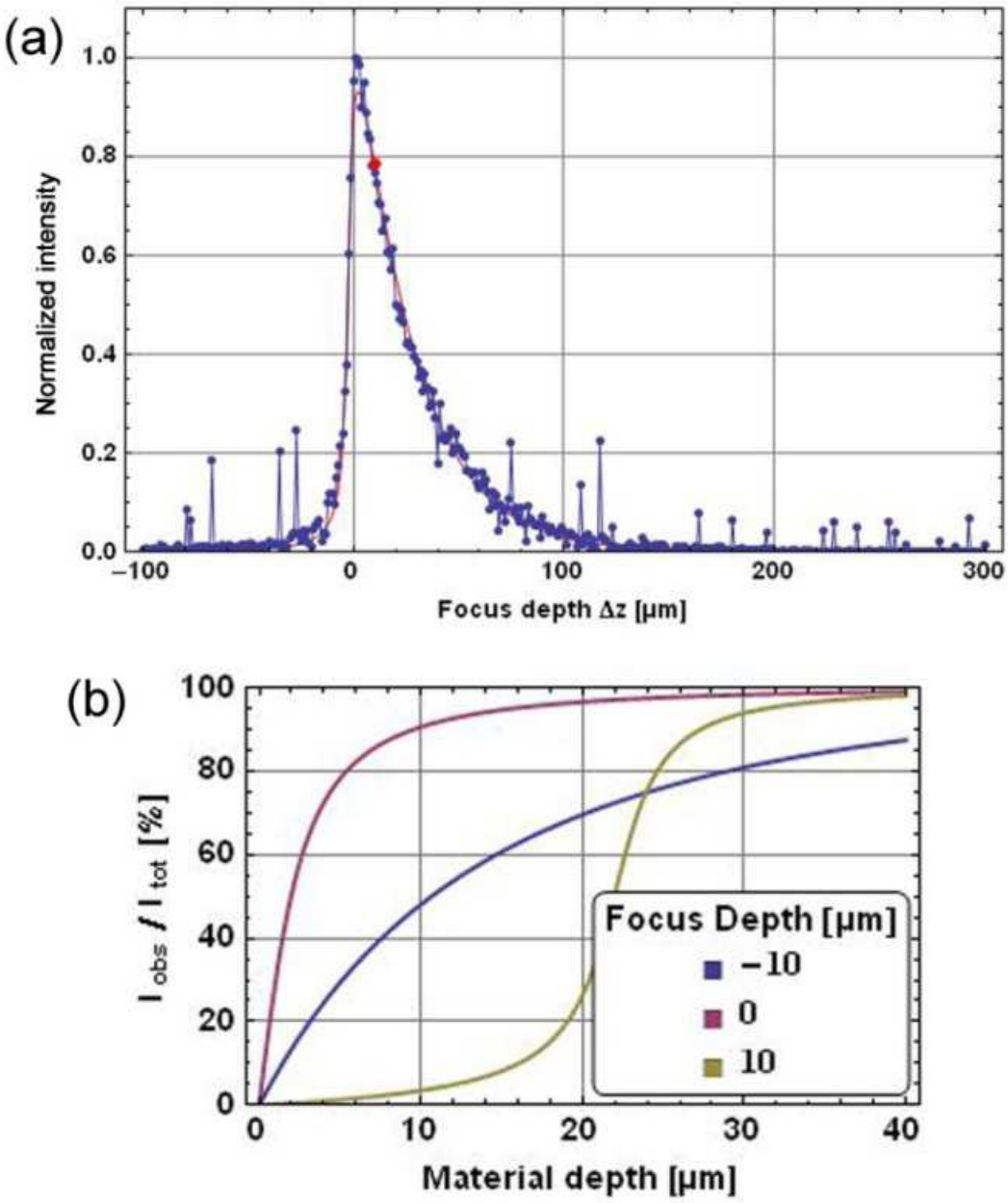

Figure 4-27. (a) Intensity profile obtained in the KNN single crystal by translating the focal plane from above the material's surface to in-depth of the material. The solid curve represents fitting with Eq. (4). (b) Calculated intensity profiles in dependence of material depth for three focal positions: z0 = -10 µm, 0 µm, 10 µm; most of the contributed intensity signal is contained into the first 10 µm below the surface when z0 = 0 µm.

The scattering intensity of a Raman mode in dependence of crystal structure and the adopted incident/scattered light polarization settings is given by the following equation [214]:

$$I_k \propto \left| e_i \Re_k e_s \right|^2 \qquad \textit{Equation 4-7}$$

where e_i and e_s are the polarization vectors of incident and scattered light, respectively, whereas $\Re_k$ is the Raman scattering tensor of the k-th mode. For the monoclinic *Pm* structure, these are given by:

$$\Re_{A'} = \begin{pmatrix} a & 0 & d \\ 0 & b & 0 \\ d & 0 & c \end{pmatrix}, \quad \Re_{A''} = \begin{pmatrix} 0 & e & 0 \\ e & 0 & f \\ 0 & f & 0 \end{pmatrix} \qquad \textit{Equation 4-8}$$

and, in the orthorhombic *Amm2* structure, by:

$$\Re_{A_1} = \begin{pmatrix} a & 0 & 0 \\ 0 & b & 0 \\ 0 & 0 & c \end{pmatrix}, \quad \Re_{A_2} = \begin{pmatrix} 0 & d & 0 \\ d & 0 & 0 \\ 0 & 0 & 0 \end{pmatrix}, \quad \Re_{B_1} = \begin{pmatrix} 0 & 0 & e \\ 0 & 0 & 0 \\ e & 0 & 0 \end{pmatrix}, \quad \Re_{B_2} = \begin{pmatrix} 0 & 0 & 0 \\ 0 & 0 & f \\ 0 & f & 0 \end{pmatrix}$$

Equation 4-9

The proportionality constant in Equation 4-7 depends on the instrumentation; hence, it is convenient to normalize the Raman tensor parameters in Equation 4-8 and Equation 4-9. From a closer look to the Raman tensors in these equations, it can be noticed that in the case of a monoclinic phase, A′ modes would be present in both *(yy)* and *(xx)* configurations, whereas A″ modes in both *(yz)* and *(xy)* configurations. On the other hand, in an orthorhombic phase A_1 modes would be present in both *(yy)* and *(xx)* configurations, however in the *(yz)* and *(xy)* ones only B_1 and A_2 modes could be Raman-active, respectively. Figure 4-28c and d report the Raman spectra of KNN single crystal collected in the $x(yz)\bar{x}$, $x(yy)\bar{x}$, $z(xy)\bar{z}$, and $z(xx)\bar{z}$ configuration [$x(yz)\bar{x}$ and $x(yy)\bar{x}$ on the (100) plane, $z(xy)\bar{z}$ and $z(xx)\bar{z}$ on the (001) plane].

Figure 4-28 displays the PFM image and Figure 4-29 presents angular variation of Raman spectra in all configurations (*i.e.* upon in-plane rotation while maintaining fixed the polarization settings). PFM image as explained in the previous section, recorded on the (001) plane of the KNN single crystal and has an average domain width of 2.6 µm. The green spot in the figure shows the dimensions of the Raman lateral resolution (~1 µm) which helped to assume that the Raman spot was contained within one domain. As can clearly be seen (Figure 4-28c-d and Figure 4-29), the number of observed Raman modes is lower than predicted by group theory for both structures, except for the *(xy)* configuration, for which in the case of an orthorhombic structure only the A_2 mode should be visible. The fact that a higher number of modes could be observed here is a clear hint that the symmetry is lower than *Amm2*. We have modelled the angular dependence (Figure 4-30) of the intensity for each mode observed in the spectra for all polarization configurations considering the Raman tensors for both the *Pm* and the *Amm2* phases, and the *Pm* case gave always the best fit. The intensity dependence was modelled using an applet programmed in the Mathematica 9 (Wolfram Research Inc., Champaign, IL) software environment, which allowed visualizing the sinusoidal variation of intensity upon changing the Raman tensor parameters (using Equation 4-7 to and expressing Raman tensors in terms of Euler angles). For the monoclinic structure, generally A′ modes possess 180° periodicity for parallel polarized configurations and 90° periodicity for the crossed ones. A″ modes possess in both cases 90° periodicity, whereas A′ and A″ mode mixing would produce the same periodicity as of A′, but with a phase shift. Both pure and mixed modes were tested in our model, and it was determined that in most of the cases a mixture of A′ and A″ modes was the best combination to represent our experimental data. Mode mixing in the monoclinic structure commonly occurs in perovskites, such is the case of morphotropic PZT [222-224]. The assignment resulting from this fitting procedure is the one reported in correspondence of the Raman modes in Figure 4-28c, d and summarized in Table 4-7 along with the results from previous authors.

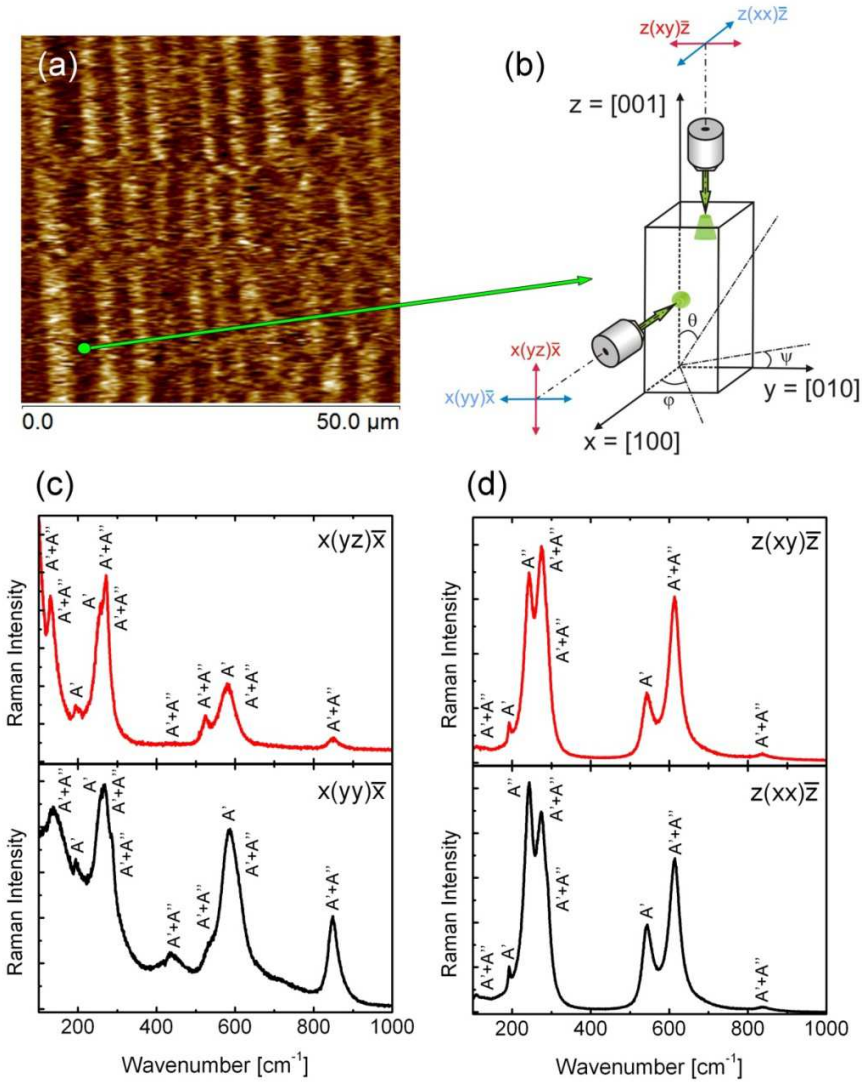

Figure 4-28. (a) PFM image recorded on the (001) plane of the KNN single crystal. The green spot has the dimensions of the Raman lateral resolution (~1 µm); the Raman spot is contained within one single domain (average domain width: 2.6 µm). (b) Schematic of the polarization settings used in our Raman experiments. Light was propagated along either the [001] or the [100] directions of the monoclinic KNN crystal. Sample rotation was performed either on the [001] or the [100] axes, and the position of the crystal with respect to the laser polarization vectors were expressed in terms of the Euler angles. (c), (d) Raman spectra of monoclinic KNN obtained on the (100) and (001) plane, respectively, for both the cross and parallel polarized configuration. The assignment of Raman modes is reported on the figure.

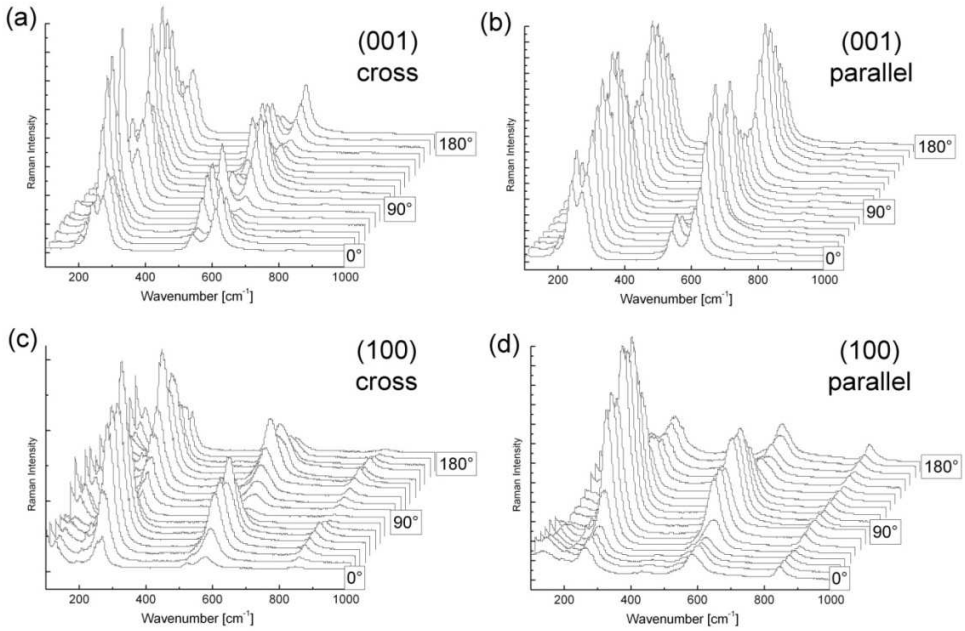

Figure 4-29. Angular dependence of the Raman spectra of monoclinic KNN on the (001) plane [(a) [33], (b) cross and parallel configuration, respectively] and on the (100) plane [(c), (d) cross and parallel configuration, respectively]. The angular dependence of the intensity was observed in the spectra for all polarization configurations.

Figure 4-30 reports the angular dependence of selected Raman modes of the investigated KNN single crystals in all investigated polarization configurations (blue = parallel; red = cross). Some of the modes (Figure 4-30a, b the mode at 105 cm^{-1} and Figure 4-30c, d the mode at 272 cm^{-1}) were visible on both the (001) and (100) planes, whereas other ones only on one plane [Figure 4-30e, mode at 243 cm^{-1} (001); Figure 4-30f, mode at 256 cm^{-1} (100); Figure 4-30g, mode at 545 cm^{-1} (001) and Figure 4-30h, mode at 576 cm^{-1} (100)]. The solid curves displayed for all modes result from the best fit procedure obtained from Equation 4-7 – Equation 4-8, assuming the crystal being a single monoclinic domain within the investigated laser volume. This is motivated by the fact that the lateral size of the laser spot (~1 µm) is consistently smaller than the average domain width, thus confirming that we were able to allocate the laser spot within one domain. In addition, from the PFM response we obtained we could conclude that the domain walls are perpendicular to the surface. Considering that 90% of the observed intensity comes from about 10 µm in-depth of the KNN crystal (as determined by

defocusing experiments, the observed Raman signal should originate from only one single ferroelectric domain.

From Figure 4-30, however, it is evident that only modes that were observed either on the (001) or the (100) plane (Figure 4-30e-h) were very well represented by our model. In cases in which the mode was present on both (001) and (100) planes (Figure 4-30a-d) a significant leakage was present in either the cross or the parallel signal. It is well-known that even in cases in which the Raman spot is allocated on a single domain, the use of high-NA objectives could produce depolarization effects [225]. Given our use of a NA = 0.8 objective, we thus interpret the observed leakage as due to the effect of neighbouring domains contributing to the Raman signal. Interestingly, this happens only when the considered Raman mode appeared on both (001) and (100) planes. This depends on the relative value of the Raman tensor parameters for those modes; we have calculated the Raman response for pure A′ and A″ or mixed modes with our Mathematica applet and concluded that modes appearing on either (001) or (100) plane have only partially-filled Raman tensors. This makes them less sensitive to contributions from diversely-oriented neighbouring domain states, and is thus the most reliable modes. The values of the Raman tensor parameters we report for these modes can be freely used as single-domain input parameters for quantitative analyses of domain distributions in KNN single and polycrystalline materials.

Table 4-7. Raman mode assignment for monoclinic KNN. For each mode the selection rules for (001) and (100) planes and the mode symmetry are reported. Normalized Raman tensor parameters resulting from the best fit procedure are also shown. The position of modes observed by other authors in KNN and similar systems (NN = $NaNbO_3$) is reported.

Mode [cm^{-1}]	**Plane**		**Type**	**Raman tensor parameters**				**KNN** [cm^{-1}] [39]	**NN** [cm^{-1}] [40]	**PZT** [cm^{-1}] [36, 38]
	(001)	(100)		a	b	c	e			
105	X	X	A′+A″	-	-	-	-	151	153	150
130	X	X	A′+A″	-	-	-	-	177	175	-
192	X	X	A′	-	-	-	-	200	201	200-205
243	X		A′	-	0.93	-1	-	224	218	220-230
256		X	A′+A″	-0.59	-	1	-0.12	248	247	252-260
272	X	X	A′+A″	-	-	-	-	280	276	280-295
288	X	X	A′+A″	-	-	-	-	-	-	-
436		X	A′+A″	1	-	-0.49	0.14	431	435	-
525		X	A′+A″	-	-	-	-	-	-	510
545	X		A′	-	0.94	-1	-	-	-	-
576		X	A′	0.67	-	-1	-	572	557	-
613	X	X	A′+A″	-	-	-	-	611	602	600
840	X	X	A′+A″	-	-	-	-	872	867	748

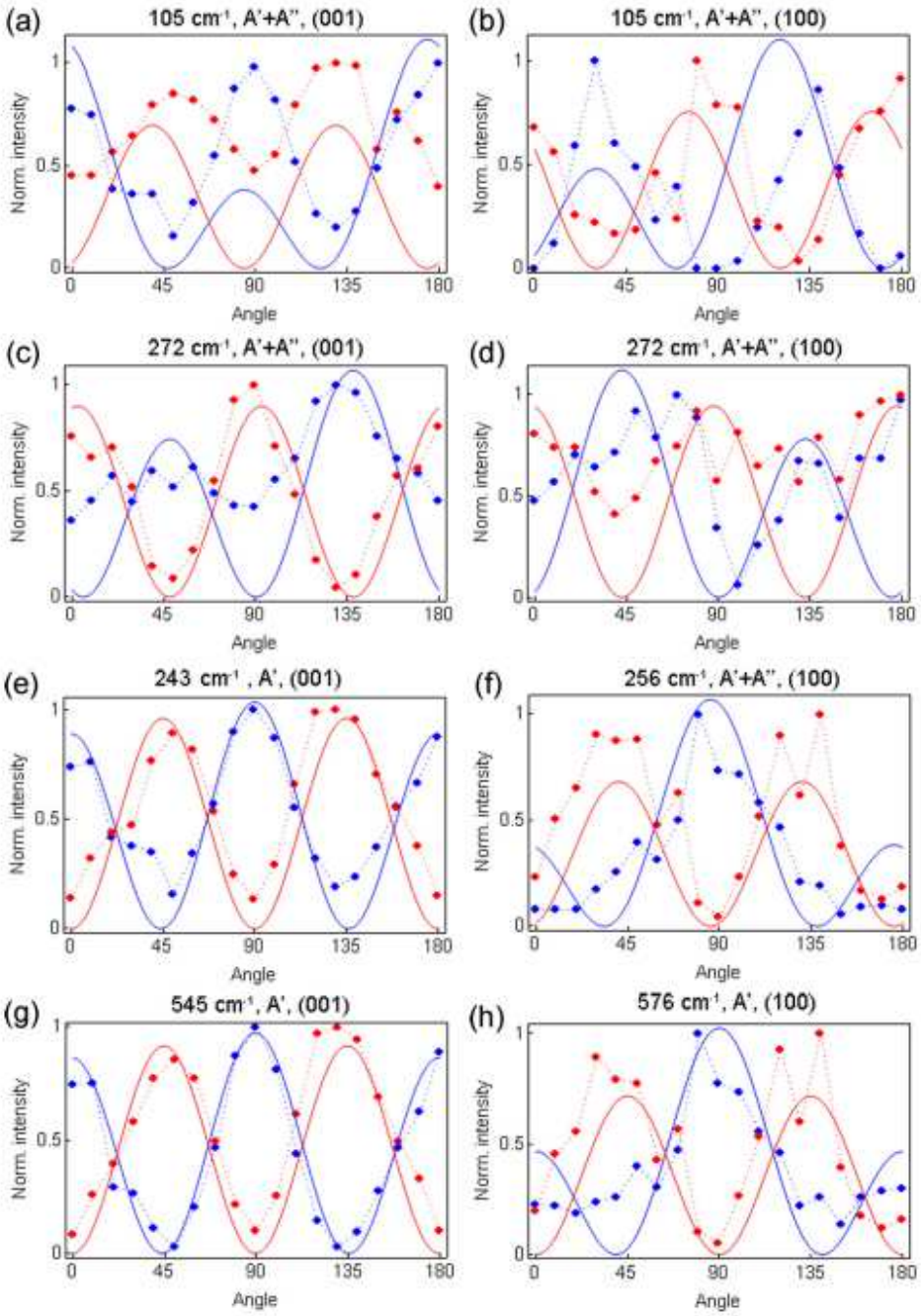

Figure 4-30. Angular intensity dependence of selected Raman modes of the monoclinic KNN crystal. The position of the mode, its symmetry and the plane on which it was retrieved are indicated on the graphs. The solid curves represent the best-fitting procedure with Equations (transformed in terms of the Euler angles), which allowed obtaining the Raman tensor parameters for the modes in (e) - (h). Blue = parallel polarized; red = cross polarized. A close match between experimental and modelled data was observed.

4.2.2.5 Conclusions

In summary, polarized Raman analyses were performed on KNN single crystals allocating the laser spot on single domains of sufficient size. By rotating the crystal using a eucentric fixture under fixed polarized light, we were able to perform a precise Raman mode assignment for the monoclinic structure of KNN. In addition, we obtained the Raman tensor parameters for modes appearing either on (001) or (100) plane of the crystal, thus opening the way to quantitative analyses of domain distribution in KNN materials. It is important to have exact knowledge of the structure to design and optimize the properties of KNN based ceramics. Figure 4-31 shows some of the conclusions of this section.

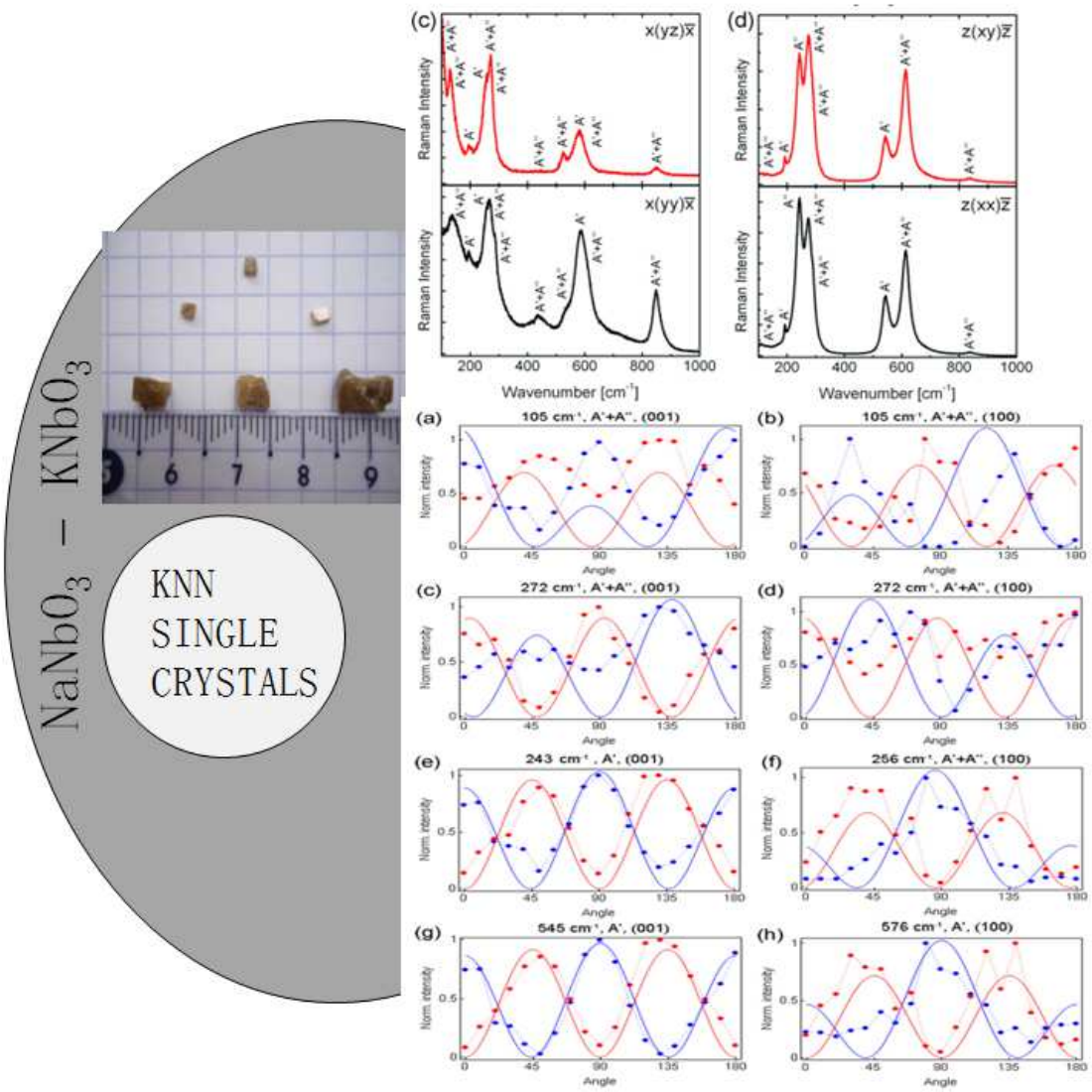

Figure 4-31. Image showing some conclusions of this section. Single crystals were assigned for the monoclinic symmetry and angular intensity dependence followed the monoclinic symmetry very well.

4.2.3 Impedance analysis and conduction mechanisms of lead free KNN single crystals and polycrystalline ceramics: a comparison study

4.2.3.1 Abstract

Impedance spectroscopy (IS) is used to compare defects and charge transport in (001) oriented $K_{0.5}Na_{0.5}NbO_3$ (KNN) single crystals and its polycrystalline counterpart. KNN single crystals show lower conductivity than polycrystalline counterpart from room temperature up to 200 ºC, but above this temperature polycrystalline KNN displays lower conductivity. The low temperature (T < 200 ºC) behaviour reflects the different processing conditions of both ceramics and single crystals, which account for less defects prone to charge transport in the case of single crystals. As temperature increases (T > 200 ºC) single crystals become now more conductive than polycrystalline samples in which grain boundaries act as barriers to charge transport. For even higher temperatures the conductivity difference between both is increased due to the contribution of ionic conduction in single crystals. Indeed the values of activation energy calculated to the high temperature range (T > 300 ºC) were 1.60 and 0.97 eV, confirming the charge

transport due to ionic conduction and ionized oxygen vacancies in single crystals and polycrystalline KNN, respectively. It is suggested that single crystals with low defects content and improved electromechanical properties could be a better choice for room temperature applications, though at high temperatures less conductive ceramics may be the choice, depending on the targeted use.

4.2.3.2 Introduction

The existences of inhomogeneities in polycrystals, such as grain boundaries (and their intrinsic defective nature) and point defects, are one of the main reasons behind this distinctive behavior. In fact, the performance of single-crystals relies on numerous factors including crystal orientation, crystal cut, temperature and phase transformations, among others; on the other hand, polycrystalline behavior is the outcome of the complex arrangement of these effects but damped by the intergranular regions and inhomogeneities. This creates an intricate network of nonlinear local effects which affects the overall material behavior [14].

In one of our recent publications, we have demonstrated by piezoforce response microscopy (PFM) that <001> - oriented potassium sodium niobate (KNN) single crystals reveal a long range ordered domain pattern of parallel 180° domains with zig-zag 90° domains and argued that the absence of such a long range ordered domain pattern in polycrystalline KNN, probably induced by the presence of the grain boundaries, accounts for the improved properties of the single crystals [16]. But the macroscopic electrical properties of ferroelectric materials, such as KNN, are also affected by the charge transport behavior, and closely related to defects and their interaction with the crystallographic structure, domain pattern and grain boundaries, as well [226]. Indeed, understanding charge transport is fundamental to understand and improve the properties of KNN ceramics.

The major defects associated with KNN, which can influence its conductivity, are oxygen vacancies, alkaline vacancies and space charges. Besides, defects may pin the domain walls movement, probably leading to a decrease of its contribution to the piezoelectric activity. Though the comparison between the electromechanical properties of KNN single crystals and ceramics has been reported before [16], the relationship at the

level of charge transport and point defects has not yet been established. Moreover the comparison between the charge transport in KNN single crystals and ceramics will facilitate the design of optimized KNN materials.

Complex impedance spectroscopy (IS) is a very useful technique to i) analyze the electrical response of materials, ii) separate bulk, grain boundary and electrode / ceramic interface contributions from the overall electrical response, iii) identify conduction mechanisms and iv) even to characterize ferroelectric phase transitions [140, 227, 228]. IS allows to map the real and the imaginary part (Z' and Z'') of the impedance of a dielectric material at various temperatures and frequencies. Furthermore, values of the activation energy for the various conduction mechanisms (ionic, electronic, etc) can be calculated, hence permitting the identification of the nature of charge carriers and conduction phenomena [229].

In the present work, a detailed and comparative investigation of the conduction behavior of high temperature self-flux grown KNN single crystals and polycrystalline ceramics was conducted by IS in the frequency and temperature ranges from 100 Hz to 1 MHz and from 30 ºC to 480 ºC, respectively. IS of KNN single crystals have not been reported so far. The investigation of defects and associated activation energies for conduction in single crystals, a grain boundary free material, is here carried out aiming to identify the role of grain boundaries in the charge transport in KNN. The insights gained with this analysis allow designing KNN based materials with optimized performance for selective uses.

4.2.3.3 Experimental procedure

(001)-oriented KNN single crystals and KNN polycrystalline ceramics were prepared as explained in Chapter 3.

For the electrical characterization, the opposite faces of the ceramic disks and single crystals were polished to ensure parallel surfaces and then high-grade silver paint was coated onto them. The electrodes were annealed at 550 °C for 20 min. Impedance spectroscopy (IS) measurements were carried out with a computer controlled precision LCR Meter (HP 4284A) under an applied field of 1 V in the frequency range from 100 Hz to 1 MHz from 30 ºC to 480 ºC. The accuracy of the measurement was better than 1

ºC. IS data analysis was conducted using different formalisms including complex impedance Z^* and complex modulus M^* which allowed to access the electrical contributions of the bulk and grain boundaries and their associated conduction mechanisms.

4.2.3.4 Results and discussion

The temperature dependence of ac conductivity of KNN single crystal and polycrystalline at frequency of 100 kHz is depicted in Figure 4-32. The intrinsic conductivity (σ_ω) response is explained in Equation 4-1. In both cases, ac conductivity follows a distinct pattern depending on the temperature range and, if below or above the transition temperature (~180 ºC): at low temperature (30 ºC < T < 200 ºC) a trend for a slight decrease of the conductivity with temperature increase is observed for KNN polycrystalline, whereas, for KNN single crystal, it shows almost a straight line. It is also worth mentioning in this range single crystal showed lower conductivity (higher resistivity) as compared to polycrystalline counterpart, while for T > 300 ºC the conductivity increases (now single crystals are more conductive) as the temperature increases in both cases of KNN single crystal and polycrystalline.

Three different regimes (I, II and III) can be distinguished in both curves: region I from (30 – 180 ºC; 205 – 300 ºC) for single crystal and (30 – 180 ºC ; 220 – 300 ºC) for polycrystalline; region II from 180 ºC to 205 ºC for single crystal and 180 ºC to 220 ºC for polycrystalline and region III from 300 ºC to 400 ºC for KNN single crystal and polycrystalline, corresponding to three different slopes.

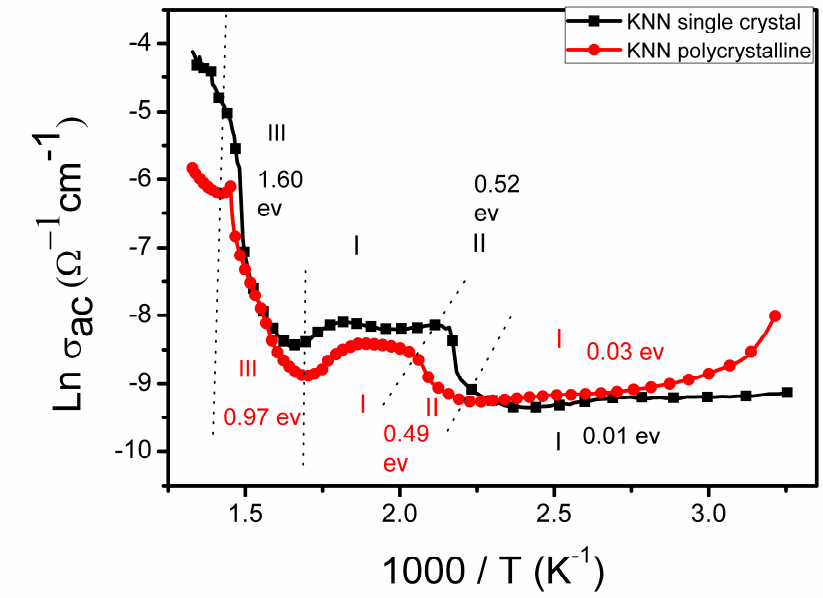

Figure 4-32. Temperature dependence of ac conductivity of KNN single crystal and polycrystalline at 100 kHz. Three different regions with different conduction mechanisms were identified and the activation energy for each region is indicated.

In order to clarify the conduction mechanisms responsible for the observed behaviour, the values of the activation energy for conduction (σ_{ac}) was calculated assuming Arrhenius behaviour as explained in the previous sections (Equation 4-2).

The activation energies for conduction obtained for KNN polycrystalline in region I was calculated to be 0.03 eV, which corresponds to hole transport in p-type ferroelectric ceramics [184, 187]. For KNN single crystals, almost a straight line was observed with activation energy of ~ 0.1 eV and it is also noticeable that KNN single crystals show lower conductivity (higher resistivity) as compared to polycrystalline counterparts at low temperatures nearly upto ~ 180 ºC. In region II, a ferroelectric phase transition occurs, responding for the observed discontinuities in the curves. In this temperature range the conductivity mechanism changes and the calculated activation energy values of 0.52 eV and 0.49 eV for KNN single crystals and polycrystalline respectively, are similar between them and to the values reported for other perovskites near the phase transition as for example for $Pb(Fe_{1/2}Nb_{1/2})O_3$ ceramics [184]. In the temperature region from 300 °C to 400 °C (region III), the calculated activation energies are 1.60 and 0.97 eV for KNN single crystals and polycrystalline respectively. In ferroelectric perovskites, activation

energies for conduction in the range of 0.4 - 1.2 eV have been linked to charge transport by oxygen defects, namely motion of ionized oxygen vacancies [184, 188], which are considered some of the most mobile ionic species in perovskites [188, 189]. Regarding the electric conduction in single crystals, it is here suggested that alkaline ions may be the charge carriers accounting for the ionic conduction taking place in this high temperature regime with activation energy values of 1.60 eV, which is higher than 1.2 eV and has been reported for La doped $PbTiO_3$ (1.17 – 1.48 eV) [230] and PZN-PT crystals (~1.3 eV) [226, 231].

The ac conductivity analysis allowed us to identify the possible conducting species / mechanisms, and their dependence on the temperature, but did not give any information about the resistance and capacitance offered by the ceramic microstructure, i.e. bulk (grain interior) and grain boundaries. This insight of the material is very important to understand the role of electrical microstructure on the ceramic electrical properties. Besides affecting the electrical response defects are also known to affects grain growth and, consequently, the ceramic microstructure and the ferroelectric domain patterns, which are responsible for the ferroelectric and piezoelectric response of these materials, as KNN. Therefore we used impedance spectroscopy (IS) to further exploit the responsible phenomena for the resistivity increase in KNN single crystal as compared to the polycrystalline counterpart.

Figure 4-33a and b depicts the frequency dependence of the imaginary part of both the complex impedance Z^* and the complex modulus M^*, i.e. Z'' and M'', for KNN single crystal at high temperatures (320 ºC - 480 ºC). The maxima of Z'' and M'' occurred at the same frequency, which indicates that an electrical circuit comprising of one resistance (*R*) and one capacitance (*C*) connected in parallel is well suited to describe these impedance and modulus spectra of KNN single crystals. *R* and *C* in the electric circuit represent the electrical contribution of the bulk of the single crystal (bulk effect). A similar behaviour has been reported for lead based single crystals of $0.91Pb(Zn_{1/3}Nb_{2/3})O_3$-$0.09PbTiO_3$ [231], PZN-4.5PT [226], $Pb(Zn_{1/3}Nb_{2/3})_{0.91}Ti_{0.09}O_3$ [232] and $LiTaO_3$ [228]. On the other hand, the polycrystalline KNN counterpart display, in the same temperature range, Z'' and M'' maxima at different frequencies, thus indicating that in this case, two *RC* (resistance in parallel to a capacitance) modules connected

in series are required to describe properly the impedance data of polycrystalline KNN ceramics. Accordingly, an equivalent electric circuit comprising a series of two *RC* circuits (*R* parallel to *C*) was used to model the impedance experimental data and assisted by Zview software (Ver. 3.2c, Scribner Associates, Inc). The two *RC* modules represent two different electrical contributions, which were assigned to different regions of the polycrystalline material i.e. the bulk (grain interior with resistance - R_b and capacitance - C_b) and the grain boundary (with resistance - R_{gb} and capacitance - C_{gb}) as detailed in previous Sections (4.1.2) [233]. The values of the resistance (*R*) and capacitance (*C*) extracted from the electric model, are presented in Table 4-8 and Table 4-4 for single crystal and polycrystalline KNN respectively. Resistance for both KNN SC and polycrystals decreased with increase in the temperature.

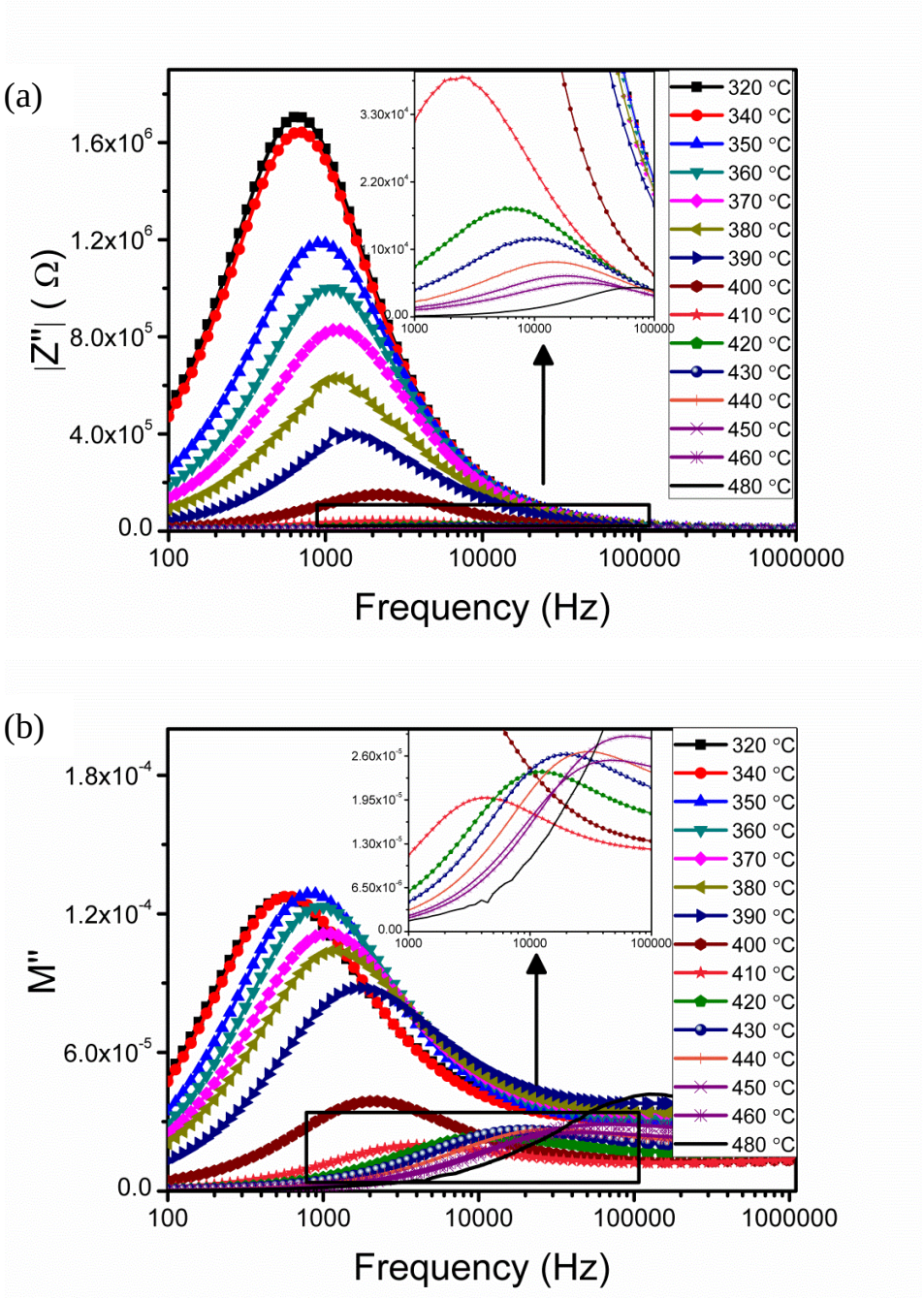

Figure 4-33. Variation of the imaginary part of impedance (a) (Z'') versus frequency and (b) (M'') versus frequency at various temperatures for KNN SC. The variation in higher temperature region (> 400 °C) in the frequency range 1 kHz to 100 kHz is shown in inset. The occurrence of peak maxima of Z´´ and M´´ at the same frequency indicated the presence of one conduction phenomena i.e. bulk contribution.

Table 4-8. Resistance and capacitance extracted from the electric model at various temperatures for KNN single crystals. A decrease in the resistance is observed with the increase in the temperature.

T	**Resistance**	**Capacitance**
°C	Ω	F
35	5.15×10^{7}	3.10×10^{-11}
100	4.33×10^{7}	6.28×10^{-11}
200	6.76×10^{7}	1.08×10^{-10}
320	3.41×10^{6}	7.00×10^{-10}
340	3.29×10^{6}	7.10×10^{-10}
350	2.37×10^{6}	7.17×10^{-10}
360	1.99×10^{6}	7.41×10^{-10}
370	1.66×10^{6}	7.96×10^{-10}
380	1.26×10^{6}	8.33×10^{-10}
390	8.64×10^{5}	9.57×10^{-10}
400	3.01×10^{5}	2.32×10^{-10}
410	8.83×10^{4}	4.07×10^{-9}
420	4.06×10^{4}	3.53×10^{-9}
430	2.97×10^{4}	3.24×10^{-9}
440	2.10×10^{4}	3.25×10^{-9}
450	1.54×10^{4}	3.42×10^{-9}
460	1.32×10^{4}	3.08×10^{-9}
480	9.55×10^{3}	2.50×10^{-9}

For any *RC* electrical module the product of *R* and *C* defines a time constant (τ), is a signature of the electrical contribution of that specific region i.e. grain interior (bulk) and grain boundary. So, it is important to understand and compare the time constant to have a better understanding of the the materials behaviour. Time constant (τ) is a product of *R* and *C* can be furthermore expressed as $\tau = \varepsilon_0 \varepsilon_r \rho$, where, ε_0, ε_r and ρ stand for the vacuum dielectric permittivity, relative dielectric permittivity and the electric resistivity of the material region modelled by RC, respectively. Therefore τ is unaffected by the geometrical details of the material region under consideration. For each *RC* module of the referred circuit models a time constant can be calculated, i.e. for the bulk of the single crystal and of the polycrystalline ceramic, and for the grain boundary of the polycrystalline ceramic as presented in Figure 4-34 It was observed that the time constant for the single crystal at low temperature is close to the time constant of the grain boundary whereas at high temperature (320 ºC), it matches more closely to the time constant of the bulk of the polycrystalline ceramic**.**

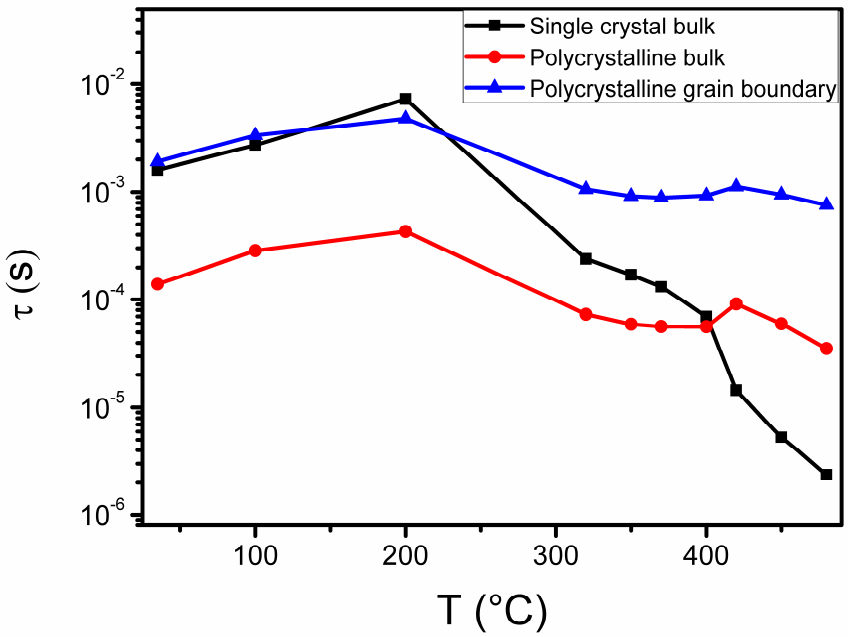

Figure 4-34. Time constant (τ, where τ=RC) of bulk of KNN single crystal and of bulk and grain boundary of polycrystalline KNN. At low temperature, the time constant of single crystal matches more closely to the grain boundary of polycrystalline KNN whereas at high temperature (~ 300 ºC) it matches more closely to the bulk of polycrystalline KNN.

This can be explained both on a mathematical and physical basis. Mathematically, time constant is dependent on resistance and capacitance ($\tau=RC$). So, in order to inspect the variation of the time constant, we draw the resistance and capacitance of bulk of KNN single crystal polycrystalline ceramic versus temperature (Figure 4-35a). It is observed that the resistance of the bulk of KNN single crystals is higher than that of the bulk of polycrystalline KNN ceramics at low temperature (Figure 4-35a), whereas at high temperature this relationship becomes inverted; concerning the capacitance values the capacitance of bulk KNN ceramics is always higher than the capacitance of SC bulk, maintaining the same difference in the whole temperature range (Figure 4-35b). So, it can be deduced that with the variation of temperature, time constant of the single crystal is predominantly affected by the variation of resistance.

Physically, this can be explained on the basis of a different defect nature of single crystals and ceramics. Besides the absence of grain boundaries, single crystals were prepared by high temperature self flux method in a covered sealed platinum crucible, which guarantees a low defect concentration, namely of vacancies of the constituent elements and compensating electronic holes; which was written as Equation 2-9 in Chapter 2. Thus, a higher resistivity at room temperature as compared to the polycrystalline counterpart should be expected, as it is indeed observed (Figure 4-32). As already mentioned, defects normally pin the domain walls and thus result in poor ferroelectric and electromechanical properties. So, the low amount of defects, higher resistivity and favourable orientation for polarization together with the absence of grain boundaries may be the reasons explaining the better ferroelectric and electromechanical properties of KNN single crystals produced in this work and by other researchers [16, 112].

In summary, it is suggested that for room temperature (or close to) applications single crystals with low defects content offer privileged conditions for maximizing ferroelectric and electromechanical properties and hence should be preferred for their related applications. On the other hand, for a high temperature regime, polycrystalline materials due to their lower conductivity seem to be a safer option for electromechanical applications.

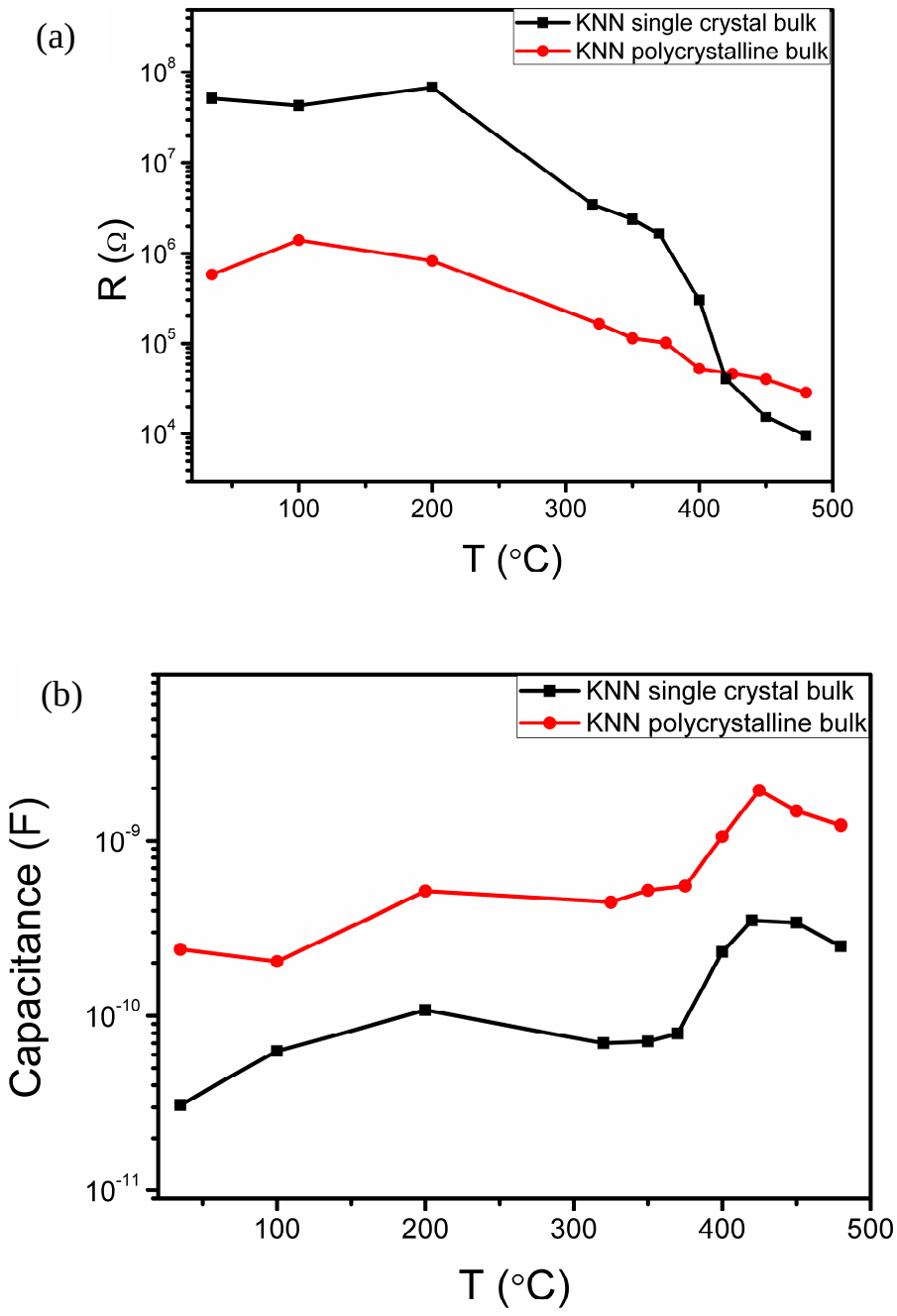

Figure 4-35. Variation of (a) resistance and (b) capacitance versus temperature of KNN single crystals and polycrystalline counterpart. With the rise in temperature, the resistance value of KNN single crystal (SC) decays significantly as compared to the polycrystalline counterpart thus a impacting significantly the SC time constant.

4.2.3.5 Conclusions

Electrical behavior of self flux grown $K_{0.5}Na_{0.5}NbO_3$ (KNN), (001) oriented single crystal and polycrystalline counterpart is assessed in this work. KNN The room temperature resistance of KNN single crystals (5.17×10^7 Ω) is much higher than that of the polycrystalline counterpart (5.83×10^5 Ω), but above this temperature KNN polycrystals exhibit higher resistance. Related with the processing conditions, it is proposed that at low temperatures the less defective nature of single crystals with defects less predisposed to charge transport accounts for their high resistance, while at temperatures above 200 ºC the grain boundaries of KNN polycrystals acting as barriers to charge transport respond for their high resistance. Indeed the activation energy for conduction in KNN single crystals and polycrystals at high temperature (> 300 ºC), calculated to be 1.60 eV and 0.97 eV respectively, and assigned to ionic conduction and oxygen vacancies, proves the different charge transport nature in KNN single and poly-crystals. It is suggested that for applications at room temperature (or close to) single crystals with low defects content offer privileged conditions for maximizing ferroelectric and electromechanical properties and hence should be preferred for their related applications. On the other hand, for a high temperature regime, polycrystalline materials due to their lower conductivity might be a better option for electromechanical applications. Figure 4-36 shows some of the conclusions of this section.

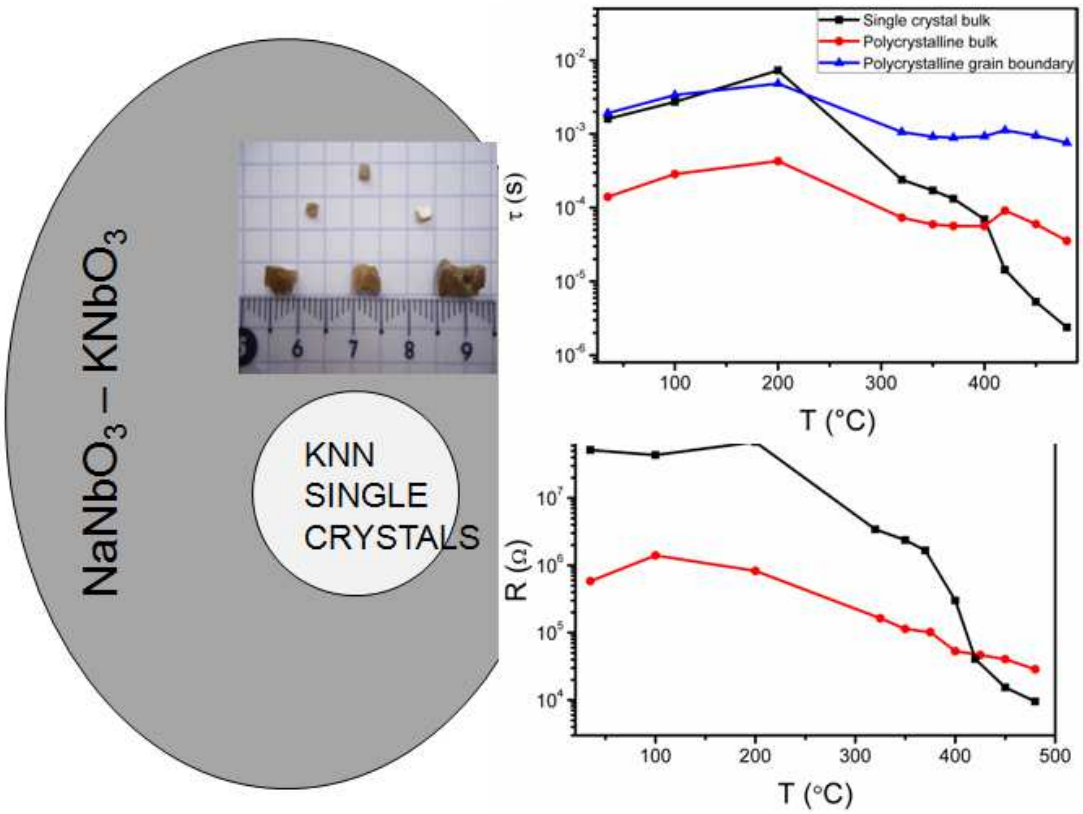

Figure 4-36. Image showing some conclusions of this section. Single crystals showed higher resistance as compared the bulk of the polycrystalline counterpart. The time constant of single crystal at low temperature were matches more closely to the grain boundary of polycrystalline KNN whereas at high temperature (~ 300 ºC) it matches more closely to the bulk of polycrystalline KNN.

4.3 Textured KNN based ceramics

4.3.1 Synthesis and characterization of textured ceramics

4.3.1.1 Abstract

Aiming at engineering the properties of KNN polycrystals towards the performance of single crystals we studied the synthesis and properties of (001) – oriented $(K_{0.5}Na_{0.5})_{0.98}Li_{0.02}NbO_3$ (KNNL) ceramics prepared by templated grain growth (TGG) using KNN single crystals as templates. The choice of KNN single crystals templates was related with the better properties and to design the microstructure for better properties. X-ray diffraction analysis revealed for the textured ceramics a monoclinic structure at room temperature and a Lotgering factor (*f*) of 40%. These textured ceramics exhibit a long range ordered domain pattern consisting of 90º and 180º domains, similar to the one observed in the single crystals. Enhanced dielectric (13017 at T_C), ferroelectric (P_r = 21.4 μC/cm^2) and piezoelectric (d_{33} = 280 pC/N) properties are observed for textured

KNNL ceramics as compared to the randomly oriented ones; this behaviour is suggested to be due to the long range ordered domain pattern observed in the textured ceramics. The obtained results are also compared with the data previously reported on texture KNN based ceramics and better properties were found due to ordered repeated domain pattern. This study provides an approach towards properties improvement of KNN-based piezoelectric ceramics.

4.3.1.2 Introduction

As mentioned in Chapter 2 and similarly to PZT, $KNbO_3$ and $NaNbO_3$ form a complete solid solution $K_{1-x}Na_xNbO_3$ (KNN) over the entire range of $0 < x < 1$ and a maximum of its properties was reported for $x = 0.5$ [33]. This is the reason why this composition has been the most studied in the literature and it is also the study object of this thesis. However, this doesn´t rule out the need of more studies to characterize the performance of compositions in the potassium and sodium rich regions of the diagram as observed in Figure 2-11. Although KNN exhibits a key property in terms of applications and an added value over PZT, the high *Tc*, its piezoelectric performance is still inferior to the best one observed for PZT. Currently a practical limitation, as clearly stated all over this thesis, it is an opportunity in terms of development. Within this context, it has been shown that the electromechanical performance of KNN can be improved by a complex doping procedure, for example by combining Li^{1+}, Ta^{5+} and Sb^{5+} and d_{33} values of 416 pC/N were reported, however at the expenses of decreasing T_C (253 ºC) [64]. Indeed the significant improvement of electromechanical properties for Li^{1+}, Ta^{5+}, and / or Sb^{5+} doped KNN was shown to be restricted to room temperature, owing to the fact that these substituents lower the $T \rightarrow M$ phase transition from ~ 210 ºC to near the room temperature [72, 98, 102, 234-237]. Normally, in the design of most actuators, compositions with $T \rightarrow M$ phase transition temperature near room temperature should be avoided as thermal cycling between ferroelectric phases leads to domain instability, depolarization, and in some cases to mechanical failure (cracking) [72]. Furthermore, the use temperature range is also limited to ½ T_C as already mentioned in Chapter 2. Since many applications require piezoelectrics that have stable piezoelectric response over a wide temperature range, it is thus important to develop KNN-based ceramics with optimised

electromechanical performance but that possess simultaneously a high temperature phase transition, as high as possible. In addition, though Li, Ta and Sb stand up among the dopants with higher effectiveness in terms of KNN properties improvement (acting as sintering aid and helping to form a phase boundary near room temperature) In addition to toxicity, which has been a major reason leading the search of lead free materials, the scarcity of elements in nature is emerging now a days as a current / novel / important issue of concern. Indeed some raw materials are under extinction or located in some geopolitical places of limited access which indirectly controls their price, hence there is a current urgent need [238]. Within this scope, Ta^{5+} which is quite expensive, and Sb^{5+} which is toxic are to be avoided. Li^{1+} still remains as a viable option to be further exploited [98, 99, 101, 239-241]. Furthermore, Li was also used as a sintering aid as reported in the literature [84].

The piezoelectric coefficient (d_{33}) depends on the relative permittivity and remnant polarization according to the equation [242, 243]

$$d_{33} = 2Q_{11}\epsilon_0\epsilon_r p_r \qquad \textit{Equation 4-10}$$

where p_r is remnant polarization, ϵ_r is the permittivityvity, Q_{11} is the electrostrictive constant of the paraelectric phase which normally varies between 0.05 and 0.1 m^4C^{-2} for different materials [244] ; the high p_r and ϵ_r, the higher d_{33} will be. Dielectric permittivity and remanent polarization can be increased by designing the microstructure and in turn increase in d_{33}. Besides doping, poling processes, texturing or grain orientation is another way of controlling ceramic microstructure and properties [18, 151]. Templated grain growth (TGG) is a promising route to control the texture / microstructure as it has already been explained in Chapter 2. In the case of KNN based textured ceramics, tape casting or screen printing by using plate like $NaNbO_3$ and $BaTiO_3$ templates, typically in amounts of 5 to 20 % were used [123-127]. The use of single crystals as templates for TGG process has been reported for other materials like $SrBi_2Ta_2O_9$ [245], but, till now, to the best of our knowledge has not been reported in KNN ceramics. The KNN single crystals as templates have been used because from our previous work (Section 4.2), (001) orientation, which is favourable polarization orientation (as explained in Chapter

2) is known. Furthermore, properties of these crystals have already been studied and it's easy to relate the properties with orientation based on previous studies. Later on, crystal of different orientation can be used and its effect on the properties can be studied and compared with the present results.

In the present study, we demonstrate that by using a conventional ceramic processing and by controlling the microstructure, aiming to mimic the polar domain structure of single crystals, the ferroelectric and piezoelectric properties of Li-doped KNN ceramics could be further enhanced, keeping simultaneously the high transition temperature. The remnant polarization can be significantly raised from P_r = 13.1 μC/cm^2 to P_r = 21.4 μC/cm^2 and the d_{33} from 135 to 280 pC/N for T_C = 430 ºC. KNN single crystals previously synthesized by a high temperature self flux method, were used as templates for TGG method. The impact of sintering time on grain orientation and properties is assessed. Electric properties of textured KNN ceramics samples are reported and a relation between ferroelectric domains and properties of randomly oriented and textured ceramics is established.

4.3.1.3 Experimental procedure

Li doped KNN, [$(K_{0.5}Na_{0.5})_{0.98}Li_{0.02}NbO_3$, KNNL] bulk and templated ceramics were prepared using KNNL mixed with KNN single crystals as described in Chapter 3. By using different sintering times between 2 h to 24 h, the ceramic texture development was varied and density of the ceramic pellets measured by the Archimedes method.

As in the previous studies, phase compositions were evaluated by X-ray diffraction (XRD, Rigaku, D/Max-B, Cu-K_α radiation) at room temperature in the 2θ range of 20° to 60°, with a step length of 0.02°. The texture fraction along (001) planes was estimated from the XRD patterns using the Lotgering approach. The Lotgering factor (*f*) is defined as the fraction of the area textured with the crystallographic plane of interest using

$$f = \frac{P_{001} - P_0}{1 - P_0} \qquad \textit{Equation 4-11}$$

where, $P_{001} = \sum I_{001} / \sum I_{hkl}$ and $P_0 = \sum I^0_{001} / \sum I^0_{hkl}$, with I_{hkl} and I^0_{hkl} being the intensities of (hkl) peaks for the textured and randomly oriented ceramic samples, respectively. Rocking curves and pole figures were used to assess the quality of orientation. Standard metallographic polishing procedure was used to prepare the surface to be observed by scanning electron microscope. Image J was used to calculate the grain size and distribution.

For the electrical characterization, parallel faces of the ceramics, perpendicular (⊥) and parallel (∥) with reference to the pressing direction (schematic shown in Figure 4-37) were polished and covered with, silver paint as electrode. Then, the dielectric constant (ε_r) was measured by a Precision LCR Meter (HP 4284A) in the frequency range from 100 Hz to 1 MHz and in the temperature range from room temperature to 550 ºC. For the determination of the polarization versus electric field hysteresis loops (*P-E*), a ferroelectric tester (Aixact TF analyzer 1000) was used. The ferroelectric domain structure was mapped by piezoresponse force microscopy (PFM) using a Multimode, NanoScope IIIA (Veeco Instruments) as explained in the previous sections (Chapter 3 and Section 4.2).

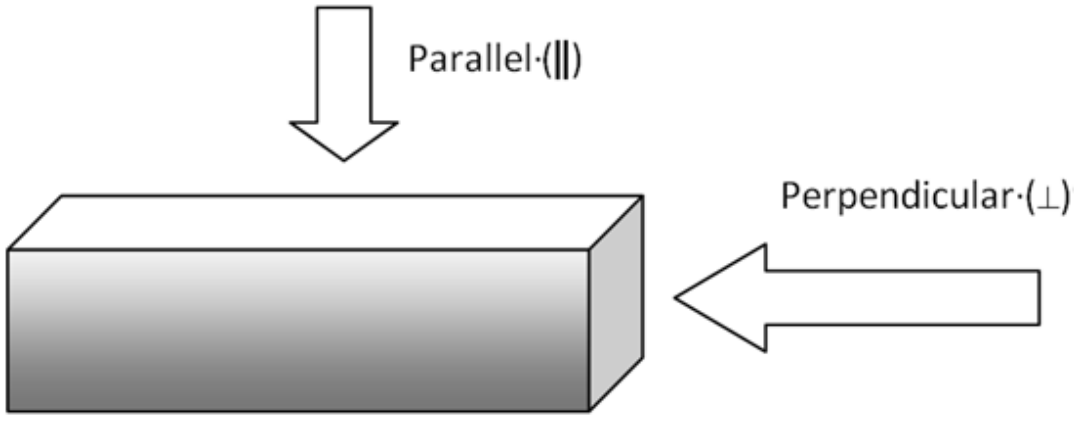

Figure 4-37. Schematic of the sample direction with reference to the uniaxial pressing.

4.3.1.4 Results and discussion

At this very early stage of the work, it was found that the undoped ceramics did not offered the necessary mechanical strength to be handled with or manipulated and thus the study of the undoped composition was abandoned. Figure 4-38a presents the XRD pattern of KNN template particles (shown in Figure 3-5) used in the present work. These templates were obtained by crushing the large single crystals as explained in Chapter 3. All the diffraction peaks can be indexed to a perovskite-structure with a high degree of crystallinity.

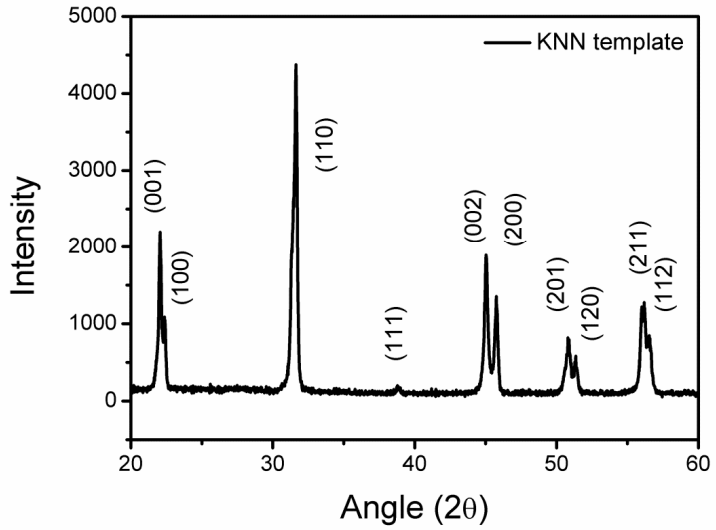

Figure 4-38. XRD pattern of KNN template particles showing the monoclinic structure.

XRD spectra of the non-templated and templated KNNL ceramics sintered during different times are presented in Figure 4-39a. we were not able to prepare textured undoped KNN ceramics and its seems that a sintering aid is required for successful preparation of the textured ceramics. Figure 4-39b shows the Rietveld refinement analysis image performed by FullProf software for randomly oriented ceramic. Observed and fitted diffraction profiles are shown by black solid circles and red line respectively. The difference between observed and fitted diffraction profiles is shown below in the figure and short vertical markers represent the Bragg's peak positions. The refinement best fit was obtained for monoclinic (*Pm* space group) with lattice parameters of

a = 4.002 Å, b = 3.946 Å, c = 3.982 Å, and β = 90º44′ similar to the previous reports of Li doped KNN ceramics [240, 241]. As also observed in Figure 4-39a, all the templated ceramics showed monoclinic perovskite structure, without secondary phases. In addition, when comparing the peaks intensities of the templated ceramics with those of the non-templated ones (Figure 4-39a), it is observed that the intensity of the (001) peak increases with the sintering time. This intensity change indicates an increase in the crystallographic (001) orientation of the templated ceramics which may be translated in terms of a crystallographic texture degree quantified via the Lotgering factor (f). As indicated in Figure 4-39a. Figure 4-39c allows comparing the dependence of the Lotgering factor (*f*) on the sintering time for both templated and non-templated samples. Non-templated ceramics maintain a low Lotgering factor, which value was kept lower than 9 % even after 24 h of sintering dwell time, whereas templated ceramics exhibit higher values of f which reached a maximum of *f* = 40 % for 24 h of sintering dwell time.

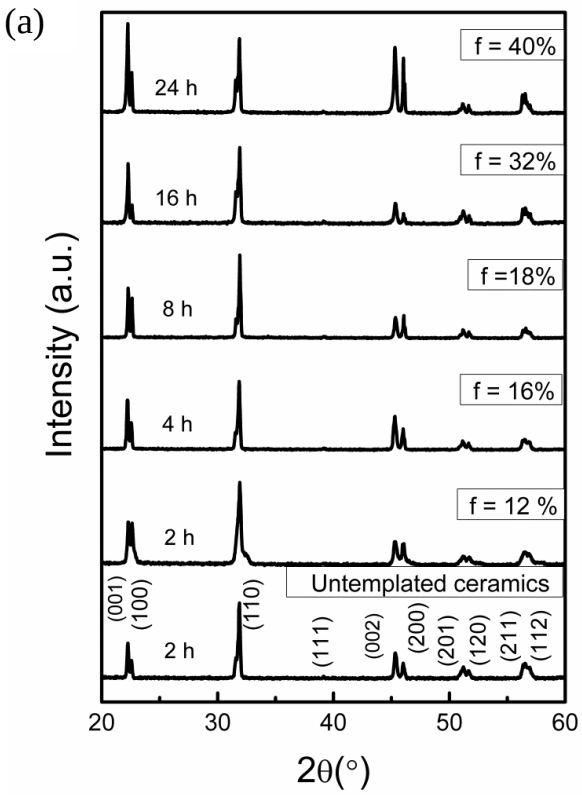

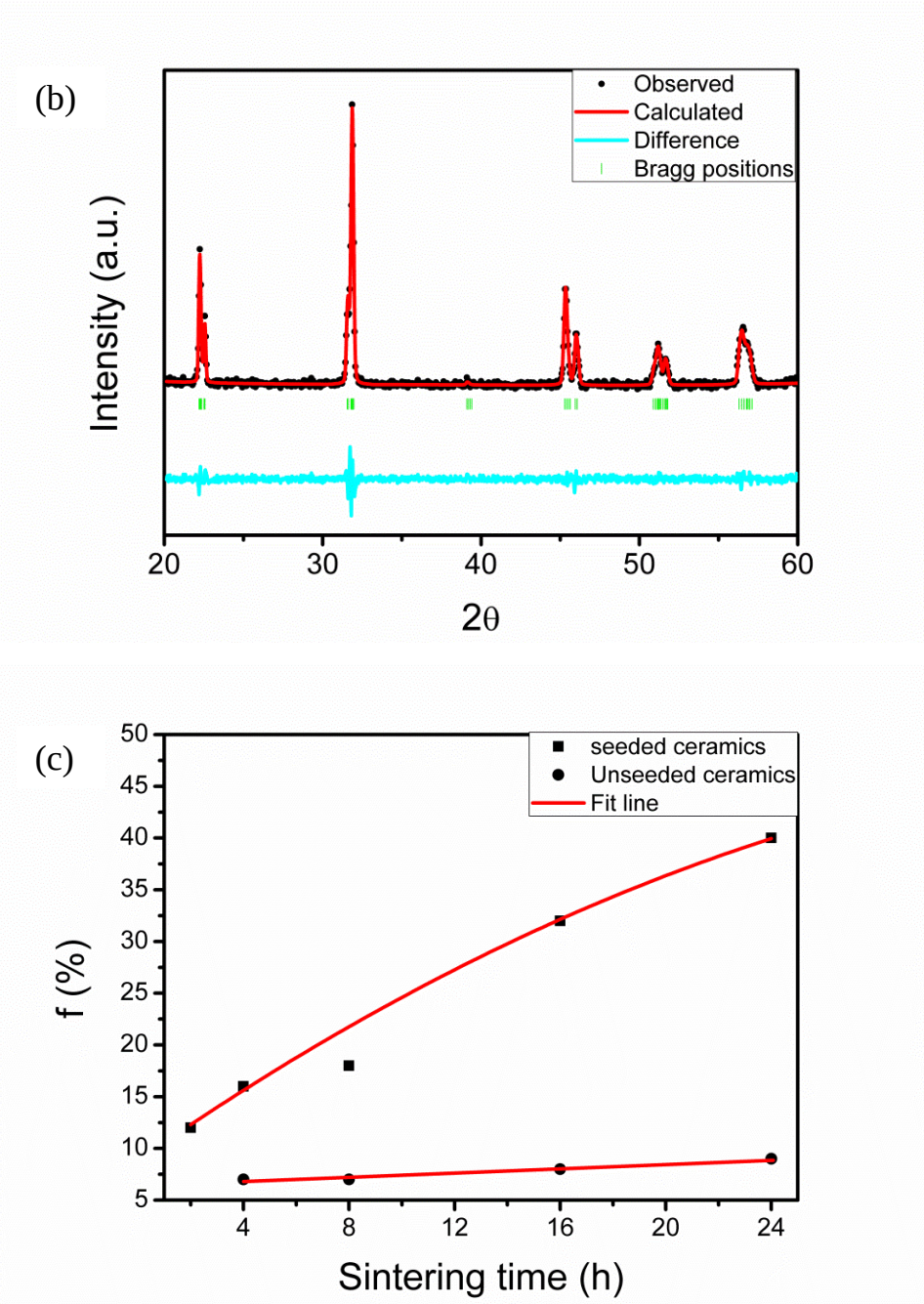

Figure 4-39. XRD patterns and crystallographic texture of KNNL ceramics: (a) XRD spectra and texture degrees (Lotgering factor, f) developed under different sintering times; (b) Rietveld refinement of the randomly oriented ceramic sintered for 2 h and (c) texture (f, %) development with the sintering time for seeded (■)and unseeded (•) ceramics. All the samples were sintered at 1100 ºC but for different sintering times. The XRD of the untemplated ceramic sintered for 2 h is taken as reference to calculate the lotgering factor.

XRD spectra can be used to quantify the crystallographic texture of ceramics but Lotgering factor (*f*) alone does not adequately characterize the texture quality and the quality of orientation can be observed from rocking curves and pole figures. XRD cannot yield accurate information about the width (full-widths at half-maximum; FWHM) of the grain orientation distribution, as can be done with the rocking curves whereas; data from pole figure reflects the preferred orientation of the crystal lattice in the material. Figure 4-40 shows the rocking curves and pole figures of the non-templated and of the templated (*f* = 40%) KNNL ceramic for (001) plane. Broad peaks were observed for the non-templated ceramics as compared to the templated ones. For the templated ceramics, a full width at half maximum (FWHM) could be calculated as 0.42º and 7.5º from the rocking curve and pole figure, respectively. These values indicate a very good texture quality which is even better than that reported for KNN based compositions, i.e. (7 - 8.5º) for Li-doped, Ta-doped and Sb-doped textured KNN ceramics calculated from rocking curves [123, 129] or than the values referred for other perovskite systems [18, 246]. These results indicate that the templated ceramics developed a preferred crystallographic orientation along (*hkl*) whereas the non-templated ceramics mostly maintained a random orientation.

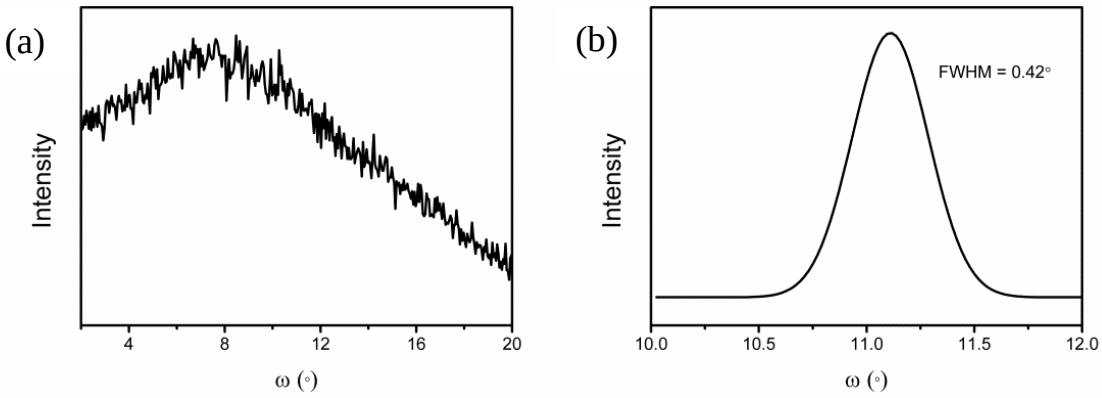

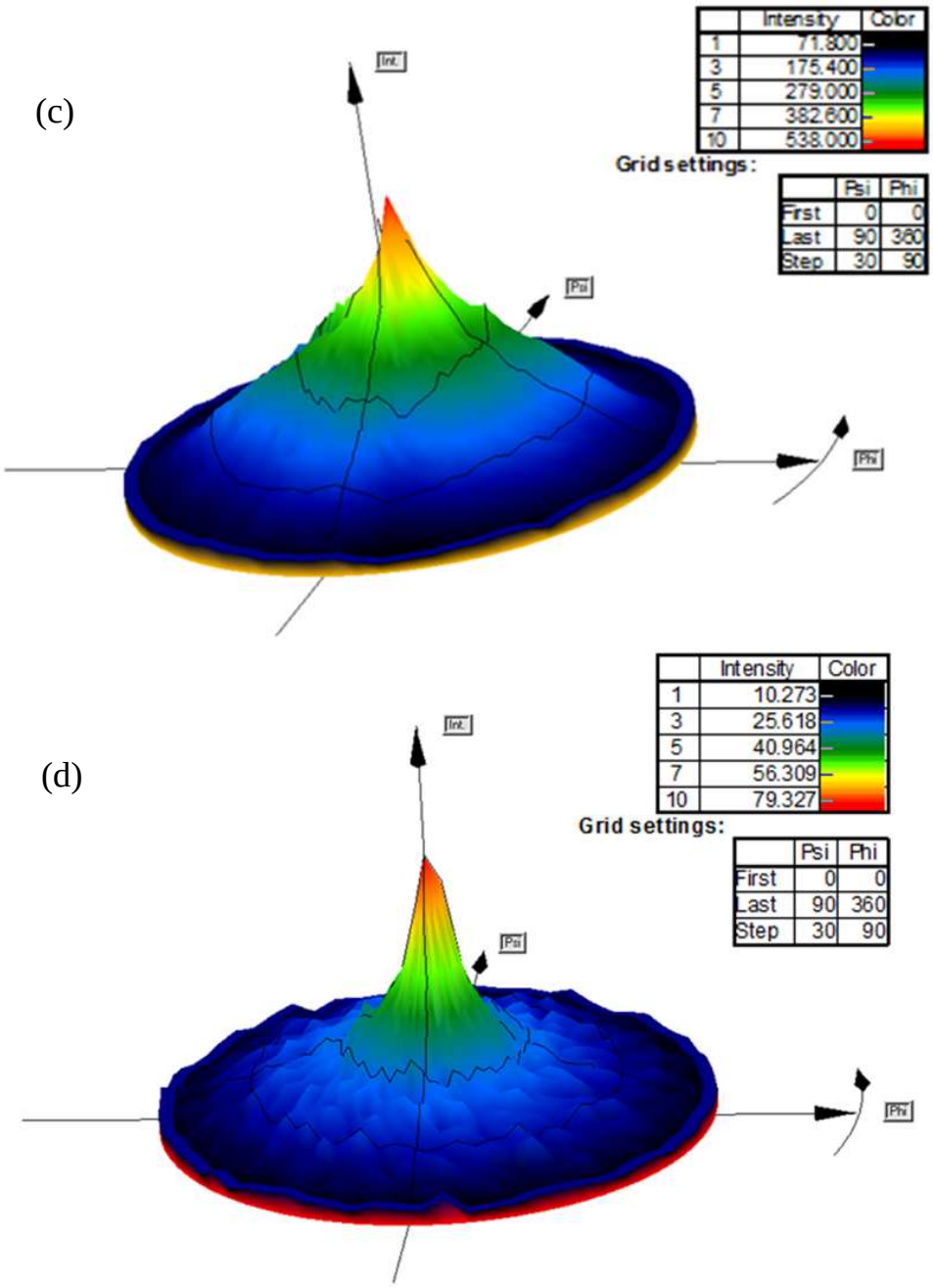

Figure 4-40. Rocking curves and pole figures of (a), (c) non-templated ceramics and (b), (d) of templated KNNL ceramics with f = 40%, respectively. Broadened peaks are observed for the unseeded ceramics as compared to the seeded ones, indicating that templated ceramics showed preferred crystallographic orientation along (001).

The microstructure of randomly oriented and textured KNNL ceramics is presented in Figure 4-41. Regardless their sintering and template conditions, all the

ceramics have a relative density of ~ 96 %. The microstructure of the randomly oriented ceramics sintered at 1100 ºC for 2 h is homogeneously composed of small sized grains having an average size of ~ 2.3 µm and a narrow size distribution (inset of Figure 4-41a). The prolonging of the sintering time till 24 h did not produce any significant change in its microstructure as confirmed by Figure 4-41b and this result is in line with the negligible variation of its Lotgering factor (*f*) as presented in Figure 4-39c.

The evolution of the templated ceramics microstructure with the sintering time, at 1100 ºC, can be analyzed in Figure 4-41c-f. As the sintering time increases, a bimodal microstructure developed, consisting of large grains surrounded by the small matrix grains. The amount of the large grains increases with the sintering time whereas the amount of matrix grains decreases and obvious from (Figure 4-41c-f).

It is also observed that the matrix grain size does not suffer a significant variation as the sintering time increases. Concerning the large grains, their sizes are seen to increase but remaining within a range between 15 and 65 µm (inset of Figure 4-41d). It is nevertheless worthy mentioning that the density of large grains, i.e. the number of large grains per unit surface area, increases as the sintering time increases too. Hence, from the microstructural analysis, it can be thus concluded that ceramics texturing is accompanied by the development of large grains, some of which are nucleated within the matrix grains, at the expense of the smaller matrix particles [18, 247]. Indeed, the degree of texture increases as the large grains develop this has also been observed in (K, Na, Li)(Nb, Ta)O_3 ceramics textured by plate like $NaNbO_3$ template grains (K, Na, Li)(Nb, Ta)O_3 [248] and $BaTiO_3$ ceramics textured by plate like $Ba_6Ti_{17}O_{40}$ template grains [249]. Figure 4-41b presents the microstructure of randomly oriented ceramics (non-templated KNNL) sintered for 24 h, a remarkable difference can be observed between the microstructure of the randomly oriented and that of the textured ceramic sintered for 24 h, which allowed concluding that the seed crystals combined with the sintering dwell times were determinant conditions for the texture development. Figure 4-41g shows the variation of the area fraction of the large grains with sintering time which reflects the increasing amount of large grains. As observed, the trend of the curve in Figure 4-41g is comparable to that found in the curve of Figure 4-39c, thus providing evidence that the

crystallographic texture development (Lotgering factor) correlates with the microstructural evolution.

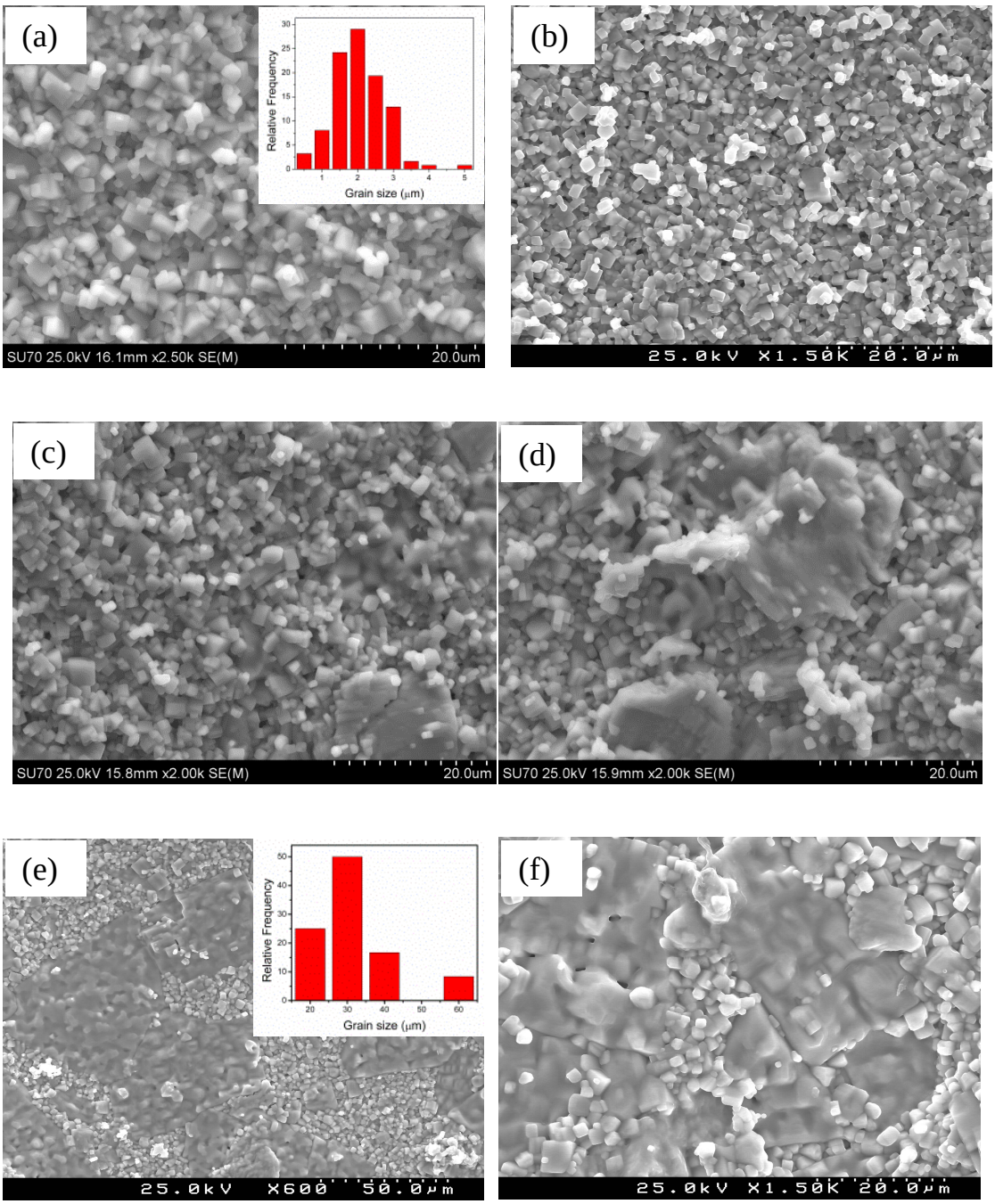

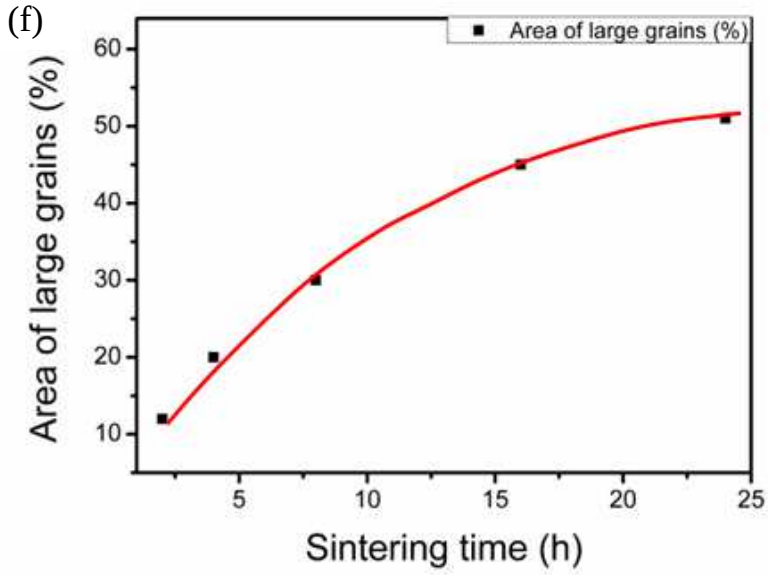

Figure 4-41. . SEM images of KNNL ceramics sintered at 1100 ºC: randomly oriented KNNL ceramic sintered for 2 h and 24 h (a and b) and textured KNNL ceramic sintered for 4 h (c),8 h (d) , 24 h (e and f) and area fraction of large grains is shown in (f), red line is guide to the eye.

Figure 4-42 shows the SEM, energy dispersive spectra (EDS) and elemental mapping of KNNL ceramics sintered for 24 h. EDS spectra reveal only K, Na, Nb and O elements on the surface of the samples. In addition, elemental mapping for K, Na, Nb and O was also performed (Figure 4-42c-f), confirming the distribution is very uniform, ascertaining the good chemical quality of the textured sample sintered for 24 h.

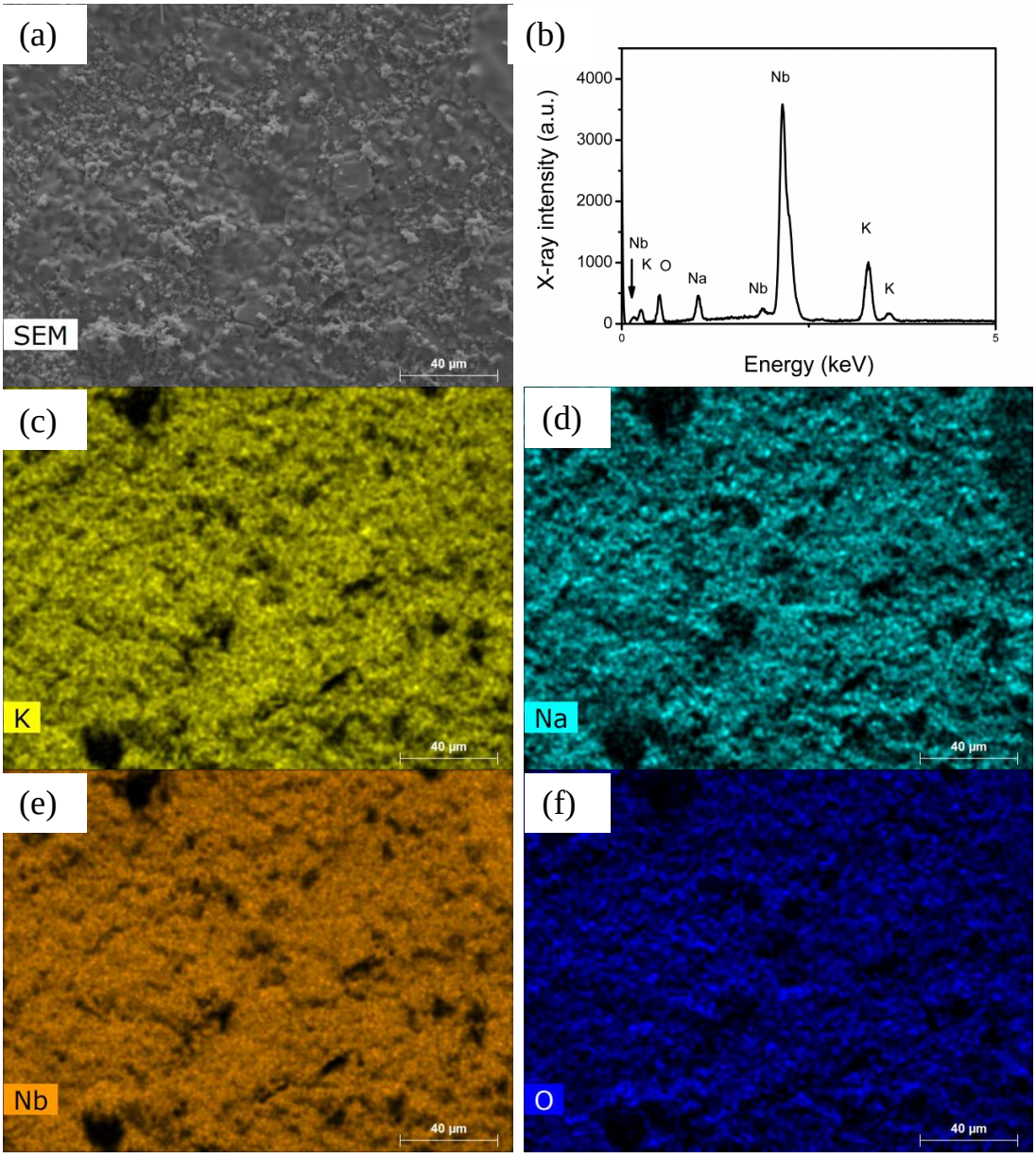

Figure 4-42. SEM and elemental mapping of KNNL ceramic with f = 40 %: (a) SEM image; (b) EDS spectrum; (c - f) potassium, sodium, niobium, and oxygen distributions on the surface of ceramic, respectively.

Figure 4-43a-c presents the topography and piezo-response image of randomly oriented KNNL ceramics. For the bulk ceramics, randomly oriented domains were observed in the both in-plane (IPP) and out-of-plane (OPP) PFM image. It was also observed that topographic image does not correlate with the IPP or OPP images. The absence of specific domain patterns repeating regularly on a long scale might reflect the

grain size and grain boundary effects, as it is already known that complex self organized domains can only be formed in ceramics with large grains of several square micrometers [29].

In the PFM images of textured KNNL ceramics Figure 4-43d-f, the bright and the dark contrasts in the PFM images represent the direction of orientation of the polarization vectors in their respective planes: dark regions represent the polarization vector pointing towards the bulk of the textured ceramic and the bright regions pointing towards the ceramic surface. It was also evidenced by these images that the PFM contrast is independent of topography effects, indicating that the acquired PFM signal has not been influenced by the cross talk with topography signal in both cases, i.e. textured ceramics and randomly oriented ceramics.

The complex domain pattern observed in the textured ceramics consists of herringbone type (V shaped) domains, assembled in a regular and repetitive fashion as shown in the OPP image of Figure 4-43f. Complex self organized domains of similar kind were reported in $BaTiO_3$ [29] with large grains of several square micrometers or in PZT single crystal [26, 250] and quite recently in our work of KNN single crystals as reported in Section 4.2 [16].

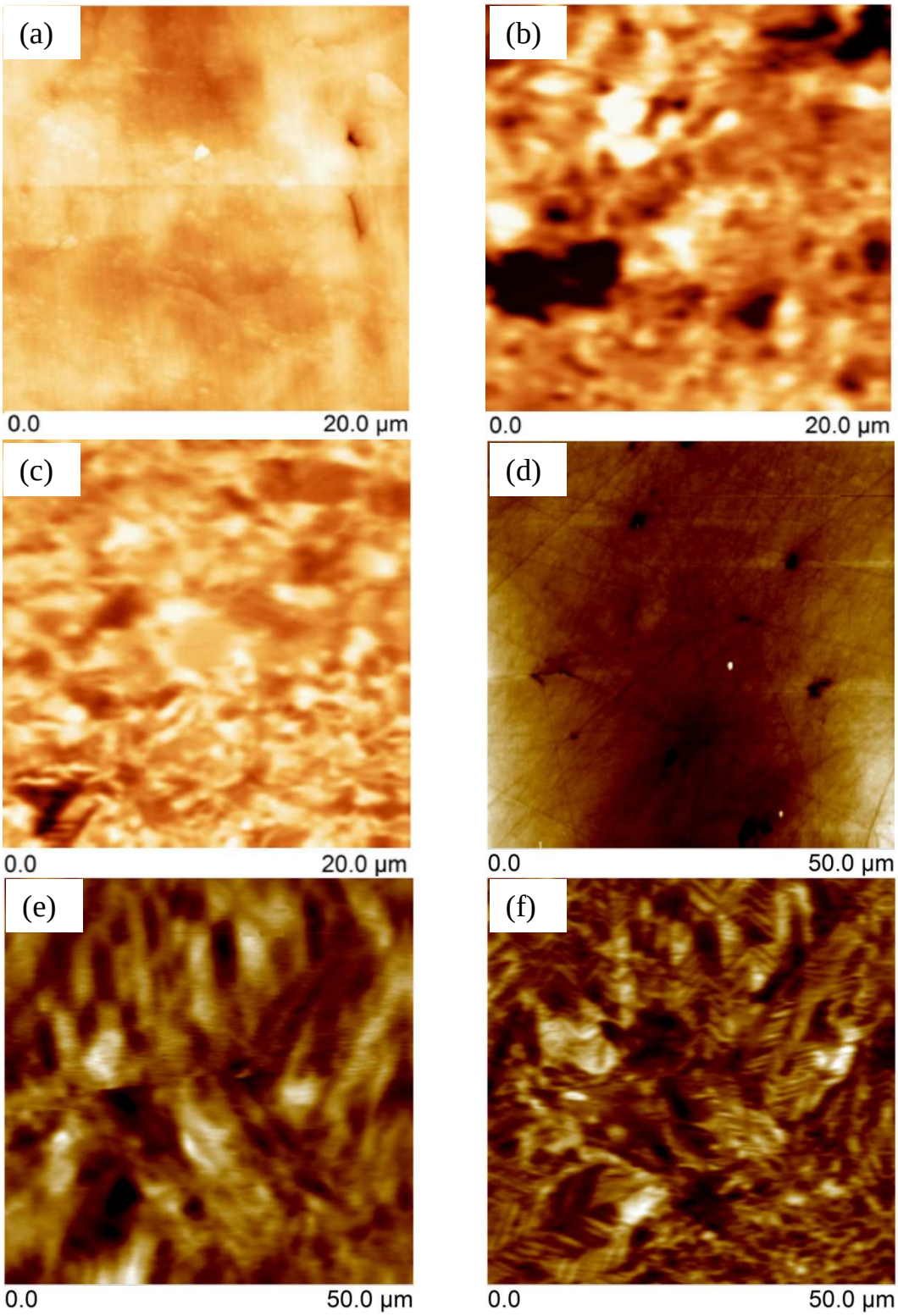

Figure 4-43. Topography, IPP and OPP images of randomly oriented (a-c) and textured (d-f) KNNL ceramics with f = 40 %. A regular repeated domain pattern can be observed for textured ceramics.

For clarity purposes a zoomed image of the herringbone area is presented in Figure 4-44a-b (topography and piezo-response image, respectively) along with schematics. In this case, as in the previous ones, the piezo-response image is free of topography influences. The domain length varies between 1.8 and 3.4 µm and the domain width varies between 0.3 and 0.9 µm as illustrated in the schematics. According to literature, internal stresses play a very important role in the formation of different type of domains, i.e. low stresses favour 180º domains whereas high stresses are more related to 90º domains [16, 30]. In our quite recent work on KNN single crystal (Section 4.2), the dominant domains were of 180º type, which was interpreted as an indication of low internal stresses. As compared to KNN single crystal, the textured ceramics presented here seem to evidence larger stresses. This can be explained on the basis of the differences between textured (bulk) ceramics and single crystals. A grain (crystallite) in a ceramic is clamped by its neighbouring grains in all the three dimensions and its deformation to some extent is possible only by cooperative motion of the adjacent grains that may result on either high internal stress or mechanical twinning, which was not the case of single crystals [29]. Based on crystal structure arguments, KNN may have 60°, 90°, 120°, or 180° domains [25, 27]. But, in our studies of polycrystalline ceramics, textured ceramics and single crystals, no evidence of 60° and 120° domains was observed as reported by Herber *et al* [25] in the PFM study of abnormally grown grain of doped KNN ceramics.

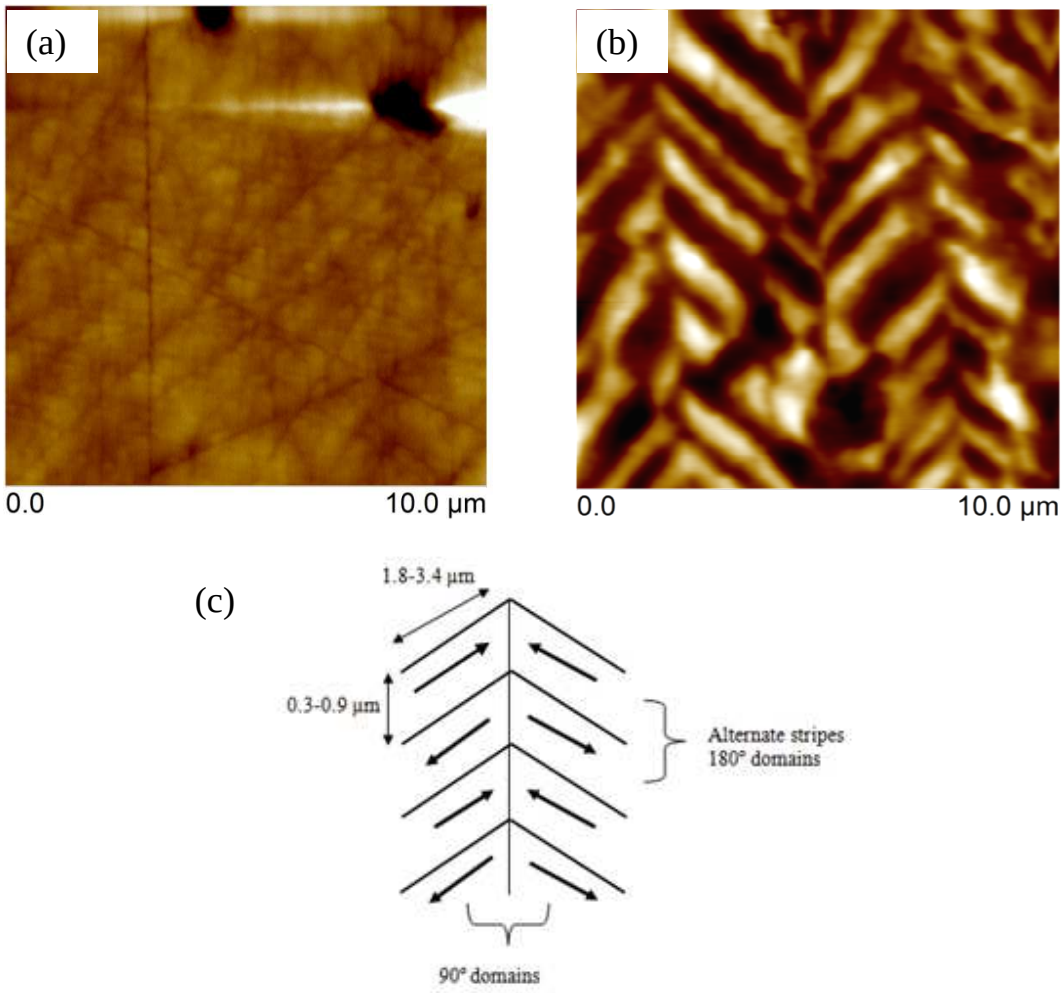

Figure 4-44. PFM images (a) topography and (b) OPP image and (c) schematic of the domain pattern of KNNL with f = 40%. A very well defined domain pattern of 90º and 180º was observed.

Concerning the macroscopic dielectric response, Figure 4-45 represents the temperature dependence of the dielectric constant at a frequency of 1 kHz. For comparative purposes, the dielectric response of randomly oriented KNN ceramics is also presented. Two peaks in the dielectric permittivity were observed in these curves, which can be correlated to the phase transition from cubic to tetragonal (T_C) and tetragonal to monoclinic ($T \rightarrow M$) upon cooling. For randomly oriented ceramics $T \rightarrow M$ and T_C was found to be 155 ºC and 439 ºC, which are close to the values reported in the literature [68]. However, for textured ceramics $T \rightarrow M$ and T_C were found to be ~ 167 ºC and 430 ºC, respectively, which is also close to the textured Li or Ta doped ceramics (439 ºC and 322

ºC) [123]. Dielectric constant of ~ 550 at room temperature was almost same for both randomly oriented and texture (f = 40 %), but the textured ceramic showed a much higher value of 13017 at T_C as compared to 7013 for randomly oriented ceramics. This behaviour is similar to the KNN single crystals observed in our previous results presented in Section 4.2. The dielectric permittivity value at T_C of randomly oriented ceramics at T_C (7013) is higher as compared to Li and Sb co-doped ceramics (~ 6500) [102], or to $0.058LiNbO_3$–$0.942(Na_{0.535}K_{0.480})NbO_3$ [85] (~ 3000 - 5000). Also, for textured ceramics, dielectric permittivity at T_C (13017) are higher than reported in literature for textured $(Na_{0.50}K_{0.47}Li_{0.03})(Nb_{0.8}Ta_{0.2})O_3$ (3000-7000 at 100 kHz) by using various sintering aids [125] and comparable to the values of MPB values of Li (4 to 8 mole %) doped KNN ceramics (~ 6000 to 15000) [251, 252]. Other than the higher dielectric constant, the $T \rightarrow M$ and T_C ~ of 167 ºC and 430 ºC are quite high as compared to the ceramics with higher amount of Li, (close to so called MPB) and lower dielectric constant values, where these values temperatures occur close to the room temperature and ~250 ºC [100, 128]. Furthermore, the randomly oriented and textured ceramics showed low dielectric losses up to 300 ºC as presented in Figure 4-45b. Figure 4-45c shows the temperature dependence of the dielectric constant for textured ceramics (f = 40%) which was measured under an electric field applied perpendicular (⊥) and parallel (∥) with reference to the pressing direction. As already mentioned, at room temperature, a dielectric constant of ~ 550 was observed along (∥) direction (for f = 40%) and of ~ 400 in the (⊥) direction. This dielectric permittivity variation of ~ 28 % is an indication of properties dependence on ceramic orientation. The higher values observed in the parallel direction as compared to perpendicular direction and to polycrystalline ceramics as well is due to the texturization and favourable polarization direction as explained in the previous sections.

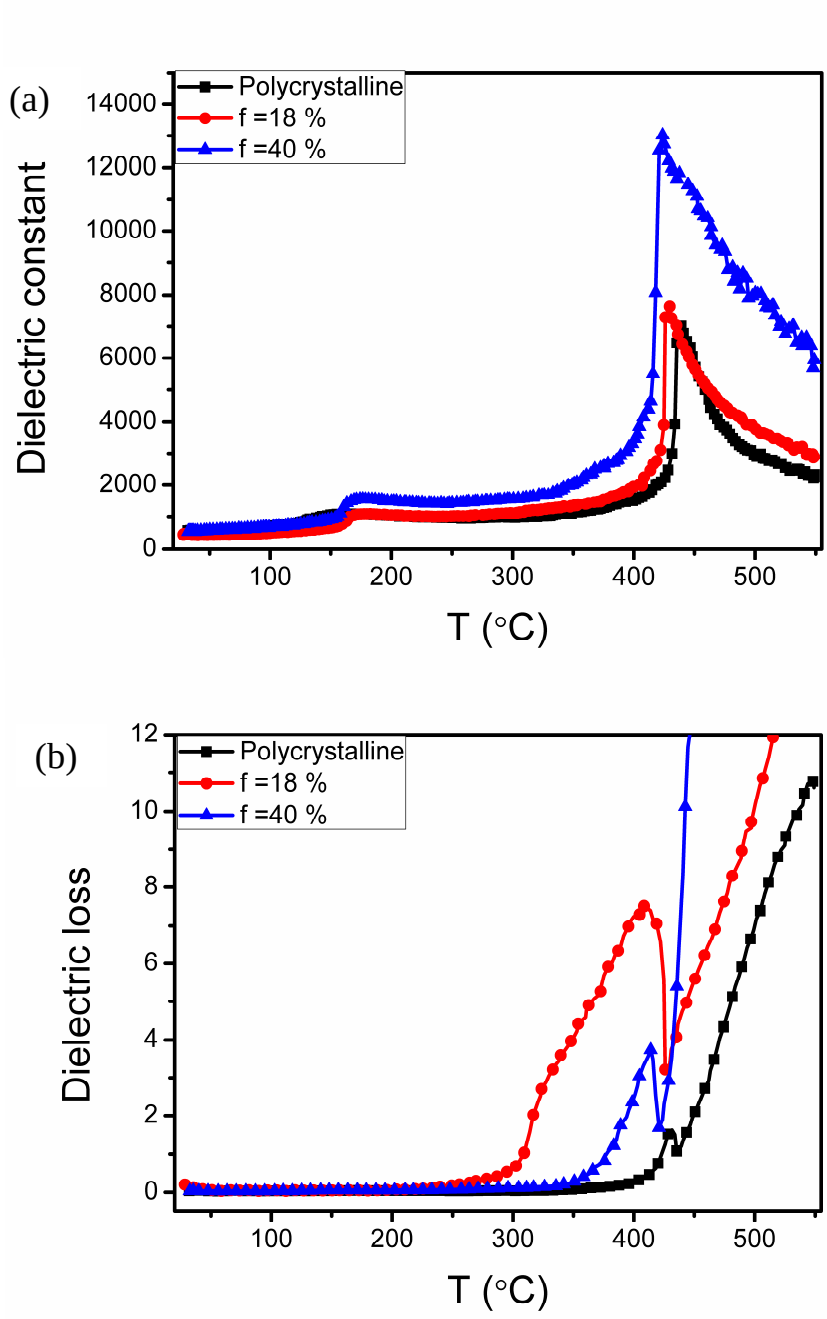
(a)
Polycrystalline
f =18 %
f =40 %
Dielectric constant
T (°C)
(b)
Polycrystalline
f =18 %
f =40 %
Dielectric loss
T (°C)

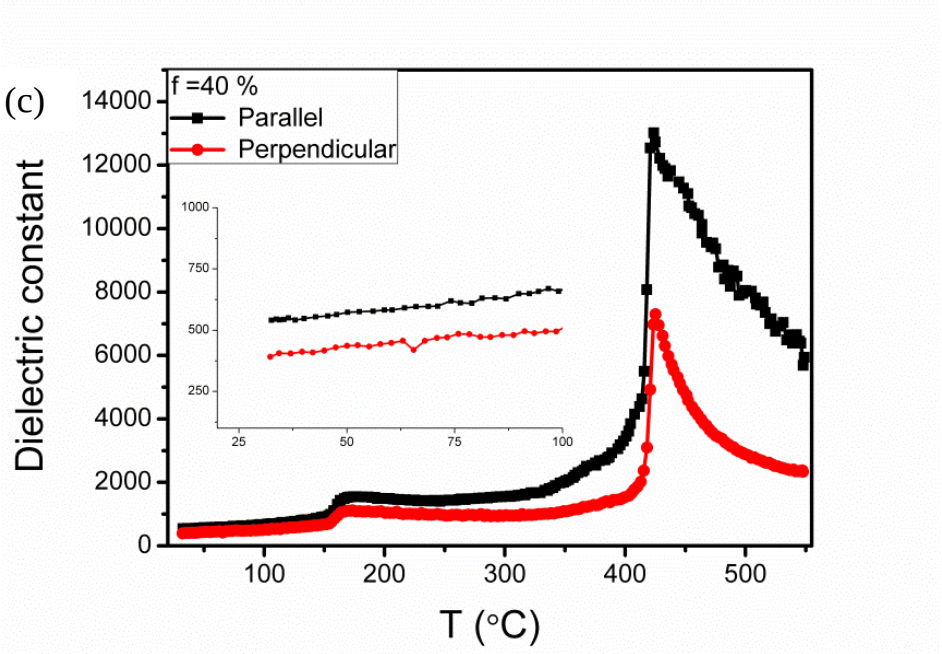

Figure 4-45. Temperature dependence of: (a) dielectric constant; (b) dielectric loss of randomly oriented and textured KNNL ceramics (f=18 and 40%) and (c) dielectric constant for textured ceramics (f = 40%) measured along the parallel (■) and perpendicular (•) directions with reference to the pressing direction.

Polarization hysteresis (*P-E*) loops measured at room temperature and at a frequency of 50 Hz are presented in Figure 4-46, for randomly oriented and for textured KNNL ceramics having *f* = 40 %. A significant improvement of remanent polarization (P_r) from 13.1 μC/cm^2 to 21.4 μC/cm^2 was observed for textured ceramics, followed by an increase of the coercive field (E_c) from9.6 kV/cm to 11.7 kV/cm was observed for textured ceramics and similar to the reported values of P_r (22.1 μC/cm^2) and E_c (12.7) for Li doped textured KNN ceramics [123]. The significant enhancement of polarization is suggested to be due to the orientation factor (texture) as is already explained in Chapter 2, that is its direction of spontaneous polarization, also reflecting the higher dielectric permittivity and more importantly due to the presence of a long range ordered domain pattern as observed by PFM. These results are also in line with the enhanced properties of KNN single crystals as compared to the randomly oriented ceramics which were also attributed to the presence of ordered domain pattern [16].

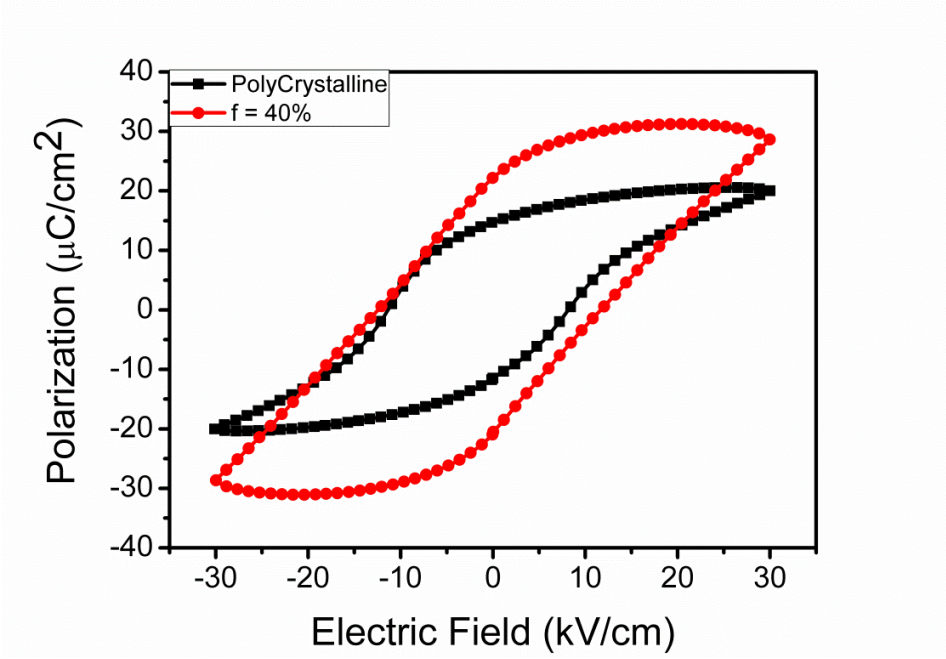

Figure 4-46. P-E loops for KNNL randomly oriented (■) and textured (•) ceramics. Oriented ceramics showed higher remanent polarization values due to favourable orientation.

The measured piezoelectric constant (d_{33}) was 280 pC/N for KNNL with f = 40% which is more than twice as compared to randomly oriented ceramics (135 pC/N). The d_{33} values for the textured ceramics presented in this work are higher than the textured Li doped KNN (192 pC/N) and Ta doped KNN (184 pC/N) [123]. As already explained in the introduction part, that d_{33} can be improved by increasing the polarization and dielectric permittivity, which has been improved due to favorable orientation, hence d_{33} is also improved.

The present results are of crucial importance from the point of view of KNN applications considering that the remanent polarization values are as good as those reported for KNN with 4-8 mole % of Li content [98, 99, 101, 239-241]. Furthermore, the present $T \rightarrow M$ (167 ºC) and T_C (430 ºC) largely exceed the corresponding values ($T \rightarrow M$; close to room temperature and T_C lying between 200 ºC and 300 ºC) of KNN doped with 4-8 mole % Li. In fact, keeping in mind that the maximum temperature of operation for piezoelectrics is normally half of the Curie temperature (T_C), it is of paramount impor-

tance to engineer piezoelectrics which combine enhanced properties with high T_C as is the case of the textured KNNL ceramics developed in this work.

4.3.1.5 Conclusions

KNNL textured ceramics with monoclinic phase at room temperature were synthesized by TGG by using single crystals as templates and conventional mixed oxide route. Textured KNNL ceramics showed high (001) - orientation (f = 40%) and as a result of (00l) texture, an improvement in dielectric ferroelectric and piezoelectric (280 pC/N) properties of KNNL was observed while maintaining a high phase transition and Curie temperature. The enhancement of properties was attributed as a consequence of the domain structure of the textured ceramics, dominated by long range ordered domains (length varies between 1.8 – 3.4 µm and width between 0.3 – 0.9 µm) which were absent in the randomly oriented ceramics. This is a successful example of improvement in electrical properties by texturing which will certainly foster further exploration towards high performance lead-free piezoceramics. Figure 4-47 shows some of the conclusions of this section.

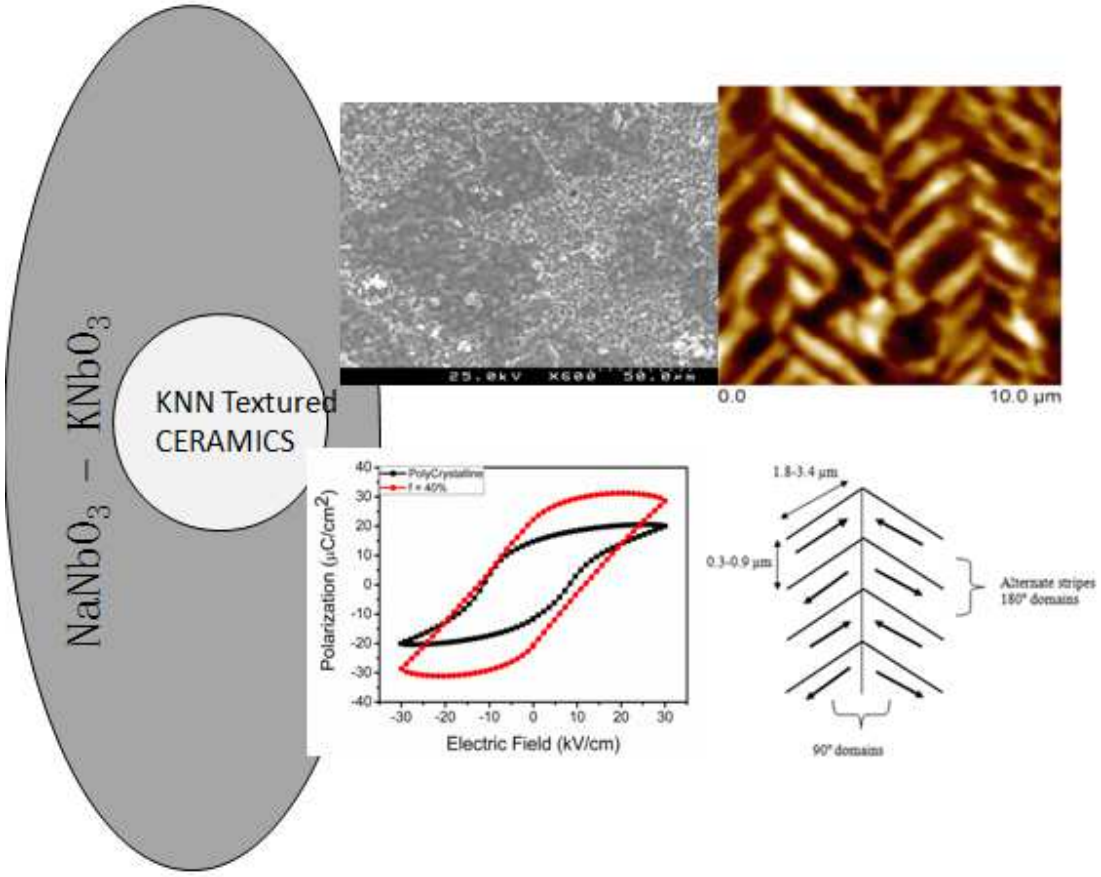

Figure 4-47. . Image showing some conclusions of this section. Textured ceramic showed a bimodal microstructure and improvement in polarization along with the repeated and well defined domain pattern as was observed for KNN single crystal.

CHAPTER 5

Conclusions, future work and output

5. Conclusions, future work and output

5.1 Conclusions

The knowledge of KNN properties, including dielectric, ferroelectric and piezoelectric properties, and its relation with structural features, such as domain structure, among others, are important prerequisites for the understanding of the electromechanical performance distinct of KNN based materials. Without this knowledge KNN will not be a strong competitor of the most current technologically important family of materials for electromechanical applications – lead based perovskites.

This need has been the main motivation behind this thesis work, as described in the thesis objectives (Chapter 1). Accordingly, the work was focused on the preparation and characterization of KNN bulk ceramics, single crystals and textured ceramics and in establishing the relations between structure – microstructure – properties of KNN based materials.

The main conclusions of this thesis work may be summarized as follows:

- KNN ceramics having density ~ 95 % were prepared and characterized, which showed some very interesting results including inherently low resistance, which was related to the leaky *P-E* loops. The Mn doping at B-site proved to be very helpful in improving the resistance and consequently the leakage free *P-E* loops. It was also observed that it's very difficult to substitute the Mn as A-site, and drastic decrease in the properties observed for A-site Mn substituted or A-site non-stoichiometric ceramics.
- High-quality (001)-oriented plate-like single crystals were successfully grown by high-temperature self-flux method at sufficiently low temperatures that allowed controlling the stoichiometry, permitting the study of their intrinsic properties and comparing it with the polycrystalline counterparts, which are required for applications in various microelectronic devices.
- Piezoforce-response microscopy (PFM) demonstrate a well defined long range order of polar domains in KNN single crystals with the coexistence of 90º and 180 º domains. The formation of such complex domain structure, which is absent in polycrystalline ceramics, was suggested to have a significant impact on the physical properties of KNN based materials.
- The high-quality of the grown single crystals was also confirmed by dielectric, ferroelectric and piezoelectric measurements, which response was considerably higher than the one observed in polycrystalline ceramics..
- Impedance spectroscopy studies confirmed only the bulk contribution and higher resistivity of KNN single crystals as compared to polycrystalline counterpart at room temperature, which proved to be helpful in obtaining a leakage free hysteresis loop.
- The KNN single crystals structure was indexed to a monoclinic one in the Raman spectra and intensities variation measured during the rotation experimental data fitted very well to the theoretical calculations. This work and the generated knowledge will contribute to the settlement of the non-destructive assessment of domain distribution in ferroelectric materials by Raman spectroscopy.
- Using KNN single crystal as templates textured KNNL ceramics were prepared by templated grain growth by conventional ceramic processing. The orientation of the original templates in sintered samples seems to be enhanced by the longer sintering times in the presence of Li in this work.

- Textured ceramics showed improved performance dielectric and ferroelectric and piezoelectric behavior along with the well defined domain pattern. The improved performance can be related to the ordered long range domain pattern and favorable polarization orientation.
- Figure 5-1 shows some of the conclusions of this work.

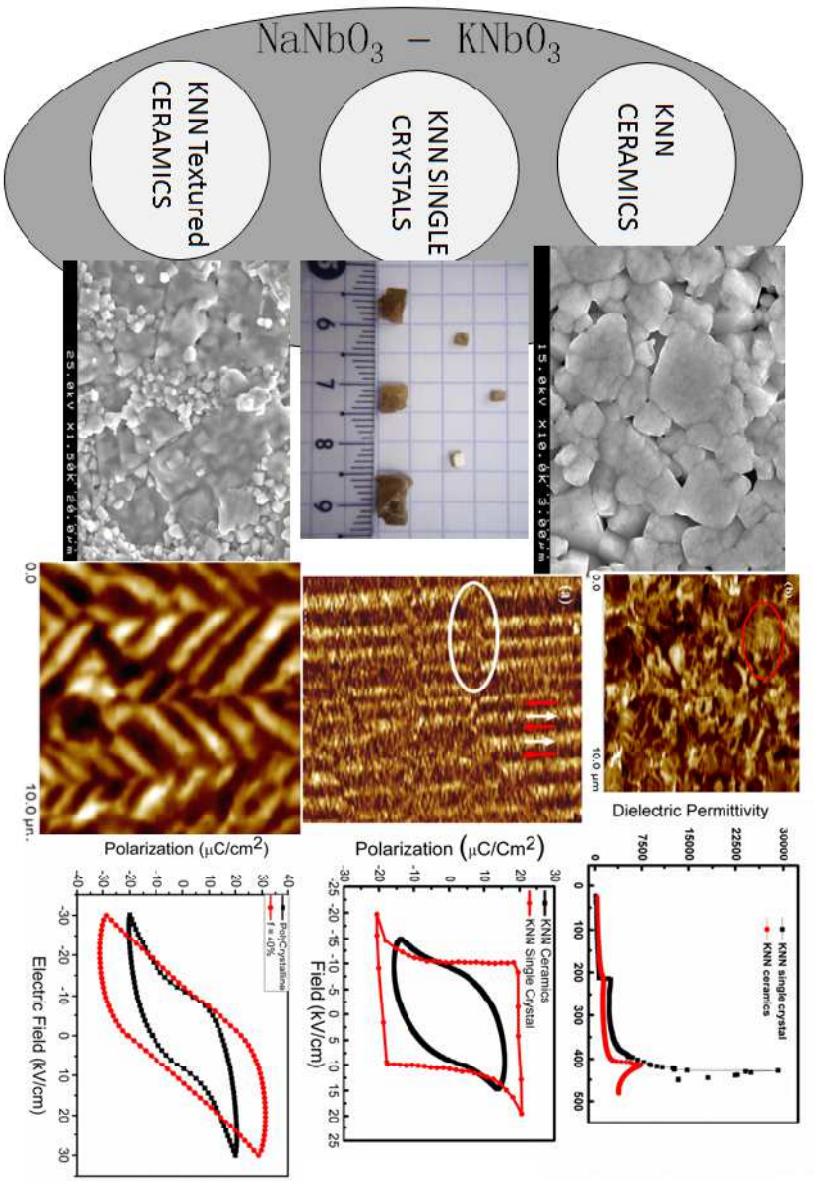

Figure 5-1. Image showing some conclusions of this work. KNN single crystals showed a repeated domain pattern with improved properties. Regular and well defined domain pattern was argued to be responsible for the better properties. Textured KNN ceramics (KNNL plus single crystal templates) showed the defined, repeated domain pattern and improved properties with higher T_C.

5.2 Future Work

The results obtained in this work emerged from a systematic study of properties of KNN undoped, doped, non-stoichiometric, single crystals as well as textured ceramics. However, further studies are required to answer some unsolved questions in this work. Hence, some future work is also proposed in this regards,

- Mn proved to be very helpful in reducing the leakage current in the undoped KNN ceramics. So, Mn along with some other additions like Ag and Cu should be tried to improve further the properties in bulk ceramics.
- KNN single crystals were grown successfully and properties were measured. However, for a deeper understanding of the growth mechanism requires a detailed study of the growth conditions such as flux viscosity, supersaturation, solute diffusion etc. This study is important for the controlled growth of undoped and doped KNN single crystals..
- Textured KNN based ceramics have been prepared with improved properties. But, still work is required to improved the degree of texture, which is still lower as compared to the values reported by other methods like tape casting, spark plasma sintering and screen printing by using the single crystal template. Thus, additives or techniques must be added to improve the degree of texture and finally the properties.
- Sintering aids like Cu, Ag in addition to Li should be tried to get highly oriented ceramics with reduced sintering dwell time.
- The experimental setup for polarization hysteresis (P-E) loops must be improved for allowing the complete electrical characterization e.g. fatigue, d_{33} and I-V curves, can be done with the same equipment with some enhancement, which are very important for understanding and applications point of view.

5.3 Output

5.3.1 Papers and extended abstracts

1. Rafiq, M. A., Costa, M. E., Vilarinho, P.M., Reaney, I. M. "Ferroelectric Domain Studies of KNN Single Crystals by Piezo-force and Transmission Electron Microscopy." Microscopy and Microanalysis 2012;18:113-14
DOI: http://dx.doi.org/10.1017/S1431927612013220

2. Rafiq, M. A., Costa, M. E., Reaney, I. M., Vilarinho, P.M. "Transmission Electron Microscopy of Mn-doped KNN Ceramics." Microscopy and Microanalysis 2013;19:99-100.
DOI: http://dx.doi.org/10.1017/S1431927613001116

3. Rafiq, M. A., Costa, M. E., Vilarinho, P.M., Reaney, I. M. "Establishing the domain structure of $(K_{0.5}Na_{0.5})NbO_3$ (KNN) single crystals by piezoforce-response microscopy " Science of Advanced Materials, 2014; 6(3): p. 426-433.
DOI: http://dx.doi.org/10.1166/sam.2014.1734

4. Rafiq, M. A., Supancic P., Costa, M. E., Vilarinho, P.M., Deluca, M., "Precise determination of phonon constants in lead-free monoclinic $(K_{0.5}Na_{0.5})NbO_3$ (KNN) single crystals" Applied Physics Letters; 2014, 104, (1), 011902-5.
DOI: http://dx.doi.org/10.1063/1.4860416

5. Rafiq, M. A., Costa, M. E., Vilarinho, P.M., "Defects and charge transport in Mn doped lead free $K_{0.5}Na_{0.5}NbO_3$" Science of Advanced Materials (accepted).

6. Rafiq, M. A., Costa, M. E., Vilarinho, P.M., "Impedance analysis and conduction mechanisms of lead free KNN single crystals and polycrystalline ceramics: a comparison study" Crystal Growth and Design (accepted).

5.3.2 Manuscripts (under Process)

1. Rafiq, M. A., Costa, M. E., Vilarinho, P.M., "Effect of non-stoichiometry on the structure and electrical properties of $K_{0.5}Na_{0.5}NbO_3$ ceramics"

2. Rafiq, M. A., Costa, M. E., Vilarinho, P.M., "Lead-free textured Li-modified (K,Na)NbO_3 with enhanced properties"

5.3.3 Oral presentations

1. Rafiq, M. A., Costa, M. E., Vilarinho, P.M., "Effect of Mn-site occupancy on the microstructure and dielectric properties of lead free $K_{0.5}Na_{0.5}NbO_3$ ceramics", VI International Materials Symposium MATERIAIS 2011 (XV meeting of SPM – Sociedade Portuguesa de Materiais) Guimarães, Portugal, 18-20 April 2011,
2. Rafiq, M. A., Costa, M. E., Vilarinho, P.M., "Ferroelectric domain studies of KNN single crystals by Piezo-force and transmission electron microscopy", 2nd Joint Congress of the Portuguese and Spanish Microscopy Societies, Aveiro, Portugal,
3. Rafiq, M. A., Costa, M. E., Vilarinho, P.M., "Non-stoichiometric lead free $(K_{0.5}Na_{0.5})_{1-x}Nb_xO_3$ and its electromechanical behaviour", MRS fall meeting, November 28 – December 02, 2011, Boston, Massachusetts, United States.
4. Vilarinho, P.M., Rafiq, M. A., Costa, M. E., "Domain studies in $K_{0.5}Na_{0.5}NbO_3$ (KNN) single crystals grown by a high temperature self flux method", MRS meeting, November 28 – December 02, 2011, Boston, Massachusetts, United States.
5. Rafiq, M. A., Costa, M. E., Vilarinho, P.M., Reaney, I. M., TEM Investigation of Mn-doped KNN Ceramics, XLVI Congresso da Sociedade portuguesa de Microscopia, SPMicros 2012, 24-25 September 2012, Lisboa, Portugal.
6. Rafiq, M. A., Costa, M. E., Vilarinho, P.M., Impedance Spectroscopy Studies on Mn doped $K_{0.5}Na_{0.5}NbO_3$ Lead-free Ferroelectric Ceramics, International Symposium on the Applications of Ferroelectrics (ISAF 2013), 21-25 July, Prague, Czech Republic.
7. Deluca, M., Rafiq, M. A., Costa, M. E., Vilarinho, P.M., and Supancic, P., "Structure and orientation of KNN single crystals by polarized micro-Raman spectroscopy", COST Action MP0904 SIMUFER Workshop "Advances in Ferroelectrics and Multiferroics" – Prague, Czech Republic , July 21st, 2013.
8. Vilarinho, P.M., Progresses in engineering the electromechanical response of $K_{0.5}Na_{0.5}NbO_3$ ceramics, 6th International Conference on Electroceramics, Joao Pessoa, Brazil, 09-13 November, 2013 – **Invited talk**.
9. Costa, M.E., Rafiq, M. A., Vilarinho, P.M., "Textured $K_{0.5}Na_{0.5}NbO_3$ for micro

electromechanical systems: Processing-structure-property relationships, MRS fall meeting, Dec. 1 – 6, 2013, Boston, Massachusetts, United States.

10. Rafiq, M. A., Costa, M. E., Vilarinho, P.M., Microstructure studies of textured potassium sodium niobate (KNN) based ceramic, Microscopy in Research, SPMicros 2013, 10-11, Dec. 2013, Lisboa, Portugal.

5.3.4 Posters

1. Rafiq, M. A., Costa, M. E., Vilarinho, P.M. "Processing–structure-property relationships in Mn doped $K_{0.5}Na_{0.5}NbO_3$ for microelectromechanical systems" MRS fall meeting, November 29 – December 03, 2010, Boston, Massachusetts, United States.
2. Rafiq, M. A., Costa, M. E., Vilarinho, P.M. "Optimization of growing conditions for obtaining ferroelectric (K,Na)NbO_3 single crystals", VIII CICECO meeting, 17-18 March 2011, Aveiro, Portugal.
3. Rafiq, M. A., Costa, M. E., Vilarinho, P.M. " Non stoichiometry-properties relationship in lead free $(K_{0.5}Na_{0.5})1\pm xNbO_3$", IX CICECO meeting, 2-3, May 2012, Aveiro, Portugal.
4. Pinho, R., Rafiq, M. A., Costa, M. E., Vilarinho, P.M., Texturization of potassium sodium niobate (KNN) ceramics in the presence of CuO and MnO, Microscopy in Research, SPMicros 2013, 10-11, Dec. 2013, Lisboa, Portugal.

6. References

1. *Smart Materials and Their Applications: Technologies and Global Markets*, http://www.bccresearch.com/report/smart-materials-technologies-markets-avm023d.html. 2011 [Accessed on 14-09-2011].
2. *Smart Materials: A Technical and Market Assessment*, http://www.bccresearch.com/report/AVM023C.html. 2005 [Accessed on 03-02-2010].
3. Wang, Z.L. and Z.C. Kang, *Functional and smart materials structural evolution and structure analysis*. 1998, New York Plenum Press.
4. Vilarinho, P.M., *Functional materials: properties, processing and applications*, in *Scanning probe microscopy: characterization, nanofabrication and device application of functional materials: proceedings of the NATO advanced study II: mathematics, physics and chemistry*, P.M. Vilarinho, Y. Rosenwaks, and A. Kingon, Editors. 2005, Kluwer Academic Publ.: Dordrecht.
5. Park, S.-E. and T.R. Shrout, *Ultrahigh strain and piezoelectric behavior in relaxor based ferroelectric single crystals.* Applied Physics Letters, 1997. **82**(4): p. 1804-1811.
6. Needleman, H., *Lead poisoning.* Annual Review of Medicine, 2004. **55**(1): p. 209-222.
7. Needleman, H., *Low level lead exposure: history and discovery.* Annals of Epidemiology, 2009. **19**(4): p. 235-238.
8. Needleman, H., *Low level lead exposure and the development of children.* The Southeast Asian Jjournal of Tropical Medicine and Public Health, 2004. **35**(2): p. 252-4.
9. *OJ L 37 19, European Parliament ant the Council* 2003.
10. Shrout, T.R. and S.J. Zhang, *Lead-free piezoelectric ceramics: Alternatives for PZT?* Journal of Electroceramics, 2007. **19**(1): p. 111-124.
11. Malic, B., A. Bencan, T. Rojac, and M. Kosec, *Lead-free piezoelectrics based on alkaline niobates: synthesis, sintering and microstructure.* Acta Chimica Slovenica, 2008. **55**(4): p. 719-726.
12. Rödel, J., W. Jo, K.T.P. Seifert, E.-M. Anton, T. Granzow, and D. Damjanovic, *Perspective on the development of lead-free piezoceramics.* Journal of the American Ceramic Society, 2009. **92**(6): p. 1153-1177.
13. Takenaka, T., K. Maruyama, and K. Sakata, *$(Bi_{1/2}Na_{1/2})TiO_3$-$BaTiO_3$ system for lead-free piezoelectric ceramics.* Japanese Journal of Applied Physics Part 1-Regular Papers Short Notes & Review Papers, 1991. **30**(9B): p. 2236-2239.
14. Webber, K.G., R. Zuo, and C.S. Lynch, *Ceramic and single-crystal (1–x)PMN–xPT constitutive behavior under combined stress and electric field loading.* Acta Materialia, 2008. **56**(6): p. 1219-1227.
15. Fu, H.X. and R.E. Cohen, *Polarization rotation mechanism for ultrahigh electromechanical response in single-crystal piezoelectrics.* Nature, 2000. **403**(6767): p. 281-283.

16. Rafiq, M.A., M.E.V. Costa, and P.M. Vilarinho, *Establishing the domain structure of ($K_{0.5}Na_{0.5}$)NbO_3 (KNN) single crystals by piezoforce-response microscopy* Science of Advanced Materials, 2014. **6**(3): p. 426-433.
17. Ursic, H., A. Bencan, M. Skarabot, M. Godec, and M. Kosec, *Dielectric, ferroelectric, piezoelectric, and electrostrictive properties of $K_{0.5}Na_{0.5}NbO_3$ single crystals.* Journal of Applied Physics, 2010. **107**(3): p. 033705-5.
18. Messing, G.L., S. Trolier-McKinstry, E.M. Sabolsky, C. Duran, S. Kwon, B. Brahmaroutu, P. Park, H. Yilmaz, P.W. Rehrig, K.B. Eitel, E. Suvaci, M. Seabaugh, and K.S. Oh, *Templated grain growth of textured piezoelectric ceramics.* Critical Reviews in Solid State and Materials Sciences, 2004. **29**(2): p. 45-96.
19. Carter, C.B. and M.G. Norton, *Ceramic materials ccience and cngineering.* 2007, New York: Springer.
20. Moulson, A.J. and J.M. Herbert, *Electroceramics materials, properties, applications*. Second ed. 2003, New York: John Wiley & Sons, Ltd
21. Haertling, G.H., *Ferroelectric ceramics: history and technology.* Journal of the American Ceramic Society, 1999. **82**(4): p. 797-818.
22. Valasek, J., *Piezo-electric and allied phenomena in Rochelle salt.* Physical Review, 1921. **17**(4): p. 475-481.
23. Soergel, E., *Visualization of ferroelectric domains in bulk single crystals.* Applied Physics B: Lasers and Optics, 2005. **81**(6): p. 729-751.
24. Shu, Y.C. and K. Bhattacharya, *Domain patterns and macroscopic behaviour of ferroelectric materials.* Philosophical Magazine B-Physics of Condensed Matter Statistical Mechanics Electronic Optical and Magnetic Properties, 2001. **81**(12): p. 2021-2054.
25. Herber, R.P., G.A. Schneider, S. Wagner, and M.J. Hoffmann, *Characterization of ferroelectric domains in morphotropic potassium sodium niobate with scanning probe microscopy.* Applied Physics Letters, 2007. **90**(25): p. 252905-3.
26. Potnis, P.R., N.-T. Tsou, and J.E. Huber, *A review of domain modelling and domain imaging techniques in ferroelectric crystals.* Materials, 2011. **4**(2): p. 417-447.
27. Fousek, J. and V. Janovec, *The orientation of domain walls in twinned ferroelectric crystals.* Journal of Applied Physics, 1969. **40**(1): p. 135-142.
28. Sapriel, J., *Domain-wall orientations in ferroelastics.* Physical Review B, 1975. **12**(11): p. 5128-5140.
29. Arlt, G., *Twinning in ferroelectric and ferroelastic ceramics: stress relief.* Journal of Materials Science, 1990. **25**(6): p. 2655-2666.
30. Inagaki, Y., K.-i. Kakimoto, and I. Kagomiya, *Crystal growth and ferroelectric property of $Na_{0.5}K_{0.5}NbO_3$ and Mn-doped $Na_{0.5}K_{0.5}NbO_3$ crystals grown by floating zone method.* Journal of the European Ceramic Society, 2010. **30**(2): p. 301-306.
31. Li, J.Y., R.C. Rogan, E. Ustundag, and K. Bhattacharya, *Domain switching in polycrystalline ferroelectric ceramics.* Nature Materials, 2005. **4**(10): p. 776-781.
32. Patel, I., *Ceramic based intelligent piezoelectric energy harvesting device*. Advances in Ceramics - Electric and Magnetic Ceramics, Bioceramics, Ceramics and Environment. 2011, Rijeka: In Tech.

33. Jaffe, B., W.R. Cook, and H. Jaffe, *Piezoelectric ceramics*. Vol. 3. 1971, London: Acadamic Press.
34. Schneider, G.A., *Influence of electric field and mechanical stresses on the fracture of ferroelectrics*, in *Annual Review of Materials Research*. 2007. p. 491-538.
35. Aggarwal, S. and R. Ramesh, *Point defect chemistry of metal oxide heterostructures.* Annual Review of Materials Science, 1998. **28**: p. 463-499.
36. Smyth, D.M., *The Defect Chemistry of Metal Oxides*. 2000, Oxford: Oxford University Press.
37. Mittemeijer, E.J., *Fundamentals of materials science: The microstructure–property relationship using metals as model systems*. 2010, Berlin: Springer.
38. Raymond, M.V. and D.M. Smyth, *Defects and charge transport in perovskite ferroelectrics.* Journal of Physics and Chemistry of Solids, 1996. **57**(10): p. 1507-1511.
39. Araujo, C.P.D., G.W. Taylor, and J.F. Scott, *Synthesis and basic properties*, in *Ferroelectric thin films*, C.P.D. Araujo, G.W. Taylor, and J.F. Scott, Editors. 1996, Gordon and Breach: Amsterdam. p. 47-92.
40. Galasso, F.S., *Structure, properties, and preparation of perovskite-type compounds*. 1969, New York: Pergamon Press.
41. Zhong, W. and D. Vanderbilt, *Competing structural instabilities in cubic perovskites.* Physical Review Letters, 1995. **74**(13): p. 2587-2590.
42. Huaxiang, F. and R.E. Cohen, *Polarization rotation mechanism for ultrahigh electromechanical response in single-crystal piezoelectrics.* Nature, 2000. **403**(6767): p. 281-3.
43. Yamamoto, T., *Ferroelectric properties of the $PbZrO_3$–$PbTiO_3$ system.* Jpn. J. Appl. Phys., 1996. **35**(Part 1, No. 9B): p. 5104-5108.
44. http://www.piceramic.com/index.php [Accessed on 16-10-2012].
45. http://www.morganelectroceramics.com/ [Accessed on 14-09-2011].
46. Ikegami, S., I. Ueda, and T. Nagata, *Electromechanical properties of $PbTiO_3$ ceramics containing La and Mn.* Journal of the Acoustical Society of America, 1971. **50**(4): p. 1060-6.
47. Damjanovic, D., T.R. Gururaja, and L.E. Cross, *Anisotropy in piezoelectric properties of modified lead titanate ceramics.* American Ceramic Society Bulletin, 1987. **66**(4): p. 699-703.
48. Lee, H.S. and T. Kimura, *Effects of microstructure on the dielectric and piezoelectric properties of lead metaniobate.* Journal of the American Ceramic Society, 1998. **81**(12): p. 3228-3236.
49. Sakata, K., T. Takenaka, and Y. Naitou, *Phase-relations, dielectric and piezoelectric properties of ceramics in the sytem $(Bi_{0.5}Na_{0.5})TiO_3$-$PbTiO_3$.* Ferroelectrics, 1992. **131**(1-4): p. 219-226.
50. Nanamatsu, S., M. Kimura, and T. Kawamura, *Crystallographic and dielectric properties of ferroelectric $A_2B_2O_7$ (A=Sr, B=Ta, Nb) Crystals and Their Solid Solutions.* Journal of the Physical Society of Japan, 1975. **38**(3): p. 817-824.
51. Kosec, M. and D. Kolar, *On Activated Sintering and Electrical Properties of $NaKNbO_3$.* Materials Research Bulletin, 1975. **10**: p. 335-340.

52. Ringgaard, E. and T. Wurlitzer. *Lead-free piezoceramics based on alkali niobates*. in *9th Electroceramics Congress*. 2004. Cherbourg, FRANCE.
53. Zhang, B.P., J.F. Li, K. Wang, and H.L. Zhang, *Compositional dependence of piezoelectric properties in $Na_xK_{1-x}NbO_3$ lead-free ceramics prepared by spark plasma sintering.* Journal of the American Ceramic Society, 2006. **89**(5): p. 1605-1609.
54. Jaeger, R.E. and L. Egerton, *Hot pressing of potassium-sodium niobates.* Journal of the American Ceramic Society, 1962. **45**(5): p. 209-213.
55. Choi, S.W., T.R. Shrout, S.J. Jang, and A.S. Bhalla, *Dielectric and pyroelectric properties in the $Pb(Mg_{1/3}Nb_{2/3})O_3$-$PbTiO_3$ system.* Ferroelectrics, 1989. **100**: p. 29-38.
56. Jaffe, H. and B. Da, *Piezoelectric transducer materials.* Proceedings of the Institute of Electrical and Electronics Engineers, 1965. **53**(10): p. 1372-1386.
57. Defense, U.S.D.o., *Military standard: piezoelectric ceramic material and measurements guidelines for sonar transducers*. 1995, MIL-STD-1376B(SH) (Naval Sea Systems Command, Arlington, VA,.
58. Berlincourt, D.A., C. Cmolik, and H. Jaffe, *Piezoelectric properties of polycrystalline lead titanate zirconate compositons.* Proceedings of the Institute of Radio Engineers, 1960. **48**(2): p. 220-229.
59. Park, S.E. and T.R. Shrout, *Characteristics of relaxor-based piezoelectric single crystals for ultrasonic transducers.* IEEE Transactions on Ultrasonics Ferroelectrics and Frequency Control, 1997. **44**(5): p. 1140-1147.
60. Li, T., A.M. Scotch, H.M. Chan, M.P. Harmer, S.E. Park, T.R. Shrout, and J.R. Michael, *Single crystals of $Pb(Mg_{1/3}Nb_{2/3})O_3$-35 mol% $PbTiO_3$ from polycrystalline precursors.* Journal of the American Ceramic Society, 1998. **81**(1): p. 244-248.
61. *California health and safety code 25214.9–25214.10.2*. 2006
62. *On the restriction of the use of certain hazardous substances in electrical and electronic equipment*, in *DIRECTIVE 2002/95/EC*. 2003: European Parliament and the Council. p. 19-23.
63. Shirane, G., R. Newnham, and R. Pepensky, *Dielectric properties and phase transitions of $NaNbO_3$ and $(Na,K)NbO_3$.* Physical Review, 1954. **96**(3): p. 581-588.
64. Saito, Y., H. Takao, T. Tani, T. Nonoyama, K. Takatori, T. Homma, T. Nagaya, and M. Nakamura, *Lead-free piezoceramics.* Nature, 2004. **432**(7013): p. 84-87.
65. Egerton, L. and D.M. Dillon, *Piezoelectric and dielectric properties of ceramics in the system potassium-sodium niobate.* Journal of the American Ceramic Society, 1959. **42**: p. 438-442.
66. Haertling, G.H., *Properties of hot-pressed ferroelectric alkali niobate ceramics.* Journal of the American Ceramic Society, 1967. **50**: p. 329-330.
67. Matsubara, M., T. Yamaguchi, W. Sakamoto, K. Kikuta, T. Yogo, and S. Hirano, *Processing and piezoelectric properties of lead-free $(K,Na)(Nb,Ta)O_3$ ceramics.* Journal of the American Ceramic Society, 2005. **88**(5): p. 1190-1196.
68. Matsubara, M., T. Yamaguchi, K. Kikuta, and S. Hirano, *Effect of Li substitution on the piezoelectric properties of potassium sodium niobate ceramics.* Japanese Journal of Applied Physics, 2005. **44**(8): p. 6136-6142.

69. Mgbemere, H.E., M. Hinterstein, and G.A. Schneider, *Electrical and structural characterization of $(K_xNa_{1-x})NbO_3$ ceramics modified with Li and Ta.* Journal of Applied Crystallography, 2011. **44**: p. 1080-1089.
70. Mgbemere, H.E., G.A. Schneider, and T.A. Stegk, *Effect of Antimony Substitution for Niobium on the Crystal Structure, Piezoelectric and Dielectric Properties of $(K_{0.5}Na_{0.5})NbO_3$ Ceramics.* Functional Materials Letters, 2010. **3**(1): p. 25-30.
71. Guo, Y.P., K. Kakimoto, and H. Ohsato, *$(Na_{0.5}K_{0.5})NbO_3$-$LiTaO_3$ lead-free piezoelectric ceramics.* Materials Letters, 2005. **59**(2-3): p. 241-244.
72. Zhang, S., R. Xia, T.R. Shrout, G. Zang, and J. Wang, *Piezoelectric properties in perovskite $0.948(K_{0.5}Na_{0.5})NbO_3$-$0.052LiSbO_3$ lead-free ceramics.* Journal of Applied Physics, 2006. **100**(10): p. 104108-6.
73. Eriksson, M., H. Yan, G. Viola, H. Ning, D. Gruner, M. Nygren, M.J. Reece, and Z. Shen, *Ferroelectric domain structures and electrical properties of fine-grained lead-free sodium potassium niobate ceramics.* Journal of the American Ceramic Society, 2011. **94**(10): p. 3391-3396.
74. Ahtee, M. and A.W. Hewat, *The structures of $Na_{0.98}K_{0.02}NbO_3$ and $Na_{0.90}K_{0.10}NbO_3$ (phase Q) at room temperature by neutron powder diffraction.* Acta Crystallographica Section A, 1975. **31**(6): p. 846-850.
75. Shiratori, Y., A. Magrez, and C. Pithan, *Particle size effect on the crystal structure symmetry of $K_{0.5}Na_{0.5}NbO_3$.* Journal of the European Ceramic Society, 2005. **25**: p. 2075-2079.
76. Shiratori, Y., A. Magrez, and C. Pithan, *Phase transformation of $KNaNb_2O_6$ induced by size effect.* Chemical Physics Letters, 2004. **391**(4–6): p. 288-292.
77. Mgbemere, H.E., R.P. Herber, and G.A. Schneider, *Effect of MnO_2 on the dielectric and piezoelectric properties of alkaline niobate based lead free piezoelectric ceramics.* Journal of the European Ceramic Society, 2009. **29**(9): p. 1729-1733.
78. Mgbemere, H.E., M. Hinterstein, and G.A. Schneider, *Structural phase transitions and electrical properties of $(K_xNa_{1-x})NbO_3$ - based ceramics modified with Mn.* Journal of the European Ceramic Society, 2012. **32**(16): p. 4341-4352.
79. Tellier, J., B. Malic, B. Dkhil, D. Jenko, J. Cilensek, and M. Kosec, *Crystal structure and phase transitions of sodium potassium niobate perovskites.* Solid State Sciences, 2009. **11**(2): p. 320-324.
80. Ringgaard, E. and T. Wurlitzer, *Lead-free piezoceramics based on alkali niobates.* Journal of the European Ceramic Society, 2005. **25**(12): p. 2701-2706.
81. Kingon, A.I. and S. Srinivasan, *Lead zirconate titanate thin films directly on copper electrodes for ferroelectric, dielectric and piezoelectric applications.* Nature Materials, 2005. **4**(3): p. 233-237.
82. Bretos, I., R. Jiménez, A. Wu, A.I. Kingon, P.M. Vilarinho, and M.L. Calzada, *Activated solutions enabling low-temperature processing of functional ferroelectric oxides for flexible electronics.* Advanced Materials, 2013: p. 10.1002/adma.201304308.
83. Li, J.F., K. Wang, B.P. Zhang, and L.M. Zhang, *Ferroelectric and piezoelectric properties of fine-grained $Na_{0.5}K_{0.5}NbO_3$ lead-free piezoelectric ceramics*

prepared by spark plasma sintering. Journal of the American Ceramic Society, 2006. **89**(2): p. 706-709.
84. Saito, Y. and H. Takao, *High performance lead-free piezoelectric ceramics in the (K,Na)NbO_3-$LiTaO_3$ solid solution system.* Ferroelectrics, 2006. **338**: p. 1433-1448.
85. Zhao, P., B.P. Zhang, and J.F. Li, *High piezoelectric d_{33} coefficient in Li-modified lead-free (Na,K)NbO_3 ceramics sintered at optimal temperature.* Applied Physics Letters, 2007. **90**(24): p. 242909-3.
86. Zhao, P., B.P. Zhang, and J.F. Li, *Enhancing piezoelectric d_{33} coefficient in Li/Ta-codoped lead-free (Na,K) NbO_3 ceramics by compensating Na and K at a fixed ratio.* Applied Physics Letters, 2007. **91**: p. 172901-3.
87. Rani, R., S. Sharma, R. Rai, and A.L. Kholkin, *Doping effects of Li-Sb content on the structure and electrical properties of [$(Na_{0.5}K_{0.5})_{1-x}(Li)_x(Sb)_x(Nb)_{1-x}O_3$] lead-free piezoelectric ceramics.* Materials Research Bulletin, 2012. **47**(2): p. 381-386.
88. Shimojo, Y., R.P. Wang, T. Sekiya, and K. Matsuzaki, *Dielectric and piezoelectric properties of $MeTiO_3$ (Me = Ba and Sr) modified (K, Na)NbO_3.* Journal of the Korean Physical Society, 2005. **46**(1): p. 48-51.
89. Zuo, R.Z., J. Rodel, R.Z. Chen, and L.T. Li, *Sintering and electrical properties of lead-free $Na_{0.5}K_{0.5}NbO_3$ piezoelectric ceramics.* Journal of the American Ceramic Society, 2006. **89**(6): p. 2010-2015.
90. Malic, B., J. Bernard, J. Holc, D. Jenko, and M. Kosec, *Alkaline-earth doping in (K,Na)NbO_3 based piezoceramics.* Journal of the European Ceramic Society, 2005. **25**(12): p. 2707-2711.
91. Malic, B., J. Bernard, J. Holc, and M. Kosec, *Strontium doped $K_{0.5}Na_{0.5}NbO_3$ based piezoceramics.* Ferroelectrics, 2005. **314**: p. 149-156.
92. Maeder, M.D., D. Damjanovic, and N. Setter, *Lead free piezoelectric materials.* Journal of Electroceramics, 2004. **13**(1-3): p. 385-392.
93. Ahn, Z.S. and W.A. Schulze, *Conventionally sintered ($Na_{0.5}K_{0.5}$)NbO_3 with barium additions.* Journal of the American Ceramic Society, 1987. **70**(1): p. C18–C21.
94. Tashiro, S. and K. Ishii, *Grain size and piezoelectric properties of (Ba, K, Na)NbO_3 lead-free ceramics.* Journal of the Ceramic Society of Japan, 2006. **114**(1329): p. 386-391.
95. Murty, S.N. and A. Bhanumathi, *Phase transitions in europium doped (Na,K)NbO_3 ceramics.* Ferroelectrics, 1989. **94**: p. 285-290.
96. Matsubara, M., T. Yamaguchi, K. Kikuta, and S. Hirano, *Sinterability and piezoelectric properties of (K,Na)NbO_3 ceramics with novel sintering aid.* Japanese Journal of Applied Physics, 2004. **43**(10): p. 7159-7163.
97. Matsubara, M., T. Yamaguchi, K. Kikuta, and S. Hirano, *Sintering and piezoelectric properties of potassium sodium niobate ceramics with newly developed sintering aid.* Japanese Journal of Applied Physics Part 1-Regular Papers Short Notes & Review Papers, 2005. **44**(1A): p. 258-263.
98. Guo, Y.P., K. Kakimoto, and H. Ohsato, *Phase transitional behavior and piezoelectric properties of ($Na_{0.5}K_{0.5}$)NbO_3-$LiNbO_3$ ceramics.* Applied Physics Letters, 2004. **85**(18): p. 4121-4123.

99. Higashide, K., K.I. Kakimoto, and H. Ohsato, *Temperature dependence on the piezoelectric property of (1-x)($Na_{0.5}K_{0.5}$)NbO_3-x$LiNbO_3$ ceramics.* Journal of the European Ceramic Society, 2007. **27**(13-15): p. 4107-4110.
100. Hollenstein, E., D. Damjanovic, and N. Setter, *Temperature stability of the piezoelectric properties of Li-modified KNN ceramics.* Journal of the European Ceramic Society, 2007. **27**(13-15): p. 4093-4097.
101. Hollenstein, E., M. Davis, D. Damjanovic, and N. Setter, *Piezoelectric properties of Li- and Ta-modified ($K_{0.5}Na_{0.5}$)NbO_3 ceramics.* Applied Physics Letters, 2005. **87**(18): p. 182905-3.
102. Zang, G.Z., J.F. Wang, H.C. Chen, W.B. Su, C.M. Wang, P. Qi, B.Q. Ming, J. Du, and L.M. Zheng, *Perovskite ($Na_{0.5}K_{0.5}$)$_{1-x}$($LiSb$)$_x$$Nb_{1-x}O_3$ lead-free piezoceramics.* Applied Physics Letters, 2006. **88**(21): p. 212908-3.
103. Elwell, D.a. and H.J. Schell, *Crystal growth from high-temperature solutions* 1975, London: Acadamic Press.
104. Couper, J.R., W.R. Penney, J.R. Fair, and S.M. Walas, *Crystallization from Solutions and Melts*, in *Chemical Process Equipment (Third Edition)*, J.R. Couper, W.R. Penney, J.R. Fair, and S.M. Walas, Editors. 2012, Butterworth-Heinemann: Boston. p. 561-589.
105. Bugaris, D.E. and H.-C. zur Loye, *Materials discovery by flux crystal growth: quaternary and higher order oxides.* Angewandte Chemie International Edition, 2012. **51**(16): p. 3780-3811.
106. Hurle, D.T.J., *Handbook of crystal growth: Bulk crystal growth. Basic techniques*. 1994, North-Holland: Elsevier Science.
107. Scott, B.A. and G. Burns, *Crystal growth and observation of the ferroelectric phase of $PbZrO_3$.* Journal of the American Ceramic Society, 1972. **55**(7): p. 331-333.
108. Fisher, J.G., A. Bencan, J. Holc, M. Kosec, S. Vernay, and D. Rytz, *Growth of potassium sodium niobate single crystals by solid state crystal growth.* Journal of Crystal Growth, 2007. **303**(2): p. 487-492.
109. Inagaki, Y. and K. Kakimoto, *Dielectric and piezoelectric properties of Mn-doped $Na_{0.5}K_{0.5}NbO_3$ Single crystals grown by flux method.* Applied Physics Express, 2008. **1**(6): p. 061602-3.
110. Kizaki, Y., Y. Noguchi, and M. Miyayama, *Defect control for low leakage current in $K_{0.5}Na_{0.5}NbO_3$ single crystals.* Applied Physics Letters, 2006. **89**(14): p. 142910-3.
111. Lin, D.B., Z.R. Li, Z. Xu, and X. Yao, *Characterization of KNN single crystals by slow-cooling technique.* Ferroelectrics, 2009. **381**: p. 1-8.
112. Gupta, S. and S. Priya, *Ferroelectric properties and dynamic scaling of <100> oriented ($K_{0.5}Na_{0.5}$)NbO_3 single crystals.* Applied Physics Letters, 2011. **98**(24): p. 242906-3.
113. Kizaki, Y., Y. Noguchi, and M. Miyayama. *Defect control for superior properties in $K_{0.5}Na_{0.5}NbO_3$ single crystals*. in *26th Electronics Division Meeting of the Ceramic-Society-of-Japan*. 2006. Tokyo, Japan.
114. Bencan, A., J. Fisher, A.S. Vernay, D. Rytz, J. Holc, and M. Kosec, *Electron microscopy studies of alkali niobate single crystals using the solid state crystal growth method.* Scanning, 2006. **28**(2): p. 123-124.

115. Fisher, J.G., A. Bencan, J. Bernard, J. Holc, M. Kosec, S. Vernay, and D. Rytz, *Growth of (Na, K, Li)(Nb, Ta)O_3 single crystals by solid state crystal growth.* Journal of the European Ceramic Society, 2007. **27**(13-15): p. 4103-4106.
116. Bencan, A., E. Tchernychova, M. Godec, J. Fisher, and M. Kosec, *Compositional and structural study of a ($K_{0.5}Na_{0.5}$)NbO_3 single crystal prepared by solid state crystal growth.* Microscopy and Microanalysis, 2009. **15**(5): p. 435-440.
117. Lin, D.B., Z.R. Li, S.J. Zhang, Z. Xu, and X. Yao, *Dielectric/piezoelectric properties and temperature dependence of domain structure evolution in lead free ($K_{0.5}Na_{0.5}$)NbO_3 single crystal.* Solid State Communications, 2009. **149**(39-40): p. 1646-1649.
118. Fisher, J.G., A. Bencan, J. Godnjavec, and M. Kosec, *Growth behaviour of potassium sodium niobate single crystals grown by solid-state crystal growth using K4CuNb8O23 as a sintering aid.* Journal of the European Ceramic Society, 2008. **28**: p. 1657-1663.
119. Barry, C.C. and M.N. Grant, *Ceramics materials, science and engineering*. 2nd ed. 2007, New York: Springer.
120. Takenaka, T. and K. Sakata, *Grain orientation and electrical properties of hot-forged $Bi_4Ti_3O_{12}$ ceramics.* Japanese Journal of Applied Physics, 1980. **19**(1): p. 31-39.
121. McKinstry, S.T., E. M. Sabolsky, S. Kwon, J. H. Yoshimura, J. H. Park, a. G. Zhang, and G. L. Messing, *Oriented films and ceramics of relaxor-ferroelectric-$PbTiO_3$ solid solutions*, in *Piezoelectric Materials and Devices*, N. Setter, Editor. 2002, Ceramics Laboratory, EPFL Swiss Federal Institute of Technology,: Lausanne 1015, Switzerland. p. 497–518.
122. West, D.L. and D.A. Payne, *Reactive-templated grain growth of $Bi_{1/2}(Na,K)_{1/2}TiO_3$: Effects of formulation on texture development.* Journal of the American Ceramic Society, 2003. **86**(7): p. 1132-1137.
123. Chang, Y., S. Poterala, Z. Yang, and G.L. Messing, *Enhanced electromechanical properties and temperature stability of textured ($K_{0.5}Na_{0.5}$)NbO_3-based piezoelectric ceramics.* Journal of the American Ceramic Society, 2011. **94**(8): p. 2494-2498.
124. Li, Y.-L., C. Hui, Y.-X. Li, and Y.-L. Wang, *Enhanced ferroelectric and piezoelectric properties of textured $K_{0.45}Na_{0.55}NbO_3$ ceramics prepared by screen-printing technique.* Journal of Inorganic Materials, 2012. **27**(2): p. 214-218.
125. Cho, H.J., M.H. Kim, T.K. Song, J.S. Lee, and J.H. Jeon, *Piezoelectric and ferroelectric properties of textured ($Na_{0.50}K_{0.47}Li_{0.03}$)($Nb_{0.8}Ta_{0.2}$)$O_3$ ceramics by using template grain growth method.* Journal of Electroceramics, 2013. **30**(1-2): p. 72-76.
126. Lv, D. and R. Zuo, *Evolution of crystallographic grain orientation and anisotropic properties of ($K_{0.5}Na_{0.5}$)NbO_3 ceramics using $BaTiO_3$ templates by reactive templated grain growth.* Journal of Alloys and Compounds, 2013. **560**(0): p. 62-66.
127. Hao, J., C. Ye, B. Shen, and J. Zhai, *Enhanced piezoelectric properties of 〈001〉 textured lead-free (K_xNa_{1-x})$_{0.946}Li_{0.054}NbO_3$ ceramics with large strain.* physica status solidi (a), 2012. **209**(7): p. 1343-1349.

128. Saito, Y., H. Takao, T. Tani, T. Nonoyama, K. Takatori, T. Homma, T. Nagaya, and, and M. Nakamura, *High performance lead-free piezoelectric material.* R&D Review of Toyota CRDL 2006. **41** (2): p. 22-28.
129. Chang, Y., S.F. Poterala, Z. Yang, S. Trolier-McKinstry, and G.L. Messing, *<001> textured $(K_{0.5}Na_{0.5})(Nb_{0.97}Sb_{0.03})O_3$ piezoelectric ceramics with high electromechanical coupling over a broad temperature range.* Applied Physics Letters, 2009. **95**(23): p. 232905-3.
130. Jenko, D., A. Bencan, B. Malic, J. Holc, and M. Kosec, *Electron microscopy studies of potassium sodium niobate ceramics.* Microscopy and Microanalysis, 2005. **11**(6): p. 572-580.
131. Rubio-Marcos, F., A. Del Campo, R. Lopez-Juarez, J.J. Romero, and J.F. Fernandez, *High spatial resolution structure of $(K,Na)NbO_3$ lead-free ferroelectric domains.* Journal of Materials Chemistry, 2012. **22**(19): p. 9714-9720.
132. Jenkins, R. and R.L. Snyder, *Diffraction theory*, in *Introduction to X-ray powder diffractometry*. 1996, John Wiley & Sons, Inc.: New York. p. 47-95.
133. Bragg, W.L. and J.J. Thomson, *The diffraction of short electromagnetic waves by a crystal.* Proceedings of the Cambridge Philosophical Society, 1914. **17**: p. 43-57.
134. Cullity, B.D., *Elements of X-Ray diffraction* 2nd ed. 1978, London: Addison-Wesley.
135. Lawes, G., *Scanning electron microscopy and x-ray microanalysis*. 1987, New York John Wiley and Sons Inc.
136. *http://imagej.nih.gov/*. [Accessed on 16-06-2012].
137. Williams, D.B. and C.B. Carter, *Transmission electron microscopy: A textbook for materials science*. 1996, New York: Plenum Press.
138. Ferraro, J.R., K. Nakamoto, and C.W. Brown, *Introductory Raman spectroscopy*. 2003, Amsterdam: Academic Press.
139. *TF analyzer 1000 instruction manual*. 2001.
140. Macdonald, J.R. and W.B. Johnson, *Fundamentals of impedance spectroscopy*, in *Impedance Spectroscopy*. 2005, John Wiley & Sons, Inc. p. 1-26.
141. Sinclair, D.C. and A.R. West, *Impedance and modulus spectroscopy of semiconducting $BaTiO_3$ showing positive temperature coefficient of resistance.* Journal of Applied Physics, 1989. **66**(8): p. 3850-3856.
142. West, A., D. Sinclair, and N. Hirose, *Characterization of electrical materials, especially ferroelectrics, by impedance spectroscopy.* Journal of Electroceramics, 1997. **1**(1): p. 65-71.
143. Chen, T.C., C.L. Thio, and S.B. Desu, *Impedance spectroscopy of $SrBi_2Ta_2O_9$ and $SrBi_2Nb_2O_9$ ceramics correlation with fatigue behavior.* Journal of Materials Research, 1997. **12**(10): p. 2628-2637.
144. Barsoukov, E. and J.R. Macdonald, *Impedance Spectroscopy: Theory, Experiment, and Applications*. 2005, New Jersey: John Wiley & Sons, Inc.
145. Gruverman, A. and A. Kholkin, *Nanoscale ferroelectrics: processing, characterization and future trends.* Reports on Progress in Physics, 2006. **69**(8): p. 2443-2474.

146. Alexe, M. and A. Gruverman, *"Nanoscale characterization of ferroelectric materials: scanning probe microscopy approach*. 2004, Berlin: Springer-Verlag.
147. Balke, N., I. Bdikin, S.V. Kalinin, and A.L. Kholkin, *Electromechanical imaging and spectroscopy of ferroelectric and piezoelectric materials: state of the art and prospects for the future.* Journal of the American Ceramic Society, 2009. **92**(8): p. 1629-1647.
148. Gruverman, A., O. Auciello, and H. Tokumoto, *Imaging and control of domain structures in ferroelectric thin films via scanning force microscopy.* Annual Review of Materials Science, 1998. **28**: p. 101-123.
149. Soergel, E., *Piezoresponse force microscopy (PFM).* Journal of Physics D-Applied Physics, 2011. **44**: p. 464003-17.
150. Ahn, C.W., C.H. Choi, H.Y. Park, S. Nahm, and S. Priya, *Dielectric and piezoelectric properties of (1-x)($Na_{0.5}K_{0.5}$)NbO_3-x$BaTiO_3$ ceramics.* Journal of Materials Science, 2008. **43**(20): p. 6784-6797.
151. Wang, K. and J.-F. Li, *Domain engineering of lead-free Li-modified (K,Na)NbO_3 polycrystals with highly enhanced piezoelectricity.* Advanced Functional Materials, 2010. **20**(12): p. 1924-1929.
152. Wang, H., D. Ruan, Y.-J. Dai, and X.-W. Zhang, *Relationship between phase structure and electrical properties of ($K_{0.5}Na_{0.5}$)NbO_3–$LiTaO_3$ lead-free ceramics.* Current Applied Physics, 2012. **12**(2): p. 504-508.
153. Zhao, P., B.P. Zhang, and J.F. Li, *Influences of sintering temperature on piezoelectric, dielectric and ferroelectric properties of Li/Ta-Codoped lead-free (Na,K)NbO3 ceramics.* Journal of the American Ceramic Society, 2008. **91**(5): p. 1690-1692.
154. Ahn, C.-W., C.-S. Park, C.-H. Choi, S. Nahm, M.-J. Yoo, H.-G. Lee, and S. Priya, *Sintering behavior of lead-free (K,Na)NbO_3-based piezoelectric ceramics.* Journal of the American Ceramic Society, 2009. **92**(9): p. 2033-2038.
155. Lee, S.C., L. Wang, H.G. Yeo, J.H. Cho, Y.S. Sung, M.H. Kim, T.K. Song, S.S. Kim, and B.C. Choi, *Effects of A-site ionic contents on piezoelectric and ferroelectric properties of lead-free ($K_{0.5}Na_{0.5}$)NbO_3-$LiNbO_3$ ceramics.* Ferroelectrics, 2009. **381**(1): p. 176-182.
156. Liu, S.J., B. Wan, P. Wang, and S.H. Song, *Influence of A-site non-stoichiometry on structure and electrical properties of $K_{0.5}Na_{0.5}NbO_3$-based lead-free piezoelectric ceramics.* Scripta Materialia, 2010. **63**(1): p. 124-127.
157. Bomlai, P., P. Wichianrat, S. Muensit, and S.J. Milne, *Effect of calcination conditions and excess alkali carbonate on the phase formation and particle morphology of $Na_{0.5}K_{0.5}NbO_3$ powders.* Journal of the American Ceramic Society, 2007. **90**(5): p. 1650-1655.
158. Acker, J., H. Kungl, and M.J. Hoffmann, *Influence of alkaline and niobium excess on sintering and microstructure of sodium-potassium niobate ($K_{0.5}Na_{0.5}$)NbO_3.* Journal of the American Ceramic Society, 2010. **93**(5): p. 1270-1281.
159. Wu, H. and P.K. Davies, *Influence of non-stoichiometry on the structure and properties of $Ba(Zn_{1/3}Nb_{2/3})O_3$ microwave dielectrics: II. compositional variations in pure BZN.* Journal of the American Ceramic Society, 2006. **89**(7): p. 2250-2263.

160. Zuo, R.Z., S. Su, Y. Wu, J. Fu, M. Wang, and L.T. Li, *Influence of A-site nonstoichiometry on sintering, microstructure and electrical properties of $(Bi_{0.5}Na_{0.5})TiO_3$ ceramics.* Materials Chemistry and Physics, 2008. **110**(2-3): p. 311-315.
161. Lin, D.M., M.S. Guo, K.H. Lam, K.W. Kwok, and H.L.W. Chan, *Lead-free piezoelectric ceramic $(K_{0.5}Na_{0.5})NbO_3$ with MnO_2 and $K_{5.4}Cu_{1.3}Ta_{10}O_{29}$ doping for piezoelectric transformer application.* Smart Materials & Structures, 2008. **17**(3): p. 035002-6.
162. Matsubara, M., K. Kikuta, and S. Hirano, *Piezoelectric properties of $(K_{0.5}Na_{0.5})(Nb_{1-x}Ta_x)O_3$ - $K_{5.4}CuTa_{10}O_{29}$ ceramics.* Journal of Applied Physics, 2005. **97**(11): p. 114105-7.
163. Rubio-Marcos, F., J.J. Romero, D.A. Ochoa, J.E. García, R. Perez, and J.F. Fernandez, *Effects of poling process on KNN-modified piezoceramic properties.* Journal of the American Ceramic Society, 2010. **93**(2): p. 318-321.
164. Mgbemere, H.E., R.P. Herber, and G.A. Schneider, *Investigation of the dielectric and piezoelectric properties of potassium sodium niobate ceramics close to the phase boundary at $(K_{0.35}Na_{0.65})NbO_3$ and partial substitutions with lithium and antimony.* Journal of the European Ceramic Society, 2009. **29**(15): p. 3271-3276.
165. He, L.-X. and C.-E. Li, *Effects of addition of MnO on piezoelectric properties of lead zirconate titanate.* Journal of Materials Science, 2000. **35**(10): p. 2477-2480.
166. Galassi, C., E. Roncari, C. Capiani, and F. Craciun, *Processing and characterization of high Q_m ferroelectric ceramics.* Journal of the European Ceramic Society, 1999. **19**(6–7): p. 1237-1241.
167. Yu, C.-S. and H.-L. Hsieh, *Piezoelectric properties of $Pb(Ni_{1/3},Sb_{2/3})O_3$-$PbTiO_3$-$PbZrO_3$ ceramics modified with MnO_2 additive.* Journal of the European Ceramic Society, 2005. **25**(12): p. 2425-2427.
168. Wang, X., M. Gu, B. Yang, S. Zhu, and W. Cao, *Hall effect and dielectric properties of Mn-doped barium titanate.* Microelectronic Engineering, 2003. **66**(1): p. 855-859.
169. Tkach, A., P.M. Vilarinho, and A.L. Kholkin, *Structure-microstructure-dielectric tunability relationship in Mn-doped strontium titanate ceramics.* Acta Materialia, 2005. **53**(19): p. 5061-5069.
170. Feng, Z.Y. and S.W. Or, *Aging-induced, defect-mediated double ferroelectric hysteresis loops and large recoverable electrostrains in Mn-doped orthorhombic KNbO3-based ceramics.* Journal of Alloys and Compounds, 2009. **480**(2): p. L29-L32.
171. Feng, Z. and X. Ren, *Aging effect and large recoverable electrostrain in Mn-doped KNbO3 based ferroelectrics.* Applied Physics Letters, 2007. **91**(3): p. 032904-3.
172. Matsumoto, K., Y. Hiruma, H. Nagata, and T. Takenaka, *Electric-field-induced strain in Mn-doped KNbO3 ferroelectric ceramics.* Ceramics International, 2008. **34**(4): p. 787-791.
173. Lundberg, M. and M. Sundberg, *Studies of phases in the KNbO3-Nb2O5 system by high-resolution electron microscopy and X-ray powder diffraction.* Journal of Solid State Chemistry, 1986. **63**(2): p. 216-230.

174. Shannon, R.D., *Revised effective ionic radii and systematic studies of interatomic distances in halides and chalcogenides.* Acta Crystallographica A, 1976. **32**: p. 751-67.
175. Wang, K. and J.F. Li, *Analysis of crystallographic evolution in (Na, K)NbO_3 based lead-free piezoceramics by x-ray diffraction.* Applied Physics Letters, 2007. **91**(26): p. 262902-3.
176. Tkach, A., P.M. Vilarinho, A.L. Kholkin, I.M. Reaney, J. Pokorny, and J. Petzelt, *Mechanisms of the effect of dopants and P(O_2) on the improper ferroelastic phase transition in $SrTiO_3$.* Chemistry of Materials, 2007. **19**(26): p. 6471-6477.
177. Tkach, A., P.M. Vilarinho, and A.L. Kholkin, *Dependence of dielectric properties of manganese-doped strontium titanate ceramics on sintering atmosphere.* Acta Materialia, 2006. **54**(20): p. 5385-5391.
178. Schierholz, R. and H. Fuess, *Symmetry of domains in morphotropic $PbZr_{1-x}Ti_xO_3$ ceramics.* Physical Review B, 2011. **84**(6): p. 064122-12.
179. Gao, J., D. Xue, Y. Wang, D. Wang, L. Zhang, H. Wu, S. Guo, H. Bao, C. Zhou, W. Liu, S. Hou, G. Xiao, and X. Ren, *Microstructure basis for strong piezoelectricity in Pb-free $Ba(Zr_{0.2}Ti_{0.8})O_3$-$(Ba_{0.7}Ca_{0.3})TiO_3$ ceramics.* Applied Physics Letters, 2011. **99**(9): p. 092901-3.
180. Woodward, D.I., J. Knudsen, and I.M. Reaney, *Review of crystal and domain structures in the $PbZr_xTi_{1-x}O_3$ solid solution.* Physical Review B, 2005. **72**(10): p. 104110-8.
181. Theissmann, R., L.A. Schmitt, J. Kling, R. Schierholz, K.A. Schonau, H. Fuess, M. Knapp, H. Kungl, and M.J. Hoffmann, *Nanodomains in morphotropic lead zirconate titanate ceramics: On the origin of the strong piezoelectric effect.* Journal of Applied Physics, 2007. **102**(2): p. 024111-6.
182. Schönau, K.A., L.A. Schmitt, M. Knapp, H. Fuess, R.-A. Eichel, H. Kungl, and M.J. Hoffmann, *Nanodomain structure of $Pb[Zr_{1-x}Ti_x]O_3$ at its morphotropic phase boundary: Investigations from local to average structure.* Physical Review B, 2007. **75**(18): p. 184117-10.
183. Jonscher, A.K., *The 'universal' dielectric response. I.* Electrical Insulation Magazine, IEEE, 1990. **6**(2): p. 16-22.
184. Raymond, O., R. Font, N. Suarez-Almodovar, J. Portelles, and J.M. Siqueiros, *Frequency-temperature response of ferroelectromagnetic $Pb(Fe_{1/2}Nb_{1/2})O_3$ ceramics obtained by different precursors. Part I. Structural and thermo-electrical characterization.* Journal of Applied Physics, 2005. **97**(8): p. 084107-8.
185. Tomczyk, M., P.M. Vilarinho, A. Moreira, and A. Almeida, *High temperature dielectric properties of $YMnO_3$ ceramics.* Journal of Applied Physics, 2011. **110**(6): p. 064116-5.
186. Jonscher, A.K., *The 'universal' dielectric response. III.* Electrical Insulation Magazine, IEEE, 1990. **6**(4): p. 19-24.
187. Prasad, N.V., G. Prasad, T. Bhimasankaram, S.V. Suryanarayana, and G.S. Kumar, *Synthesis, impedance and dielectric properties of $LaBi_5Fe_2Ti_3O_{18}$.* Bulletin of Materials Science, 2001. **24**(5): p. 487-495.

188. Pelaiz-Barranco, A., J.D.S. Guerra, R. Lopez-Noda, and E.B. Araujo, *Ionized oxygen vacancy-related electrical conductivity in* $(Pb_{1-x}La_x)(Zr_{0.90}Ti_{0.10})_{1-x/4}O_3$ *ceramics.* Journal of Physics D-Applied Physics, 2008. **41**(21): p. 215503-5.
189. Saiful Islam, M., *Ionic transport in* ABO_3 *perovskite oxides: a computer modelling tour.* Journal of Materials Chemistry, 2000. **10**(4): p. 1027-1038.
190. Liu, L., Y. Huang, C. Su, L. Fang, M. Wu, C. Hu, and H. Fan, *Space-charge relaxation and electrical conduction in* $K_{0.5}Na_{0.5}NbO_3$ *at high temperatures.* Applied Physics A: Materials Science & Processing, 2011. **104**(4): p. 1047-1051.
191. Takahashi, M., Y. Noguchi, and M. Miyayama, *Electrical conduction mechanism in* $Bi_4Ti_3O_{12}$ *single crystal.* Japanese Journal of Applied Physics Part 1-Regular Papers Short Notes & Review Papers, 2002. **41**(11B): p. 7053-7056.
192. Noguchi, Y. and M. Miyayama, *Effect of Mn doping on the leakage current and polarization properties in* $K_{0.14}Na_{0.86}NbO_3$ *ferroelectric single crystals.* Journal of the Ceramic Society of Japan, 2010. **118**(1380): p. 711-716.
193. Steinsvik, S., R. Bugge, J. Gjonnes, J. Tafto, and T. Norby, *The defect structure of* $SrTi_{1-x}Fe_xO_{3-y}$ *(x = 0-0.8) investigated by electrical conductivity measurements and electron energy loss spectroscopy (EELS).* Journal of Physics and Chemistry of Solids, 1997. **58**(6): p. 969-976.
194. Dunn, S., C.P. Shaw, Z. Huang, and R.W. Whatmore, *Ultrahigh resolution of lead zirconate titanate 30/70 domains as imaged by piezoforce microscopy.* Nanotechnology, 2002. **13**(4): p. 456-459.
195. Wu, A., P.M. Vilarinho, V.V. Shvartsman, G. Suchaneck, and A.L. Kholkin, *Domain populations in lead zirconate titanate thin films of different compositions via piezoresponse force microscopy.* Nanotechnology, 2005. **16**(11): p. 2587-2595.
196. Chen, Y.-C., G.-F. Wang, H.-H. Tai, J.-W. Chen, Y.-C. Huang, J.-C. Yang, and Y.-H. Chu, *Non-volatile domain nucleation and growth in multiferroic* $BiFeO_3$ *films.* Nanotechnology, 2011. **22**(25): p. 254030-7.
197. Inagaki, Y., K.-i. Kakimoto, and I. Kagomiya, *Ferroelectric domain characterization of orthorhombic sodium–potassium niobate piezoelectric crystals.* Journal of the American Ceramic Society, 2010. **93**(12): p. 4061-4065.
198. Anbusathaiah, V., D. Kan, F.C. Kartawidjaja, R. Mahjoub, M.A. Arredondo, S. Wicks, I. Takeuchi, J. Wang, and V. Nagarajan, *Labile ferroelastic nanodomains in bilayered ferroelectric thin films.* Advanced Materials, 2009. **21**(34): p. 3497-3502.
199. Kalinin, S.V., B.J. Rodriguez, S. Jesse, J. Shin, A.P. Baddorf, P. Gupta, H. Jain, D.B. Williams, and A. Gruverman, *Vector piezoresponse force microscopy.* Microscopy and Microanalysis, 2006. **12**(03): p. 206-220.
200. Bdikin, I.K., J.A. Pérez, I. Coondoo, A.M.R. Senos, P.Q. Mantas, and A.L. Kholkin, *Ferroelectric domain structure of* $PbZr_{0.35}Ti_{0.65}O_3$ *single crystals by piezoresponse force microscopy.* Journal of Applied Physics, 2011. **110**(5): p. 052003-7.
201. Ahtee, M. and A.M. Glazer, *Phase transitions in sodium niobate-potassium niobate solid solutions.* Ferroelectrics, 1974. **7**(1): p. 93-95.

202. Noheda, B., D.E. Cox, G. Shirane, J.A. Gonzalo, L.E. Cross, and S.E. Park, *A monoclinic ferroelectric phase in the $Pb(Zr_{1-x}Ti_x)O_3$ solid solution.* Applied Physics Letters, 1999. **74**(14): p. 2059-2061.
203. Noheda, B., D.E. Cox, G. Shirane, R. Guo, B. Jones, and L.E. Cross, *Stability of the monoclinic phase in the ferroelectric perovskite $PbZr_{1-x}Ti_xO_3$.* Physical Review B, 2000. **63**(1): p. 014103-9.
204. Oka, K., T. Koyama, T. Ozaaki, S. Mori, Y. Shimakawa, and M. Azuma, *Polarization rotation in the monoclinic perovskite $BiCo_{1-x}Fe_xO_3$.* Angewandte Chemie International Edition, 2012. **51**(32): p. 7977-7980.
205. Deluca, M., T. Sakashita, C. Galassi, and G. Pezzotti, *Investigation of local orientation and stress analysis of PZT-based materials using micro-probe polarized Raman spectroscopy.* Journal of the European Ceramic Society, 2006. **26**(12): p. 2337-2344.
206. Pojprapai, S., J.L. Jones, and M. Hoffman, *Determination of domain orientation in lead zirconate titanate ceramics by Raman spectroscopy.* Applied Physics Letters, 2006. **88**(16): p. 162903-3.
207. Deluca, M., T. Sakashita, and G. Pezzotti, *Polarized Raman scattering of domain structures in polycrystalline lead zirconate titanate.* Applied Physics Letters, 2007. **90**(5): p. 051919-3.
208. Deluca, M., M. Higashino, and G. Pezzotti, *Raman tensor elements for tetragonal $BaTiO_3$ and their use for in-plane domain texture assessments.* Applied Physics Letters, 2007. **91**(9): p. 091906-3.
209. Hu, L.J., Y.H. Chang, M.L. Hu, M.W. Chang, and W.S. Tse, *Effect of doping on the Raman modes in MgO-doped lithium niobate crystals.* Journal of Raman Spectroscopy, 1991. **22**(6): p. 333-337.
210. Zhu, W., J. Zhu, M. Wang, B. Zhu, X. Zhu, and G. Pezzotti, *Raman tensor analysis of $(K_{0.5}Na_{0.5})NbO_3$–$LiSbO_3$ lead-free ceramics and its application to study grain/domain orientation.* Journal of Raman Spectroscopy, 2012. **43**(9): p. 1320-1328.
211. Pigeon, M., R.E. Prudhomme, and M. Pezolet, *Characterization of molecular-orientation in polyethylene by Raman-spectroscopy.* Macromolecules, 1991. **24**(20): p. 5687-5694.
212. Perez, R., S. Banda, and Z. Ounaies, *Determination of the orientation distribution function in aligned single wall nanotube polymer nanocomposites by polarized Raman spectroscopy.* Journal of Applied Physics, 2008. **103**(7): p. 074302-9.
213. Okai, K., W. Zhu, and G. Pezzotti, *Domain structures in multilayer ceramic capacitors studied by polarized Raman spectroscopy* Physica Status Solidi A, 2011. **208**(5): p. 1132-1140.
214. Loudon, R., *Raman effect in crystals.* Advances in Physics, 1964. **13**(52): p. 423-482.
215. Rubio-Marcos, F., M.A. Bañares, J.J. Romero, and J.F. Fernandez, *Correlation between the piezoelectric properties and the structure of lead-free KNN-modified ceramics, studied by Raman Spectroscopy.* Journal of Raman Spectroscopy, 2011. **42**(4): p. 639-643.

216. Damen, T.C., S.P.S. Porto, and B. Tell, *Raman effect in zinc oxide.* Physical Review, 1966. **142**(2): p. 570-574.
217. Lipkin, D.M. and D.R. Clarke, *Sample-probe interactions in spectroscopy: Sampling microscopic property gradients.* Journal of Applied Physics, 1995. **77**(5): p. 1855-1863.
218. Atkinson, A., S.C. Jain, and S.J. Webb, *Convolution of spectra in optical microprobe experiments.* Semiconductor Science and Technology, 1999. **14**(6): p. 561-564.
219. Guo, S. and R.I. Todd, *Confocal fluorescence microscopy in alumina-based ceramics: Where does the signal come from?* Journal of the European Ceramic Society, 2010. **30**(3): p. 641-648.
220. *http://refractiveindex.info/?group=CRYSTALS&material=KNbO3*. [Accessed on 24-08-2012].
221. Kroumova, E., M.I. Aroyo, J.M. Perez-Mato, A. Kirov, C. Capillas, S. Ivantchev, and H. Wondratschek, *Bilbao crystallographic server : useful databases and tools for phase-transition studies.* Phase Transitions, 2003. **76**(1-2): p. 155-170.
222. Lima, K.C.V., A.G.S. Filho, A.P. Ayala, J.M. Filho, P.T.C. Freire, F.E.A. Melo, E.B. Araújo, and J.A. Eiras, *Raman study of morphotropic phase boundary in $PbZr_{1-x}Ti_xO_3$ at low temperatures.* Physical Review B, 2001. **63**(18): p. 184105-5.
223. Souza Filho, A.G., K.C.V. Lima, A.P. Ayala, I. Guedes, P.T.C. Freire, F.E.A. Melo, J. Mendes Filho, E.B. Araújo, and J.A. Eiras, *Raman scattering study of the $PbZr_{1-x}Ti_xO_3$ system: Rhombohedral-monoclinic-tetragonal phase transitions.* Physical Review B, 2002. **66**(13): p. 132107-4.
224. Deluca, M., H. Fukumura, N. Tonari, C. Capiani, N. Hasuike, K. Kisoda, C. Galassi, and H. Harima, *Raman spectroscopic study of phase transitions in undoped morphotropic $PbZr_{1-x}TixO_3$.* Journal of Raman Spectroscopy, 2011. **42**(3): p. 488-495.
225. Tarrach, G., P.L. L, R.H. Z, F. Schlaphof, C. Loppacher, and L.M. Eng, *Nanometer spot allocation for Raman spectroscopy on ferroelectrics by polarization and piezoresponse force microscopy.* Applied Physics Letters, 2001. **79**(19): p. 3152-3154.
226. Kobor, D., B. Guiffard, L. Lebrun, A. Hajjaji, and D. Guyomar, *Oxygen vacancies effect on ionic conductivity and relaxation phenomenon in undoped and Mn doped PZN-4.5PT single crystals.* Journal of Physics D-Applied Physics, 2007. **40**(9): p. 2920-2926.
227. Suchanicz, J., *The low-frequency dielectric relaxation $Na_{0.5}Bi_{0.5}TiO_3$ ceramics.* Materials Science and Engineering B-Solid State Materials for Advanced Technology, 1998. **55**(1-2): p. 114-118.
228. Sinclair, D.C. and A.R. West, *Electrical properties of a $LiTaO_3$ single crystal.* Physical Review B, 1989. **39**(18): p. 13486-13492.
229. Guiffard, B., E. Boucher, L. Eyraud, L. Lebrun, and D. Guyomar, *Influence of donor co-doping by niobium or fluorine on the conductivity of Mn doped and Mg doped PZT ceramics.* Journal of the European Ceramic Society, 2005. **25**(12): p. 2487-2490.

230. Bidault, O., P. Goux, M. Kchikech, M. Belkaoumi, and M. Maglione, *Space-charge relaxation in perovskites.* Physical Review B, 1994. **49**(12): p. 7868-7873.
231. James, A.R., S. Priya, K. Uchino, K. Srinivas, and V.V. Kiran, *Investigation of intrinsic defect structure in 0.91Pb($Zn_{1/3}Nb_{2/3}$)O_3-0.09$PbTiO_3$ single crystal through AC conductivity.* Japanese Journal of Applied Physics Part 1-Regular Papers Short Notes & Review Papers, 2002. **41**(8): p. 5272-5276.
232. Singh, B.K. and B. Kumar, *Impedance analysis and high temperature conduction mechanism of flux grown Pb($Zn_{1/3}Nb_{2/3}$)$_{0.91}Ti_{0.09}O_3$ single crystal.* Crystal Research and Technology, 2010. **45**(10): p. 1003-1011.
233. Rafiq, M.A., M.E. Costa, and P.M. Vilarinho, *Defects and charge transport in Mn doped lead free $K_{0.5}Na_{0.5}NbO_3$.* Science of Advanced Materials, 2013. **Accepted**.
234. Chang, Y.F., Z.P. Yang, Y.T. Hou, Z.H. Liu, and Z.L. Wang, *Effects of Li content on the phase structure and electrical properties of lead-free ($K_{0.46-x/2}Na_{0.54-x/2}Li_x$)($Nb_{0.76}Ta_{0.20}Sb_{0.04}$)$O_3$ ceramics.* Applied Physics Letters, 2007. **90**(23): p. 232905-3.
235. Akdogan, E.K., K. Kerman, M. Abazari, and A. Safari, *Origin of high piezoelectric activity in ferroelectric ($K_{0.44}Na_{0.52}$)$Li_{0.04}$) - ($Nb_{0.84}Ta_{0.1}Sb_{0.06}$)$O_3$ ceramics.* Applied Physics Letters, 2008. **92**(11): p. 112908-3.
236. Skidmore, T.A., T.P. Comyn, and S.J. Milne, *Temperature stability of ([$Na_{0.5}K_{0.5}NbO_3$]$_{0.93}$-[$LiTaO_3$]$_{0.07}$) lead-free piezoelectric ceramics.* Applied Physics Letters, 2009. **94**(22): p. 222902-3.
237. Dai, Y.J., X.W. Zhang, and G.Y. Zhou, *Phase transitional behavior in $K_{0.5}Na_{0.5}NbO_3$-$LiTaO_3$ ceramics.* Applied Physics Letters, 2007. **90**(26): p. 262903-3.
238. *Critical raw materials for the EU, Report of the Ad-hoc Working Group on defining critical raw materials* http://ec.europa.eu/enterprise/policies/raw-materials/files/docs/report-b_en.pdf. 2010 [Accessed on 14-09-2013].
239. Song, H.C., K.H. Cho, H.Y. Park, C.W. Ahn, S. Nahm, K. Uchino, and S.H. Park, *Microstructure and piezoelectric properties of (1-x)($Na_{0.5}K_{0.5}$)NbO_3-x$LiNbO_3$ ceramics.* Journal of the American Ceramic Society, 2007. **90**(6): p. 1812-1816.
240. Klein, N., E. Hollenstein, D. Damjanovic, H.J. Trodahl, N. Setter, and M. Kuball, *A study of the phase diagram of (K,Na,Li)NbO_3 determined by dielectric and piezoelectric measurements, and Raman spectroscopy.* Journal of Applied Physics, 2007. **102**(1): p. 014112-8.
241. Ge, W., Y. Ren, J. Zhang, C.P. Devreugd, J. Li, and D. Viehland, *A monoclinic-tetragonal ferroelectric phase transition in lead-free ($K_{0.5}Na_{0.5}$)NbO_3-x%$LiNbO_3$ solid solution.* Journal of Applied Physics, 2012. **111**(10): p. 103503-6.
242. Park, S.-E. and T.R. Shrout, *Characteristics of relaxor-based piezoelectric single crystals for ultrasonic transducers.* Ultrasonics, Ferroelectrics and Frequency Control, IEEE Transactions, 1997. **44**(5): p. 1140-1147.
243. Shrout, T.R., R. Eitel, and C. Randall, *High performance, high temperature perovskite piezoelectric ceramics*, in *Piezoelectric materials in devices*, N. Setter, Editor. 2002, Ecole polytechnique fédérale de Lausanne. p. 413-432.

244. Safari, A. and E.K. Akdogan, *Piezoelectric and acoustic materials for transducer applications*. 2008, New York: Springer
245. Amorin, H., M.E.V. Costa, and A.L. Kholkin, *Microstructure and electrical properties of $SrBi_2Ta_2O_9$ ceramics processed by templated grain growth.* Advanced Materials Forum II, 2004. **455-456**: p. 35-39.
246. Brosnan, K.H., S.F. Poterala, R.J. Meyer, S. Misture, and G.L. Messing, *Templated grain growth of <001> textured PMN-28PT using $SrTiO_3$ templates.* Journal of the American Ceramic Society, 2009. **92**: p. S133-S139.
247. Amorin, H., A.L. Kholkin, and M.E.V. Costa, *Templated grain growth of $SrBi_2Ta_2O_9$ ceramics: Mechanism of texture development.* Materials Research Bulletin, 2008. **43**(6): p. 1412-1419.
248. Kimura, T., Y. Yi, and F. Sakurai, *Mechanisms of texture development in lead-Free piezoelectric ceramics with perovskite structure made by the templated grain growth process.* Materials, 2010. **3**(11): p. 4965-4978.
249. Kimura, T., Y. Miura, and K. Fuse, *Texture development in barium titanate and PMN-PT using hexabarium 17-titanate heterotemplates.* International Journal of Applied Ceramic Technology, 2005. **2**(1): p. 15-23.
250. Choudhury, S., L.Q. Chen, and Y.L. Li, *Correlation between number of ferroelectric variants and coercive field of lead ziconate titanate single crystals.* Applied Physics Letters, 2007. **91**(3): p. 032902-3.
251. Wang, K., J.-F. Li, and N. Liu, *Piezoelectric properties of low-temperature sintered Li-modified $(Na,K)NbO_3$ lead-free ceramics.* Applied Physics Letters, 2008. **93**(9): p. 092904-3.
252. Du, H., W. Zhou, F. Luo, D. Zhu, S. Qu, and Z. Pei, *An approach to further improve piezoelectric properties of $(K_{0.5}Na_{0.5})NbO_3$-based lead-free ceramics.* Applied Physics Letters, 2007. **91**(20): p. 202907-3.